

# **ULTRASONIC INSPECTION OF RAILROAD RAILS BY ELECTROMAGNETIC ACOUSTIC TRANSDUCERS (EMATs)**

**LLOYD J. GRAHAM  
JIM F. MARTIN**

**ROCKWELL INTERNATIONAL SCIENCE CENTER  
1049 Camino Dos Rios  
Thousand Oaks, CA 91360**



**MAY 1986**

**FINAL REPORT**

Document is available to the U.S. public through the  
National Technical Information Service,  
Springfield, Virginia 22161

**Prepared for**

**U.S. DEPARTMENT OF TRANSPORTATION  
FEDERAL RAILROAD ADMINISTRATION  
Office of Research and Development  
Washington, DC 20590**

This document is disseminated under the sponsorship of the Department of Transportation in the interest of information exchange. The United States Government assumes no liability for the contents or use thereof.

The United States Government does not endorse products or manufacturers. Trade or manufacturers' names appear herein solely because they are considered essential to the object of this report.

1. Report No. Report No. FRA/ORD-86/09	2. Government Accession No.	3. Recipient's Catalog No.	
4. Title and Subtitle ULTRASONIC INSPECTION OF RAILROAD RAILS BY ELECTROMAGNETIC ACOUSTIC TRANSDUCERS (EMATs)		5. Report Date MAY 1986	
		6. Performing Organization Code	
		8. Performing Organization Report No. SC5286.FR	
7. Author(s) Lloyd J. Graham and Jim F. Martin		10. Work Unit No. (TRAIS)	
9. Performing Organization Name and Address Rockwell International Science Center 1049 Camino Dos Rios Thousand Oaks, CA 91360		11. Contract or Grant No. DTFR53-80-C-00121	
		13. Type of Report and Period Covered Final Report September 30, 1980 to October 31, 1984	
		14. Sponsoring Agency Code	
12. Sponsoring Agency Name and Address U.S. Department of Transportation Federal Railroad Administration Office of Research and Development Washington, D.C. 20590			
15. Supplementary Notes			
16. Abstract <p>EMATs offer unique characteristics that appear to be advantageous for inspection of railroad rails. These characteristics include the features that EMATs do not require a liquid couplant or physical contact with the object being tested, they can generate ultrasonic wave modes that cannot be produced by conventional transducers and their ultrasonic beams can be steered electronically. This report describes the principal elements, results and conclusions of a four-year program for the development of EMAT systems for the ultrasonic detection and characterization of potentially hazardous defects in railroad rails. Testing in the laboratory on naturally occurring defect specimens and in the field under actual rail testing conditions has shown that EMATs can be adapted for field testing, can detect all the serious types of defects at the required sensitivity level and may be more sensitive to two types of serious defects, the transverse defects and vertical split head defects, than currently available test methods. A long-term side-by-side comparison with existing methods in a field test environment is still needed to confirm that additional defect detection reliability can be achieved by these attractive new rail inspection tools.</p>			
17. Key Words EMATs, electromagnetic acoustic transducers, railroad rails, defects, ultrasonic inspection, laboratory testing, field testing, shear-horizontal waves, shear-radial waves		18. Distribution Statement Document is available to the U.S. public through the National Technical Information Service, Springfield, Virginia 22161	
19. Security Classif. (of this report) UNCLASSIFIED	20. Security Classif. (of this page) UNCLASSIFIED	21. No. of Pages 239	22. Price

## PREFACE

This report describes the principal elements, results and conclusions of a four-year program for the development of electromagnetic acoustic transducers (EMATs) for the ultrasonic detection and characterization of potentially hazardous defects in railroad rails. Laboratory studies were performed at Rockwell International Science Center in Thousand Oaks, CA and at Magnasonics, Inc. in Albuquerque, NM. Field testing of a preliminary rail test cart was performed at the Santa Fe Railroad test track in Albuquerque, NM and at the FRA's Transportation Test Center in Pueblo, CO.

Throughout the program, assistance has been provided from several sources by the supply of rail defect specimens, other related material, and advice and consultation. Support has been received from the Sperry Rail Service Division of Automation Industries, Inc., the Santa Fe Railroad, the Association of American Railroads, and the Department of Transportation Transportation Systems Center. Dr. R.B. Thompson of Ames Laboratory and Dr. G.A. Alers of Magnasonics, Inc., both of whom did pioneering research on EMATs while at the Rockwell Science Center, have provided consultation for the program since leaving the Science Center. Additional rail defect specimens were provided by the Boston and Main, Burlington Northern, and the Seaboard System Railroads.

We particularly appreciate the valuable technical support of the following individuals: R.J. McCown of FRA; V. Hobbs of TSC; Dr. R. Steele of AAR; T.B. Hendricks and P. van Hemert of Sperry; C. Stearns and H. Beene of Santa Fe; A. Manzanares, D. MacLaughlan, L. Burns, H. Maiseri and C. Dziurzynski at Magnasonics; R. McCredie, C. Chisholm and R. Reiff of TTC; and Dr. P. Beckham, H. Feathers, Dr. W. Guthmiller, J. Liska, M. Mahoney, W. Peterson and C. Ruokangas of the Science Center.



## TABLE OF CONTENTS

	<u>Page</u>
1.0 EXECUTIVE SUMMARY.....	1
1.1 SUMMARY OF RESULTS.....	2
1.2 CONCLUSIONS AND RECOMMENDATIONS.....	4
2.0 INTRODUCTION.....	5
2.1 LIMITATIONS OF CURRENT RAIL INSPECTION METHODS.....	5
2.2 HISTORY OF THIS PROGRAM.....	7
2.3 GOALS OF THIS PROGRAM - MILESTONES.....	8
3.0 DESCRIPTION OF RAIL DEFECTS.....	10
3.1 TYPES OF RAIL DEFECTS CONSIDERED.....	10
3.2 DETECTION SENSITIVITY REQUIRED.....	11
4.0 EMATs FOR DETECTION OF RAIL DEFECTS.....	14
4.1 BASIC PRINCIPLES OF EMAT OPERATION.....	14
4.2 EMAT BEAM GEOMETRIES FOR DEFECT DETECTION.....	18
4.3 DESCRIPTION OF EMATs.....	19
4.3.1 Electromagnet.....	19
4.3.2 SR EMATs.....	21
4.3.3 SV EMATs.....	23
4.3.4 SH EMATs.....	24
4.4 ADVANTAGES OF EMATs FOR RAIL INSPECTION.....	26
5.0 LABORATORY TEST RESULTS.....	29
5.1 DESCRIPTION OF TEST FACILITIES.....	29
5.1.1 Laboratory Test Cart.....	29
5.1.2 Dynamic Laboratory Testing.....	36
5.1.3 Hand Mapping.....	37
5.2 RAIL DEFECTS TESTED.....	37
5.3 DEFECT DETECTABILITY RESULTS.....	39
5.3.1 Transverse Defects.....	41
5.3.2 Longitudinal Defects.....	48
5.3.3 Rail Conditions.....	58
5.3.4 Dynamic Effects.....	60
6.0 FIELD TEST RESULTS.....	67
6.1 FIELD TEST VEHICLE.....	67
6.2 DESCRIPTION OF FIELD TEST SITES.....	69
6.2.1 Santa Fe Test Track.....	71
6.2.2 Mainline Track and Siding.....	71
6.2.3 FAST Track.....	74

## TABLE OF CONTENTS

	<u>Page</u>
6.3 SUMMARY OF RESULTS.....	75
6.3.1 Santa Fe Results.....	75
6.3.2 Isleta Results.....	84
6.3.3 FAST Results.....	89
6.4 FACTORS ADVERSELY AFFECTING EMAT PERFORMANCE.....	94
6.4.1 Defect Detection.....	94
6.4.2 False Indication of Defects.....	101
7.0 REFERENCES.....	103
APPENDIX A - HARDWARE DESCRIPTION.....	A-1
APPENDIX B - DEFECT DOCUMENTATION.....	B-1
APPENDIX C - EXPERIMENTAL DATA.....	C-1

# LIST OF FIGURES

	<u>Page</u>
FIGURE 2-1 A CONVENTIONAL ULTRASONIC WHEEL PROBE UNIT.....	6
FIGURE 3-1 SHAPE AND POSITION OF SOME TYPICAL RAIL FLAWS.....	10
FIGURE 4-1 A PULSED WIRE ( $I_{ac}$ ) AND DC MAGNETIC FIELD ( $H_{dc}$ ) COMBINE TO PRODUCE A LOCALIZED FORCE WITHIN THE SAMPLE (F).....	14
FIGURE 4-2 THE ANGLE OF THE BEAM CAN BE CHANGED BY CHANGING THE FREQUENCY OF CURRENT IN THE COIL.....	15
FIGURE 4-3 THE AFFECT OF LIFT-OFF DISTANCE ON THE SIGNAL SIZE IS DEPENDENT ON BOTH EMAT GEOMETRY AND FREQUENCY OF OPERATION.....	17
FIGURE 4-4 SCHEMATIC OF EMAT BEAM GEOMETRY.....	18
FIGURE 4-5 ORIENTATION OF ELECTROMAGNET OVER THE RAIL WITH (A) SH EMAT POLE PIECES; (B) SR AND SV EMAT POLE PIECES.....	20
FIGURE 4-6 SIDE-BY-SIDE COMPARISON OF SR AND ST GEOMETRIES.....	21
FIGURE 4-7 SIDE-BY-SIDE COMPARISON OF TM AND PPM GEOMETRIES.....	25
FIGURE 5-1 LABORATORY RAIL TEST FACILITY.....	30
FIGURE 5-2 LABORATORY TEST CART.....	31
FIGURE 5-3 COMPONENTS OF THE LABORATORY RAIL INSPECTION SYSTEM.....	32
FIGURE 5-4 FUNCTIONS OF THE SIGNAL CONDITIONING AND DISPLAY ELECTRONICS.....	34
FIGURE 5-5 MOTION EMULATION MACHINE FOR EVALUATING EMAT PERFORMANCE UNDER DYNAMIC CONDITIONS.....	36
FIGURE 5-6 RESULTS OF HAND MAPPING THE TRANSVERSE DEFECT IN RAIL SPECIMEN NO. 320.....	38
FIGURE 5-7 APPERANCE OF THE DEFECT IN RAIL SPECIMEN NO. 320 AFTER BREAKING THE RAIL.....	38
FIGURE 5-8 THREE MODES FOR DETECTION OF TDS WITH UNIDIRECTIONAL SH EMATS.....	40
FIGURE 5-9 EXAMPLE OF TD DETECTION WITH SH AND SR EMATS.....	43
FIGURE 5-10 SIGNAL-TO-NOISE RATIO FOR SH WAVE DETECTION OF THE SIX TRANSVERSE DEFECTS EXPOSED BY RAIL BREAKING.....	46

# LIST OF FIGURES

	<u>Page</u>
FIGURE 5-11 DETECTION OF VSH DEFECTS WITH SR EMAT.....	50
FIGURE 5-12 DETECTION OF VSH DEFECT WITH SR, SH AND SV EMATS.....	51
FIGURE 5-13 DETECTION OF A CF DEFECT WITH SR EMAT.....	52
FIGURE 5-14 DETECTION OF A HSH DEFECT WITH SR EMAT.....	53
FIGURE 5-15 DETECTION OF HWS WITH SR EMAT.....	53
FIGURE 5-16 DETECTION OF BHC WITH SR EMAT.....	55
FIGURE 5-17 SIGNAL PATTERN FROM BOLT HOLES FOR SV EMAT OPERATING IN THE PITCH-CATCH MODE.....	56
FIGURE 5-18 SIGNAL PATTERN FROM BOLT HOLES FOR SV EMAT OPERATING IN THE PULSE-ECHO MODE.....	56
FIGURE 5-19 DISTRIBUTION OF NORMAL MAGNETIC FIELDS IN THE GAP AT ZERO AND 30 MPH SPEEDS.....	61
FIGURE 5-20 DEMONSTRATION OF THE PERFORMANCE OF THE FOAM AND WEAR PLATE METHOD OF SUPPORTING EMAT COILS.....	63
FIGURE 5-21 ULTRASONIC SIGNALS OBSERVED WITH SH WAVE EMATS OPERATING AT 0 AND 30 MPH.....	64
FIGURE 5-22 DEPENDENCE OF SIGNAL AND NOISE AMPLITUDES AT 30 MPH ON THE MAGNETIC FIELD AND DIRECTION OF ROTATION.....	65
FIGURE 6-1 EXPERIMENTAL EMAT RAIL INSPECTION TEST CART.....	68
FIGURE 6-2 DETAILS OF THE MAGNET SUPPORT WHEELS, EMAT POSITIONER AND DISTANCE ENCODER MOUNTING.....	69
FIGURE 6-3 TEST CART BEING TOWED AT FAST TRACK.....	70
FIGURE 6-4 TEST CART BEING UNLOADED AT THE SANTA FE TEST TRACK.....	70
FIGURE 6-5 LOCATION OF SANTA FE TEST TRACK IN SWITCH YARD.....	72
FIGURE 6-6 IDENTIFICATION OF SANTA FE TEST TRACK RAIL SECTIONS.....	72
FIGURE 6-7 MAP OF ISLETA TOWING TEST LOCATION.....	73
FIGURE 6-8 FACILITY FOR ACCELERATED SERVICE TESTING (FAST).....	74

## LIST OF FIGURES

	<u>Page</u>
FIGURE 6-9 THREE MODES OF DETECTION OF LARGE TDS WITH SH EMAT IN NO. 9E. TOP TRACE INDICATES LOCATION OF FIVE TDS CONFIRMED BY HAND-SCANNING.....	81
FIGURE 6-10 ILLUSTRATING THE POOR DETECTABILITY OF LARGE TD IN NO. 5W, POSSIBLY DUE TO AN ELECTROMAGNETIC COUPLING ANOMALY.....	82
FIGURE 6-11 DETECTION OF 1/4 IN. DEEP SAW CUT IN SIDE OF RAIL HEAD IN NO. 7W.....	83
FIGURE 6-12 THE TOWING TEST LOCATION; A) THE EMAT TEST CARRIAGE BEING TOWED ON THE MAINLINE TRACK; B) CURVE WHERE MOST OF THE MEASUREMENTS WERE MADE.....	86
FIGURE 6-13 LOCATION AND TYPE OF EACH RAIL JOINT IN 1200 FT LONG CURVE TRANSITION REGION SOUTH OF THE SIDING SWITCH.....	87
FIGURE 6-14 THE GAUGE SIDE WEAR PATTERN ON THE OUTSIDE RAIL IN THE CURVE.....	87
FIGURE 6-15 FORWARD AND REVERSE REFLECTION TRACES BY SH EMATS FROM LARGE UNMARKED TD IN INSIDE RAIL IN FAST SECTION NO. 10.....	92
FIGURE 6-16 MARGINAL DETECTION OF 3% TD IN FAST SECTION NO. 7.....	93
FIGURE 6-17 HISTOGRAMS OF SH DIRECT TRANSMISSION SIGNAL AMPLITUDE AND VARIABILITY WITHIN A RAIL SECTION FOR THE SANTA FE TEST TRACK RAILS.....	96
FIGURE 6-18 DEPENDENCE OF SIGNAL AMPLITUDE ON APPLIED BIAS MAGNETIC FIELD AT SELECTED POINTS ON FAST RAILS.....	98
FIGURE 6-19 AMPLITUDE OF RAYLEIGH WAVES EXCITED BY A MAGNETOSTRICTIVE MECHANISM IN LABORATORY RAIL SPECIMENS RELATIVE TO A FLAT PLATE OF ANNEALED STEEL.....	99

## LIST OF TABLES

		<u>Page</u>
TABLE 2-1	LIST OF PROGRAM MILESTONES.....	9
TABLE 3-1	LIST OF DEFECTS CONSIDERED IN THIS PROGRAM.....	12
TABLE 4-1	EMATS FOR RAIL INSPECTION.....	27
TABLE 5-1	LABORATORY RAIL DEFECT SPECIMENS.....	40
TABLE 5-2	TRANSVERSE DEFECTS TESTED IN THE LABORATORY.....	45
TABLE 5-3	LONGITUDINAL DEFECTS TESTED IN THE LABORATORY.....	49
TABLE 5-4	A SUMMARY OF THE INSENSITIVITY OF THE SH EMAT TO RAIL "CONDITIONS".....	59
TABLE 6-1	NATURAL DEFECTS IN FAST TRACK - 11 DECEMBER 1983.....	76
TABLE 6-2	SUMMARY OF ACCOMPLISHMENTS DURING FIELD TESTING AT SANTA FE.....	77
TABLE 6-3	DEFECTS IN EAST RAIL OF SANTA FE TEST TRACK.....	79
TABLE 6-4	DEFECTS IN WEST RAIL OF SANTA FE TEST TRACK.....	80
TABLE 6-5	DEFECTS IN ISLETA SIDING TRACK.....	90
TABLE 6-6	FAST SECTION NO. 10 INSTALLED TDS.....	91
TABLE 6-7	CURVE-FIT PARAMETERS FROM MAGNETIC FIELD DEPENDENCE TESTS.....	97



## 1.0 EXECUTIVE SUMMARY

This report describes the principal elements, results and conclusions of a four-year program to develop electromagnetic acoustic transducer (EMAT) systems for the ultrasonic detection and characterization of potentially hazardous defects in railroad rails. The program was a cooperative effort of Rockwell International, the Federal Railroad Administration (FRA) of the Department of Transportation, Sperry Rail Services, Magnasonics, Inc., Santa Fe Railroad, and the Association of American Railroads.

EMATs employ a combination of bias magnetic fields and pulsed coils to create ultrasonic waves in steel and other electrically conducting materials. They do not require contact, in principle, and therefore do not require any coupling fluids. In railroad rails, because the sound is generated in the surface of the steel itself, EMATs can be made insensitive to thin layers of oil or other lubricants on the surface. In addition, EMATs can generate types or modes of ultrasonic waves that cannot be produced by conventional rail inspection transducers and their beams can be steered electronically as well as mechanically. Finally, because the transducing elements themselves can be reduced to printed circuits on thin sheets such as mylar or kapton, the cost of replacing the sensors damaged in use can be made much lower than conventional rail inspection transducers.

This program was founded on earlier research funded by the FRA, and had two primary objectives. First, it was necessary to develop an EMAT that was capable of detecting and characterizing naturally occurring transverse defects (TDs) in the rail head and to demonstrate its operation. Second, it was necessary to construct a test vehicle that incorporated the EMAT technology necessary to detect and characterize all of the major defect types and demonstrate it in motion in the field. The approach involved development and testing at Rockwell International's Science Center in Thousand Oaks, CA, construction of the test vehicle at Magnasonics, Inc. in Albuquerque, NM, and field testing on Santa Fe tracks in New Mexico and FRA's Transportation Test Center in Pueblo, CO.

Testing in both the laboratory and the field was performed with a minimum of simulated rail defects, concentrating instead on a large collection of natural defects collected from numerous commercial rail lines in the

country. Three major types of EMATs were successfully adapted for field testing and were shown to detect all the serious classes of naturally occurring rail defects. In addition, the results indicate that EMATs may exhibit a higher degree of sensitivity than conventional rail transducers to two important defect classes, vertical split heads and transverse defects in the head. The final demonstration was carried out in Pueblo, where the test vehicle successfully detected and characterized all major defects in a section of track selected by the FRA.

A key result of this program was the investigation, feasibility testing and demonstration in the field of the value of pure shear horizontal (SH) acoustic waves for inspection of the rail head. EMATs can easily generate this form of ultrasound to flood the head of the rail like a searchlight beam for several tens of centimeters in either direction. Their sensitivity and potential for effectiveness in a regular field inspection program appear to match or exceed conventional inspection technology.

#### 1.1 SUMMARY OF RESULTS

During this program, a completely new type of EMAT never previously built, the twin magnet shear horizontal (SH), was designed, constructed, tested and modified, and successfully used to detect and characterize TDs in the rail head. Two other types of EMATs, the shear vertical (SV) and shear radial (SR), were redesigned for use in the program, and constructed and used to detect and characterize the other defect classes. A large number of natural rail defects were collected and used for testing EMATs in the laboratory and for calibration of the mobile EMAT test vehicle. Dynamic testing of all three EMAT designs was conducted on a laboratory setup capable of creating 30 mph surface speeds for a simulated rail geometry, and the sensitivity of the EMATs as a function of velocity was established. An EMAT test vehicle was designed, constructed and used as a mobile base for all of the sensors, signal conditioning, and electronics needed for testing the three EMAT types.

Testing of the EMATs developed in this program and those developed in previous programs were conducted under laboratory conditions, and under field conditions during sometimes rather severe weather, including subfreezing temperatures and blowing snow. Thirty-three rail specimens were employed in the laboratory, 26 of which possessed one or more defects. The other seven pos-

sessed some identifiable condition, such as severe head checking, that was not a defect. All but two were detected and adequately characterized using only EMATs. In the field, 56 defects were detected and characterized and nine non-defective conditions were encountered. All but one of these defects were detected and adequately characterizing using only EMATs. Another significant accomplishment was the detection of a very large unmarked TD (not constrained with safety straps) in the track at the FRA Transportation Test Center. If it had remained undetected, serious consequences might have resulted from its failure under the weight of a heavily loaded test train.

Out of 83 defects and the 16 conditions with which the EMAT sensors were tested, only three produced substantially inaccurate measurements by the EMATs. Two defects that were in fact large TDs were inaccurately characterized as such small TDs that the reflected signals would not have exceeded any reasonable detection criteria, and therefore would not have been detected. However, the SH EMAT configuration in this program was designed to provide a through-transmission signal used for calibration and a usually redundant inspection for TDs in the rail head. In both of these cases, the large TD flaws produced a large, easily detectable drop in the transmission signal. The third inaccuracy was that a sliver at an engine burn, characterized as a condition that was not a defect, produced a signal large enough to be classified as a small TD. There was no instance where a defect best suited for detection by the SR EMAT was missed. This includes all of the potentially serious VSH defects. The SV EMAT is best suited for detecting nearly vertically oriented bolt hole cracks (BHCs), but there were none of this type of defect available for testing.

The resulting score of 97% correct detection and characterization fell well above the 80% criterion established by the DoT early in the program as a yardstick against which the EMAT results were to be compared.

The significant disadvantages of EMATs established in this program are as follows. First, the SH transducers necessary for TD detection must at present be operated at frequencies ten times lower than that of conventional transducers. This results in substantially lower spatial resolution which becomes a problem near the rail ends. Second, all of the EMATs are sensitive to radio frequency radiation from electromagnetic machinery such as power generators. Third, the SH EMAT, operating at a frequency of 250 kHz, experienced

interference from acoustic noise generated by components of the EMAT system rubbing on the rail surface; this limited its operating speed to about 2-3 mph, although it had operated satisfactorily up to 30 mph under laboratory conditions. The SR EMAT, operating at about 2 MHz, did not experience this difficulty up to the maximum of 8 mph that the test vehicle could be safely operated in the field.

The significant advantages of the EMATs built and tested in this program are as follows. First, they do not require any fluid couplant and are insensitive to thin coatings (less than a few thousandths of an inch) of lubricants, paint or dirt on the rails. Second, they can generate SH acoustic waves, which have never been used in rail inspection, and because of their unique mode of propagation promise a higher detection reliability than conventional transducers. Third, the SH and SV EMATs can be configured so that they can electronically steer their acoustic beams within the rail without any physical reorientation of the sensor itself. Fourth, the cost of replacement EMAT sensors can probably be reduced to less than a few dollars apiece, which is quite inexpensive compared to conventional transducers. Finally, they possess the intrinsic potential for operating without being in contact with the rail surface at all. In this program, the largest liftoff from the rail that was achieved was about 1/8 in. with the SR EMATs. The SV and SH EMATs could not be removed as far as that, but were successfully operated at distances up to 0.040 in. from the rail surface.

## 1.2 CONCLUSIONS AND RECOMMENDATIONS

In our opinion, it has now been established that EMATs can in principle successfully detect and characterize all rail defects with an acceptable ability to reject nondefective rail conditions. This capability has been demonstrated on a moving test vehicle in the field under severe environmental conditions. More development is needed, particularly in the area of improved SH EMATs. In addition, it is now timely to conduct a serious long-term side-by-side comparison of EMATs with conventional rail inspection transducers in a controlled test facility that accurately represents field conditions. We therefore recommend two parallel programs: a small but steady research effort to improve SH EMATs so they can be used at higher frequencies and practical speeds, and a large multi-year evaluation of state-of-the-art EMAT technology at a FRA field test site.

## 2.0 INTRODUCTION

Railroads are one of the safest and most efficient means of transportation in use, and will continue to be a vital part of the nation's commerce and defense systems for the foreseeable future. The integrity of the rail they operate over is protected by a number of vigorous, proven nondestructive evaluation programs based on decades of experience with ultrasonic and magnetic field techniques. However, despite their very high safety record, some accidents do occur that are caused by rail defects. In recent years, the number of such accidents per year has averaged about 800, representing about \$37 million per year in damage to equipment and track. Both the railway companies and the federal government are committed to reducing these numbers, and support research and development efforts on a variety of fronts. The objectives of these efforts fall into three general classes: study of the sources of rail defects; the conditions that cause them to grow; and improvements in the techniques for detecting them. The program described in this report addressed the latter objective.

### 2.1 LIMITATIONS OF CURRENT RAIL INSPECTION METHODS

Ultrasonic transducers currently in use for rail inspection are made from piezoelectric elements contained in a liquid-filled cavity, either a wheel or a skid ("sled"). There are generally several of these transducers contained inside the skid or wheel that is in contact with the railhead, and either slides or rolls along the rail during the inspection process. The ultrasonic beam generated by each transducer propagates through the liquid, through the base of the skid or wheel, through a liquid couplant that is squirted onto the railhead in front of the transducer unit, and then into the rail. The ultrasonic energy reflected off a defect or other reflecting surface in the rail follows the reverse path back to the same transducer (pulse-echo) or to another transducer that is positioned properly for the particular rail geometry (pitch-catch). Figure 2-1 shows the geometry of one configuration of piezoelectric transducers that is commonly used.

The principal problem experienced with these ultrasonic probe units is the difficulty in maintaining adequate acoustic coupling at the contact between the probe and the rail surface. Under nonideal conditions, such as

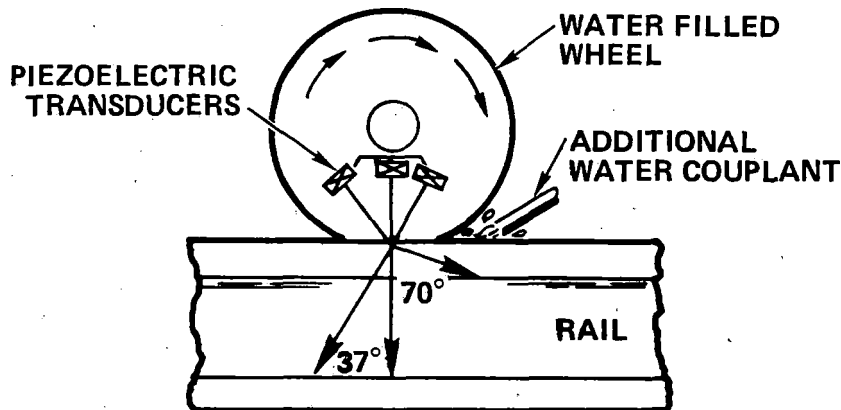


FIGURE 2-1 A CONVENTIONAL TYPE OF ULTRASONIC WHEEL PROBE UNIT.

when the rail surface is pitted or corroded, or when covered with a nonconductor such as sand, coal dust or grease, the acoustic coupling can be lost. For example, lubrication of the rails, a fuel conservation step introduced recently in rail transportation, leaves a continuous thin layer of grease on the rail surface that interferes with coupling. It is also inconvenient to have to provide storage for the large quantity of liquid couplant on the rail inspection vehicle for wetting the rail surface ahead of the ultrasonic probe unit and it is difficult to keep it from freezing in cold weather.

In addition, the need to transmit the ultrasonic beam through the fluid couplant and into the rail surface generates refraction due to the differences in the ultrasonic transmission velocity in the couplant and the rail steel. The refraction at the rail surface limits the angle at which beams can be transmitted into the rail; angles greater than about  $70^\circ$  risk trapping the beam entirely within the surface of the rail, thereby failing to provide an inspection of the entire volume of the head of the rail and potentially failing to detect critical defects growing deep within the head. At a beam angle of  $70^\circ$  in the rail, less than a  $2^\circ$  misalignment of the transducer in the wheel and/or a tilt of the surface of the rail head will cause this to happen.



The work described in this report was focused on the development of a new technology for ultrasonic detection of rail defects, electromagnetic acoustic transducers (EMATs). With EMATs, the mechanism for generating the ultrasonic beam in the rail is completely different than with piezoelectric transducers. Instead of generating the ultrasonic beam within the transducer and transmitting it into the rail, the EMAT generates the ultrasonic beam directly within a thin surface layer of the rail itself. The EMAT transducer is a pattern of electrical conductors, which may be wires or printed-circuit patterns, suspended near the rail surface. A constant "background" magnetic field is applied to magnetize the rail surface under the transducer. A pulse of radio frequency energy is applied to the EMAT, inducing eddy currents in the nearby rail surface. The magnetic fields of the eddy currents and the constant "background" magnetic field forces interact within the rail surface to produce compression and tension patterns which generate ultrasonic energy. Patterning of the EMAT conductors in a manner similar to the patterning of radio transmission "beam" antennas causes the ultrasonic energy generated within the rail to also be transmitted as a beam within the rail.

Since the EMAT coupling mechanism is electromagnetic rather than mechanical, in principle no direct contact is required between the EMAT and the rail, although signal strength limitations make operation very close to the rail surface necessary. In addition, EMAT transducers eliminate the need to carry large quantities of couplant material, and EMAT transducers can generate beam polarizations within the rail which cannot be transmitted through the fluids required with existing piezoelectric systems. These new polarizations are expected to provide substantially increased abilities to detect flaws which are difficult or impossible to detect with present systems.

A more detailed discussion of EMAT principles and the advantages and disadvantages of both methods of generating the ultrasonic beam is presented later in this report after the EMATs used in this program are described.

## 2.2 HISTORY OF THIS PROGRAM

The program was first funded in 1980 by the Federal Railroad Administration (FRA) of the Department of Transportation and performed by the Rockwell International Science Center. It extended and optimized for rail inspection basic work done there on EMAT technology in the later 1970's. The FRA

and Rockwell both recognized that these new transducers offered unique characteristics that appeared to be advantageous to rail inspection. The EMAT transducers also exhibited disadvantages, including low transduction efficiency, but it was felt that the new capabilities deserved exploration in depth.

This program represents one phase of an effort (Contract No. DTFR53-80-C-00121) to further develop EMAT technology for rail inspection and to transfer it from the laboratory to an experimental field test unit. A previous effort, called Phase A, was funded under Contract No. DOT-FR-9143,<sup>1</sup> and provided initial laboratory validation of the basic approach for all of the major defect types except transverse defects (TDs).

### 2.3 GOALS OF THIS PROGRAM - MILESTONES

The overall objective of this program was to develop an EMAT-based system which is both capable of operating in the railroad environment and fundamentally suitable as a starting point for development of a high speed rail inspection system that would have fully automated classification of flaws as to type and severity. It was expected to provide detection and classification performance at least comparable to that of present systems, with the possibility for increasing the reliability of detection of several types of serious rail defects. This expectation has been attained, but complete proof-testing of EMATs will require extensive side-by-side comparison with current devices on a rail inspection vehicle.

The scope of the effort is illustrated by the list of program milestones presented in Table 2-1.

TABLE 2-1. LIST OF PROGRAM MILESTONES

Milestone #1

The interim technical goals which correspond to the EMAT system performance required to show feasibility in the lab will be set. Target values for parameters such as transmitter power, frequency of operation, receiver recovery time, magnetic field amplitude and liftoff will be established. In conjunction, for each flaw type, a size will be determined which represents the minimum detection capability needed.

Milestone #2

The amount of degradation of EMAT performance under dynamic conditions will be determined in the laboratory.

Milestone #3

A determination will be made of the degree of feasibility of detection of all flaw types with EMATs. This determination will include at least an adequate conceptual basis for detection.

Milestone #4

A demonstration will be made of adequate laboratory signal-to-noise ratio for each critical flaw type with the finalized EMAT configurations, magnetic fields, frequencies of operation and minimum liftoff.

Milestone #5

A demonstration will be performed of the degree of characterization of each flaw type which can be expected with the EMAT system in the field.

Milestone #6

A demonstration of feasibility will be performed for basic system operation in dynamic conditions in the laboratory. The degree of both detection and characterization will be determined.

Milestone #7

The prototype system will be installed on a rail inspection vehicle.

Milestone #8

Evaluation and documentation of the prototype system will be completed.

### 3.0 DESCRIPTION OF RAIL DEFECTS

The defects that are of concern in railroad rails are areas of separation within the volume of steel rails which results in a decrease in the ability of the metal to support tensile and/or shearing forces. These defects generally initiate at microscopic volume defects in the rail steel, such as inclusions or porosity, and grow under the cyclic application of mechanical and thermal stresses while the rails are in service. Inspection of the rails is required periodically to detect these growing defects before they attain a critical size for the maximum imposed stresses that the rails must support.

#### 3.1 TYPES OF RAIL DEFECTS CONSIDERED

Rail defects are categorized by the plane in which they lie. If their areas lie predominantly in a plane that is perpendicular to the length of the rail, they are classified as transverse defects. If their areas lie in the vertical or horizontal planes extending along the rail length, they are classified as longitudinal defects. They are further classified according to whether they exist in the head, web or base of the rail section. Some typical examples of rail defects that were of concern in this program are illustrated in Fig. 3-1.

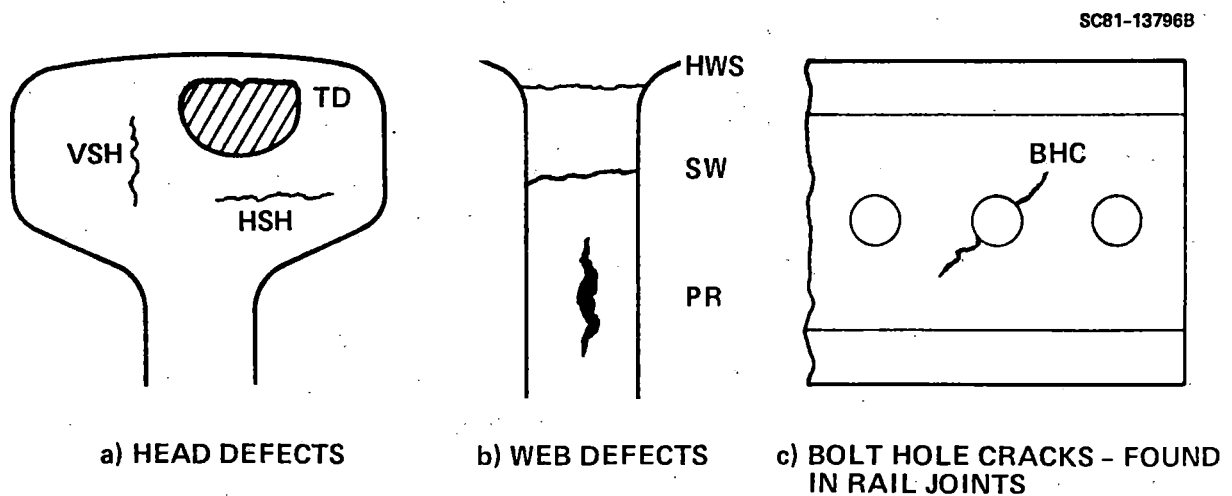


FIGURE 3-1 SHAPE AND POSITION OF SOME TYPICAL RAIL FLAWS.

Head defects can lie in any of the three orthogonal planes. The vertical split head (VSH) and horizontal split head (HSH) are characterized by the distance that they extend along the length of the rail. The transverse defect (TD) is more localized and is characterized by the percentage of its area relative to the cross sectional area of the railhead. Transverse defects are further classified as to their cause or detailed morphology, such as from an engine burn (EBF), a weld defect (DWP), a detail fracture from surface shelling or head checking (TDD or DF), a compound fissure which has some non-transverse components of fracture surface (TDC or CF), and a true transverse fissure (TDT) which usually initiates at an internal inclusion.

Web defects are similar to the VSH and HSH, and are characterized by their length along the rail. These are the head web separation (HWS), the split web (SW) and the piped rail (PR). Another web defect associated with the drilled holes used to fasten adjacent rail sections together is the bolt hole crack (BHC). Defects that might occur in the base of the rail are generally detected by visual inspection and were not addressed in this program.

### 3.2 DETECTION SENSITIVITY REQUIRED

The flaws present in in-service rails have been grouped into twelve separate types based on the identification of flaw types which appear in the FRA Track Safety Standards document (TSS). For each type, Table 3-1 shows the value of minimum detectable size which was judged to be essential performance for the system development activities undertaken in this research effort. It must be noted that the values selected and shown in Table 3-1 are not intended to imply that smaller defects are not critical or hazardous, or that defects smaller than these sizes need not be detected and reported. These values were selected based on discussions with knowledgeable industry and government sources to represent values for which detection is absolutely mandatory for any system which is to be acceptable for practical use by the railroads. Values in excess of those stated were determined to represent entirely unacceptable risk levels if the system failed to detect them.

The values shown are recognized to be arbitrary to some extent because the exact levels of risk presented by the various types and sizes of defects are not well understood. Many factors are believed to affect the growth rates, and hence the risk of flaws in track. These factors include the

TABLE 3-1. LIST OF DEFECTS CONSIDERED IN THIS PROGRAM

Defect or Hazardous Condition Type	Abbreviation	Acceptable Minimum Detectable Size
1. Transverse Fissure	TD	10% of railhead area
2. Compound Fissure	CF	10% of railhead area
3. Detail Fracture from Shelling or Head Checking	DF	10% of railhead area
4. Transverse Defect from Engine Burn	EBF	10% of railhead area
5. Defective Weld	DWP	10% of railhead area
6. Horizontal Split Head	HSB	3 in.
7. Vertical Split Head	VSH	12 in.
8. Split Web	SW	2 in.
9. Piped Rail	PR	6 in.
10. Head-Web Separation	HWS	2 in.
11. Bolt Hold Crack	BHC	1 in.
12. Ordinary Break	---	Not applicable

tonnage of trains passing over the defect, rail metallurgical condition, rail stress states, track stiffness and temperature-induced stresses.<sup>2</sup> Inspection intervals vary substantially between railroad companies and between various stretches of track of each company. All of these factors militate against setting absolute flaw size limits as measures of risk.

Furthermore, flaw sizes are extremely difficult to measure precisely. The apparent flaw size varies as a function of the impingement direction of the ultrasonic beam, the polarization of the beam, the compression or tension state of the material around the flaw and the exact transmission characteristics of the flaw (i.e., is the flaw an open crack, a fluid-filled crack, or a solid but nonmetallic inclusion in a weld). These factors may vary depending on the time of inspection; temperature variations alone have been observed to cause changes of over 20% in apparent flaw sizes in rail.<sup>2</sup>

The complexities inherent in the detection, sizing and risk assessment of flaws cause most railroad companies to act to remove any detected flaw



of critical types such as listed in Table 3-1. The FRA Track Safety Standards mandate remedial actions, up to and including replacement of the rail, for Types 1-5 whenever detected, regardless of size. The values shown in Table 3-1 were derived to provide realistic targets to assess the basic adequacy of EMAT transducers for application to rail flaw detection in the field.

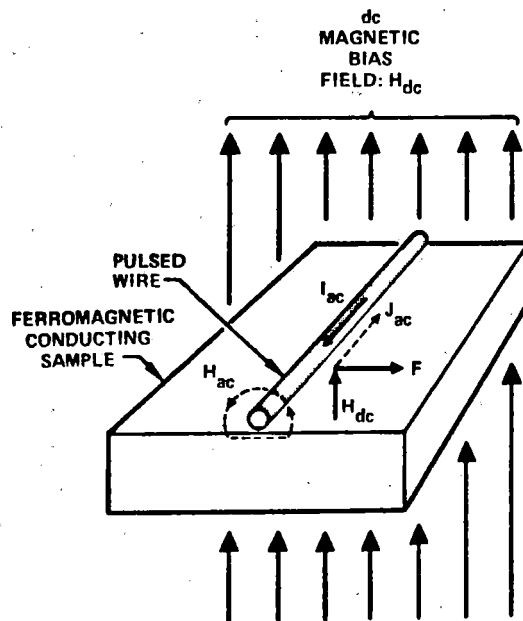
## 4.0 EMATs FOR DETECTION OF RAIL DEFECTS

This section contains a complete description of the EMATs used in this program, how they work and their advantages and disadvantages.

### 4.1 BASIC PRINCIPLES OF EMAT OPERATION

Figure 4-1 shows a pulsed wire that induces a magnetic field  $H_{ac}$  which, in turn, induces an eddy current  $J_{ac}$  in the very near surface of a nearby conducting sample. If a separate bias magnetic field  $H_{dc}$  is imposed over the same region with the right geometry, the combination of the bias magnetic field and the eddy current produces a sideways force on the eddy current. This force is then transferred to the lattice of the sample with the same frequency as the original pulsed current in the wire.

If the geometry of the transducer coil and its current are repeated with alternating signs under the bias magnet, the pattern of instantaneous lattice forces that are produced within the test object propagates as an ultrasonic beam. The directions of propagation and polarization of this beam



SC83-20860

FIGURE 4-1 A PULSED WIRE ( $I_{ac}$ ) AND DC MAGNETIC FIELD ( $H_{dc}$ ) COMBINE TO PRODUCE A LOCALIZED FORCE WITHIN THE SAMPLE ( $F$ ).

are determined by the geometry of the EMAT coil, or more specifically, the pattern of the eddy currents that are induced in the surface of the test object by the coil, and the direction of the bias magnetic field vector at the surface of the part. This mechanism of generating the ultrasonic beam within a surface layer of the test object itself, rather than in the transducer, is why an EMAT does not have to be in physical contact with a conductor to generate or receive an ultrasonic beam. However, the EMAT coil must be close to the part since the magnitude of the eddy currents, hence, that of the ultrasonic beam, decreases approximately exponentially with the separation distance (lift-off).

Figure 4-2 illustrates the EMAT generation of a shear wave that is polarized vertically, or a shear vertical (SV) wave. This is the same as that produced by mode-converting a longitudinal wave which impinges on the surface at an angle through a plastic wedge, a water bath or a water-filled ultrasonic inspection wheel. The propagation direction of the mode-converted shear wave

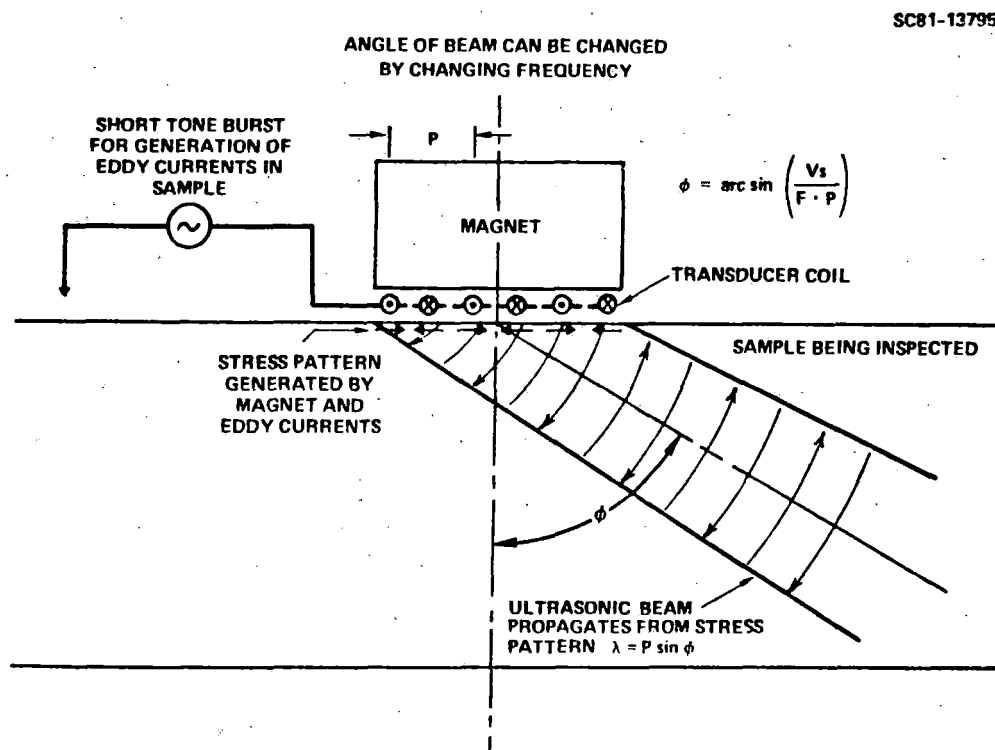


FIGURE 4-2 THE ANGLE OF THE BEAM CAN BE CHANGED BY CHANGING THE FREQUENCY OF CURRENT IN THE COIL.

can be predicted using the acoustic Snell's law of refraction, the wave velocities in the two media, and the incident angle of the longitudinal beam. With piezoelectric transducers, the shear wave angle is changed by mechanically changing the angle of the longitudinal wave transducer or tilting the test piece.

A similar situation exists for determining the propagation direction of the shear wave produced by an SV EMAT, although the controlling factors are different, as illustrated in Fig. 4-2. In this case, the periodicity of the EMAT coil,  $P$ , the frequency of the electrical tone burst,  $F$ , and the shear wave velocity in the sample,  $V_s$ , are the controlling factors. The propagation angle of the shear wave is determined by the relation shown at the upper right in this figure,  $\phi = \arcsin (V_s/FP)$ . This figure illustrates, in slightly more depth, the mechanism of ultrasonic beam-forming by EMAT transducer. Further, it graphically illustrates how beam scanning can be performed electronically by merely changing the driving frequency rather than mechanically tilting, which can be useful and more convenient for some applications. Changing the beam angle might be necessary, for example, if two SV EMATs a fixed distance apart were used for rail inspection in the pitch-catch mode and the height of the rail changed in going from one section of track to another.

There is another feature of these transducers that is not illustrated: the basic symmetry of the coil causes a second ultrasonic beam to be generated at an angle  $-\phi$  in addition to the one shown. This bidirectional feature is common to most basic EMAT types and may or may not be useful in a particular application. In a development described later, this property was defeated to produce a unidirectional shear horizontal (SH) wave that propagates at  $90^\circ$  within the railhead for the detection of transverse defects. The third type of wave used in this program, the shear radial (SR), propagates at  $0^\circ$  in the rail, and is therefore inherently unidirectional.

Although the noncontact operation of EMATs is one of the features that makes them a valuable addition to the arsenal of ultrasonic inspection transducers, they need to be in close proximity to the test object for effective production of eddy currents. Figure 4-3 shows that the closer the EMAT coil is to the specimen, the higher the S/N ratio will be. These data exhibit an approximately exponential decrease in the received signal amplitude with

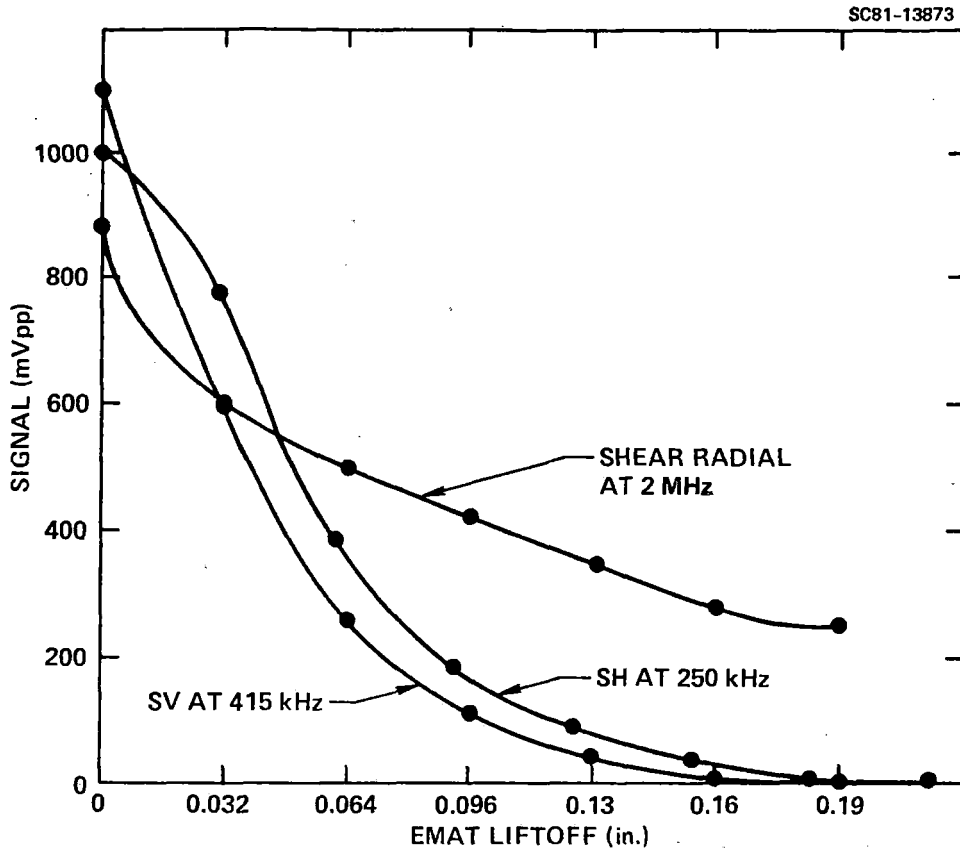


FIGURE 4-3 THE AFFECT OF LIFT-OFF DISTANCE ON THE SIGNAL SIZE IS DEPENDENT ON BOTH EMAT GEOMETRY AND FREQUENCY OF OPERATION.

increasing lift-off spacing as predicted by theory. The optimum point to operate on these curves and how much loss in signal strength is acceptable depends on the application.

The rail inspection environment is fairly severe; for example, the vertical mismatch at rail ends can be as large as 1/4 in. We have studied several approaches for attaining full noncontact operation in this environment since it is an attractive concept, but it also appears extremely challenging to achieve. In this program, it was established that the high transmitter power and large magnetic fields required to operate at the 1/4 in. lift-off are beyond the present state-of-the-art. In addition, a servo mechanism track-following system required to maintain the EMATs at a fixed lift-off distance would be cumbersome and expensive. The alternative approach that we have taken is to take advantage of the low inertial mass and flexibility of the EMAT coils and let them just slide along in light contact with the rail-head. They are protected by a thin (less than 20 mil thick), ski-tipped, flexible

wear plate that permits them to ride up over the bumps in the rail surface. This EMAT skid assembly is held down against the rail surface by light spring pressure provided by a reticulated foam backing. This technique also maintains a constant signal strength by minimizing variations in the EMAT lift-off distance. Signal strengths are attenuated only 2-3 dB from their zero lift-off values by the wear plate. This concept was tested in the laboratory in this program using a flywheel with 1/4 in. bumps attached, moving at a rim speed of 30 mph. In a separate program, it has also been reduced to practice for gas pipeline inspection, where girth weld beads on the inside of the pipes also extend 1/4 in. above the surface of the pipe walls, at about 16 mph by Magnasonics, Inc. It has worked very well for rail testing in both the laboratory and the field, and is simple and economical to implement.

#### 4.2 EMAT BEAM GEOMETRIES FOR DEFECT DETECTION

Three separate EMAT systems were used in the various rail defect measurements. The three types of EMATs each generate shear waves which are distinguished by their directions of propagation and polarization. These directions dictate the types of rail defects they detect. Figure 4-4 indicates the beam geometries for the three basic EMAT types; the shear radial (SR), shear vertical (SV) and shear horizontal (SH). These EMAT geometries were selected as a result of the Phase A research efforts.<sup>1</sup>

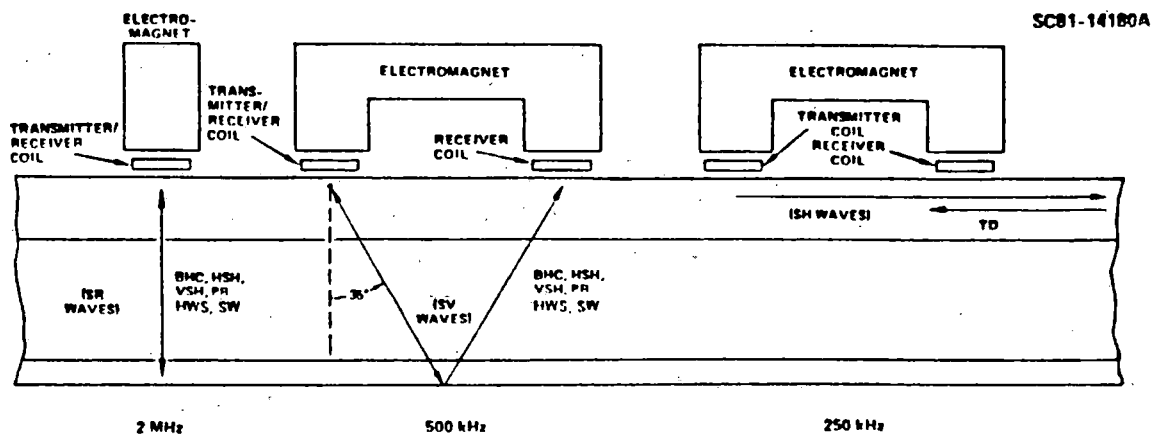


FIGURE 4-4 SCHEMATIC OF EMAT BEAM GEOMETRY.



The shear radial, or SR EMAT at the left in Fig. 4-4 produces a radially polarized shear wave; that is, the wave has shearing components polarized outwards throughout the entire 360° of its circumference. The direction of propagation is straight down, at 0° to the surface normal, and it interacts with defects lying both perpendicular and parallel to its direction of propagation. This type of wave cannot easily be produced using piezoelectric transducers.

The shear vertical, or SV EMAT, produces a shear wave that propagates at an angle to the surface normal and is polarized in the plane formed by the surface normal and propagation directions. This is exactly the same type of wave produced by mode conversion when a longitudinal wave produced by a piezoelectric transducer is directed at an angle onto the surface of the test object, as described previously. However, the angle of propagation of the EMAT beam can easily be changed by changing the frequency of the transmitter pulse.

The shear horizontal, or SH EMAT, produces a shear wave that propagates out from under the transducer nearly parallel to the object's surface with a polarization that is parallel to the surface. This is not a surface wave but a bulk shear wave which floods the railhead with ultrasonic energy. Like the shear radial wave, this type of wave also cannot be easily produced by piezoelectric transducers.

#### 4.3 DESCRIPTION OF EMATS

EMATs are generally designated by the type of ultrasonic wave that is produced, but usually there is more than one way to produce each type of wave. The particular variations that were used in this program will be described in detail in the following sections. In all but one case, the same electromagnet was used for supplying the bias magnetic field.

##### 4.3.1 Electromagnet

The solenoid for generating the bias magnetic field for the EMAT coils is shown in Fig. 4-5. It has an iron core 2 in. x 6 in. cross section (12 sq in. area) and has two encircling coils consisting of 1700 turns of #12 copper wire each. At its normal operating condition, it draws 6 amps and dissipates 300 W of electrical power. Its total weight is approximately

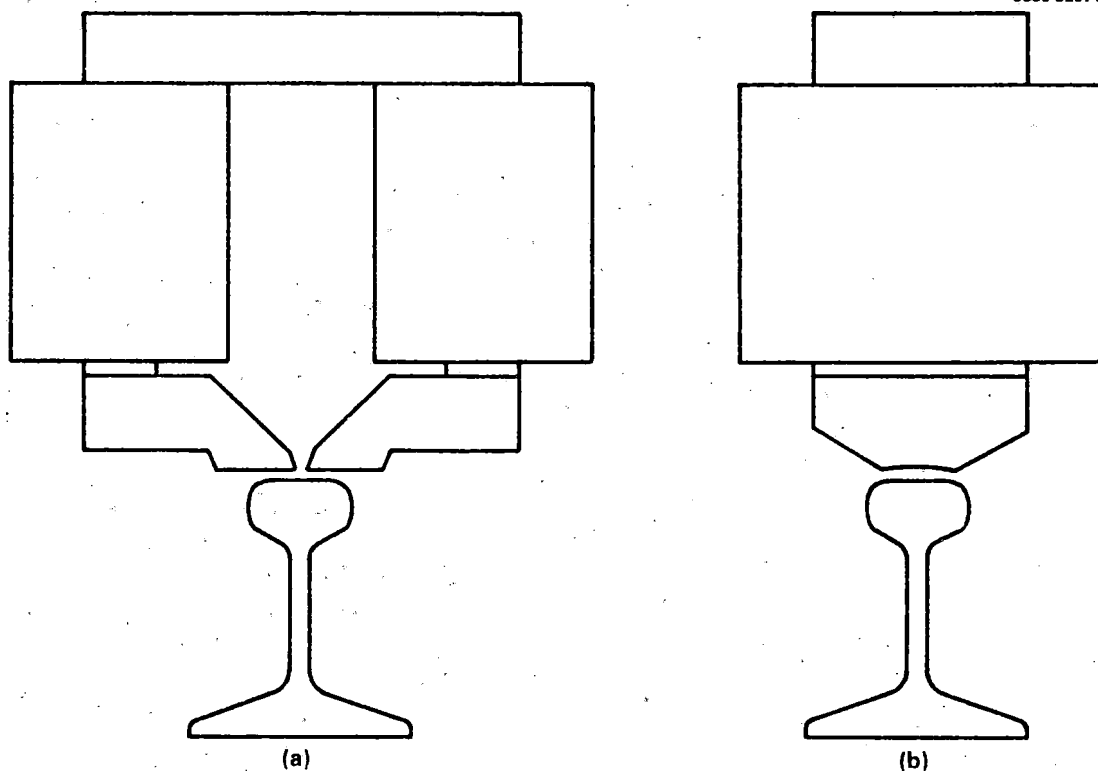


FIGURE 4-5 ORIENTATION OF ELECTROMAGNET OVER THE RAIL WITH (A) SH EMAT POLE PIECES; (B) SR AND SV EMAT POLE PIECES.

315 lbs. This solenoid was already available and proved to be adequate for the experiments performed in this program. However, future programs will probably require a somewhat differently shaped electromagnet designed to fit under a rail inspection car and capable of delivering more magnetic flux through the EMAT to the rail.

The pole pieces which attach to the electromagnet and "focus" the magnetic flux into the railhead play a critical role in the performance of the EMATs. Different configurations are required for the SH EMAT than for the SR and SV EMATs, and the electromagnet also must be rotated 90° for the two configurations. The final pole piece designs used in this program are indicated in Fig. 4-5. Their detailed dimensions are given in Appendix A. The nominal spacing between the pole piece and the rail surface is 1/4 in., but this is not a critical dimension. The normal component of magnetic field was measured to be 8 kGauss at the SH EMAT and 11 kGauss at the SR and SV EMATs.

#### 4.3.2 SR EMATs

The SR EMAT is a simple spiral coil underneath a single magnet pole piece. A variation on this is the shear transverse (ST) EMAT, which can be readily fabricated as a two-sided printed circuit board. A side-by-side comparison of the SR and ST geometries is shown in Fig. 4-6. The SR EMAT produces a radially polarized shear wave which propagates at  $0^\circ$ ; that is, normal to the surface of the railhead. Measurements on the rails showed that the amplitude of the signal reflected off the base of the rail was a maximum for two positions of the EMAT as it was moved sideways across the railhead. These positions corresponded to each half of the circular spiral being centered over the rail web. This indicates that the direction of polarization of the shear wave that propagates preferentially down through the rail web is in the transverse plane.

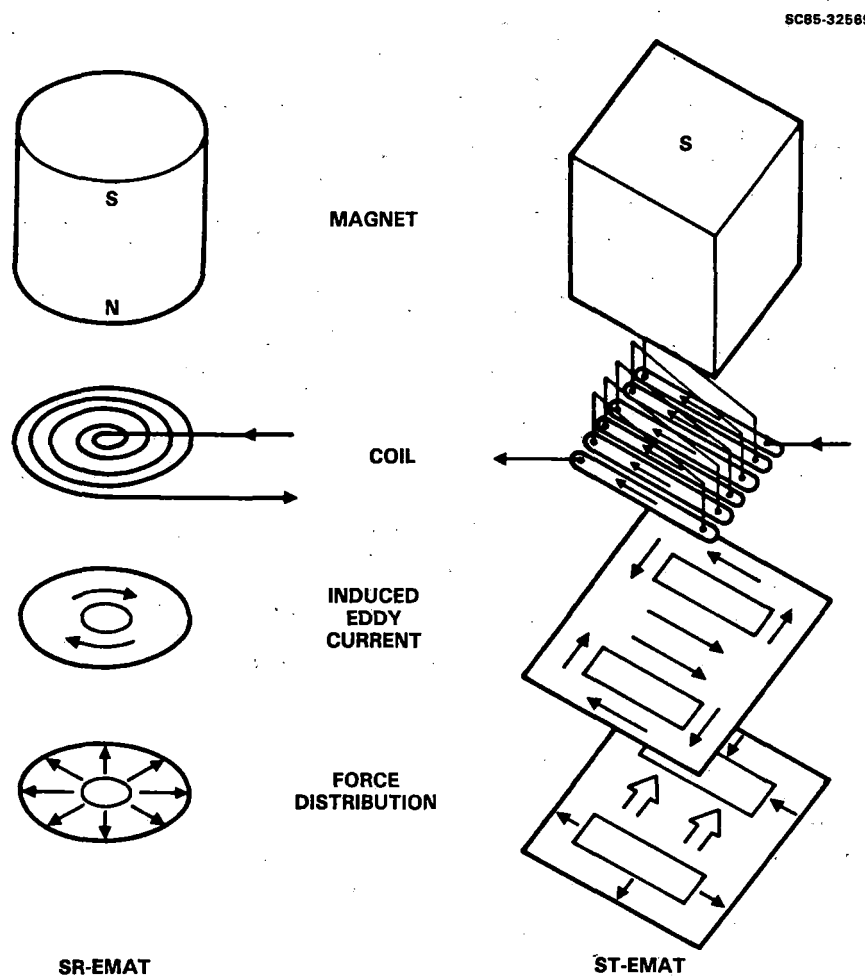


FIGURE 4-6 SIDE-BY-SIDE COMPARISON OF SR AND ST GEOMETRIES.

The ST EMAT, although having quite a different geometry, is in effect two overlapping SR coils. In the overlap region between the two eddy current loops that it produces, the shear force is enhanced which increases the signal-to-noise ratio of the return signal. However, there are unwanted shear waves generated on either side of the main beam that can reverberate within the railhead and create spurious signals. The electrical return elements of the EMAT are on top of the circuit board and do not contribute to the generation of the eddy currents in the rail surface. The orientation of the ST EMAT was selected so the polarization was also in the transverse plane as with the SR EMATs.

All of the laboratory measurements were made with the SR EMATs. The advantage of the ST EMAT was realized at about the same time the field measurements were started and was used thereafter. The shear radial transmitter and receiver EMATs were two separate spiral-wound coils of wire placed side by side in a single unit (Serial No. R172) which fit under a single pole piece. Both spiral coils were the same and consisted of about 40 concentric turns of 6 mil copper wiring, forming a flat pancake about 1/2 in. in diameter. The spacing of the two coils in the EMAT unit was 1 in. between centers, and they were aligned under the pole pieces so that one followed the other along the rail. A copper foil shield between and above the two spirals reduced the radiative pickup of the transmitter pulse by the receiver coil to a practical level. Frequency of operation was 1.9 MHz.

Attachment and alignment with the pole pieces was accomplished by glueing a layer of reticulated foam material between the back surface of the EMAT coils and a thin sheet of transformer steel. Magnetic force held this assembly firmly in position during operation, but still allowed adjustment of the alignment by tapping on the edge of the transformer steel. The EMAT coil was separated from the railhead by a 15 mil thick plastic insulator and a 5 mil low electrical conductivity titanium wear plate. The wear plate, used with all EMATs in this program, had ski-tipped leading and trailing edges to guide the EMAT over rail end steps and other surface irregularities.

The ST EMAT served as both transmitter and receiver in the pulse-echo mode. It consisted of eight parallel conductors, each about 1 in. long and

covering an area 0.8 in. wide on one side of a PC board. Interconnects between the conductors were provided on the reverse side of the PC board.

The transducer was mounted under one of the magnet pole pieces through the use of an aluminum frame which fit around the pole piece. A strip of 10 mil thick wear-resistant, high molecular weight plastic clamped to the leading and trailing edges of the frame served as a wear plate between the EMAT and the rail surface. A reticulated foam material between the back of the EMAT and the pole piece loaded it lightly against the top of the rail. Thumbscrew adjustment provided correct positioning of the aluminum frame and EMAT sideways across the railhead.

#### 4.3.3 SV EMATs

The SV EMATs were simple meander coils printed on one side of a PC board. For pitch-catch operation, the transmitter and receiver EMATs were under separate pole pieces which were about 10 in. apart and followed one another along the railhead, as in Fig. 4-4. This distance is determined by the angle of the shear wave beam from vertical and the distance between the surface of the railhead and some other reflecting surface, usually the bottom surface of the rails. For pulse-echo operation, the transmitter and receiver were placed one on top of the other under a single pole piece.

The SV meander coils were about 1-1/2 in. wide and 2-1/2 in. long on PC boards and were both identical (Serial Nos. V124 and V125). They had a periodicity of 12.2 mm, which combined with their frequency of operation of 460 kHz produced an ultrasonic beam at 35° from the vertical. Attachment and alignment with the pole pieces were the same as for the SR transducers in laboratory tests. The primary advantage of the SV wave is to provide another angle for interrogating a bolt hole area in case a bolt hole crack is oriented nearly vertically and cannot be seen by the 0° SR wave. The ability to generate this angle beam is necessary if a system comprised entirely of EMATs is to be used to detect all critical rail defects, such as bolt hole cracks. However, the polarization and propagation characteristics of the EMAT-generated 35° SV beam are virtually identical to the 35° beam now in use on existing systems so its flaw detection capabilities are well understood. The flaw detection capabilities of the other EMAT transducer types were not as well understood. Their development also addresses the major issues which are

anticipated for the development of the 35° SV transducers, such as mounting methods and magnet requirement. Accordingly, the use of the 35° transducers was limited to initial laboratory testing to focus the available resources on the evaluation of the new and different characteristics inherent in the SR/ST and SH EMAT types.

#### 4.3.4 SH EMATs

The SH EMAT is more complex than the other two types. The magnet for it has a twin pole structure, giving it the name twin magnet or TM, which can be implemented with an electromagnet, as shown in Fig. 4-5, with the solenoid rotated 90° from its SR or SV position. The circuit coil for it uses a thin two-sided PC board which has current going one way in the top and the opposite way in the bottom conductors. This TM version of the SH EMAT, for which a patent has been applied for, was first reduced to practice during this program.

An earlier version of the SH EMAT uses a simpler coil, but requires several periodic alternating magnetic poles which can be implemented more easily using permanent magnets than electromagnets. Figure 4-7 compares the periodic permanent magnet and the twin magnet SH EMATs in greater detail; they are nearly the same in their effect. In the TM version, the two straight, long magnetic poles of opposite polarity substitute for the straight, long electrical conductors of opposite current direction in the PPM version. Likewise, the meandering current conductor in the TM substitutes for the periodic magnetic pole configuration in the PPM EMAT. Both configurations produce the desired force distribution, indicated by the large arrows at the bottom of the figure. The new TM version is not quite as efficient, however, because part of the available energy goes into the production of forces at right angles to the desired direction, indicated by the small arrows at the bottom of the figure. However, the disadvantage of the PPM EMAT for use in testing ferromagnetic materials is that Barkhausen noise is produced if the PPM transducer is moved at any appreciable speed. In a railhead, the magnetic domains in the rail are flipped back and forth between north and south polarizations as the magnet segments of alternating polarization pass over, producing acoustic noise signals that can be comparable in amplitude to the flaw signals. Therefore, the PPM EMAT cannot be used as a moving receiver on a ferromagnetic

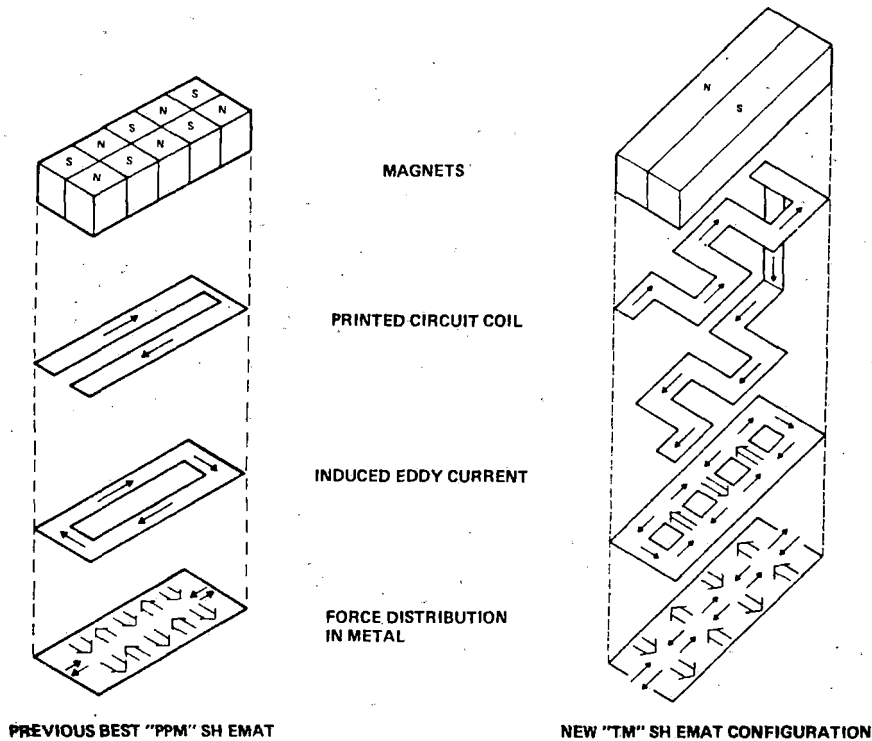


FIGURE 4-7 SIDE-BY-SIDE COMPARISON OF TM AND PPM GEOMETRIES.

material. However, it can be used as a transmitter, since the Barkhausen noise is small compared to the amplitude of the ultrasonic wave generated by the EMAT. In this program, a PPM EMAT was used as a transmitter because of its greater efficiency, and a TM EMAT was used as a receiver because it causes far less Barkhausen noise.

The PPM SH wave transmitter that was used (Serial No. H1603) consists of a single loop conductor, about 1/4 in. wide and 2 in. long, made up of 20 turns of fine copper wire underneath 16 samarium cobalt permanent magnets arranged with alternating polarity. The spacing between magnets with the same polarity of 12.6 mm determined the operating frequency of 250 kHz. The EMAT was all self-contained within an aluminum housing, 3/4 in. x 3/4 in. x 3 in. It was guided along the rail by a gimbal trailer hitch attached to the electromagnet pole pieces. It slid along the railhead separated from it by 3 mil thick insulating plastic and a 5 mil titanium or 10 mil plastic wear plate.

The receiver transducer (Serial No. H212) was of a new design not previously used. It was basically of the TM configuration, except that two meander coils were formed on the PC board, offset from each other by one-fourth of the meander coil period. The two coils were insulated from each other and had separate output leads which connected to a combined impedance matching and quadrature detector circuit. Two separate outputs from this circuit provided signals detected by the transducer that arrived from two separate directions along the length of the rail. This is termed a "unidirectional SH wave receiver", since signals arriving from both the forward and reverse directions are separately available with a 16 dB discrimination in their amplitudes.

The size of the meander coils for this transducer was about 1/4 in. wide and 2 in. long, and with the same periodicity and operating frequency as the transmitter. The electromagnet pole pieces extended in from above the sides of the rail and were separated by 1/4 in. at their closest points at a position above the edge of the meander coils at the center of the rail. The coils were held in position by attachment to a semi-rigid plastic sheet bolted to the pole pieces. The plastic sheet allowed vertical movement while maintaining horizontal alignment, so that the EMAT could follow surface irregularities in the railhead under a light spring loading. This loading was provided by a reticulated foam material in the space between the EMAT and the magnet pole pieces. The meander coil was separated from the railhead by 15 mil plastic insulation and either the titanium or plastic wear plate.

#### 4.4 ADVANTAGES OF EMATS FOR RAIL INSPECTION

At this point, it is useful to compare the relative merits of EMATs with conventional ultrasonic wheel probe units. Table 4-1 shows a summary of the relative advantages and disadvantages of using EMATs for inspection of rails. The first advantage is related to the lack of a requirement for mechanical contact to obtain predictable coupling. EMATs are much more tolerant than fluid-filled probe units to nonideal surfaces, such as those which are pitted or corroded, or those which are covered with a nonconductor such as coal dust or oil. They are more tolerant of temperature variations than the fluid-filled wheels. They have a potential for high speed because of their



TABLE 4-1. EMATs FOR RAIL INSPECTION

Advantages	Disadvantages
No contact is required	Low efficiency
<ul style="list-style-type: none"> <li>• Predictable coupling</li> <li>• Nonideal surface tolerance</li> <li>• Potential high speed</li> <li>• Temperature variation tolerance</li> <li>• No water path delay</li> <li>• No wheel reverberation/noise</li> </ul>	Large magnet required Limited resolution Sensitive to lift-off
SH elastic wave at 90° possible	
<ul style="list-style-type: none"> <li>• Sensitive to TD, VSH</li> </ul>	New technology
No refractive index effect	<ul style="list-style-type: none"> <li>• Complex electronics</li> <li>• Limited field experience</li> </ul>
SR elastic wave at 0° possible	
<ul style="list-style-type: none"> <li>• Very sensitive to VSH</li> </ul>	

noncontact property and because there is no water path delay. For most conventional wheel probes, the delay within the water is actually twice the delay that occurs within the steel; hence, in addition, there is elastic wave reverberation within the wheel that appears as noise in the ultrasonic waveform. The second major advantage is that the SH elastic wave at 90° is possible. This ultrasonic wave is not currently used in rail inspection and promises to be much better than the conventional high angle SV waves for finding transverse defects. Third, the EMATs do not suffer from the refractive index effect that the ultrasonic wheel does. The speed of sound in water is one-fourth the speed of sound in steel. As a result, a 2° misalignment of the wheel with the rail surface will result in an 8° misalignment of the beam within the rail. Fourth, the SR EMAT produces a 0° shear wave, which is difficult to produce by any other means for rail inspection, and which appears to be particularly sensitive to the VSH defects.

The foremost disadvantage of EMATs is that they are inefficient for generating ultrasonic energy compared to piezoelectrics. They also require a large bias magnet, which means that the inspection car has to be capable of supplying a substantial amount of electric power. They have limited resolution because the pulses in the rf coils have to be relatively long (temporally)

to compensate for the low efficiency. Due to the electromagnetic nature of the generation of the wave patterns, the signal levels vary exponentially with the lift-off gap which must be compensated for or carefully controlled. Finally, this is a new technology which has not had the benefit of 50 years of development, testing and field use.

## 5.0 LABORATORY TEST RESULTS

This section contains detailed descriptions of the laboratory rail testing facility, the rail defect specimens, and the defect detectability results using the three EMAT systems.

### 5.1 DESCRIPTION OF TEST FACILITIES

All of the early rail defect measurements in this program were done one rail specimen at a time by moving the EMAT transducers in increments along the rail and plotting the defect signal amplitudes point-by-point. This was adequate for optimizing the system design and for establishing detectability for a few defects, but was slow and did not include the dynamic time windowing, peak reading and stripchart recording (or other type of real-time display) required of an inspection system. For Milestone 4 and 5 measurements, an expanded test facility was established using the optimized EMAT systems and additional electronics to more closely approximate the data collection and display methods that would be used in field testing. These electronic components were later assembled together on a rail utility cart under a subcontract to Magnasonics, Inc. to provide a self-contained, mobile test vehicle for field testing. A third facility, also provided by Magnasonics, Inc., was used to meet the requirements of Milestone 2 to evaluate EMAT performance under dynamic conditions in the laboratory. These facilities are described in the following sections. A brief description of the hand-mapping methods used to independently characterize the rail defects using conventional ultrasonics is also included.

#### 5.1.1 Laboratory Test Cart

Figure 5-1 is a photograph of the rails test laboratory constructed at the Science Center. Forty feet of rail were laid out in a line at one time and bolted to the floor. The rail defect specimens ranged in length from 2 ft to 8 ft so that, on the average, about eight defects were in place for testing in any given setup.

The magnet support cart maintained alignment of the EMATs with the rail head and a magnet-to-rail gap of about 1/4 in. as it was moved down the line of rails. The EMATs and EMAT holders, the magnet power supply, the EMAT

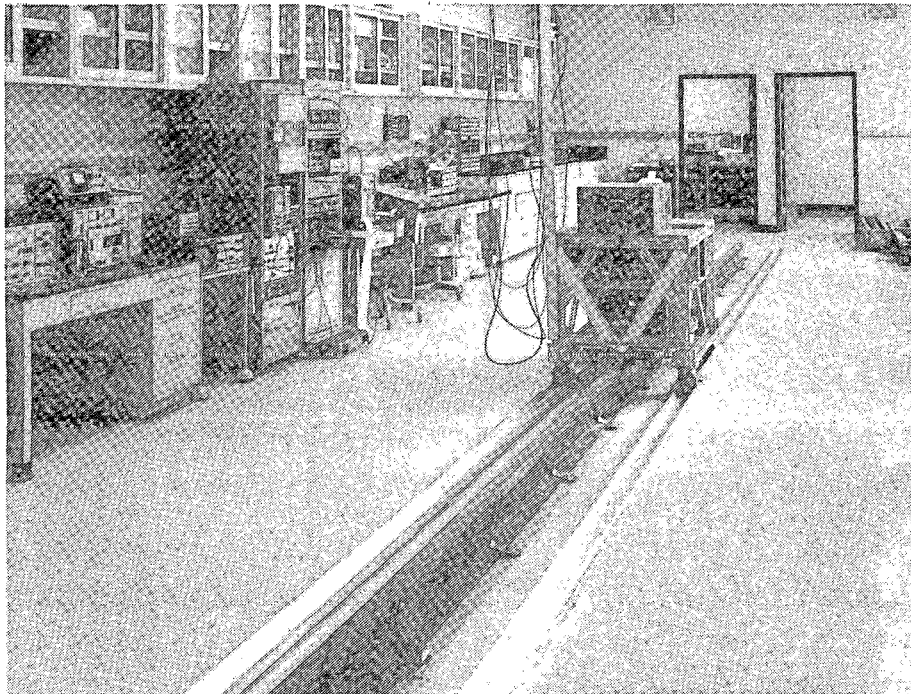


FIGURE 5-1 LABORATORY RAIL TEST FACILITY

impedance matching electronics, and the EMAT receiver preamplifier were also located on the cart.

The rest of the electronics was contained in the two tall equipment racks at the left center of Fig. 5-1, and a two-channel strip chart recorder was on the adjacent table. Overhead, 50 ft long coax cables provided the interconnection to the cart. In the right background the edge of the stockpile of rail defect specimens is visible. An overhead chain hoist on a track running the length of the room was used to handle and position the rail specimens.

Figure 5-2 shows a closer view of the magnet support cart. A distance encoder attached to the base of the cart rolled along the rail and provided synchronization between the strip chart recorder drive, the EMAT transmitter pulses and the cart movement. Also mounted on the cart in back of the distance encoder was a water-filled ultrasonic inspection wheel. It had two piezoelectric transducers inside, one to generate a  $0^\circ$  longitudinal wave in the rail (vertical) and the other to generate a  $70^\circ$  mode-converted shear wave. A water supply was kept on the cart to provide acoustic coupling between the

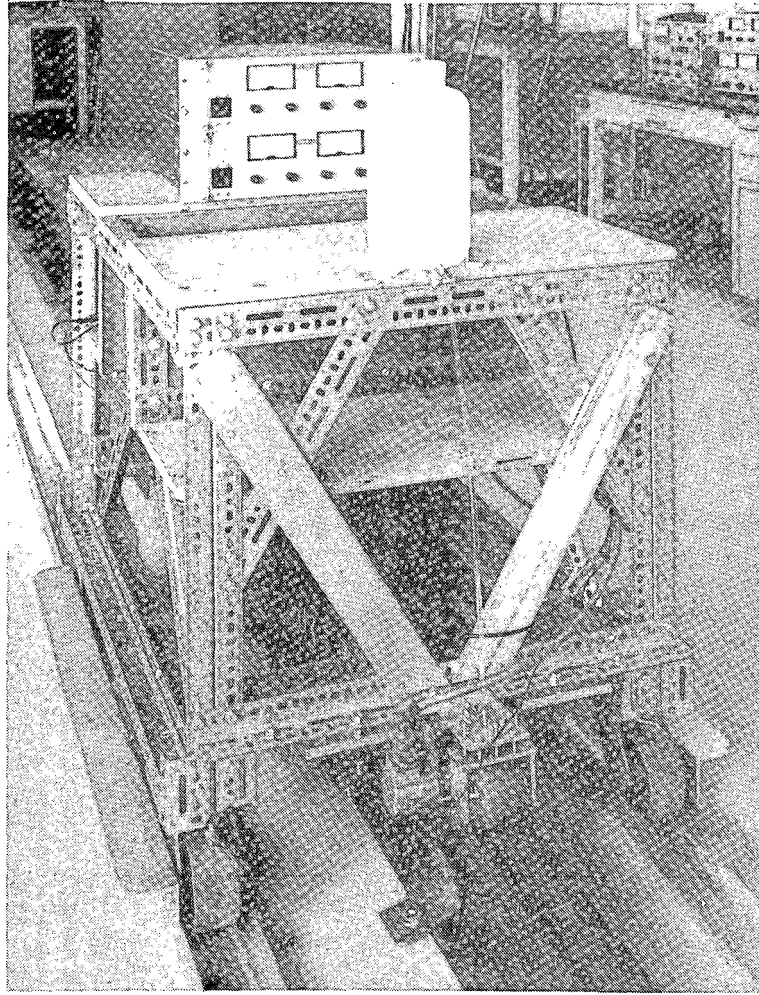


FIGURE 5-2 LABORATORY TEST CART.

rubber wheel and the rail head. Water-filled wheels of this sort are in current usage for rail inspection, and it was our intent to record the outputs from the wheel and the EMATs simultaneously on the two-channel strip chart recorder for direct comparison. However, we soon found that correct operation of the ultrasonic wheel required automatic mechanical alignment jigs that were too costly for the program budget to allow, and that any comparisons made without such alignment would have very little meaning. We soon abandoned attempts at comparison and no further discussion of the laboratory results with the ultrasonic wheel will be given in this report.

EMAT Transducers and Electronics: Three separate EMAT systems were used in the various rail defect measurements. Figure 5-3 is a block diagram of the components of the rail inspection system. The components to the right side of the vertical dashed line were located on the test cart. The three separate EMAT systems were operated separately rather than simultaneously as

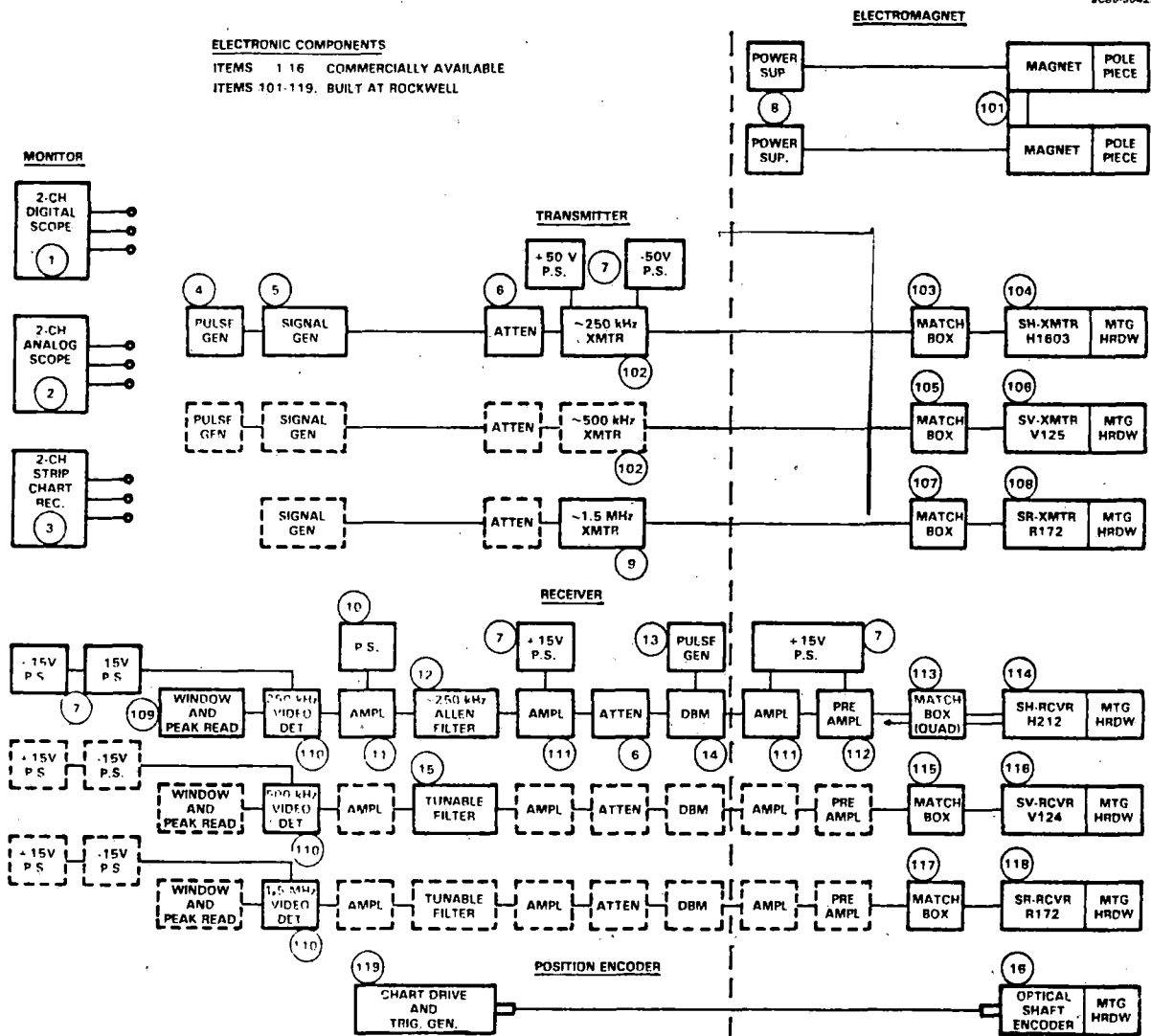


FIGURE 5-3 COMPONENTS OF THE LABORATORY RAIL INSPECTION SYSTEM.

they would be for actual rail inspection to avoid duplication of several of the components. The components that were common to each system are indicated by dashed outlines in Fig. 5-3. A complete description of each component is included in Appendix A.

Several new components were added to the electronic systems after the Milestone 3 work was completed, primarily to facilitate data collection and display. These included a distance encoder to report the EMAT position along the length of the rails, additional signal conditioning electronics and a stripchart recorder for producing continuous records of ultrasonic signal amplitudes with position along the rails. Although it has been our practice to use commercially available equipment whenever possible throughout this program, the requirements for most of these items could not be met commercially, and so they had to be designed and constructed in our laboratory.

Distance Encoder: The distance encoder system consisted of an optical shaft encoder (BEI Electronics, Inc., Model H25) and a custom-built pulse division circuit. As the encoder wheel rolled along the rail with the EMAT test cart, it produced 8192 electrical pulses per revolution which were supplied to the divider circuit. There were two outputs from this circuit. One provided pulses to the EMAT transmitter so that it could be triggered at fixed distances along the rail independent of the test cart speed. The distance between transmitter pulses could be selected in  $1/32$  in. increments between  $1/32$  in. and  $1/2$  in. A setting of  $1/4$  in. per trigger pulse was commonly used during the rail defect measurements, which corresponds to a transmitter pulse repetition frequency of 70 Hz for a cart speed of 1 MPH.

The second output of the pulse divider circuit controlled the chart drive speed of the stripchart recorder to provide for a correspondence between positions on the rails and on the chart recordings. The distance scale factor could be selected in unit increments from 1:1 to 16:1 for greater or lesser distance resolution in the chart recordings. Some charts were made at a 1:1 scale, for example, for determining the resolution of bolt hole crack sizing, but most were made with a 10:1 length reduction (5 ft rail = 6 in. chart).

Signal Conditioning Electronics: The additional signal conditioning electronics implemented during this phase of the test program were in the receiver section to the left of the vertical dashed line in Fig. 5-3. Their functions are illustrated in Fig. 5-4.

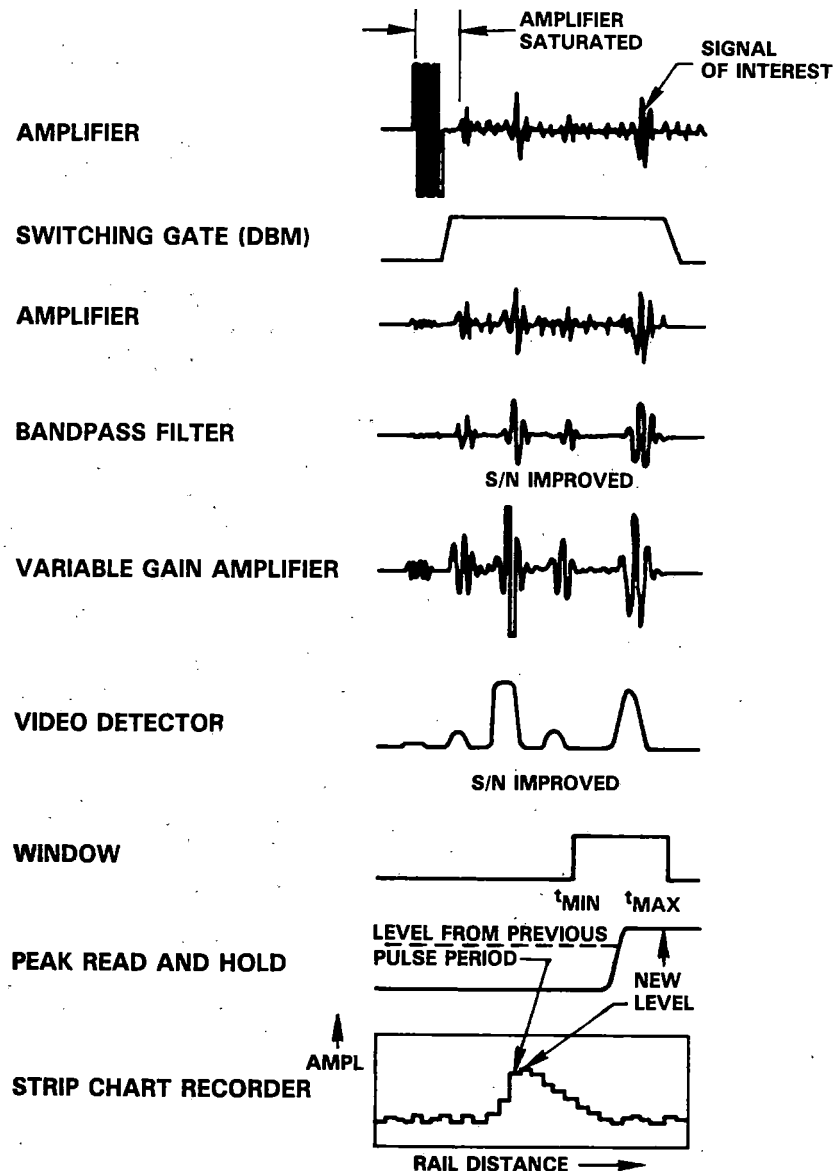


FIGURE 5-4 FUNCTIONS OF THE SIGNAL CONDITIONING AND DISPLAY ELECTRONICS.

After the first, fixed gain amplifier stage, a switching gate was added (Hewlett-Packard double balanced mixer, Model 10514) to reduce the amplitude of the transmitter feedthrough pulse ("main bang") to prevent saturation dead-time from occurring in subsequent stages of amplification. The switch was turned on just after the main bang by a synchronized pulse generator and was turned off after all ultrasonic signals of possible interest had occurred.



Without this switch, the amplifier dead-time extended into the time period where the bolt hole reflection occurred in some of the lighter rail specimens.

After a further fixed gain stage of amplification, a bandpass filter centered at the particular EMAT operating frequency was used to increase the signal-to-noise ratio (S/N). A passive filter centered at 250 kHz (Allen Avionics, Inc., Model F2463) provided an improved S/N for the SH EMAT system over the active Krohnkite filter used early in the program.

A final variable gain amplifier stage was implemented so that the amplitude of the signal selected for monitoring could be optimized to the dynamic range of the following video detector stage. The adjustment of the signal amplitude was actually accomplished by step attenuators having a total range of over 100 dB in 1 dB steps in conjunction with an amplifier stage. The attenuator readings also provided a convenient means for recording relative signal amplitude levels among various test conditions.

Three separate video detectors were constructed for use at the three EMAT operating frequencies (about 250 kHz, 460 kHz and 1.8 MHz). These detectors produced waveforms whose instantaneous voltage was roughly the square of the amplitude of the envelope of the rf waveforms. Thus, the amplitudes of the larger signals, which are of more interest than the smaller, spurious signals due to grain scattering reflections in the rails, are accentuated, resulting in a further increase in the S/N.

To detect and record the presence of defects or distinguishing conditions in the rails, a second, adjustable switching gate (or time window) and a voltage peak read and hold circuit were provided. The position and width of the time window were independently adjustable to accommodate detection of ultrasonic signals reaching the receiver EMAT over a variety of different paths. These parameters could be predicted and set beforehand for a given rail geometry, defect type and EMAT type. For example, for the detection of the reflection from a bolt hole and/or a bolt hole crack using a 0° SR EMAT, the time window would be adjusted to be fairly narrow ( $\sim 50 \mu\text{s}$ ) and to occur shortly after the main bang (depending upon the size of the rail,  $t_{\text{min}} = 60\text{--}100 \mu\text{s}$ ); for the detection of a transverse defect using a 90° SH EMAT, the window would be wider (200–300  $\mu\text{s}$ ) and would start further out in time.

In any case, the maximum positive voltage excursion that occurred

within the selected time window was detected by a peak reading voltmeter for each occurrence of the transmitter pulse. That reading was held and displayed by the stripchart recorder (Gould, Inc., Model 2200S) until the next transmitter pulse occurred and a new reading was taken. In this way, a semicontinuous recording of the signal amplitude that occurred within a selected time window was made as the test cart was moved down the length of the rail. Many examples of the recordings that were made for various rail defects will be shown in the next section of this report.

#### 5.1.2 Dynamic Laboratory Testing

A requirement of Milestone 2 was that the amount of degradation of EMAT performance under dynamic conditions be determined in the laboratory. This was accomplished by construction and use of a motion emulation machine.

A 20 in. diameter solid steel wheel was fabricated with a 1/2 in. thick by 3 in. wide flange machined in place around its circumference. This wheel was mounted on a shaft which was driven by a 3 hp motor through a double belt pulley system to provide the capability for making measurements at variable rim speeds up to 30 mph. A photograph of this machine is shown in Fig. 5-5. The EMAT support shoe, to the right of the photo, was attached to a

SC36616

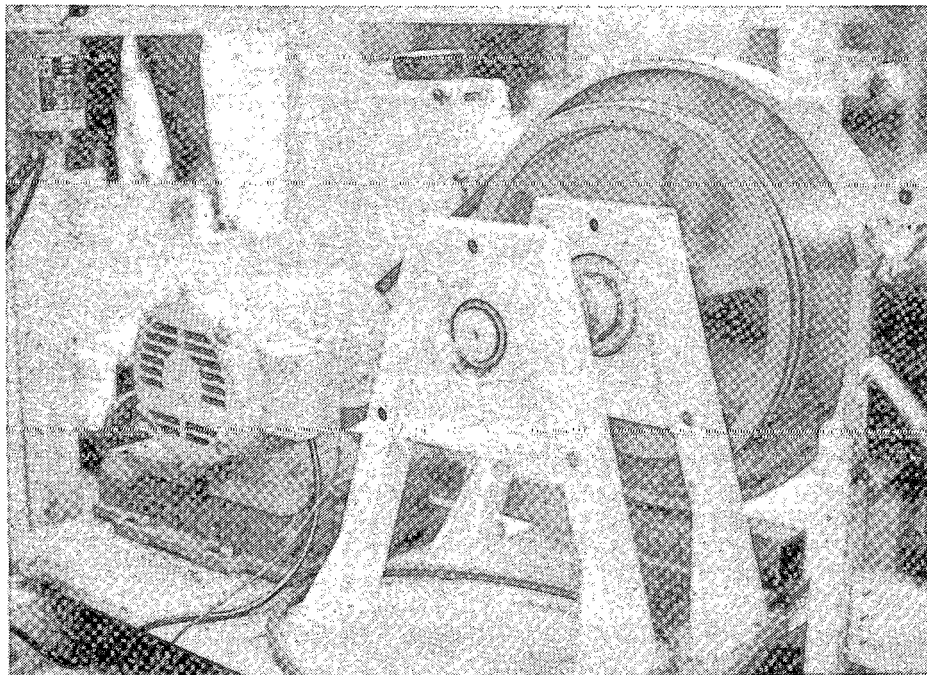


FIGURE 5-5 MOTION EMULATION MACHINE FOR EVALUATING EMAT PERFORMANCE UNDER DYNAMIC CONDITIONS.

fixed frame through a movable parallelogram linkage that allowed a pneumatic cylinder to hold the EMAT against the wheel with an adjustable force.

Several different types of tests were made with this machine to demonstrate the various aspects of dynamic operation of the EMATs. The first was the development and proof-testing of the compliant EMAT support and the flexible titanium foil wear plate concepts. As part of this development, a 1/4 in. high by 3/4 in. long protrusion was fastened to the wheel simulating a rail end mismatch. It was shown that the EMAT support survived more than 30,000 of these bumps at 30 mph. Without the bumps, the titanium survived hundreds of hours when wearing against a smooth surface, but its life was reduced considerably if grit was applied to the wheel. Realistic estimates of the mean time between failure of this structure cannot be made without extensive field testing.

Other measurements were made of the bias magnetic field distributions under the electromagnet pole pieces under dynamic conditions, EMAT signal strengths and motion-induced noise. The results of these measurements are presented elsewhere in this report.

#### 5.1.3 Hand Mapping

Hand mapping of all the laboratory rail defect specimens was done using a Krautkramer-Branson Sonoray 303B UT transmitter/receiver with conventional 0° longitudinal, and 45° and 70° mode-converted shear waves depending on the defect orientation. The time-of-flight of the signal reflected from the defect and the ultrasonic beam angle defined a point on the surface of the defect. Points at which the amplitude of the reflected signal were down 6 dB from the maximum were taken to be its lateral boundaries. An example of the results of hand mapping results is shown in Fig. 5-6. A photograph of the defect surface taken after the rail was broken (Fig. 5-7) shows good agreement with the hand mapping result, although this good agreement was not always found for other rail defects. Documentation of these results are included in Appendix B.

#### 5.2 RAIL DEFECTS TESTED

There were 83 rail defects tested during this program. All were naturally occurring and were either tested in the laboratory in 1 to 9 ft

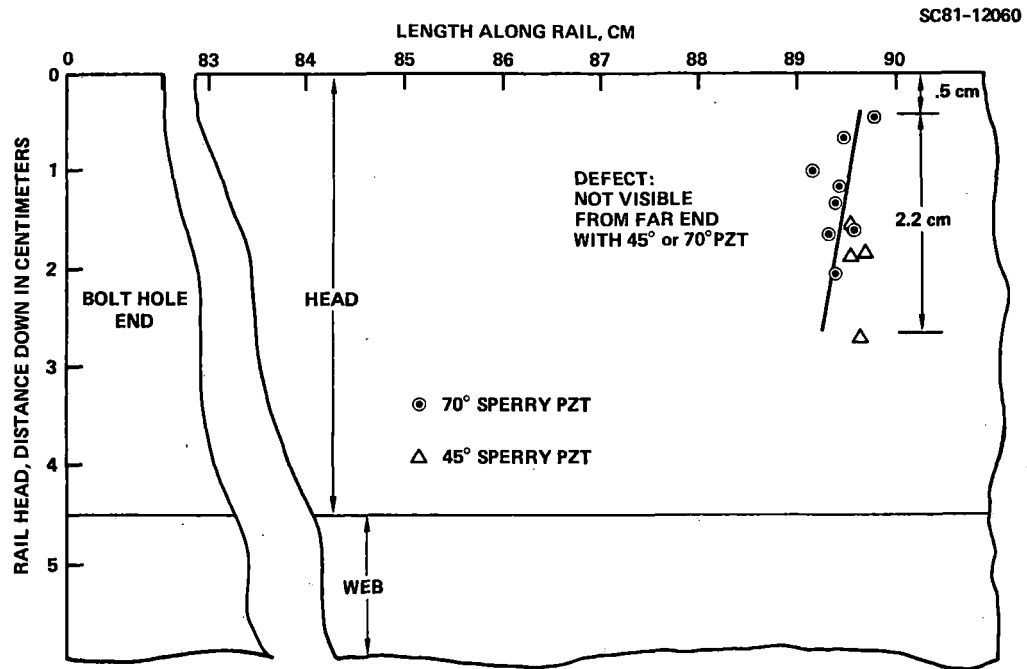


FIGURE 5-6 RESULTS OF HAND MAPPING THE TRANSVERSE DEFECT IN RAIL SPECIMEN NO. 320.

SC36617

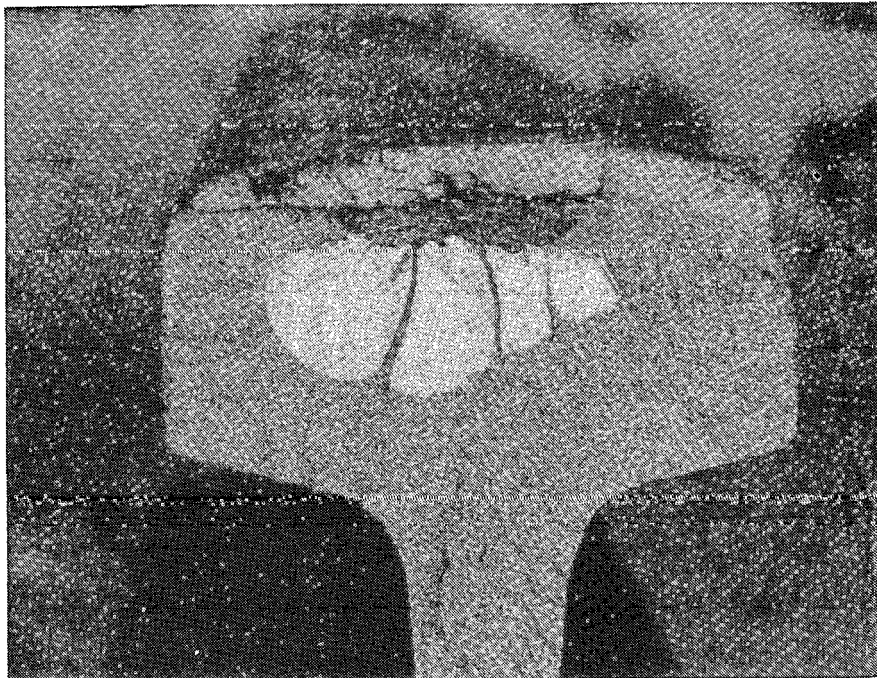


FIGURE 5-7 APPEARANCE OF THE DEFECT IN RAIL SPECIMEN NO. 320 AFTER BREAKING THE RAIL.

lengths of rail that had been removed from service or were tested in the field in operational track. In addition, there were laboratory specimens of different types of new rail and of defect-free used rail with different types and degrees of wear. A description of all the rail specimens tested in the laboratory is presented in this section.

A total of 44 rail specimens were received from various sources, mostly from Sperry Rail Services, for testing in the laboratory. The 33 containing defects or exhibiting different types of surface wear that can affect defect detectability are listed in Table 5-1. The predominance of transverse defect and vertical split head specimens indicates the relative importance placed on evaluating the performance of EMATs in this program for detecting these serious types of defects. A complete listing and documentation of all the rail specimens are presented in Appendix B.

### 5.3 DEFECT DETECTABILITY RESULTS

Detection of a particular type of defect was usually best accomplished with a particular EMAT because of its ultrasonic beam geometry. In general, the transverse defects were most reliably detected by the 90° SH EMAT and the longitudinal defects were best detected by the 0° SR EMAT. However, each defect is neither truly transverse nor longitudinal, so, in many cases, the defects were detected by both types of waves. None of the defects were detected best by the 35° SV EMAT, although there may be some, such as a nearly vertical BHC, where this should be the case. In the following two subsections, the degree of detectability and characterization will be summarized for each type of defect in each of the two defect classes, along with some representative chart recordings for each of the defect types. These data will generally be for the best EMAT, but examples will also be shown where particular defects were detected by more than one EMAT type.

In the third subsection following, the rail specimens having conditions such as head checking, shelling and engine burn that might mask the presence of a defect will be discussed. Measurements will be summarized in terms of the minimum size defect that could be detected in the presence of the particular rail conditions and the possibilities for false calls.

In the fourth subsection, results of the dynamic test results in the laboratory will be presented.

Table 5-1. LABORATORY RAIL DEFECT SPECIMENS

SRS No.	Specimen Length (in.)	Rail Height (in.)	Defect Type	Defect Size	Remarks
303	100	7.0	TDT	(10%)*	True trans. def./small
305	91	7.0	TDT	1.4%	Head-free rail
308	110	7.0	TDD	41%	Possible compound
304	103	7.0	TDD	(15%)	High in head
306	92	7.0	TDD	(6%)	Deep in head
330	65	7.0	DF (two)	11%, 37%	Under shelling
320	64	7.2	TD	29%	Under Stellite field
319	60	7.0	EBF	(10%)	weld patch
302	102	7.0	DWP	(6%)	Curve worn rail
331	77	7.0	DWP	86%	Under shelling
316	63	6.6	CF	(> 10%)	HSH component of 2.8 in.
6	12	7.0	HSH	7 in.	
323	55	5.8	HSH	5 in.	
310	96	7.0	VSH	38 in.	
311	39	7.0	VSH	4 in.	Head-free rail; most
334	67	5.2	VSH	48 in.	of VSH cut off
335	62	5.2	VSH	43 in.	
336	26	6.5	VSH	26 in.	
337	70	6.5	VSH	21 in.	
338	80	6.5	VSH	56 in.	
339	65	6.5	VSH	21 in.	
340	70	6.5	VSH	14 in.	
341	72	6.5	VSH	17 in.	
342	77	6.5	VSH	26 in.	
219	24	7.1	HWS	5 in.	
32	24	7.0	BHC	2 in.	
318	59	7.0	---		Engine burn, no defect
328	73	7.0	---		Severe head checking
307	95	7.0	---		Moderate shelling
332	85	7.0	---		Shelling
333	70	7.0	---		Shelling
315	72	7.0	---		Crushed head
343	73	6.5	---		Crushed head

\* The transverse defect sizes in parentheses are estimates from conventional ultrasonic measurements. The others were measured after breaking the rails at the defects.

### 5.3.1 Transverse Defects

There are three opportunities for detecting a transverse defect using the unidirectional SH EMAT. This is illustrated in Fig. 5-8. As the EMATs travel down the rail and a TD comes into range, as in the top diagram, some of the transmitted pulse is reflected back from it directly into one of the two "unidirectional" receivers described previously. The TD will be in range for about 6-12 in. of travel, depending on its size, during which time the signal amplitude will increase from zero, go through a maximum, and again decrease to zero as the receiver passes over it. This may or may not be the optimum direction for detection of the TD depending on which direction it is tilted.

The second detection mode occurs while the TD is between the transmitter and receiver which are separated by about 10 in. As this occurs, the direct forward transmitter pulse seen by receiver No. 1 is attenuated by the presence of the TD, as indicated by the dashed line in the center sketch.

The third chance for detection occurs after both EMATs have passed over the TD as illustrated at the bottom. Now the backward directed transmitter pulse can reflect off the TD and if the tilt angle was wrong before, it is

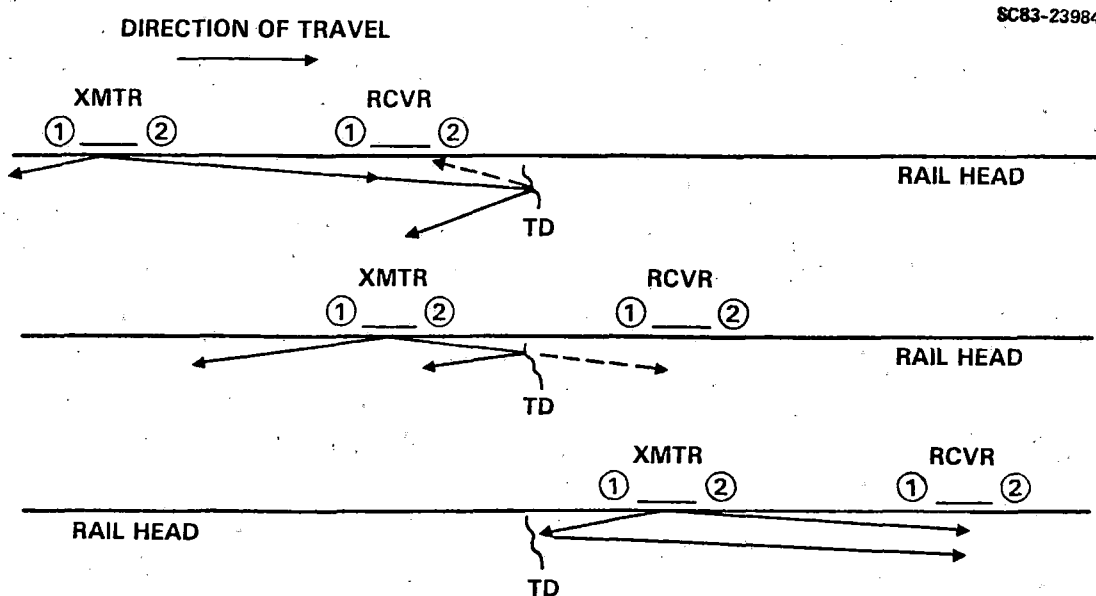


FIGURE 5-8 THREE MODES FOR DETECTION OF TDS WITH UNIDIRECTIONAL SH EMATS.

now right for reflecting the signal to the receiver, but receiver No. 1 detects it rather than receiver No. 2.

An example of the strip chart recordings produced by these three modes of detection is shown in Fig. 5-9. At the top is a drawing of the side of rail specimen No. 304 to the same scale as the chart recordings showing the position of the TD in the rail head, the relative spacing of the transmitter (T) and receiver (R) EMATs, and the positions of bolt holes and one rail end. Below that is a recorder trace of the amplitude of the signal received by the forward looking receiver as the EMATs move from left to right along the rail. The two large peaks are due to reflections first off the TD and then off the end of the rail. The width of the peaks is determined by the width of the detection time window. This is adjusted to be somewhat less than the time that the TD or rail end is within range so that the detection of spurious reflections, such as the small peak to the left of the trace, is minimized.

The next chart recording shows the amplitude of the forward-directed transmitter signal as detected directly by the rear-looking receiver. This signal is amplified so as to saturate the recorder except where the transmitter and receiver are straddling a discontinuity such as the TD or rail end. As this occurs, the signal is attenuated creating the dip in the chart recording. The detection time window in this instance can be made very narrow since the T-R separation distance is fixed so the direct transmission signal always arrives at the same time delay. The width of the dip in the chart recording is equal to the T-R transducer separation distance.

The third chart recording shows the amplitude of the signal reflected off the TD after both EMATs have passed over it. This is again the output of the rear-looking receiver, but in a later time window than for reception of the direct transmission signal. This signal is smaller than from the forward-looking direction, indicating that the top of the TD is tilted toward the rail end. Also seen in this trace is evidence of reception from the forward direction (TD) and (RE) reflections, but the amplitudes of these signals are down 16 dB from those detected by the forward-looking receiver shown in the top chart recording.



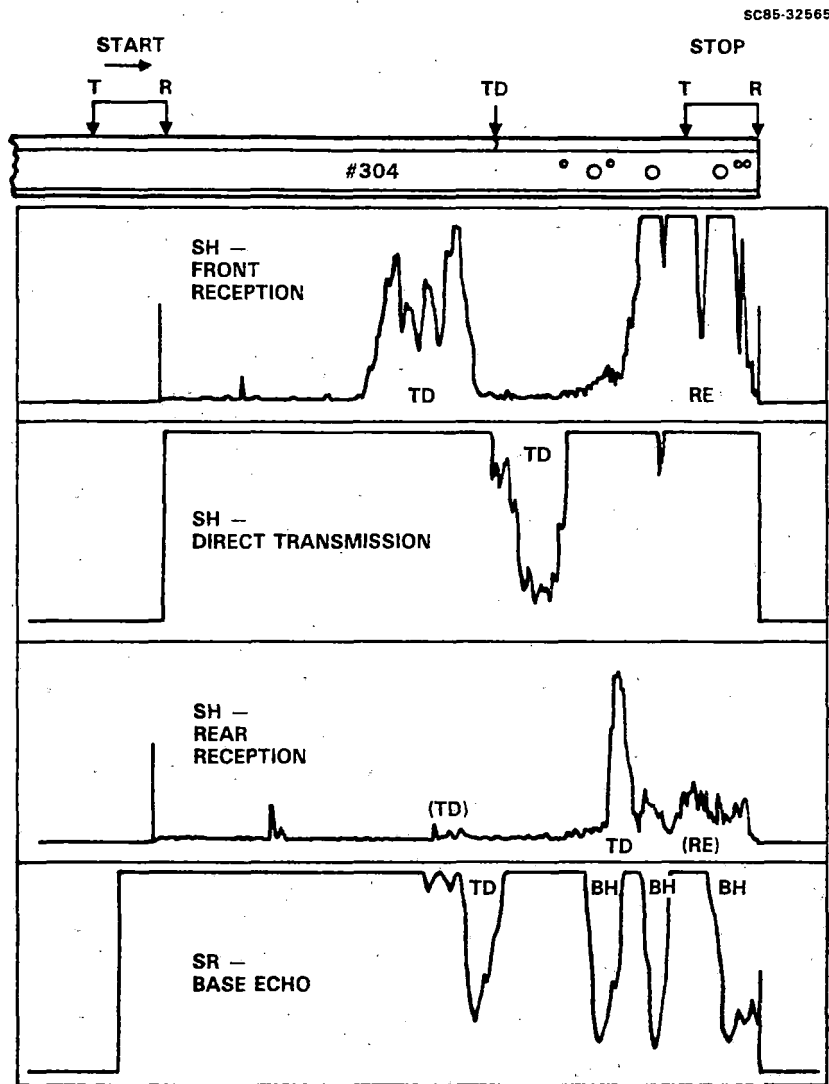


FIGURE 5-9 EXAMPLE OF TD DETECTION WITH SH AND SR EMATS.

The bottom chart recording shows that the SR EMAT can sometimes also detect TDs. This recording is the amplitude of the  $0^\circ$  shear wave that is reflected off the base of the rail. As with the direct transmit SH signal, the amplifier gain is set to saturate the recorder except where a discontinuity, such as the bolt holes (BH), intercepts the base echo. If a TD in the rail head extends over the rail web, it can also intercept the base echo, particularly if it is tilted or has a horizontal fracture component associated with it such as with a DF or CF defect. An SV EMAT pair could also detect this TD in the pitch-catch mode.

A summary description of the ten transverse defects that were available for testing in the laboratory is given in Table 5-2. The values shown for the estimated size, in percentage of the area of the rail head cross section, and tilt angle were determined by hand-scanning using 2 MHz contact 70° angle beam ultrasonic transducers. Positions on the surface of the rail head were determined where the amplitude of the reflected signal was 6 dB down from the maximum amplitude, and then these positions were geometrically mapped to give the three-dimensional outline of the defect within the rail head. It can be seen by comparing these estimated defect sizes with the actual sizes that this measurement procedure did not always produce accurate results. The actual sizes and tilt angles for six of the defects were determined by breaking the rail specimens at the location of the defects and physically measuring them.\* Photographs of the broken rail ends at these defects are shown in Appendix B.

The signal-to-noise (S/N) ratio values are for the SH signal received from the optimum direction. An indication that the S/N depends on the tilt angle of the transverse defect as well as other factors is shown in Fig. 5-10. Here, the measured S/N is plotted against the actual size of the defects for the six rail specimens that were broken open for examination. The tilt angles for these defects were either 5° or 20°, with the exception of the defect in specimen No. 320 which consisted of several separate fracture planes having different tilt angles ranging from nearly vertical to about 20° (see Fig. 5-7). The plotted points in Fig. 5-10, although few in number, seem to indicate that the closer the defect is to being vertical, the larger the reflected signal, as is expected for the 90° SH wave. The defect in specimen No. 331 gave an anomalous result in the amplitude of the reflected signal, although it was still detected by a strong attenuation of the direct transmit signal. The reason for this anomaly (and a similar anomaly for one of the TDs at the Santa Fe Test Track) is not clearly understood. A possible explanation is that the fracture surface was more planar and smoother than those of the other TDs that were broken open, which could have resulted in a more specular rather than a diffuse reflection causing the reflected beam to be directed away from the

---

\* This service was graciously provided by the Sperry Rail Service Division of Automation Industries, Inc., Danbury, CT.

Table 5-2 TRANSVERSE DEFECTS TESTED IN THE LABORATORY

Rail No.	Defect Type	Est. Size	Act. Size	Est. Tilt	Act. Tilt	SH S/N	Dist. From RE	Pertinent Rail Features, Conditions
303	TDT	10%	---	30°	---	5:1	30"	
304	TDD	15%	---	20°	---	10:1	29"	
305	TDT	3%	1.4%	10°	5°	3:1	8"	Head-free
306	TDD	6%	---	10°	---	3:1	17"	Coal
308	TDT	>10%	41%	10°	5°	6:1	16"	Minor compounding
319	EBF	10%	---	5°	---	5:1	25"	Engine burn fracture
320	TDC	30%	29%	24°	0-20°	5:1	35"	Compound fissure from surface weld separation
330 <sub>L</sub>	TDD	7%	37%	45°	20°	4:1	26"	Large detail fracture from surface hardened zone. Shelly rail
330 <sub>S</sub>	TDD	<5%	11%	45°	20°	2.5:1	35"	Small detail fracture from surface hardened zone. Shelly rail
331	DWP	15%	86%	10°	20°	2:1	35"	From small slag inclusion at flash butt weld. Shelly rail

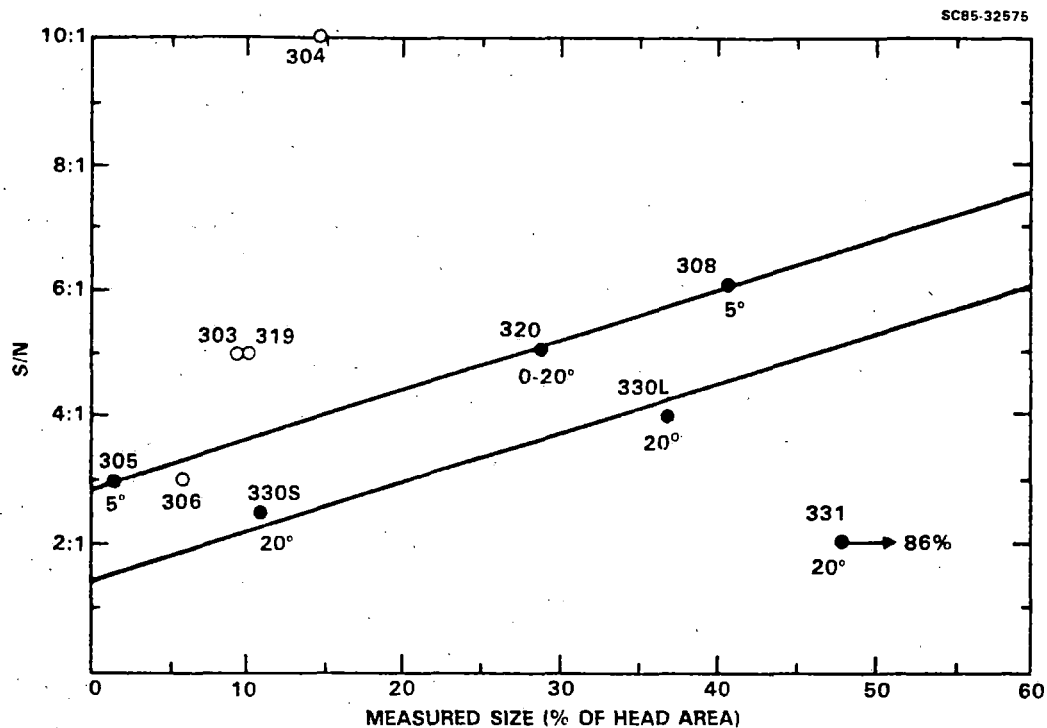


FIGURE 5-10 SIGNAL-TO-NOISE RATIO FOR SH WAVE DETECTION OF THE SIX TRANSVERSE DEFECTS EXPOSED BY RAIL BREAKING.

receiver EMAT. A further observation in support of this speculation is that the conventional hand-held transducer could only detect this very large defect from one side.

Inspection of the S/N values for the four TDs in Table 5-2 that were not broken open compared to their estimated size shows No. 306 to be in agreement with the trends in Fig. 5-10, Nos. 303 and 319 may be about 30% defects rather than 10% as estimated by conventional ultrasonics and No. 304 may be much larger than the estimated 15% size. These discrepancies, if true, would not be particularly surprising in view of similar discrepancies between the estimated and actual sizes of three of the six (Nos. 308, 330L and 331). These observations tend to indicate that the amplitude of the reflected signal using SH EMATs is a better measure of the size of a transverse defect than can be obtained by geometric mapping using conventional ultrasonics. However, more work is needed to make this conclusion.

Summarizing the results for defect detectability of all the transverse defects listed in Table 5-2, all were detected by a reflected SH wave. The smallest one, the 1.4% TDT in specimen No. 305 was favorably positioned

near the center of the rail head and had a small tilt angle which combined to provide a good reflected S/N ratio. In contrast to this, the largest one, the 86% DWP in specimen No. 331 was only marginally detected in reflection (but was detected by loss of the direct transmit signal as discussed earlier). Between these two extremes, all of the other TDs produced defect indications much as expected.

A possible advantage of using the EMAT-produced SH wave for detecting transverse defects was explored to a limited extent for the special cases where the defect occurred in conjunction with certain types of otherwise innocuous rail surface conditions. The SH wave essentially floods the rail head with ultrasonic energy as it propagates and the direction of polarization of the shearing action is parallel to the rail surface and interacts very little with that surface. It was therefore able to propagate underneath the Stellite weld patch from either direction in specimen No. 320 and reflect off of the compound fissure under the weld patch. The 70° vertically polarized shear wave generated by the conventional hand-held wedge-type transducer was only able to detect this defect from one direction. Similarly, the SH wave produced a strong indication of the transverse defect under the engine burn on the surface of specimen No. 319.

A limitation of the SH EMAT is in its spatial resolution. In its present state of development, it is operated as a narrow-band device to obtain adequate defect detection sensitivity. This requires the transmitter to be driven by a tone burst of about 10 cycles at the operating frequency, which results in a propagating ultrasonic wave packet many times greater in duration than is generated by piezoelectric transducers. Also for sensitivity, the EMAT transmitter and receiver are separate transducers separated by a distance of several inches along the rail head. Both of these factors affect the ability of the SH EMATs to detect transverse defects located near some other discontinuity such as a rail end.

Under the favorable condition that the top of the TD is tilted slightly toward the rail head end so that the EMATs can both be inboard of the defect for its detection, the defect can be as close as 7 in. from the rail end for its reflection to be resolved from the large rail end reflection. This is evidenced by detection of the 1.4% TD in specimen No. 305 which was well resolved at only 8 in. from the end of the rail.

Under the very unfavorable condition that the TD has a large tilt away from the rail end and the EMATs have to be between the defect and the rail end for its detection, then the defect must be at least 24 in. from the end of the rail. This restriction depends on the size of the defect, since a large defect reflection received from the forward EMAT receiver direction might be resolved at an even closer distance from a smaller rail end reflection received from the reverse EMAT direction. This is illustrated somewhat by chart recorder traces in Fig. 5-9 for the defect in specimen No. 304 which was 29 in. from the rail end even though its tilt was favorable for detection from the side away from the end of the rail.

The spatial resolution limitation of the current SH EMATs is not an inherent theoretical boundary, but is a practical one at present because of the need to achieve detection sensitivity as mentioned before. Development of broad-band EMATs with enough sensitivity and a much better spatial resolution indicates that detection of transverse defects in the range of 1 in. to 6 in. from the end of the rail, depending on their tilt direction, may be possible.

### 5.3.2 Longitudinal Defects

The rail specimens containing longitudinal defects are listed in Table 5-3. Their detectability and the methods of detection used depend upon the orientation and positions of these defects in the rail, vertically in the head (VSH or piped rail in the web), horizontally (CF, HSH and HWS) or the BHC which can run at any vertical angle from a bolt hole in the web. These three subclasses of longitudinal defects will be discussed separately.

Vertically Oriented Defects. The primary means for detecting VSH (and probably piped web, although no specimens have been available for testing) is with the 0° SR EMAT. The ultrasonic detection of a crack-like defect oriented parallel to the ultrasonic beam direction is generally considered to be unreliable with the usually used longitudinal waves. The successful detection of VSH defects in the rails apparently is because the SR EMAT generates a shear wave with a component of polarization perpendicular to the crack faces that is effectively scattered by those faces. This is indicated by a loss of the base-echo signal when the SR EMAT is over the VSH, as illustrated in

TABLE 5-3. LONGITUDINAL DEFECTS TESTED IN THE LABORATORY

Rail No.	Defect Type	SR-EMAT Size (in.)	Actual Size (in.)	Pertinent Rail Features, Conditions
310	VSH	31	38	Head-free rail; most of VSH cut off Could not resolve; BH interference Could not resolve; BH interference VSH curved toward side of rail head
311	VSH	2.9	4	
334	VSH	>48	48	
335	VSH	>43	43	
336	VSH	26	26	
337	VSH	20	21	
338	VSH	56	56	
339	VSH	24	21	
340	VSH	4	14	
341	VSH	13	17	
342	VSH	26	26	
316	CF	3.2	2.8	Compound fracture, > 10% TD 12 in. rail length hard to hold down At RE
6	HSH	-	7	
323	HSH	5.4	5.0	
219	HWS	6.6	4.6	
32	BHC	1.7	1.5	At hole nearest RE, 50° from horizontal

Fig. 5-11 for rail specimens No. 310 and 311. Above each strip chart recording is a same scale representation of the result of mapping the location of the VSH defect using a conventional hand-held transducer on the side of the rail head. This measurement only defines the side-to-side position of the crack with position along the length of the rail, but does not have the resolution to define its vertical position or its height. It is presumed that the crack tapers down in vertical height near its ends, and that effect plus the tendency of the crack to curve toward the side of the rail head accounts for the failure to attenuate the base-echo signal near the ends of the cracks. However, the base-echo is effectively attenuated for 31 in. of the 38 in. length of the VSH in No. 310 and 2.9 in. of the 4.0 in. in No. 311. The amount of attenuation is about 100%, as can be deduced by comparison with the signal level at the 1-3/8 in. diameter bolt holes in No. 310. The S/N for detecting these defects is then just the ratio of the normal base-echo amplitude to the electronic noise level which is greater than 10:1 in most of the rail specimens.

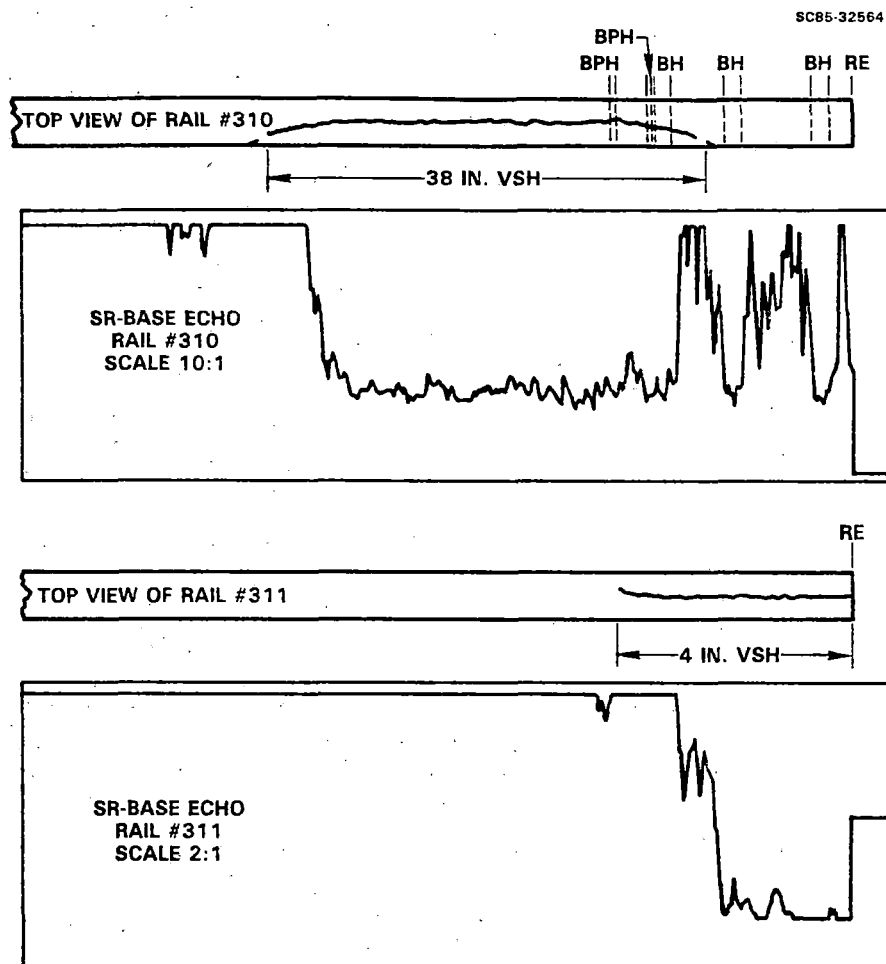


FIGURE 5-11 DETECTION OF VSH DEFECTS WITH SR EMAT.

Detection of VSH defects is also possible using the SH and SV EMATs. This is illustrated by the three strip chart recordings in Fig. 5-12 for the defect in specimen NO. 310. The direct transmission signal from the SH transmitter to the receiver, located about 9 in. away along the rail head, is attenuated by the VSH nearly as effectively as is the SR base-echo signal. Both of these ultrasonic waves have the same shear polarization relative to the crack faces so they are expected to be attenuated similarly. However, there is a greater proportion of the SH beam width that travels in the rail head parallel to the VSH defect than in the SR beam which travels vertically through the web to the base of the rail and back. Therefore, the effective attenuation of the SH wave by a VSH may not always produce as large a S/N for defect detection as the SR wave. The spatial resolution of the SH detection is not as good for this type of defect either, especially near the ends of a



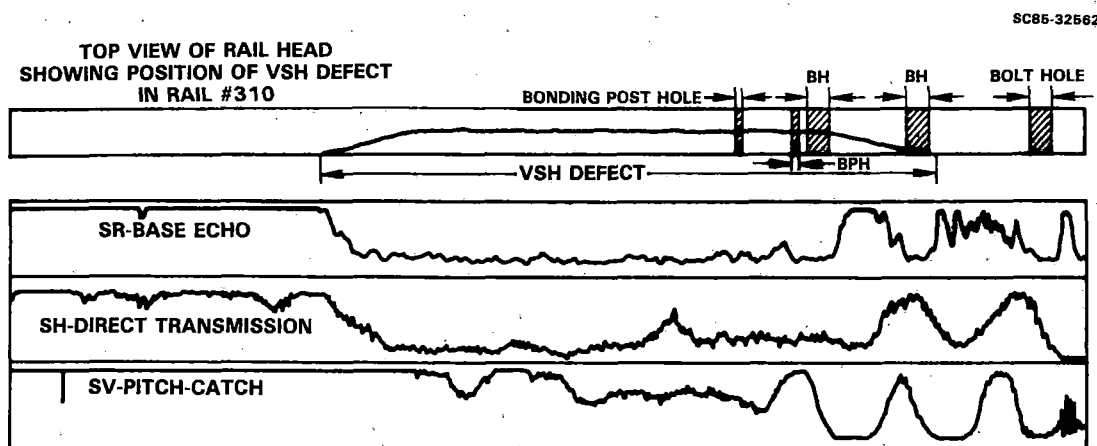


FIGURE 5-12 DETECTION OF VSH DEFECT WITH SR, SH AND SV EMATS.

rail section, because of the separation of the transmitter and receiver. Incidentally, for the examples shown in Fig. 5-12, both the SR and the SH EMATs detected nearly the full 38 in. length of the VSH, achieved by critically positioning the EMATs on the rail head.

The SV wave has a shear polarization which is parallel to the VSH crack faces, and there is apparently less interaction and scattering of this polarization. However, there is some loss in amplitude of the signal, as seen in the bottom chart recording in Fig. 5-12, when the SV wave is reflected at  $35^\circ$  off of the base of the rail past the VSH defect in the pitch-catch mode. This mode of operation is achieved when the transmitter and receiver EMATs are positioned under separate magnet pole pieces 10 in. apart, as opposed to the pulse-echo mode where the EMATs are one on top of the other under a single pole piece. Both of these modes can be useful for the detection of BHC defects, as will be discussed later.

Horizontally Oriented Defects. The three defect specimens tested in this class were an extended CF (No. 316), a HSH (No. 323) and a HWS (No. 219). The horizontal orientation of these cracks extinguish the base-echo for the SR and the SV EMATs equally, but have little effect on SH wave transmission, except in the case of the CF where there is a vertical component to the fracture surface.

Chart recordings of the SR base-echo amplitude with position along the length of the rails are shown in Figs. 5-13, 5-14 and 5-15. Rail section Nos. 316 and 323 were at the end of a string of rails, and the position of the alignment wheels on the test cart allowed measurements to be made over only part of the rail lengths. The position of the SR EMAT and the magnet pole pieces (P) at the beginning and the end of each chart are indicated on the scale drawings at the top of each figure. Also shown are the locations and the extent of the defects determined using hand mapping with conventional 0° and 70° piezoelectric transducers.

The compound fracture has a horizontal length of 2.8 in. with very small vertical components at each end, as determined by using a 70° wedge transducer. The SR base-echo was completely blocked for a distance of 3.2 in. which, accounting for the size of the EMAT, accurately represents the size of the defect to within 0.1 in. The S/N is that of the base-echo amplitude above electronic noise or greater than 10:1.

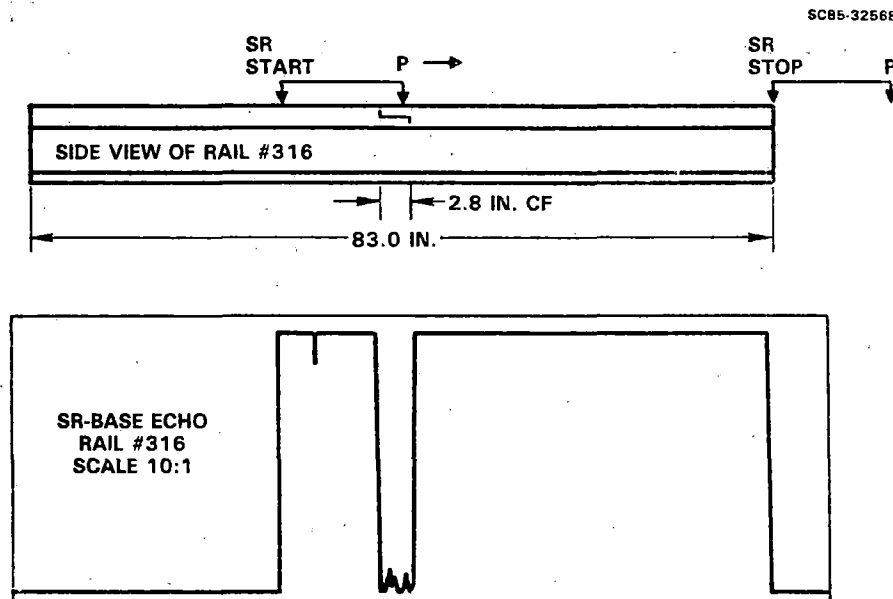


FIGURE 5-13 DETECTION OF A CF DEFECT WITH SR EMAT.

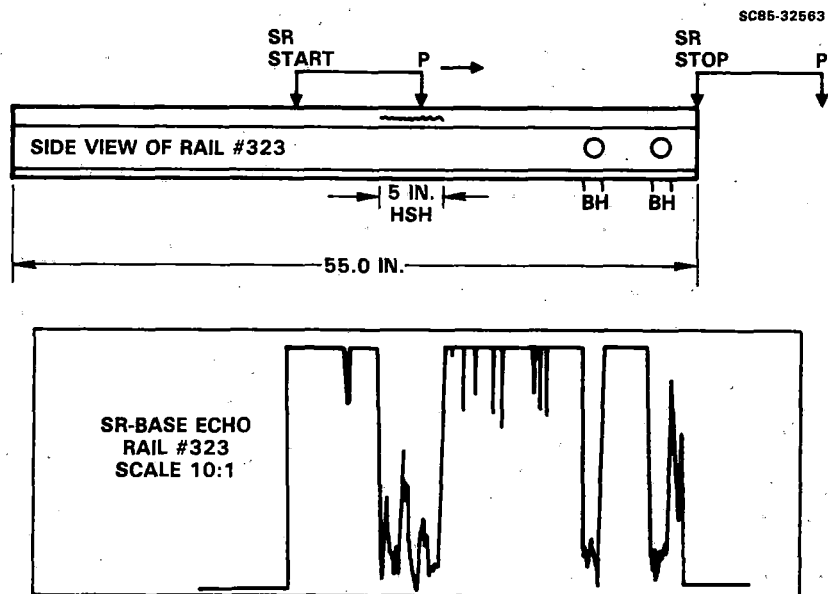


FIGURE 5-14 DETECTION OF A HSH DEFECT WITH SR EMAT.

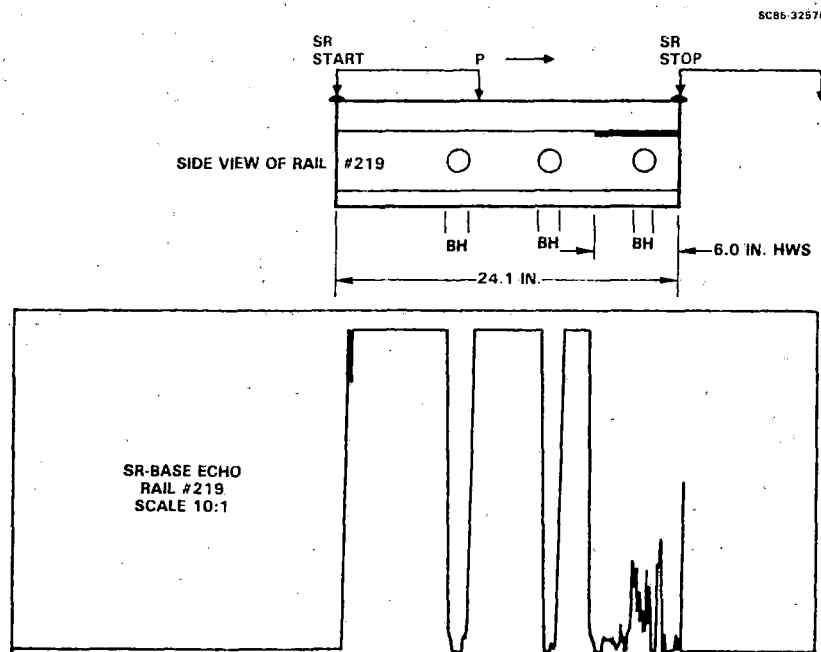


FIGURE 5-15 DETECTION OF HWS WITH SR EMAT.

The HSH and HWS specimens also had bolt holes in addition to the defects, and it can be seen in the chart recordings that the defects are as effective as the bolt holes at blocking the base-echo signals. In both of these cases, however, there is a small signal that appears in the time window set for base-echo detection when the transducer is over the defect due to multiple reflections of the ultrasonic energy between the defect and the top surface of the rail head. Aside from this effect, the S/N for defect detection and the size resolution is the same as for the CF.

Bolt Hole Cracks. A BHC can propagate in any direction from its point of initiation at a bolt hole. Optimal detection will be with an ultrasonic beam propagating at right angles to the plane of the crack so that the largest projected crack surface area is available for reflecting the ultrasonic wave back to the EMAT (in the pulse-echo mode), or for intercepting the base-echo reflection (in the pitch-catch mode).

Only one BHC specimen, No. 32, was available for testing (except for specimen No. 303 which had a 1/4 in. deep horizontal saw cut at a bolt hole). A scale drawing of the side view of specimen #32 is shown in Fig. 5-16, indicating the location, size and orientation of a service induced BHC. Also shown to scale are the 1/2 in. diameter spiral wound SR transmitter and receiver EMATs located close together under one of the magnet pole pieces and operating essentially in the pulse-echo mode. Below the drawing are strip chart traces of the amplitudes of the signal reflected off of the base of the rail and off of the bolt holes and the bolt hole crack, obtained by two different settings of the position of the detection time window. From the width of the base-echo extinction region, the bolt hole diameter and the length of the horizontal projection of the BHC could be reproducibly determined to within 0.1 in. (by analysis of many chart recordings of both specimens Nos. 32 and 303). The bolt hole echo pattern does not as reliably provide a quantitative measure of the projected crack length, since there may not always be facets along the entire length of the crack that are oriented properly to reflect the ultrasonic energy back to the receiver transducer. However, an anomalously wide reflection pattern was observed in all of the strip chart recordings which at least indicated the presence of the crack (or the saw cut in No. 303).

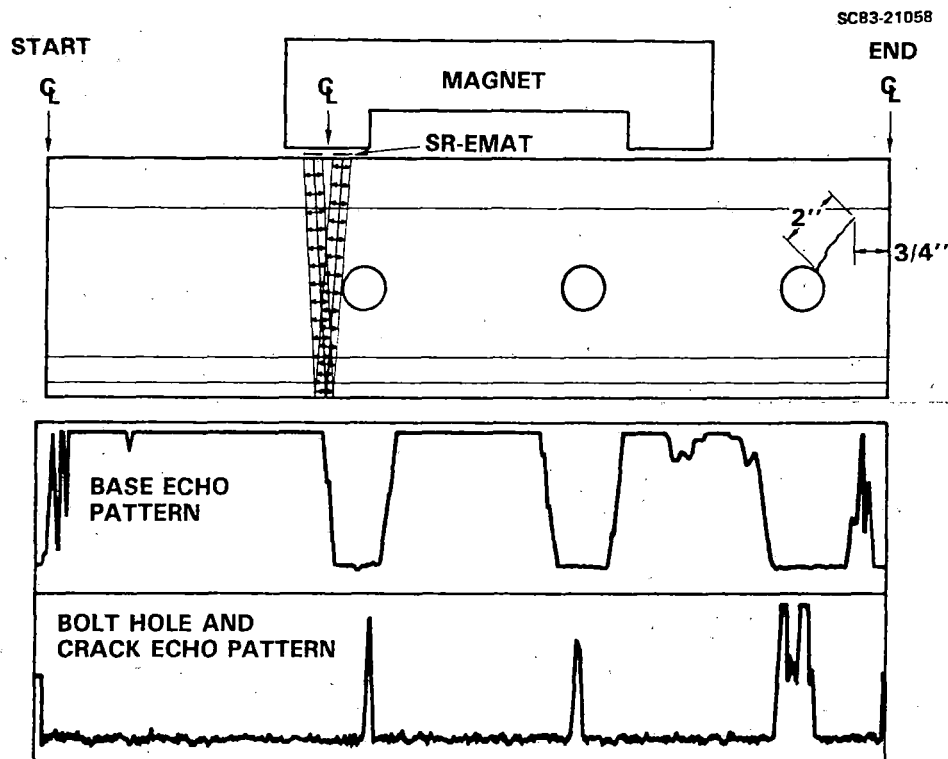


FIGURE 5-16 DETECTION OF BHC WITH SR EMAT.

The use of the 35° SV wave for detecting and measuring the length of a BHC is conceptually the same as for a 0° SR wave when the bolt hole is located away from a rail end. The different beam angle provides an additional measure of BHC detection to allow for the possibility of the crack plane lying entirely within the shadow of the bolt hole for either one of the ultrasonic beam angles. There are "blind spots" for BHC detection for either beam angle and, in particular, the proximity of the BHC in specimen No. 32 to the rail end. The reason for this can be understood in terms of the more complex ultrasonic beam geometries of the SV EMATs in both the pitch-catch and pulse-echo modes, as illustrated in Figs. 5-17 and 5-18. For the case of pulse-echo detection, the path of the ultrasonic beam from the transmitter to the base of the rail is designated as T, and the path between the base of the rail and the receiver is designated as R. In rail specimen #310, there are three 1-3/8 in. diameter bolt holes drilled through the web designated as H1, H2 and H3 in the scale drawing in Fig. 5-17, and two 3/8 in diameter bonding post holes desig-

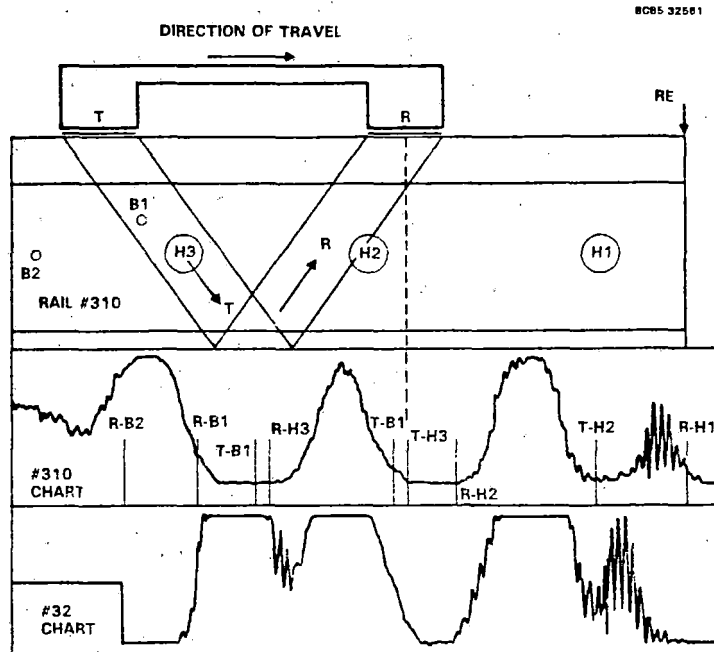


FIGURE 5-17 SIGNAL PATTERN FROM BOLT HOLES FOR SV EMAT OPERATING IN THE PITCH-CATCH MODE.

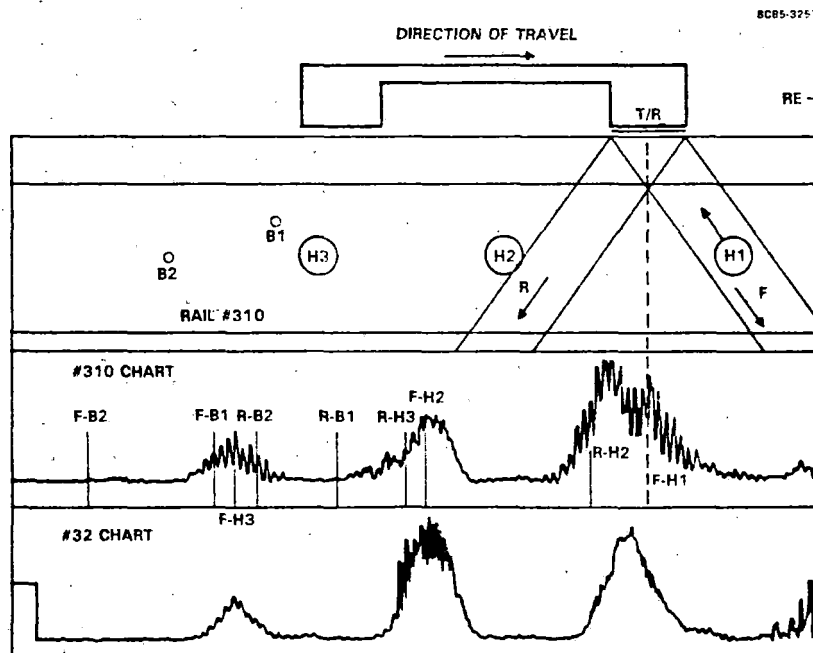


FIGURE 5-18 SIGNAL PATTERN FROM BOLT HOLES FOR SV EMAT OPERATING IN THE PULSE-ECHO MODE.

nated as B1 and B2. If any of these holes lie within either of the ultrasonic paths, T or R, there is an attenuation of the base-echo amplitude at the receiver. The vertical lines drawn on the strip chart recording for specimen No. 310 indicate the position of the receiver EMAT when each of the holes is at the center of one or the other ultrasonic beam paths. It is seen that there is a nearly complete loss of base-echo when a bolt hole intercepts the beam.

The geometry of the ultrasonic beam shown in the figure is, of course, idealized for simplicity, but still explains many of the features of the strip chart recordings. However, the localized maxima and minima in the base-echo amplitude that are seen at the right end of the strip chart recording when the receiver was near the rail end are not explained within the context of the simple model. They are caused by phase interference of ultrasonic energy arriving at the receiver over two or more paths. These paths occur due to divergence and side lobes in the ultrasonic beam and the presence of the rail end to act as a second reflecting surface in addition to the base of the rail. A complete analysis of this phenomenon has not been warranted in this program, since a lesser emphasis has been placed on the use of SV EMATs for rail flaw detection, but conceptually such effects are predictable. Changes in the interference pattern by the introduction of a third reflection surface in the vicinity of the rail end, such as the BHC in specimen No. 32, can also be predicted. Qualitatively, this prediction is apparently confirmed by the marked difference between the interference patterns seen in the two strip chart recordings in Fig. 5-17 for specimens with and without a BHC near the rail end. Differences in the base-echo amplitude patterns in other parts of the chart recordings can be accounted for by the presence of the VSH defect and the two bonding post holes in specimen #310, and slight differences in the spacings of the bolt holes and in the rail heights between the two specimens. These differences can be accounted for using the simple beam geometry.

The use of the 35° SV wave in the pulse-echo mode is illustrated in Fig. 5-18. The EMATs are inherently bidirectional so ultrasonic energy is transmitted and received in both the forward (F) and the reverse (R) directions simultaneously. As with the SH EMATs, however, there are variations in the design of the SV EMATs that are possible that provide for unidirectional operation. These are more complex and more difficult to implement and were not applied in this program.

The top strip chart recording in Fig. 5-18 shows the bolt hole echo pattern obtained for specimen No. 310 with the vertical lines indicating the position of the transmitting and receiving EMATs when each of the bolt holes, in turn, is centered in either the forward looking or reverse looking ultrasonic beams. The bottom strip chart recording was obtained for specimen No. 32 which had no bonding post holes, but which did have the BHC at H1. Again, the patterns of the reflected signal amplitudes are quite different, even though somewhat less understandable.

Complicated interference patterns such as the ones shown in these figures would require considerable theoretical and experimental effort to understand completely. This effort was not justified because of the alternatives possible for BHC detection and was not possible because of the lack of a variety of BHC specimens to experiment with. Future development of EMATs for BHC detection should include the investigation of unidirectional SV ultrasonic beams.

### 5.3.3 Rail Conditions

There are discontinuities in the rail head other than defects that are considered nonhazardous "conditions" and should be ignored by the ultrasonic inspection system. The rail specimens having some of these conditions are listed in Table 5-1 and identified as to type of condition under "Remarks". Most of these conditions have to do with imperfections, caused by wear, on the surface of the rail head extending generally no more than 1/8 in. under the surface. Shelling, for example, is a progressive horizontal separation, generally at the upper gauge corner. It extends longitudinally, not as a true horizontal or vertical crack, but at an angle related to the amount of rail wear and is prevalent on curves where gauge side wear is accelerated. It is not a serious condition, but can lead to a transverse crack if the horizontal separation turns downward.

Head checking is similar, but is generally within 1/32 in. of the surface and appears as flaked out pits.

Engine burns are depressions on the rail head caused by friction of slipping locomotive drivers. There may be small thermal cracks caused by the intensive frictional heating that can grow into serious transverse defects. A crushed head has a similar appearance, but the depression may extend for



several inches caused by a soft spot in the rail head which gives way under heavy wheel loads.

Ultrasonic surface waves would interact with these rail head conditions, but the SH wave is a bulk wave which skims below the surface. It floods the entire rail head like a searchlight beam and is relatively insensitive to the condition of the rail surface. Table 5-4 summarizes the results found and the specimen identification numbers in which surface conditions were involved. Only one engine burn specimen without a fracture was available; it yielded a definite signal that was above the threshold for detection. However, its signature was quite different from those of the EBF specimen and the other TDs. Therefore, additional signal processing would probably allow discrimination of an EB from and EBF. For this defect type, more specimens would be needed to confirm this discrimination capability.

TABLE 5-4. A SUMMARY OF THE INSENSITIVITY OF THE SH-EMAT TO RAIL "CONDITIONS"

Shelling	Signal less than a 3% TD (307, 330, 331, 332, 333)
Head Check	Signal less than a 1% TD (328)
Engine Burn	Can distinguish EB from EBF? (318, 319)
Weld Repair	Can detect TD at weld repair (320)

The crushed heads occurred very near rail ends and could not be inspected using the SH EMATs.

Curve worn rail was not found to be a particular problem for the SH EMATs, since their ultrasonic beam patterns are wide enough to accommodate off-center positioning of the transducer on the rail head. This was a problem with the SR EMATs, however, since their beam needs to be directed vertically down the rail web to reflect off the base of the rail. Positioning of the EMATs across the width of the rail head is maintained relative to the gauge side of the head and if this is appreciably worn, as is common on curves, the EMAT is no longer centered over the web. The ST EMAT design produces a wider effective beam than the SR EMAT, as discussed previously, which governed its choice for use during the later field testing stage of the program. It will still require repositioning on heavily worn rail using hydraulic or mechanical actuators as is currently being done with the ultrasonic wheel transducer.

The rail specimens with shelling and head checking presented no particular problem for the SR EMATs. A satisfactory base echo was obtained in all the specimens and in those that contained transverse defects as well (Nos. 330 and 331) the defects were detected by an extinction of the base echo.

The engine burn and crushed head specimens also caused extinction of the base echo in the region of those conditions. This is not desirable, since these conditions can therefore not be distinguished from the various types of defects (HSH, HWS, VSH) by the 0° SR signal alone. However, it was also found that the 0° longitudinal wave generated by a hand-held transducer would not penetrate these regions, so the current ultrasonic wheels have the same problem. Whether the SH EMATs provide the needed discrimination capability for these types of conditions remains to be determined.

#### 5.3.4 Dynamic Effects

The steel flywheel that was used to determine the operating characteristics of EMATs under dynamic conditions in the laboratory was described in Sec. 5.1.2. This section presents the principle results of these tests.

The objective of these tests was to determine the amount of degradation in EMAT performance to be expected under dynamic conditions. To achieve this goal, it was necessary to:

1. Assemble a mechanical system to generate 30 mph relative motion.
2. Develop an EMAT support carriage that could withstand 1/4 in. high steps.
3. Evaluate various materials to be used in the best support structure.
4. Investigate and minimize any noise signals generated by the motion.
5. Demonstrate acceptable EMAT operation at 30 mph.

Since there was neither time nor money available for a comprehensive attack on each of the five tasks, the approach was to make an educated guess as to what system might work best and then to test and improve that system until optimum performance had been achieved. Optimum performance was taken to mean the observation of ultrasonic signals at 30 mph that appeared as good as those obtained at 0 mph.

Dynamic Magnetic Field Distribution. The electromagnet used for these experiments contained 3,400 turns of No. 12 copper wire wound around a 2 in. x 6 in. iron core. Its electrical resistance at room temperature was  $6.7 \Omega$  and it was usually operated at 7 A. Special pole pieces with faces curved to fit the rim of the 20 in. diameter wheel were made and mounted above the wheel.

When the wheel was rotated so that its surface speed was 30 mph, the distribution of magnetic field along a circumferential path was modified as shown in Fig. 5-19 for two pole piece to wheel air gap distances.

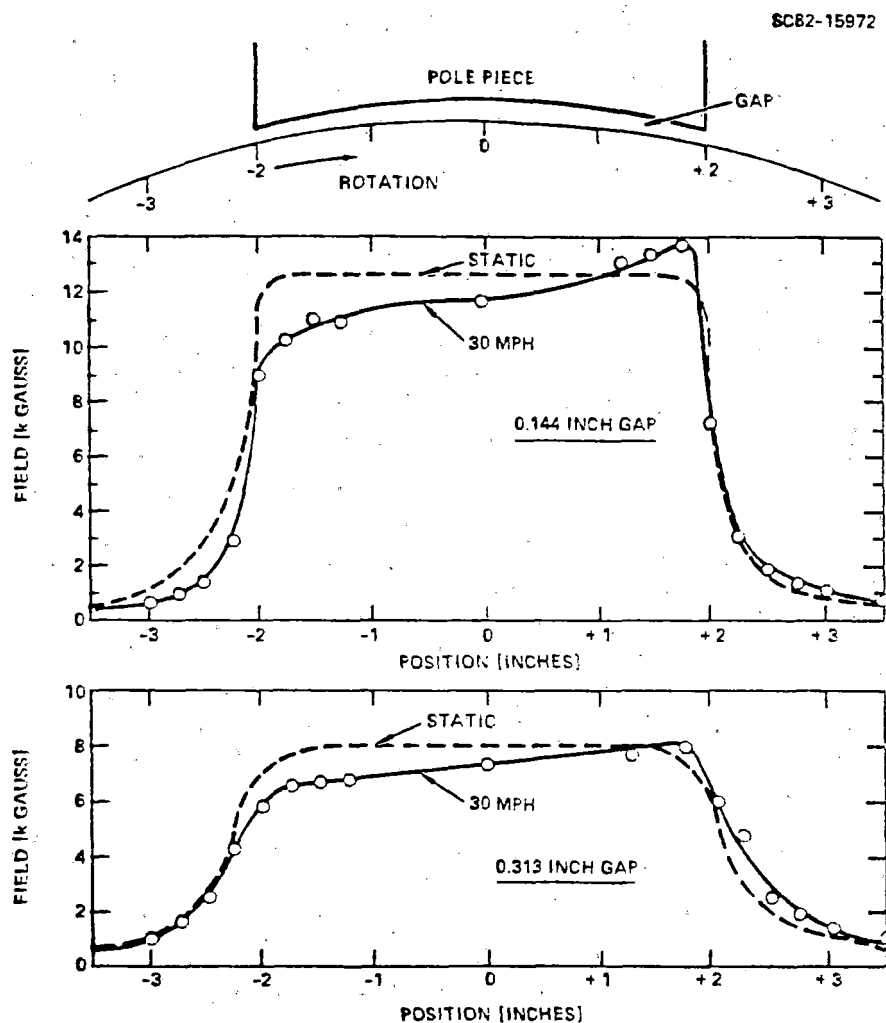


FIGURE 5-19 DISTRIBUTION OF NORMAL MAGNETIC FIELDS IN THE GAP AT ZERO AND 30 MPH SPEEDS.

Ultrasonic Wave Studies. The SH wave EMAT coil was fabricated by cutting a meander coil out of 5 mil copper foil. This coil had a conductor spacing of 0.21 in. (0.42 in. wavelength) and an aperture of 0.75 in. It was 5-1/2 wavelengths long and had only one turn of wire at each SH wave generating location.

Dynamic tests were also performed using SV meander coils designed for operation at 2 MHz.

Figure 5-20 shows that optimum performance was indeed obtained with the 2 MHz meander coil EMATs whose acoustic characteristics make them the least sensitive of all railroad-applicable EMATs to conditions at the interface between the rail and the EMAT. Note that this performance was obtained even when a 1/4 in. high step was present and passed under the EMAT support structure over eight times per second for the duration of the test.

To obtain Fig. 5-20, the electromagnet used to provide the magnetic field to the EMAT coils was best supported by a sturdy frame that connected to the shaft of the wheel through ball bearings. The best support structure for the EMAT coils took full advantage of their light weight and consisted of a thin, flexible wear plate between the coil and the wheel backed by a foam material, which provided both a spring load on the wear plate and damped out vibrations caused by crossing 1/4 in. high discontinuities.

The second signal shown arriving in front of the main signal in Fig. 5-20 is of confirmed origin. Since the main signal was obtained from ultrasonic energy that had bounced twice on its trip from transmitter to receiver, this early arriving signal appears to be part of the first bounce ultrasonic energy. Its appearance only under conditions of motion indicates that the moving metal disturbs the position of the SV EMATs, causing their positions to be closer together so that the receiver detects both the first and second bounce.

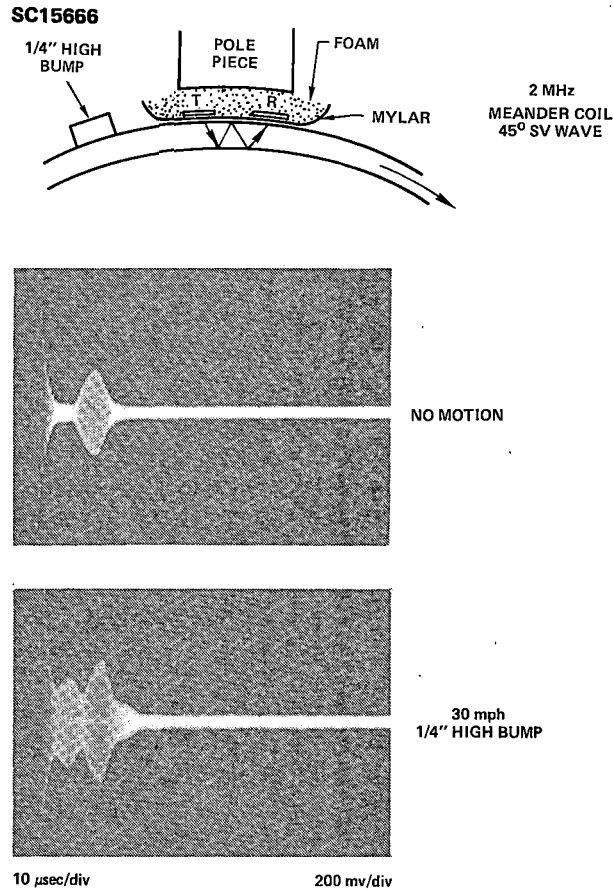


FIGURE 5-20 DEMONSTRATION OF THE PERFORMANCE OF THE FOAM AND WEAR PLATE METHOD OF SUPPORTING EMAT COILS.

Figure 5-21 demonstrates that similar performance was achieved with the TM concept for exciting SH waves except that no 1/4 in. high step was involved. This was because the electromagnet was not able to achieve adequate magnetic fields for SH wave excitation when the gap between the wheel and the pole piece was more than the 1/4 in. needed to accommodate the step. It is obvious that operation at 30 mph does not seriously degrade the ultrasonic signals and the noise level is only slightly higher. The multitude of signals following the "main bang" probably result from acoustic echos in the pole pieces because, for these experiments, the EMATs were taped to the pole pieces to make a large air gap next to the moving wheel.

SC15667

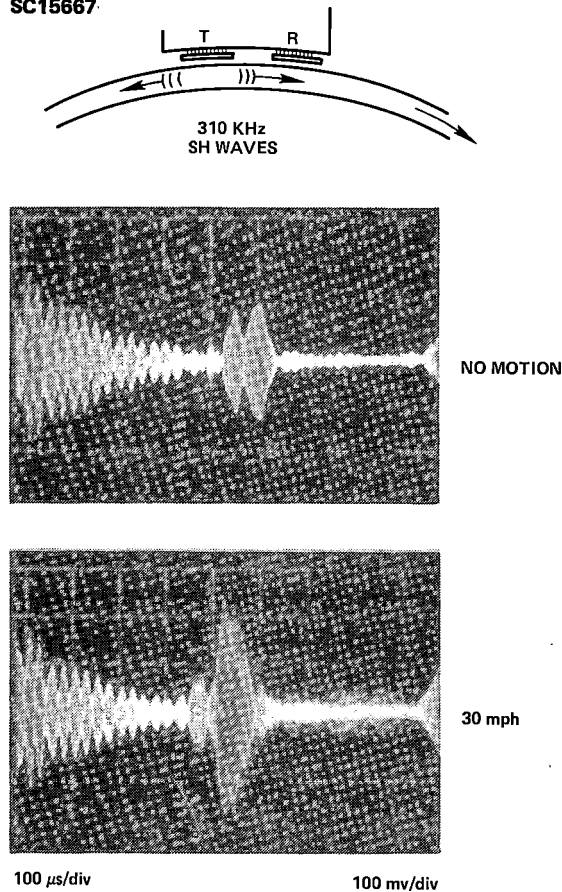


FIGURE 5-21 ULTRASONIC SIGNALS OBSERVED WITH SH WAVE EMATS OPERATING AT 0 AND 30 MPH.

Motion-Induced Noise. Previous experiments have shown that a large noise signal can appear when an EMAT coil and its associated magnet are moved relative to an iron surface. Since large magnetic fields appeared to suppress this noise signal, it was assumed to arise from Barkhausen noise generated by the magnetization process taking place in the iron as it approached the region of magnetic field variations around the EMAT coil.

During the wear plate studies, it was found that a thin sheet of titanium (Ti) made an excellent cover plate for protecting the EMAT coil from damage as it rubbed against the surface of the iron object to be inspected. Unfortunately, when the EMAT coil behind a Ti sheet was connected to a receiver, the noise increased by almost a factor of ten when the wheel was moving at 30 mph. At high gain and with a slow sweep speed, the noise could be seen to consist of large, short duration spikes. Each spike consisted of a

damped sine wave at the band-pass frequency of the receiver. In all cases, this noise did not decrease at high fields as would be the case with true Barkhausen noise, but increased linearly with field. It is this dependence on magnetic field that indicates that the noise is acoustic in origin.

If the Ti were removed and the EMAT coils were held against the pole pieces by adhesive tape, the noise signals were much smaller and it was observed that the location of the EMAT receiver coil relative to the edge of the magnet pole pieces had a striking influence on the noise. Figure 5-22 shows how the signal and noise varied with magnetic field and direction of rotation of the wheel. In this case, the transmitter and receiver were

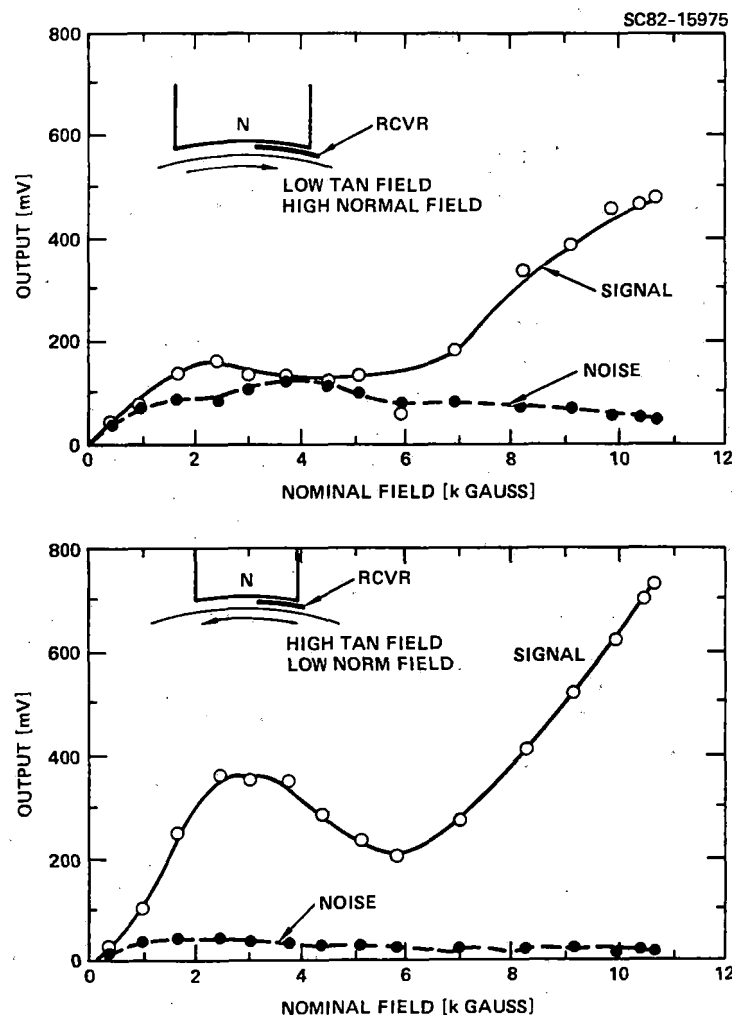


FIGURE 5-22 DEPENDENCE OF SIGNAL AND NOISE AMPLITUDES AT 30 MPH ON THE MAGNETIC FIELD AND DIRECTION OF ROTATION.

between the north and south pole pieces in the arrangement that should excite SH waves. When the receiver was at the trailing edge (higher normal field but lower tangential fields), the noise was higher and the signals lower than when the EMAT coil was at the leading edge. This result would indicate that the small amount of noise seen when no Ti wear plate was present was from Barkhausen noise associated with the component of the field tangential to the wheel surface between the north and south poles of the electromagnet.

Additional evidence that the Ti wear plate is the source of the large noise signals was obtained by interposing a piece of Mylar between the Ti and the moving wheel. This electrically insulating layer of high acoustic damping material greatly reduced the noise. If soft copper was placed between the Ti and the wheel, the noise was also reduced, although not eliminated. Brass shim stock at the rubbing interface caused a small reduction of the noise. Placing strips of Scotch tape on the Ti so that the wheel contacted the tape instead of the Ti was also very effective at reducing the noise.

As a tentative explanation of the noise, we postulate that microscopic asperities on the metal surfaces strike each other, weld together and break in so short a time that impulsive acoustic waves are generated in the low damping and hard Ti sheet. Mylar, being more compliant and having high damping, is not so easily excited into vibration by microscopic asperities in the surface of the steel wheel.



## 6.0 FIELD TEST RESULTS

After the unique capabilities of EMATs for rail flaw detection were demonstrated in the laboratory, it was important to move the apparatus out of the laboratory and put it on a railroad track in the field. In this way, its potential advantages could be verified in a manner that could satisfy the railroad industry that an improved inspection method is available. This section describes the demonstration field test vehicle that was constructed, the three field test sites that were used, and the results of the field testing both with respect to the environmental conditions that were encountered and in the defect detectability of the EMAT systems.

### 6.1 FIELD TEST VEHICLE

The foundation for the field test vehicle was a Nolan tool cart donated to the program by the Santa Fe Railroad. Modification of the cart for installation of the EMAT apparatus was performed by Magnasonics, Inc., with support from the Association of American Railroads (AAR). The Nolan cart consisted of a frame 58 in. long x 46 in. wide, with 5 in. diameter railroad wheels at each corner and a heavy wire mesh floor covering its upper surface. The key criteria for the EMAT carriage design using this cart were: 1) to support the electromagnet pole pieces 1/4 in. above the rail, 2) to maintain lateral tracking of the pole pieces over the center of the railhead, 3) to make the interchange of EMAT coils and pole pieces in the field as convenient as possible, and 4) to maximize the space on the cart surface for mounting power supplies and electronic instrumentation.

Figure 6-1 is a photograph of the assembled test cart on a section of test track laid out at Magnasonics, Inc. The magnet is in position for operation with the SR and SV EMATs, but could be rotated 90° and locked in position for SH operation as well. It was lifted off the rail with the help of the counterweight on the support arm to change pole pieces and service the EMATs. The 1/4 in. separation of the pole pieces from the railhead was maintained by auxiliary support wheels bolted onto the pole pieces.

Lateral tracking of the magnet pole pieces above the railhead was maintained by forcing the cart wheel flanges to stay in contact with the gauge side of the rail being inspected. This was accomplished by two pneumatic

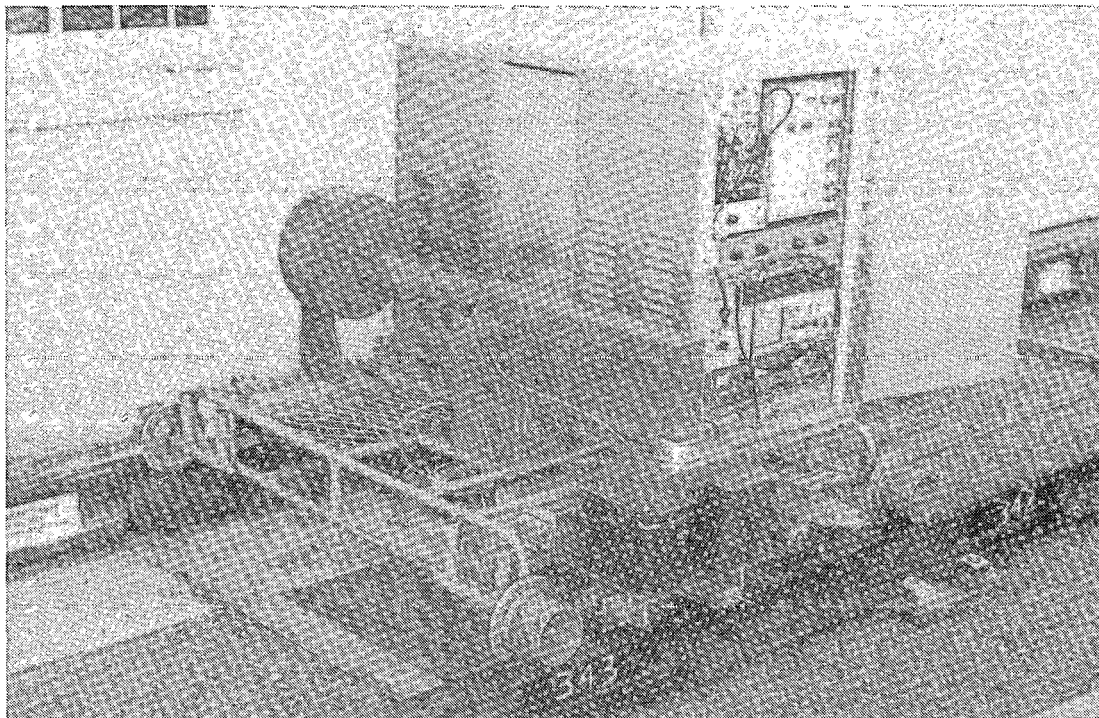


FIGURE 6-1 EXPERIMENTAL EMAT RAIL INSPECTION TEST CART.

cylinders that pushed auxiliary gauging wheels against the side of the opposite rail. Precise positioning of the EMATs over the center of the rail web was provided by a sliding EMAT holder attached to the pole pieces, as shown in Fig. 6-2. A similar fine adjustment is made for current ultrasonic wheel units using hydraulic actuators for tracking, particularly on curves where there is substantial gauge side wear on the railhead. On this experimental test cart, the adjustment was made using a thumbscrew.

The EMAT impedance matching networks and preamplifiers were located on a shelf near the electromagnet, but all of the rest of the electronics and data display equipment was installed on top of the cart in waterproof racks that had security doors for overnight storage. The 800 W of electrical power required for operation was supplied by a portable gasoline-powered 3 kW motor generator. For measurements at the Santa Fe test track, this was placed beside the track and a 100 ft long extension cord allowed mobility of the test cart. During the towing tests, it was carried on the towing vehicle.

SC36619

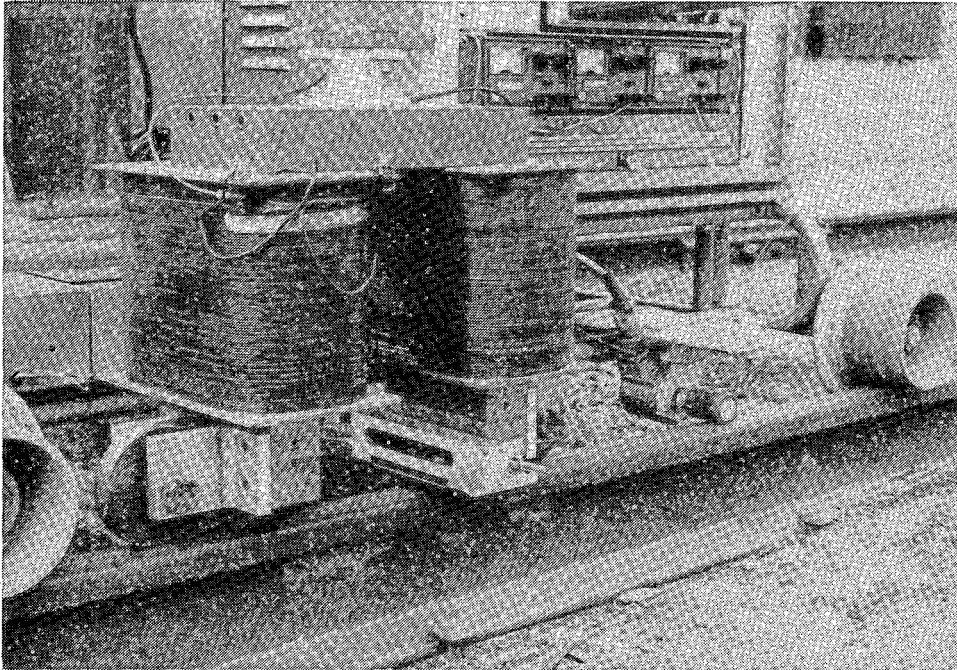


FIGURE 6-2 DETAILS OF THE MAGNET SUPPORT WHEELS, EMAT POSITIONER AND DISTANCE ENCODER MOUNTING.

Figure 6-3 shows the test cart being towed at the FAST track facility with the magnet rotated 90° for operation of the SH EMATs. The TM unidirectional receiver is under the electromagnet and the PPM transmitter is being towed along in back of it.

Figure 6-4 shows the ~ 1500 lb test cart being installed on the track at the Santa Fe test track grade crossing by Alfonso Manzanares from Magnasonics, Inc. It should be emphasized at this time that the design of this experimental cart was based on the use of laboratory test equipment that was available, with no emphasis placed on minimizing bulk, weight or electrical power requirements. It is estimated that a prototype system could be assembled using an electromagnet and electronic components, each comprising 1/10 the volume of the units that were used in this demonstration system.

## 6.2 DESCRIPTION OF FIELD TEST SITES

After the laboratory test phase had shown the capability of EMATs for detecting all of the serious types of rail defects considered in this program, the experimental self-contained test cart was assembled that could be either manually pushed or towed behind a rail inspection vehicle for measurements on

SC36620

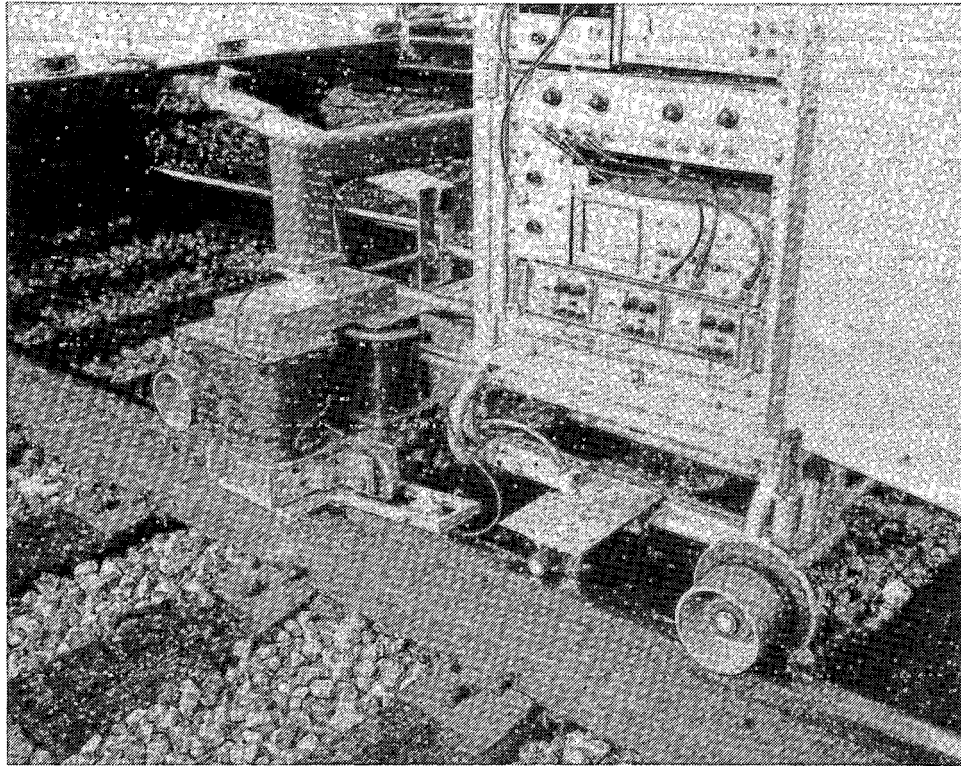


FIGURE 6-3 TEST CART BEING TOWED AT FAST TRACK.

SC36621



FIGURE 6-4 TEST CART BEING UNLOADED AT THE SANTA FE TEST TRACK.

real railroad tracks. The experimental test cart had the capability of making measurements with only one type of EMAT at a time on one of the rails. Therefore, repeated measurements were made with the different types of EMATS and on both rails where possible or desirable. This section contains a description of the three areas of track in which this was done

#### 6.2.1 Santa Fe Test Track

The Santa Fe Railroad maintains a section of test track within the switching yard in Albuquerque, NM that has a variety of known defects. It is maintained for use in periodically calibrating the defect detection devices on the Santa Fe rail inspection vehicles, and for experimental use in evaluating improvements in those devices. Access to this section of test track was very generously volunteered by Santa Fe for use in this program.\*

The immediate vicinity of the test track in the switch yard is sketched roughly to scale in Fig. 6-5, showing the grade crossing used to get the test cart on the track and the switches that had to be traversed to reach the test track. The test track is approximately 400 ft long, consisting of 23 bolted sections of 90 lb/yd rail extending from Switch No. 316 to a point about 100 ft from a dead end. This last 100 ft is an older 4.5 in. high, 66 lb/yd rail. The rail sections in the test track were each given a number designation, as shown in Fig. 6-6. The defect locations were noted in inches from the north end of each rail section on the east side of the track, and from the south end of each rail section on the west side of the track. The locations of most of the larger defects were indicated by paint markings on the side of the rails. In addition to natural defects, there were a few 3/8 in. diameter holes drilled through the rail web and saw cuts in the edges of the railhead serving as artificial flaws.

#### 6.2.2 Mainline Track and Siding Near Isleta

The experimental test cart was transported to a section of mainline track about 20 miles south of Albuquerque, near Isleta, where there was a good

---

\* The almost daily provision of advice and assistance by Charlie Stearns and Harlow Beene throughout the tests is gratefully acknowledged.

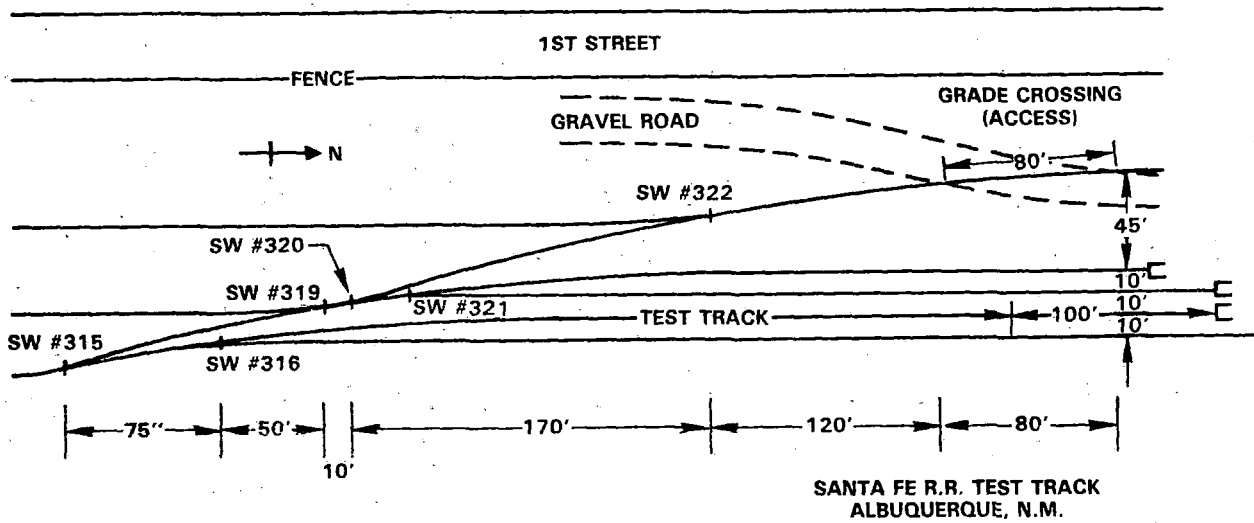


FIGURE 6-5 LOCATION OF SANTA FE TEST TRACK IN SWITCH YARD.

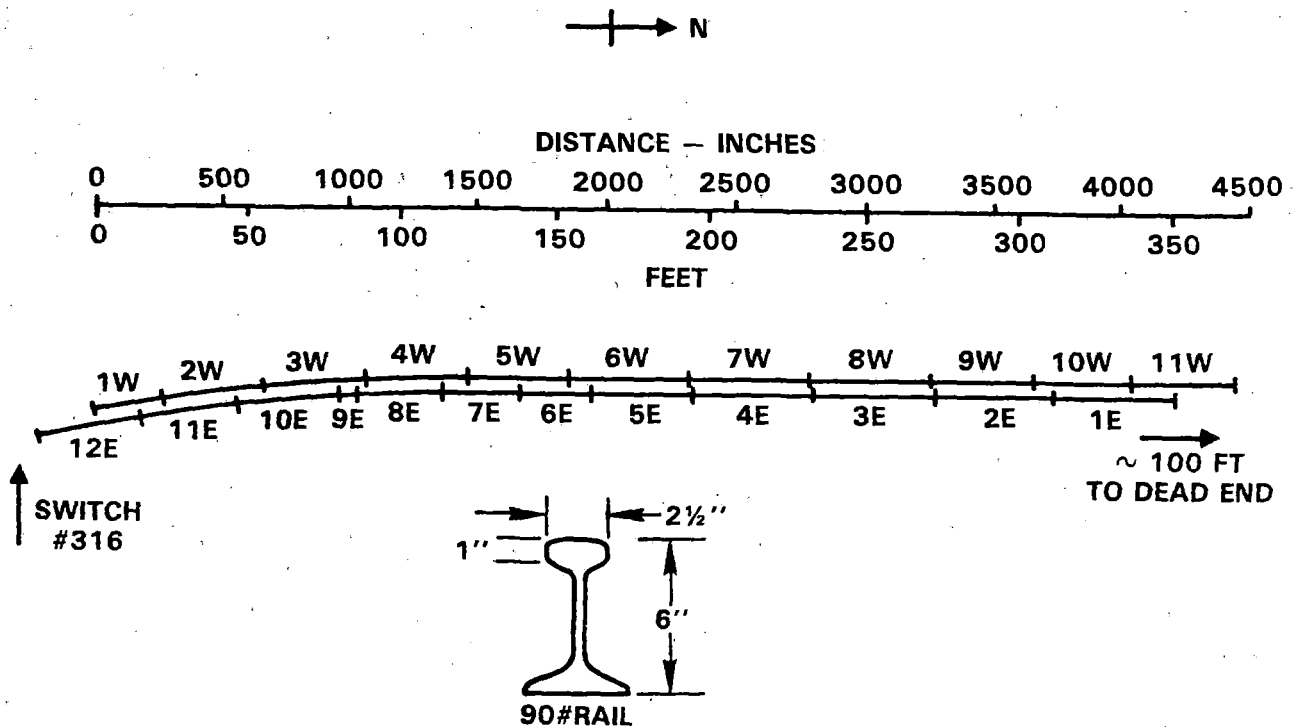


FIGURE 6-6 IDENTIFICATION OF SANTA FE TEST TRACK RAIL SECTIONS

example of a curve-worn and shelly rail. Shelling is a rail surface condition that can cause false defect indications, and the purpose of the test was to see how well the EMATs could look under this surface condition, and if they would maintain a stable signal in the curve-worn rail. Transverse defects can initiate from shelling, but there were no known defects in this section of track. However, there were some HSH defects found unexpectedly in a siding that was used to clear the mainline track to allow trains to pass.

A rough map of the area is shown in Fig. 6-7, indicating the access point and the areas where data were obtained using two different EMAT types, the SH and ST EMATs. All measurements were made on the outer rail where the wear was the greatest while being towed behind Santa Fe Ultrasonic Rail Test Car No. 16\* at speeds of 3 mph or less.

SC85-32574

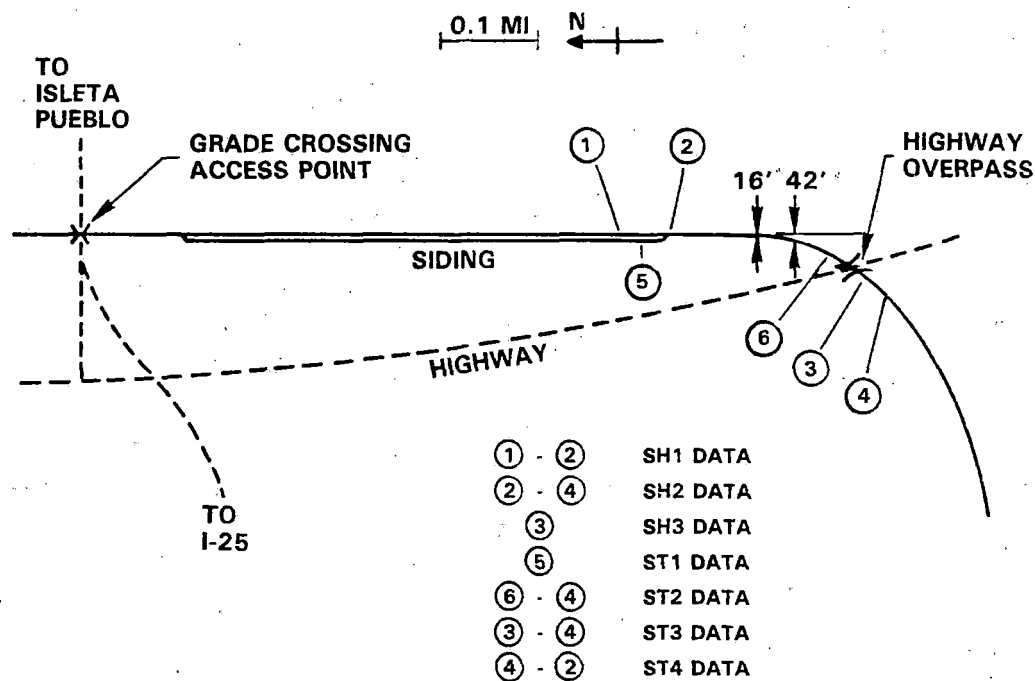


FIGURE 6-7 MAP OF ISLETA TOWING TEST LOCATION.

\* The cooperation, helpful suggestions and patience of the test car operators, Reilly and Ted, while making these measurements are gratefully acknowledged.

### 6.2.3 FAST Track

As a final field demonstration of EMAT performance, the experimental test cart was taken to the FRA Transportation Test Center located about 20 miles east of Pueblo, CO. One of the test facilities there is the Facility for Accelerated Service Testing (FAST). Its purpose was primarily to monitor defect growth rates under various conditions, and at the time of our visit there were a total of 82 known and well-characterized defects in this 4.8 mile section of track. Many of these defects were inspected daily with a FRA rail flaw detection vehicle using either conventional ultrasonic wheel probes or a more precise ultrasonic rail flaw display image system (URFDIS), which generates C-scan type of defect images in each of the three principal planes using computer reconstruction. This level of defect documentation provided an excellent basis for evaluation of the EMAT capabilities.

A map of the FAST track facility is shown in Fig. 6-8. Access to the track was just outside of the maintenance building, which also served as over-

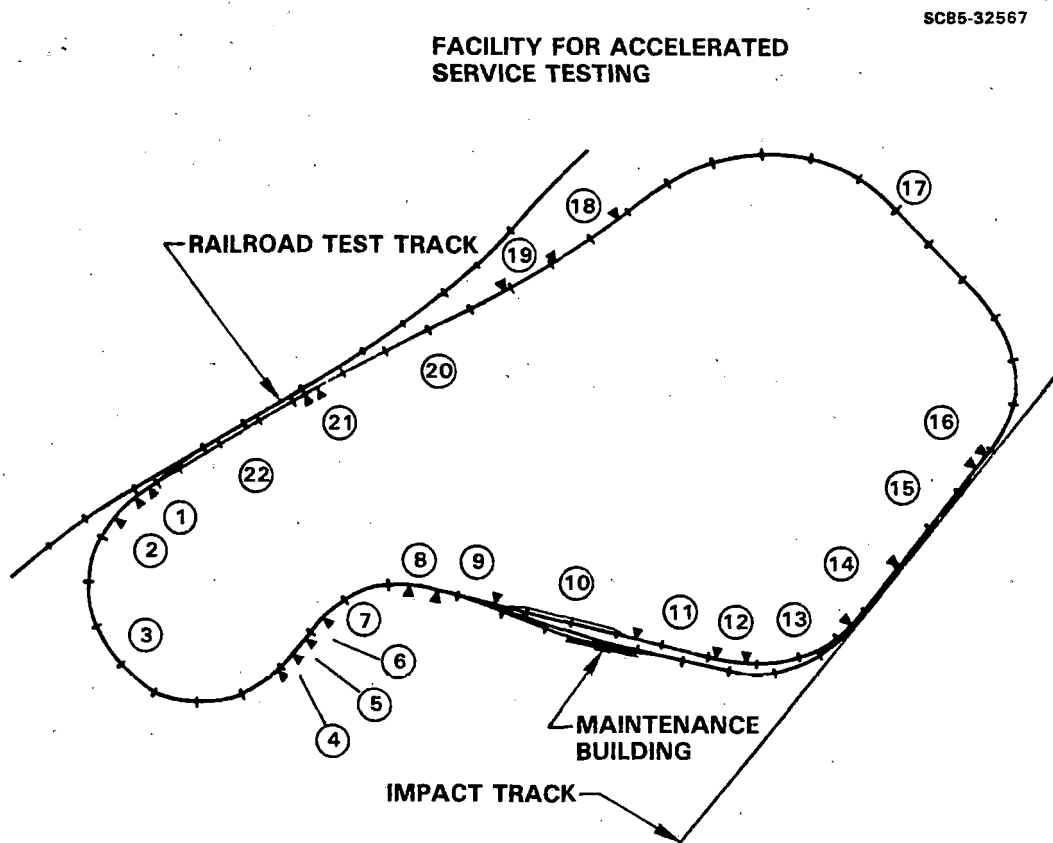


FIGURE 6-8 FACILITY FOR ACCELERATED SERVICE TESTING (FAST).



night protection for the EMAT test cart from snow storms that occurred during the week-long series of tests. A list of the FAST track defects is shown in Table 6-1. The starred defects in the inside rail of Section 7 and the outside rail of Section 10 were measured with the EMAT system. In addition, at a program review meeting demonstration in February, 1985, measurements were made on the inside rail of Section 10, where a large, unanticipated, transverse defect was discovered by the EMAT system. All measurements were made while being towed behind the FRA rail flaw detection vehicle.\*

### 6.3 SUMMARY OF RESULTS

All the defects that were known to exist in the field test track were detected with the EMAT system with only two possible exceptions. A large TD at the Santa Fe Test Track produced an anomalously small reflected signal similar to the result found for laboratory specimen No. 331 (see page 42). Second, a 3% TD at FAST produced only a barely detectable reflection. In addition, however, there were quite a few defects detected by the EMATs that were previously unmarked both in the Santa Fe Test Track and the Isleta siding. Also, one large unmarked TD was discovered at FAST, as mentioned previously, that could have led to serious consequences if it had remained undetected and failed while a train was passing over it.

This section summarizes the results of defect detection during the field tests with emphasis on the more unusual cases as described above. Strip chart recordings showing successful detection of many of the other defects are included in Appendix C.

#### 6.3.1 Santa Fe Results

A list of the major accomplishments during the laboratory preparations and field testing at the Santa Fe Test Track is shown in Table 6-2. This provides an overview of the activities involved in the field testing,

---

\* The cooperation, helpful suggestions, patience and hot coffee provided by test vehicle operators, Ron McCredie and Chuck Chisholm, while making these measurements are gratefully acknowledged.

TABLE 6-1 NATURAL DEFECTS IN FAST TRACK - 11 DECEMBER 1983

Sec. No.	OUTSIDE						INSIDE					
	TD (%)	HSB (in.)	BHC (in.)	Weld (%)	Shell (in.)	EB (in.)	TD (%)	HSB (in.)	BHC (in.)	Weld (%)	Shell (in.)	EB (in.)
1												
2												
3	9					1	1	1/2				
4	12					1						
5	8											
7							3*				2*	
							7*				3*	1*
8		2					3					
9		2					3					
							1					
							1					
10	32*	1*			1*		17*	3				
	24*	2*			4*		17*					
	27*	4*			2		22*					
	25*	1*					Unk.*					
	39*											
11		3					3	1/2				
		3										
12												
13	30				1							
	46											
	12											
14		1			12		4				3	
					6		2					
15							3				2	
		1					2					
		2					3					
		1					2					
		1					4					
		4										
		3										
		24										
		1										
16					24							
17	3			8	5						8	
18							1					
19							1					
20							2					
21		2										
		3										
22	11	1		3	18						40	
	6	2			10						8	
		1			6							
Total#	14	23	0	2	11	2	6	15	2	0	8	0
Total by Type	20	30	2	2	19	2						
Total# Defects	83											

TABLE 6-2 SUMMARY OF ACCOMPLISHMENTS DURING FIELD TESTING AT SANTA FE

Improved Instrumentation

- Constructed new 0° EMAT holders
- Compared SR and ST 0° shear EMATs
- Determined effects of rail head wear on magnetic field

Detected Nine New VSH Defects Successfully

- Compared SR and ST sensitivity
- Established detectability of VSH with SH

Constructed Rails Test Carriage

- Provided self-contained ST, SH and SV measurement systems
- Operated with motor/generator electric power

Provided Means for Transporting Test Carriage

- Devised loading and unloading methods
- Provided tarpaulin protective cover
- Made system immune to vibration

Field Hardened Instrumentation

- Eliminated RFI at 1.6 MHz
- Improved test rail gauging
- Improved chart recorder ink flow

Detected Various Rail Defects with ST and SH EMATs

- 3 - VSH
- 8 - Large TD
- 3 - Medium TD
- 12 - Small TD
- 3 - Small TD?
- 1 - EBF?
  - 1/4 in. deep saw cut in side of rail head
  - 3/8 in. diameter drilled holes in web

Verified Defects by Hand Measurement

many of which have been discussed previously in this report. Potential problem areas for future testing that were encountered will be discussed in detail in later sections.

All of the defects detected in the Santa Fe Test Track are listed in Tables 6-3 and 6-4. There were quite a few transverse defects and one vertical split head detected by the EMATS that were not previously marked, and all of these were confirmed to be present by measurements with a conventional 70° shear wave piezoelectric wedge transducer or a 0° longitudinal transducer. No attempt was made to estimate the sizes of the transverse defects beyond just a small, medium or large rating. Many of these hand measurements were reconfirmed by Santa Fe rail inspection personnel, particularly for the smaller defects.

An example of detection of the unmarked TDs in rail section No. 9E is shown in Fig. 6-9. At the top is shown the chart recording trace of the direct transmission SH signal with the locations of the five TDs that were confirmed to be present by hand measurements. Below that are the traces of the reverse reflected (SH-R) and forward reflected (SH-F) signals with bars drawn in indicating the predicted time windows for the reflected signals. As before, (TD) and (RE) in parenthesis indicate signals reflected back to the SH unidirectional receiver from the wrong direction, yet still detected at about a 16 dB reduced amplitude. It appears that four of the five TDs can be resolved in the trace of the direct transmission signal, the two small TDs being too close to be separately resolved. Only the larger TDs can be resolved in the traces of the reflected signals because of the proximity of either these TDs or the rail ends to the other defects. The detection S/N for these larger TDs is 10:1 or greater.

In contrast, the traces for the one large TD that was not detected well is shown in Fig. 6-10. Here, the S/N is barely 2:1. Visual inspection indicated this defect to be surface-emerging on the gauge side of the rail head, a feature in common with the defect in laboratory specimen No. 331 that was also difficult to detect. The trace of the crack visibly extended for about 1 in. straight across the top of the rail head and in a curving arc averaging about 45° from vertical extending from just under a rolled lip at the top of the gauge side of the rail head just to the bottom of the side of the head. The apparent extreme angle of this defect might have been the

TABLE 6-3. DEFECTS IN EAST RAIL OF SANTA FE TEST TRACK

Rail No.	Position (in. from North end)	Description
1E	242.5 244.3	* 3/8 in. hole drilled thru web at ~ 1/2 height * 3/8 in. hole drilled thru web at ~ 1/2 height
2E	211.0 213.0	* 3/8 in. hole drilled thru web at ~ 1/2 height * 3/8 in. hole drilled thru web at ~ 1/2 height
3E	317.3 362.6 405.0-458.4	TD, small TD, small? * VSH, 53 in. long
4E	211.4 212.8	* 3/8 in. hole drilled thru web at ~ 1/2 height * 3/8 in. hole drilled thru web at ~ 1/2 height
5E	260.8	* Corner saw cut ~ 1/4 in. deep, bottom corner, G
6E	42.5	* Corner saw cut ~ 1/4 in. deep, bottom corner, G
7E	196.8 199.5	* Bonding post hole * Bonding post hole
8E	11.5 13.2	TD, small TD, small
9E	14.4 22.0 23.3 51.0 55.0	TD, large TD, small TD, small TD, large TD, medium
10E	127.0 191.9-234.4	TD, small? * VSH, 42 in. long
11E	24.0 207.5	TD, large TD, small
12E	301.6	TD, small?

\* Marked by Santa Fe or artificial flaw

NOTE: G designates the gauge side of the railhead and F the field side

TABLE 6-4. DEFECTS IN WEST RAIL OF SANTA FE TEST TRACK

Rail No.	Position (in. from South end)	Description
1W	---	-----
2W	61.0 333.0	TD, small TD, medium (possibly EBF)
3W	161.6 199.8 218.1	TD, small TD, small * TD, large
4W	85.7 156.4 265.4	* TD, large, surface emerging on F * TD, small * TD, large, surface emerging on F
5W	202.3 349.5	TD, large * TD, large, surface emerging on G
6W	41.8	* Corner saw cut ~ 1/4 in. deep, bottom corner G
7W	267.5	* Side saw cut ~ 1/4 in. deep, vertical on F
8W	---	---
9W	126.0 188.5 198.0 241.1	TD, small TD, small, deep in head Shell? 1/2 in. longitudinal crack 0.6 in. from G TD, medium
10W	235.0 243.0 331.5 329.0	* 1 in. bolt hole through web * 1 in. bolt hole through web * 1 in. bolt hole through web * 1 in. bolt hole through web
11W	316.3 329.4-334.0	TD, medium VSH, 5 in. long

\* Marked by Santa Fe or artificial flaw

NOTE: G designates the gauge side of the railhead and F the field side

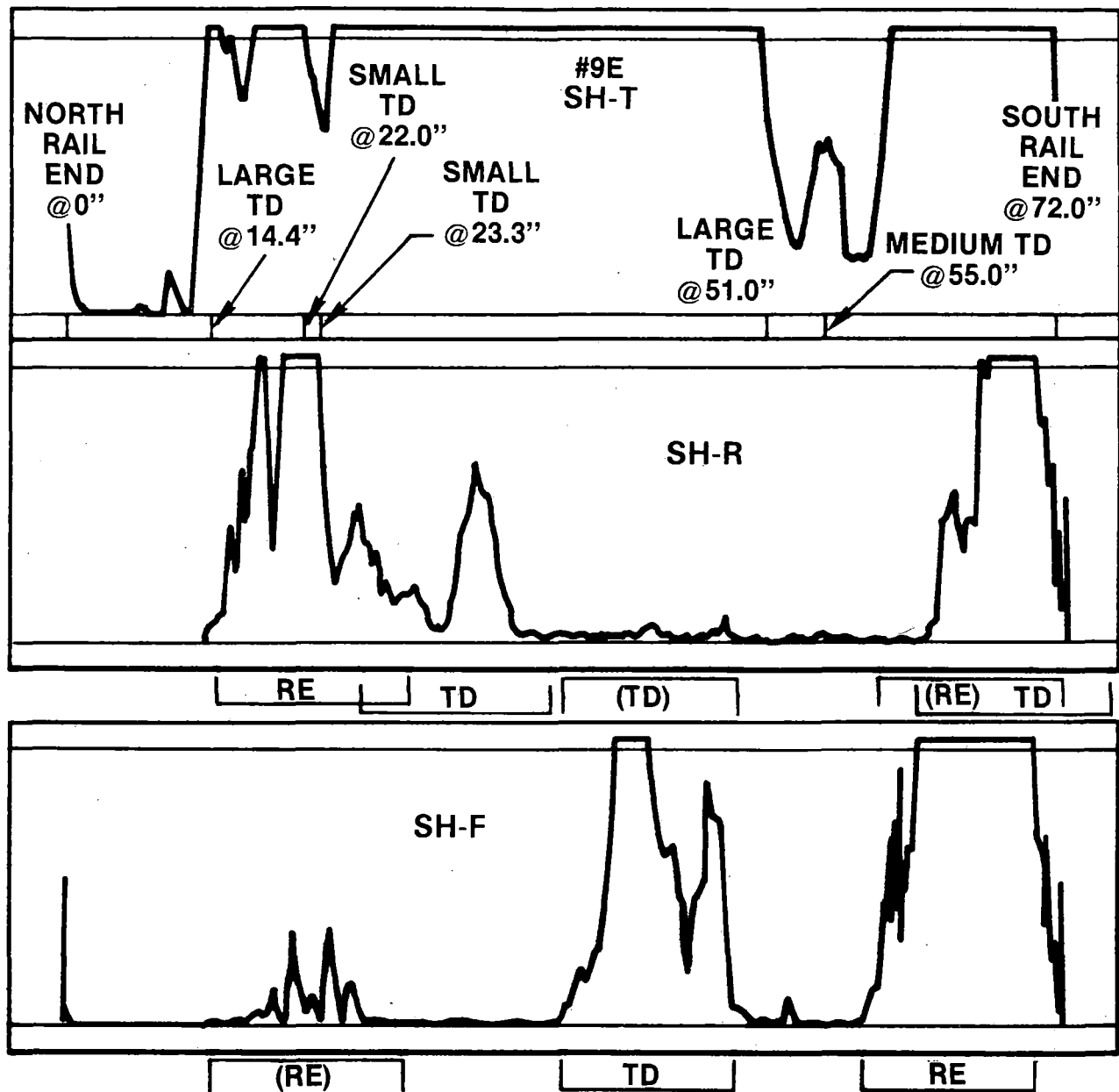


FIGURE 6-9 THREE MODES OF DETECTION OF LARGE TDS WITH SH EMAT IN NO. 9E. TOP TRACE INDICATES LOCATION OF FIVE TDS CONFIRMED BY HAND-SCANNING.

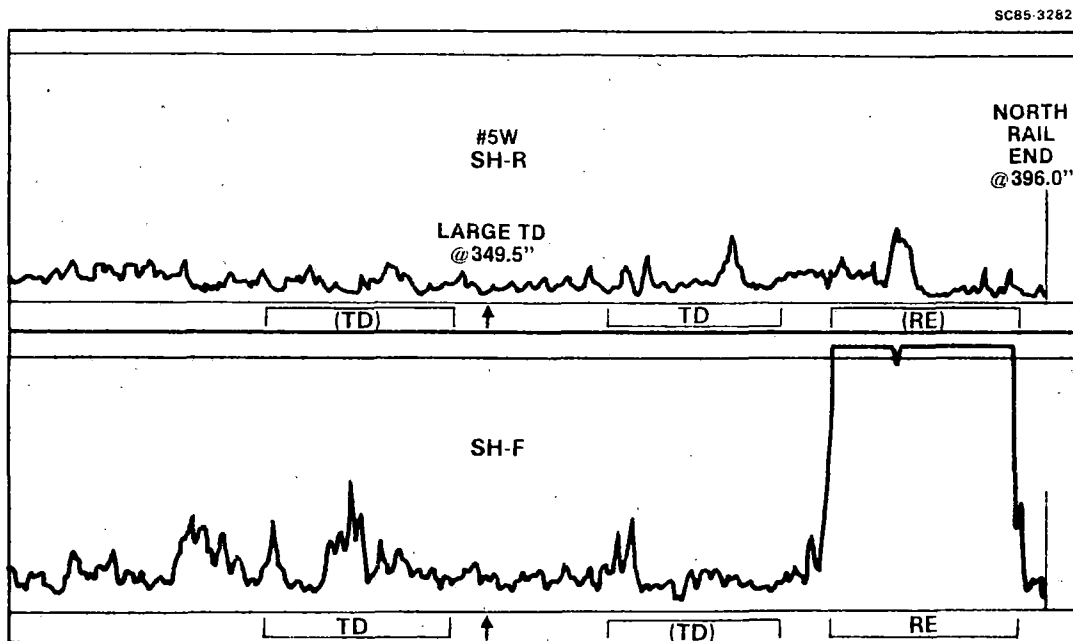


FIGURE 6-10 ILLUSTRATING THE POOR DETECTABILITY OF LARGE TD IN NO. 5W, POSSIBLY DUE TO AN ELECTROMAGNETIC COUPLING ANOMALY.

reason for its poor detection. Smoothing of the fracture surfaces by rubbing and/or oxidation might also have been a contributing factor. A third possible factor was that the electromagnetic coupling efficiency in this particular section of rail, as measured by the relative amplitude of the direct transmit signal, was 4 dB lower than the median of all the other rail sections and was the lowest efficiency observed. Whatever the reason, the poor detectability of this particular TD must be seriously considered, although its contribution to the overall evaluation of the EMATs performance should await more extensive field test experience in comparison with existing inspection methods.

A final example of the performance of the SH EMATs is the detection of the artificial transverse defects. Section 5E, 6E and 6W each had saw cuts made in the lower corner of the rail head perpendicular to the rail length either on the gauge or field side. They were roughly triangular in shape with a maximum depth of about 1/4 in. and an area of about 3% of the cross section of the rail head. They were detectable with a 70° hand-held wedge transducer, but only over a very limited range of transducer positions. They were not detected by the SH EMATs even after several attempts at repositioning the SH transmitter to try to optimize the transmission and reflection angles.



A fourth simulated transverse defect was a vertical saw cut also about 1/4 in. deep on the field side of rail section 7W. Its area was about 6% of the head area and was indicated very strongly from both directions in reflection and even resulted in a small decrease in the direct transmit signal when it was between the SH transmitter and receiver EMATs. The chart recordings of the reflected signals, shown in Fig. 6-11, also exhibit the detection of reverberation in the rail head when the SH receiver is directly over the saw cut. The detection time window was adjusted so as not to detect the direct transmit signal or signals reflected off the saw cut when the receiver was directly over it. However, multiple reflections apparently occurred in the rail head that persisted in time to where they were detected. This phenomenon also was observed for the TDs in rail sections 11E and 4W and the VSHs in sections 10E and 11W, providing another indication of the presence of these defects.

SC85-32829

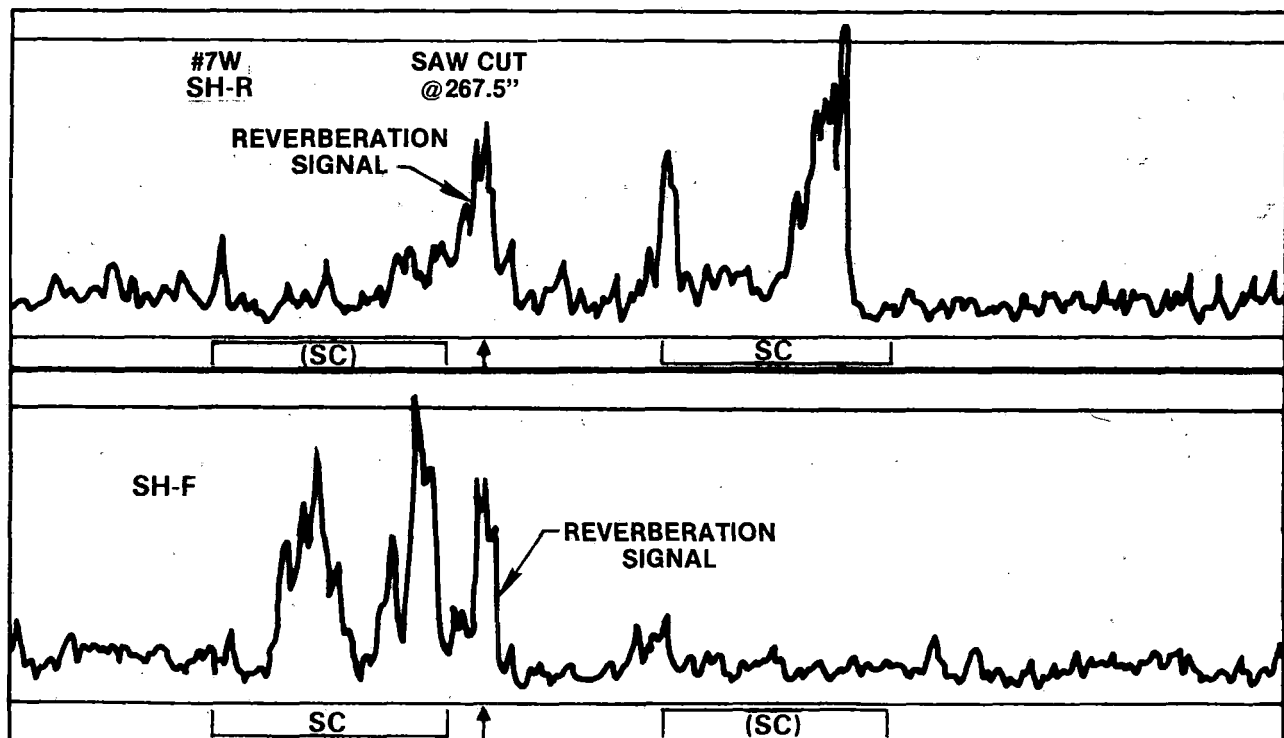


FIGURE 6-11 DETECTION OF 1/4 IN. DEEP SAW CUT IN SIDE OF RAIL HEAD IN NO. 7W.

Operation of the ST EMAT was quite successful in detecting the VSH defects, the 1-3/8 in. diameter bolt holes near the rail ends, the 3/8 in. diameter holes drilled through the web at various locations and some of the larger TDs. The only persistent problem encountered was the loss of base echo at the location of tie plates, the metal plates between the wood cross-ties and the base of the rail, and near rail ends where angle bars tie two rail sections together. These are regions where corrosion of the web and the base of the rail are most likely to occur and corrosion products to be trapped. This could cause a different coupling or a damping of the ultrasonic wave, and hence an attenuation of the base echo signal.

A correlation was noted between where the tie plates caused a loss of base echo and where dirt and sand covered the base of the rail. Conversely, loss of base echo was rarely seen where the surface of the gravel rail bed was clean and below the top of the wood ties. This problem was also not encountered at any of the other field test sites. It was later learned that the current Santa Fe rail inspection system detected the same kind of effect, so it is not endemic to the EMAT system nor is it a particular problem for rail NDE in general.

#### 6.3.2 Isleta Results

Preparations for the Isleta towing test had to be made within a 1-1/2 day period of time to take advantage of the availability of the Santa Fe Ultrasonics Rail Test Car No. 16 in the Albuquerque area for a few days. The very generous offer by Santa Fe personnel had been made previously to use one of their test cars as a towing vehicle for the EMAT test carriage, but the opportunity to do so came with very short notice.

The preparations included obtaining permission from the central dispatcher to get onto the section of mainline track selected for testing, designing and fabricating a tow bar and trailer hitch and providing electrical power for the EMAT electronics. There was sufficient electrical power on board the Santa Fe test car from its alternator/battery/inverter set, but when we tried to power the EMAT test carriage from that source the dc magnet power supply would not work (everything else did, however). Apparently, the dc rectifiers in the magnet power supply cannot operate on the 60 Hz square wave

voltage produced by the inverter. Fortunately, there was a convenient location on the front bumper of the test car to mount the motor/generator that had been in use at the Santa Fe test track. Photographs of the EMAT test carriage being towed on the mainline track are shown in Fig. 6-12.

The mainline track was made of 119 lb/yd welded rail. The section where all the data were taken was mapped in detail, as shown in Fig. 6-13. Most of the welds were factory welds, but a few were thermite field welds that additionally had safety straps bolted across the weld joints, as can be seen in Fig. 6-12B. There were also two insulated and bolted rail joints for signal activation. The rail ends at these joints, the bolt holes through the web, and the base of the rail acted as ultrasonic reflectors to provide signals for judging the performance of the EMATs.

About 500 ft of strip chart recordings were made during the towing tests at a scale factor of 16:1. The specific locations where recordings were made were shown previously in Fig. 6-7. The 90° SH wave measurements were made in both the direct transmission and reflection modes over a range of amplifier gain settings. The 0° ST wave measurements were all of the base echo amplitude, also using a range of gain settings and transducer positions across the rail head. Since there were no known defects in the track, the ranges in the EMAT settings were used to explore the effects of the curve worn and shelly rail on the potential ability of the EMATs to detect defects had they been present.

Traveling south along the track, the start of the curve was just past the siding switch. The first indication of minor shelling was on the outside rail at about weld joint W6 in Fig. 6-13. By W10, the shelling was almost continuous on the rail head, and it became progressively worse beyond the point as did the gauge side wear on the outer rail. A photograph of the rail surface in the curve is shown in Fig. 6-14.

Some observations about the performance of the EMAT systems obtained from a study of the chart recordings follow:

1. There were no major problems or major surprises experienced during the tests.

SC36623



(A)



(B)

FIGURE 6-12 THE TOWING TEST LOCATION: A) THE EMAT TEST CARRIAGE BEING TOWED ON THE MAINLINE TRACK; B) CURVE WHERE MOST OF THE MEASUREMENTS WERE MADE.

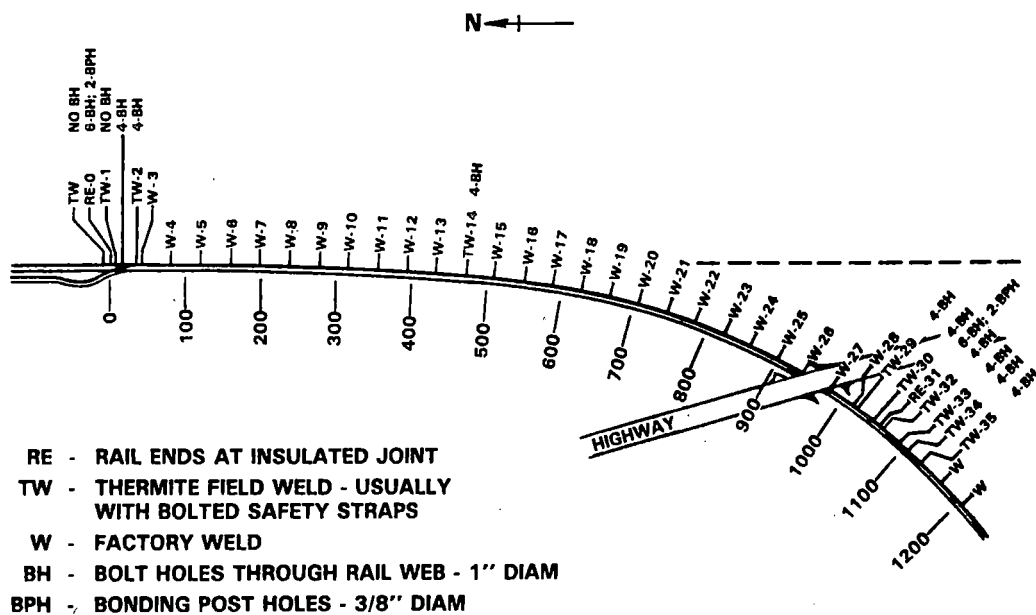


FIGURE 6-13 LOCATION AND TYPE OF EACH RAIL JOINT IN 1200 FT LONG CURVE TRANSITION REGION SOUTH OF THE SIDING SWITCH.

SC36622

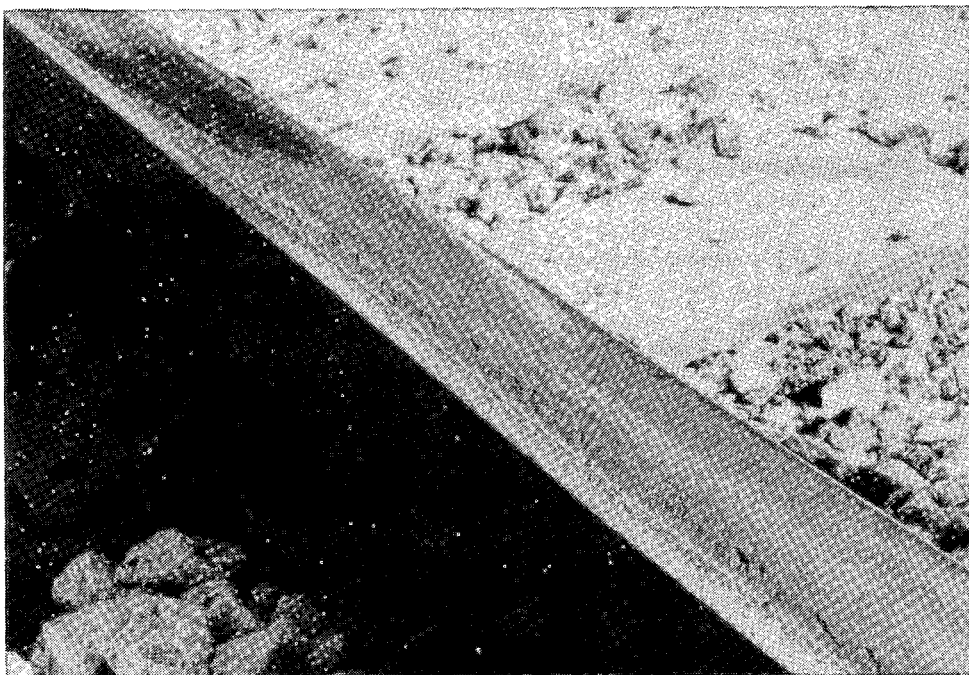


FIGURE 6-14 THE GAUGE SIDE WEAR PATTERN ON THE OUTSIDE RAIL IN THE CURVE.

2. Gauge side tracking was adequately provided by the air shock absorbers attached to the gauging wheels even on the slanted track in the curve.
3. There were no indications recorded that were interpreted as rail defects (except those in the siding as noted previously).
4. No SH wave reflections were seen from weld joints.
5. There was some loss of direct transmit SH wave signal amplitude at some but not all welds.
6. There was no appreciable SH wave reflection or loss of transmission due to the shelly surface condition of the rail head.
7. There was loss of base echo at some but not all weld joints using the ST wave.
8. No loss of base echo was observed at tie plates.
9. There was no loss of base echo at a few of the bolt holes. This surprising result is interpreted as due to an extremely tight fit of these few bolts in the holes with perhaps some corrosion products between the bolt and the hole adding to the ultrasonic wave transmissability.
10. The base echo amplitude changed systematically by a maximum of 3 dB when passing from one section to another of the welded rail.
11. There was no substantial change in the base echo amplitude in going from the curved to the straight section of rail for the same position of the EMAT on the rail head.

All of the observations above lend positive encouragement that the types of rail conditions experienced in this test do not adversely affect the ability of the EMAT systems for detection of defects in rails.

Although there were no defects in the mainline track, there were some found in the siding that was used around noon to get out of the way of mainline traffic. The siding was made of 90 lb/yd bolted rail which at one time had been in mainline use. Some sections had extreme gauge side wear and these sections had been reversed when installed in the siding, so the wear is now on the field side. One 40 ft section of rail near the switch had several visible defects which were identified by the Santa Fe test car operators as horizontal split heads (HSH). They placed chalk marks on the side of the rail where five of the more obvious of these were located, and these chalk marks corresponded precisely with subsequent indications found by measurements with the ST EMAT system. Descriptions of these five defects, marked by asterisks, and several other defects located by the EMAT measurements are given in Table 6-5. All of the defects had surface-emerging cracks associated with them, as indicated in the sketches. Measurements at a later time using conventional hand-held piezoelectric transducers confirmed that each also had a horizontal component of separation that blocked the ultrasonic base echo.

### 6.3.3 FAST Results

Measurements at FAST with the EMAT test carriage were made during the week of December 12-16, 1983 and again on February 13, 1985 during a demonstration for the Technical Advisory Panel. Most of the first week was spent measuring the flaws in the outside rail of Section No. 10 (see Table 6-1) and in determining the dependence of the test carriage towing speed on the EMAT signals. (Many of these measurements were made during several snow storms that passed through during that week.) During times when the FAST track was in use for other purposes, magnetic field dependence measurements were made on sections of spur track near the maintenance shed. On the last day of that week, measurements were also made on the defects in the inside rail of Section No. 7 during 12°F temperatures that caused intermittent failure due to icing of the motor/generator used to power the EMAT systems. The EMATs themselves experienced no difficulties with the inclement weather conditions, however.

Measurements of the defects in the inside rail of Section No. 10 were made during more favorable weather conditions on the February date.

TABLE 6-5. DEFECTS IN ISLETA SIDING TRACK

Position (in. from N end)	Description
21	* HSH - similar to 1
59	Engine burn - depression in head
75	* HSH - similar to 1
84	HSH - similar to 3
90	HSH - similar to 3
97	* HSH - similar to 1
131	* HSH - similar to 1
148	HSH - sketch 3; similar to 2, but cracks not as open
156	HSH - sketch 4
167	HSH - similar to 4
178	* HSH - worst one (sketch 1)
203	HSH - sketch 2
275	Engine burn - depression in head

6C85-32586

SKETCH 1

SKETCH 2

SKETCH 3

SKETCH 4



The eight marked transverse defects in Section No. 10 were all naturally occurring flaws that had been removed from mainline track and installed in the FAST track for testing purposes. Each was contained in a 6-10 ft section of rail which was welded in place in the FAST track. Safety straps were bolted onto the rail web across each TD to prevent complete separation in case of failure. The sizes of each of these eight flaws were measured daily after a full night's operation of a heavily loaded train around the 4.8 mi FAST track. Three independent measurements of the size of each TD were made using the Transportation Test Center's URFDIS flaw imaging system and the average of the three measurements recorded. These average size measurements for each of the five days in the week preceding the EMAT tests are indicated in Table 6-6. The variability in these measured sizes reflects the lack of precision inherent in attempting to determine defect size ultrasonically.

At the bottom of Table 6-6 are the values of the S/N of the three types of SH EMAT signals, the attenuation of the direct transmit signal, the reverse reflection amplitude and the forward reflection amplitude. The measurements of the five TDs in the outer rail show large S/N values not inconsistent with the large sizes of the defects. The measurements of the three TDs in the inner rail made two months later show even larger values of S/N, suggesting that these flaws had grown in size from the smaller values measured in December.

TABLE 6-6. FAST SECTION NO. 10 INSTALLED TDS  
Sizes of TDs as Measured by "URFDIS"

TD No. Tie No.	SP-24 659-0	SP-8 611-0	SP-29 560-0	SP-32 513-0	SP-25 472-0	DRG-5 466-I	UP-4 592-I	UP-5 629-I	Unk. ~ 650-I
Dec. 5	38%	30%	38%	24%	45%	18%	20%	14%	--
Dec. 6	24%	20%	26%	26%	26%	16%	15%	24%	--
Dec. 7	26%	19%	26%	21%	35%	18%	17%	22%	--
Dec. 8	33%	24%	33%	22%	38%	17%	15%	23%	--
Dec. 9	38%	28%	10%	33%	50%	18%	16%	26%	--

S/N of SH EMAT Signals									
	December 12					February 13			
SH-T	>2.5dB	> 0dB	>5.0db	>3.8dB	>5.5dB	--	--	--	--
SH-R	2:1	12:1	2:1	17:1	3:1	8:1	14:1	5:1	20:1
SH-F	6:1	11:1	12:1	12:1	12:1	15:1	13:1	11:1	12:1

Also detected in February with the SH EMATs was an unmarked TD in the inner rail. The S/N of the signal reflected from this defect were larger than from any of the other eight TDs. The traces of the forward reflected and reverse reflected signals from this defect are shown in Fig. 6-15.

The two other TDs measured with the SH EMATs were the 3% and 7% TDs in Section No. 7. Both of these were only marginally detected with S/N of about 1-1/2:1. The 7% TD, in particular, was only 8 in. from a rail weld joint which also reflected a small amount of ultrasonic energy, so the signal reflected from the TD was difficult to resolve. The traces for the 3% TD are shown in Fig. 6-16.

Of the five shells that were inspected with the SH EMATs, only one resulted in a measurable reflected signal which was about the size of that produced by the 3% TD in Fig. 6-16. Shelling is not considered to be a defect but a rail surface condition that is preferred not to be detected by the inspection system.

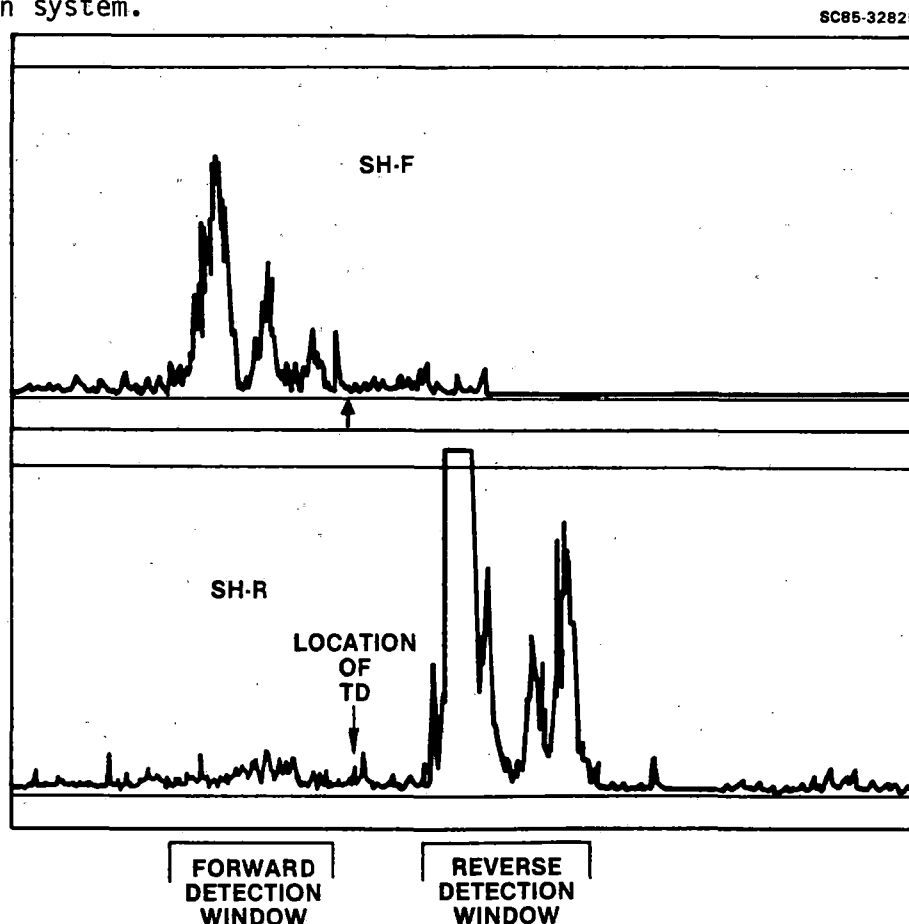


FIGURE 6-15 FORWARD AND REVERSE REFLECTION TRACES BY SH EMATs FROM LARGE UNMARKED TD IN INSIDE RAIL IN FAST SECTION NO. 10.

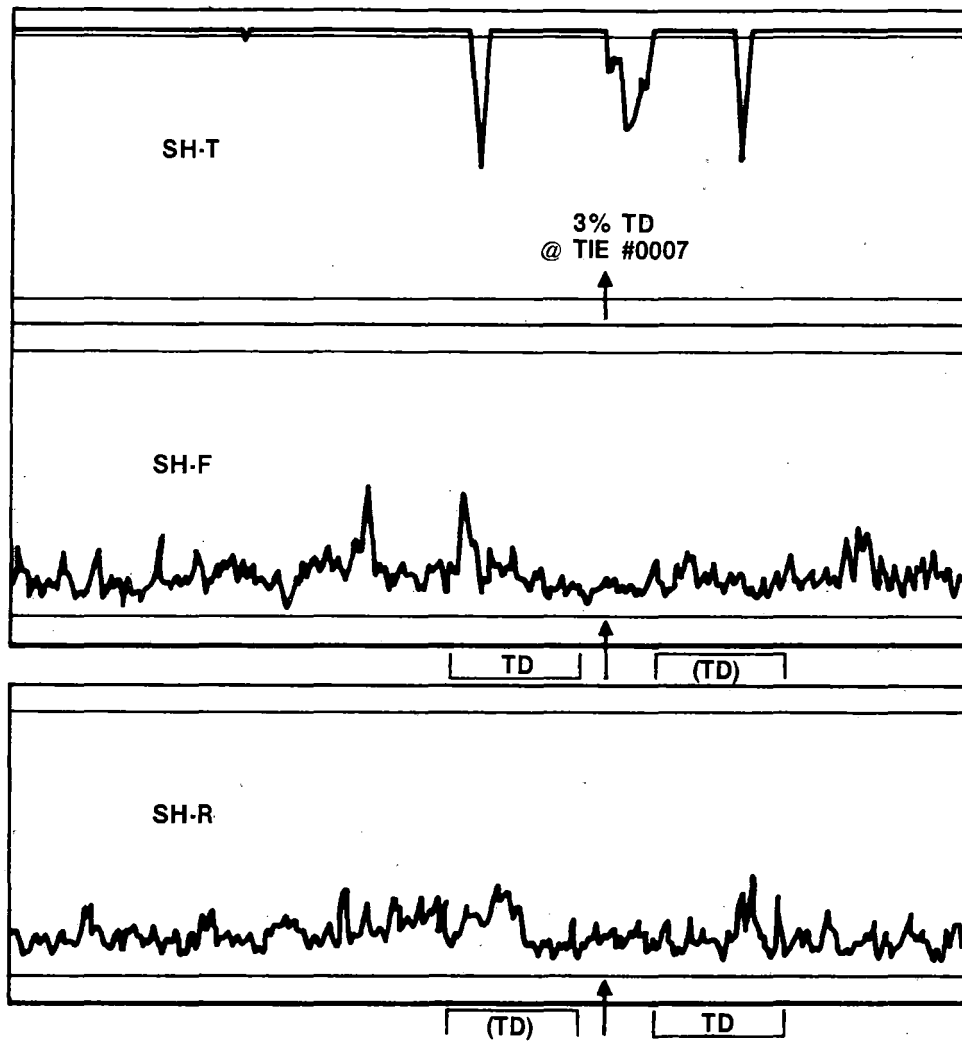


FIGURE 6-16 MARGINAL DETECTION OF 3% TD IN FAST SECTION NO. 7.

The operation of the ST EMAT was also largely successful, although there were only a few defects inspected at FAST that were amenable for detection by the 0° shear wave. These were the four HSH defects in the outer rail of Section No. 10, all of which were detected as a loss of base echo. In addition, each of the five large TDs in that rail section were similarly detected, although the ST wave is not primarily relied on for that purpose. The shelly regions resulted in a loss of base echo as well, a result to be expected if there is a large component of horizontal separation just below the surface of the rail head.

#### 6.4 FACTORS ADVERSELY AFFECTING EMAT PERFORMANCE

This section focuses on conditions that were encountered during the field test that could adversely affect the EMAT system's ability to detect defects during future tests. The tone of these comments should not be misconstrued as an overall negative rating for EMATs, but as a detailed examination of possible problems in an otherwise very successful demonstration of the capability of EMATs for defect detection in the field environment. This examination provides the data for planning more extensive investigations that would qualify EMATs for routine NDE of tracks.

The factors adversely affecting the performance of the EMAT systems have been divided into two groups for discussion: 1) those factors that might affect the detection of defects; and 2) the factors that might lead to false indications of the presence of defects.

##### 6.4.1 Defect Detection

During the field testing phase of the program, there were several conditions that were not experienced during the laboratory specimen testing that affected defect detectability. Solutions were found for the problems that these conditions caused and these solutions were implemented during the field testing where possible. The solutions as well as further systems modifications that are recommended for future testing are described in the following paragraphs.

EMI/RFI. The only persistent source of electromagnetic interference (EMI) that was experienced was caused by the motor/generator used to supply

electrical power to the EMATs. Other possible sources of EMI that were anticipated, such as switching and communication signals normal to operation of the railroad, were not detected. Even interference from electric arc welding only 20 ft away (inside the maintenance building at FAST) was not detected.

The source of the EMI caused by the motor/generator was investigated to determine its source. The ignition system of the gasoline engine which drove the generator was eliminated as the source so the characteristics of the generator were studied. Visualization of the 115 V, 60 Hz output of the generator on an oscilloscope showed a nominally sinusoidal waveform of 325 V peak-to-peak, but with several large, short duration voltage excursions superimposed. At two points within each cycle, these excursions were about 100 V and these corresponded with the occurrence of voltage spikes on the EMAT receiver output signal which had a voltage amplitude of about 100 times (20 dB) the normal noise level. These noise spikes were not synchronous with the EMAT pulse repetition frequency and only infrequently coincided in time with the 100-200  $\mu$ s long EMAT signal detection window. When they did, a very short duration spike would occur on the chart recording which was easily recognizable as such and could be ignored.

Several different types of line filters, noise suppressors and isolation transformers were tried without success to eliminate these noise spikes. Six brands of motor/generators were also tried and only one of these did not create the same problem, but it had some other characteristics (weight and poor voltage regulation) which made it unusable. The inconvenience of having the noise spikes present on the recorded traces was therefore endured during the field testing.

The radio frequency interference (RFI) problem initially was so severe as to prohibit the use of the ST EMAT system at the Santa Fe Test Track. Neither the SR or SH system operation were affected. Testing showed the RFI to be due to the railroad rail acting as an antenna for commercial AM radio signals distributed across the frequency band of 0.6 to 1.7 MHz and reradiating into the EMAT transducers. The geometry and center frequency of 1.8 MHz of the ST EMAT provided a very efficient receiver for this signal which saturated its amplifier stage. The RFI was completely eliminated, however, by adding a custom high rejection ratio filter ahead of the amplifier and no further problem with RFI was experienced.

Electromagnetic Coupling Variability. During the rail testing, local variations in the coupling efficiency of the EMATs were observed within a given section of rail, as well as systematic variations between sections. This variability could be most directly quantified by measuring the amplitude of the direct transmit signal between the SH transmitter and receiver since it does not depend on the reflective or geometric variations of, for example, the rail end or the base of the rail. Measurements of this variability were made for the rail sections at the Santa Fe Test Track from strip chart recordings of the direct transmit signal amplitude. For each rail section, the variation in the average signal amplitude along the entire length of the rail section was noted, as well as the maximum value of local variations, excluding variations due to known defects. Figure 6-17 shows histograms of the results of these measurements, as well as for the relative average signal amplitude between rail sections. In this later histogram, at the bottom of Fig. 6-17, the one rail section displaying the lowest transduction efficiency was section No. 5W, which contained the large TD that had the anomalously low reflected signal amplitude.

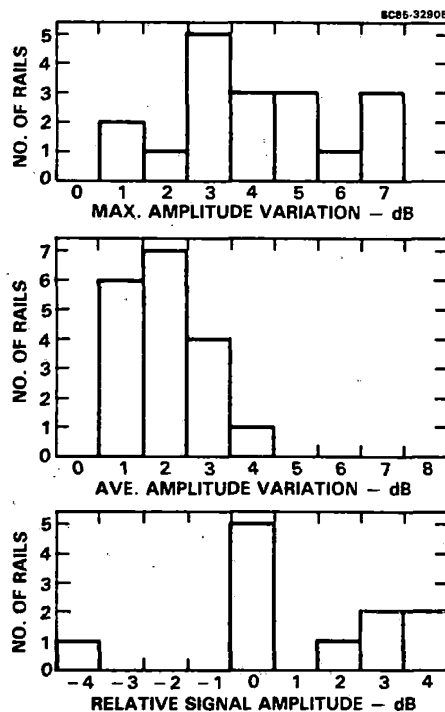


FIGURE 6-17 HISTOGRAMS OF SH DIRECT TRANSMISSION SIGNAL AMPLITUDE AND VARIABILITY WITHIN A RAIL SECTION FOR THE SANTA FE TEST TRACK RAILS.

In an attempt to understand the cause of the variable transducer efficiency with position, a set of measurements were made of the magnetic field dependence of the signal amplitude. While at FAST, measurements were made where the signal amplitude was the largest and where it was the smallest. The dc current to the electromagnet was changed in steps, and measurements were made of the normal component of the magnetic field in the gap between the pole piece at the SH receiver EMAT and the rail head, and of the amplifier gain required to maintain a constant amplitude of the direct transmit signal. These data fit the relationship  $V = V_0 (B + B_0)^n$  with a correlation coefficient of 0.997 or better for a value of  $n = 1$  as predicted from theory (since the bias magnetic field at the PPM transmitter EMAT was not changed during the measurements). Similar measurements of the base echo amplitude were made with the ST EMAT at two locations and the data were fit to the same relationship with a value of  $n = 2$ , since both the transmitter and receiver EMATs are involved here.

The data from these tests are shown plotted in Fig. 6-18 and the results of the curve fitting are given in Table 6-7. The variability of  $B_0$  and  $V_0$  in these experiments is due entirely to the magnetic and electrical properties in a thin layer of steel at the surface of the rail. These properties are strongly affected by the amount of cold work in this layer which is believed to be the major cause for the variation in EMAT transduction efficiency that was observed.

TABLE 6-7. CURVE-FIT PARAMETERS FROM MAGNETIC FIELD DEPENDENCE TESTS

Test No.	V @ B = 10 kg	$B_0$	$V_0$
SH	1	0.810	+3.80
	2	0.642	+4.80
	3	0.358	-1.16
	4	0.245	+1.47
ST	5	1.075	-0.48
	6	0.357	-3.00

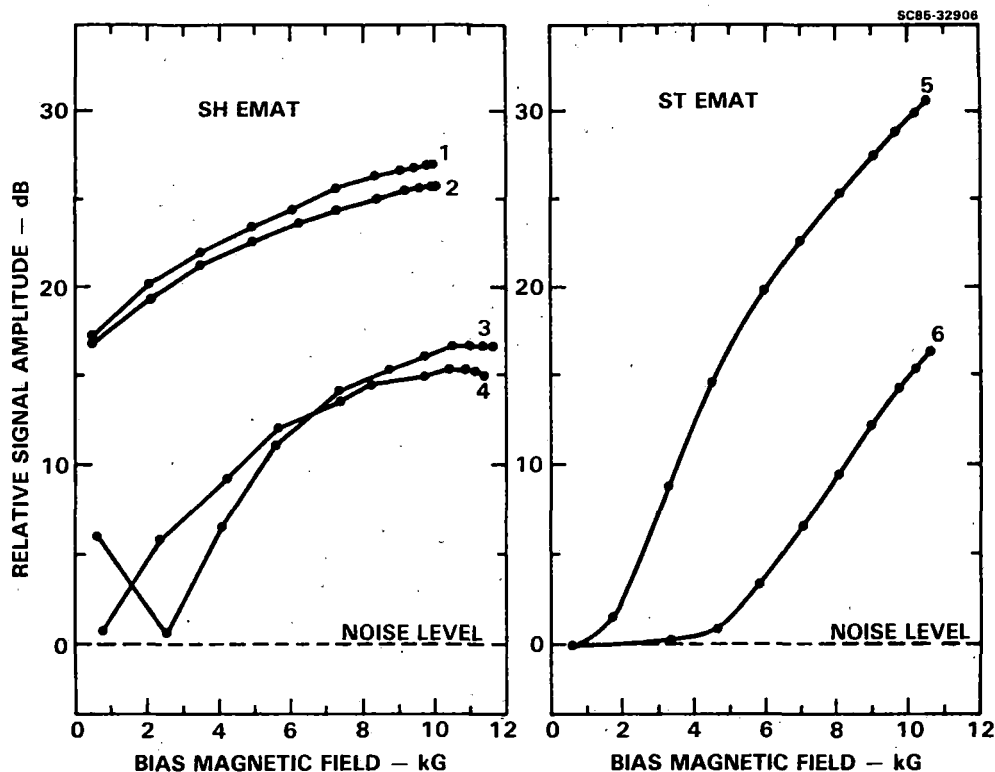


FIGURE 6-18 DEPENDENCE OF SIGNAL AMPLITUDE ON APPLIED BIAS MAGNETIC FIELD AT SELECTED POINTS ON FAST RAILS.

Implementation of automatic gain control (AGC) in the ST and SH EMAT receiver amplifiers using the SH direct transmit signal amplitude as the reference would eliminate most of the variability that was observed. Logarithmic amplification of the SH direct transmission and ST base echo signals would also increase the contrast between these relatively minor variations and the large signal attenuation caused by defects.

Another set of measurements were made at Magnasonics on the laboratory rail test specimens that, while of only incidental relevance to the present work, are important in the consideration of future developments of the EMAT systems for rail NDE. Rayleigh waves were generated and detected on the surface of the rail specimens using the tangential magnetic field to generate the wave through a magnetostrictive interaction. These measurements were compared to those on a plate of well annealed steel to arrive at a relative measure for the strength of the magnetostriction in cold worked rails. The histogram in Fig. 6-19 shows the results of these measurements. Most of the rails are less efficient by 10 to 15 dB, but some are down by as much as



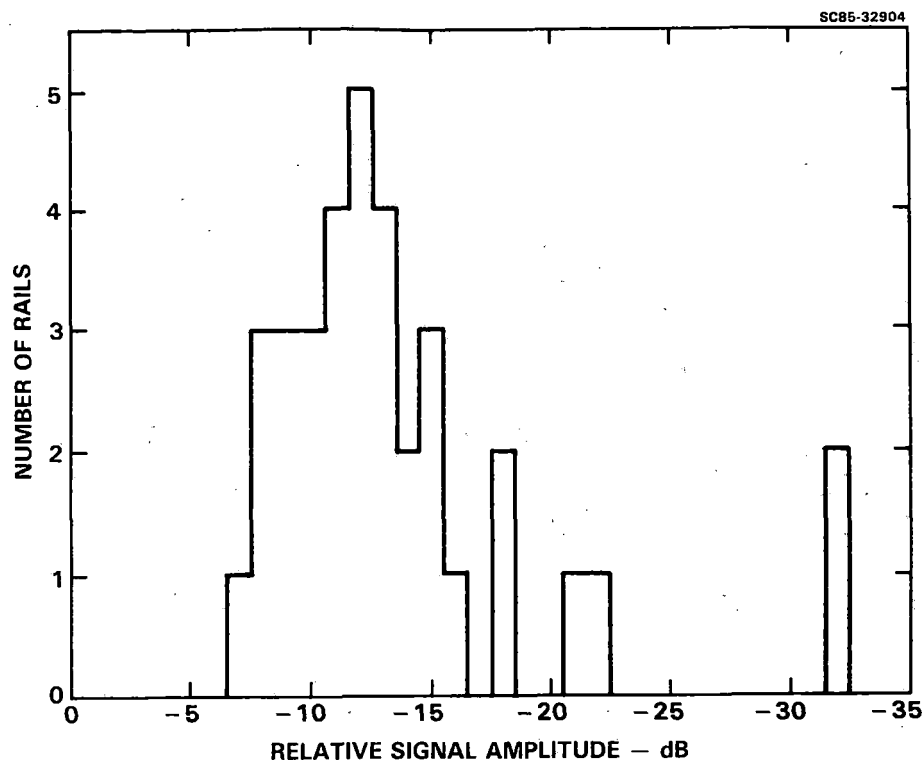


FIGURE 6-19 AMPLITUDE OF RAYLEIGH WAVES EXCITED BY A MAGNETOSTRICTIVE MECHANISM IN LABORATORY RAIL SPECIMENS RELATIVE TO A FLAT PLATE OF ANNEALED STEEL.

30 dB. This large decrease in efficiency would seem to indicate that magnetostriction would not be reliable for rail inspection, but data available at Magnasonics shows that magnetostriction can be as much as 36 dB more efficient at generating ultrasonic waves than the periodic permanent magnet EMATs used on this rail inspection program. Thus, there is reason to believe that the least efficient magnetostriction case would be comparable to the present SH wave EMATs. Therefore, magnetostrictive coupling and the smaller magnets that it requires should be considered for future rail inspection systems.

Speed Dependence. The performance of the ST and SH EMAT systems at increased speed was evaluated in the field by towing the test carriage at FAST at various speeds up to 8 mph. This was the maximum speed considered to be safe with the 5 in. diameter wheels and the weight of the test carriage. The factors considered in judging the EMAT's performance were their susceptibility to incidental mechanical or magnetic Barkhausen noise and their spatial resolution in detecting flaws at higher speeds.

No appreciable increase in the noise level up to 8 mph was seen for the ST EMAT at its operating frequency of 1.8 MHz. Its spatial resolution was limited, however, by the 100 Hz transmitter pulse repetition frequency (PRF). This explains the rapidly deteriorating detection of the 1 in. diameter bolt holes near rail ends above 4 mph ( $\sim 70$  in./s), since at that speed the bolt holes were within the EMAT's beam pattern for two pulses at most. This is not an inherent limitation of the EMAT system, since a much faster PRF can be built into the system. An achievable PRF of about 1400 Hz would be required to resolve BHC cracks to 1/8 in. at 10 mph, for example, but this was not one of the goals of the present program.

With the SH EMATs, a serious mechanical noise problem was observed at speeds above 2-3 mph. At that speed, the amplitude of the noise approached that of the signals reflected off the large TDs. Spatial resolution was not as much of a problem for TD detection since they are in range of the SH wave for 6-10 in. of travel along the rail. It is believed that the source of the mechanical noise was mainly the rubbing of the EMAT plastic wear plate on the rail surface, although the steel magnet support wheels rolling along the rail could also have contributed. The noise amplitude was seen to increase with increasing amounts of dirt on the rail surface, but this would affect the rolling friction of the wheels and the sliding friction of the EMAT in the same way.

Several possible solutions to this noise problem are suggested. The most direct and probably most fruitful is to increase the operating frequency from the present 250 kHz to just below the lower end of the AM radio broadcasting band (640 kHz). Laboratory tests with the dynamic motion simulator should be performed to confirm that this frequency is higher than that of the mechanical noise. Second, a rubber tread should be added to the magnet support wheels and to the test carriage wheels to eliminate the metal-to-metal contact at those points. Third, the EMAT holder design can be optimized to reduce the contact area and normal force against the top of the rail. Fourth, a nonmagnetic shield should be formed around the magnet pole pieces to prevent the accumulation of iron filings and other debris, and fifth, a wiper pad or brush could be added to remove grit from the rail surface ahead of the EMAT.

Mechanical Stability. A future prototype EMAT rail inspection vehicle will probably provide for inspection of both rails in a track simultane-

ously. This will present new problems in tracking the 0° ST ultrasonic beams over the rail webs that were not faced with the experimental test carriage, particularly in curves where there may be considerable wear on the gauge side of the rails. Other factors affecting mechanical stability were experienced with the present device and these should be considered in future designs.

Larger wheels should be provided on the prototype vehicle. The 5 in. diameter wheels on the experimental test carriage tended to ride up onto the rails at higher travel speeds affecting both stability and safety. Larger wheels will also naturally contribute to the clearance required for traversing grade crossings where the pavement may be several inches higher than the rail surface. This added clearance will also be required for traversing guarded frogs which are sometimes placed where tracks cross and have raised flanges inside the gauge side of the rails to provide additional guidance for train wheels.

The components of the prototype EMAT system can be made much lighter, perhaps by as much as a factor of 10, and much more compact than the experimental system which will lower the center of gravity of the test vehicle and add to its stability as well.

#### 6.4.2 False Indication of Defects

It is important for maintaining speed and efficiency in rail inspection that the rate of false indications of defects be kept as low as possible. The potential advantages of using the new types of ultrasonic wave modes provided by EMATs for looking around certain harmless rail conditions was recognized at the start of this development program. This aspect of the EMAT's performance in the rail testing will now be discussed.

Local Variations in Electromagnetic Coupling. This rail "condition" is unique to the EMAT inspection method and is somewhat analogous in its effect on false indications to the loss of acoustic coupling by the presently used ultrasonic wheels or skids, although the cause is different. As was shown in Fig. 6-16, the maximum local variations observed at the Santa Fe Test Track were 7 dB or about a factor of 2 in signal amplitude. The attenuation of the SH direct transmit signal and the ST base echo signal at defects was more in the range of 12 to 20 dB so the local variations in signal strength due to electromagnetic coupling, while reducing the dynamic range for defect

detection, should not contribute seriously to the number of false indications.

Shelling. Several examples of severe shelling were available for testing both in the laboratory and in the field. The amplitude of the SH wave signals reflected from this type of surface condition was less than that from a 3% TD. At some of the larger shells there was a loss of base echo with the ST wave as would be expected.

## 7.0 REFERENCES

1. George A. Alers, et al, "Development of a Prototype EMAT System for Inspection of Rails," U.S. Dept. of Transportation, Report No. DOT-FR-9143, March 1980.
2. Oscar Orringer, "Detail Fracture Growth in Rails: Part 1, Test Results," to appear in J. Theor. and Appl. Fract. Mech., early 1986.

## APPENDIX A - HARDWARE DESCRIPTION

Where possible, commercially available components were used to assemble the EMAT systems developed for this program. Where this was not possible, special-purpose units were designed and fabricated. Each of these items is indicated in the block diagram of Fig. A-1, along with identifying numbers keyed to their descriptions in Table A-1 and their photographs, circuit diagrams, chassis layout, etc. in the figures following.

A description of the EMAT construction is coded into the identification numbers as follows:

Wave type	Dimension (mm)	Periods	Turns	ID Number		RCVR, xx = even XMTR, xx = odd T/R, 7x (odd,even)
				No. of Magnets = m;		
SH	Period	N	n	H	m xx	
SV	Period	N	n	V	1 xx	
SR	Diameter	1	n	R	1 xx	
ST	Diameter	1	n	T	1 xx	

Example: SH - 13 - 4 - 20 - H1603

This describes a PPM SH EMAT having 16 permanent magnets with four periods of 13 mm each (250 kHz) and a wire coil winding with 20 turns. It is designed and impedance-matched to be used as a transmitter (03 in ID number).

Some of these EMAT transducer designs are protected by Rockwell patents 4,127,035 and 3,850,028.

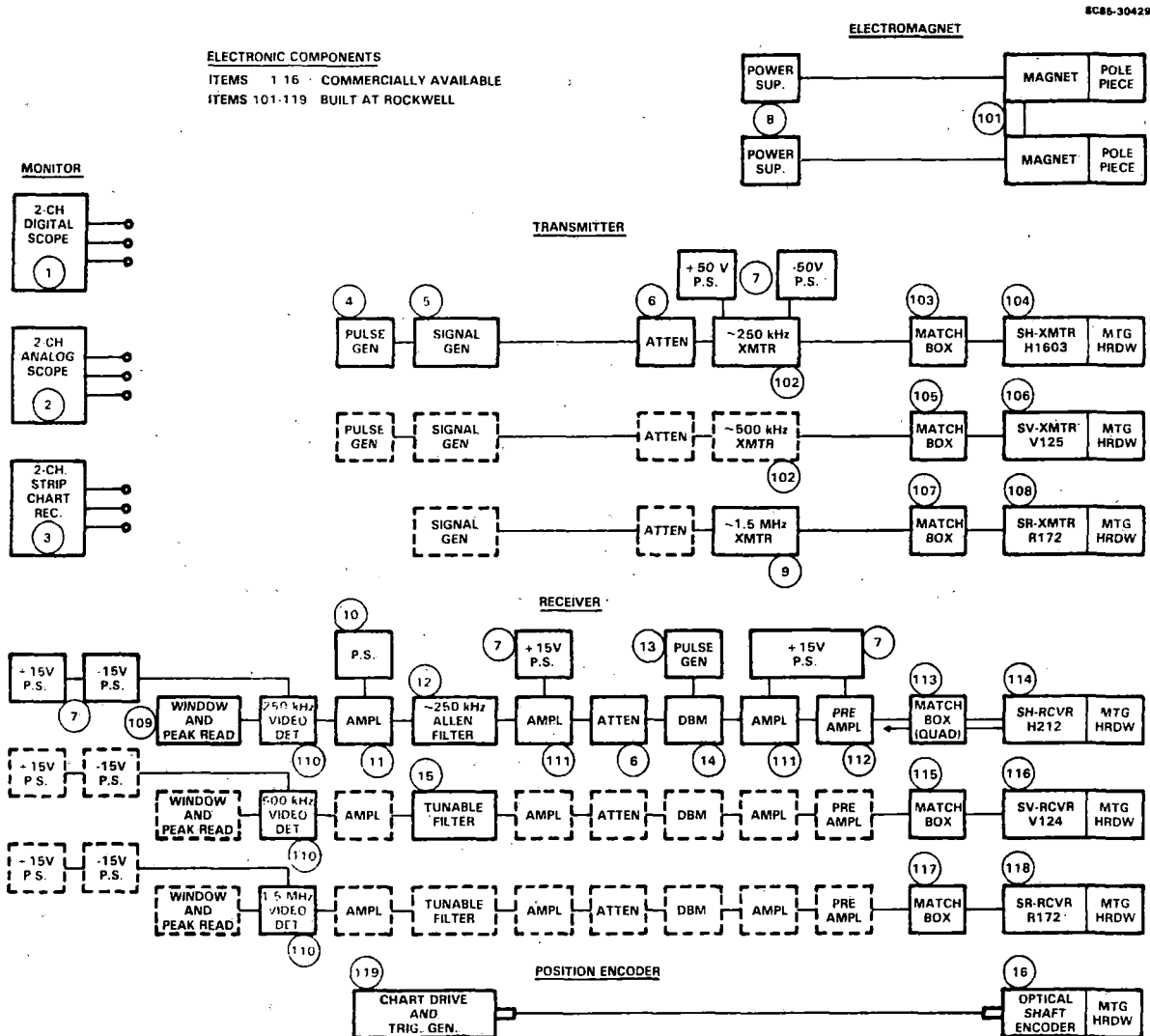


Figure A-1. Components of rail inspection system.

TABLE A-1. DESCRIPTION OF SYSTEM COMPONENTS

Item No.	Description	Make	Model No(s).
<u>COMMERCIALLY AVAILABLE EQUIPMENT</u>			
1	Digital Storage Oscilloscope	Tektronix	468
2	Analog Oscilloscope	Tektronix	2215A
3	Strip Chart Recorder	Gould	2200S
4	Pulse Generator	Tektronix	PG501
5	Signal Generator	Tektronix	FG502
6	Attenuator	Hewlett-Packard	355C, 355D
7	Power Supply	Hewlett-Packard	6212A, 6216A
8	DC Power Supply	Hewlett-Packard	6439B
9	Gating Modulator & RF Gated Amplifier	Matec	5100, 515
10	Power Supply	Keithley	1081
11	Amplifier	Keithley	109
12	Bandpass Filter	Allen Avionics	F2463
13	Pulse Generator	Hewlett-Packard	8012B
14	Double Balanced Mixer	Hewlett-Packard	10534A
15	Filter	Krohnkite	3202
16	Optical Encoder	BEI Electronics	H25E-F3-SB- 2048-P4ZC- 8830-SM18
<u>MANUAL DEFECT CHARACTERIZATION EQUIPMENT</u>			
A	UT Transmitter/Receiver Branson	Krautkramer- 303B	Sonoray
B	Shear Wave Transducer	Automation Ind.	LTZ 70
C	Longitudinal Wave Transducer	Automation Ind.	LTZ 45



TABLE A-1. DESCRIPTION OF SYSTEM COMPONENTS (Cont'd)

Item No.	Description
<u>SCIENCE CENTER DESIGNED AND BUILT COMPONENTS</u>	
101	Electromagnet and Pole Pieces
102	Transmitter Power Amplifier
103	SH Transmitter Impedance Matching Network
104	SH PPM Transmitter EMAT
105	SV Transmitter Impedance Matching Network
106	SV Transmitter EMAT
107	SR Transmitter Impedance Matching Network
108	SR Transmitter EMAT
109	Peak Detector and Window
110	Video Detector
111	Receiver Amplifier
112	Low Noise Preamplifier
113	SH Receiver Impedance Matching Network and Quadrature Detector
114	SH Unidirectional Receiver EMAT
115	SV Receiver Impedance Matching Network
116	SV Receiver EMAT
117	SR Receiver Impedance Matching Network
118	SR Receiver EMAT
119	Optical Shaft Encoder I/O - Trigger Generator/Chart Drive

## FIGURE CAPTIONS

- Item 101 Electromagnet photo.
- Item 101 Pole pieces for SV and SR EMATs.
- Item 101 Electromagnet dimensions.
- Item 101 Pole piece dimensions for SV and SR EMATs (two required).
- Item 101 Pole piece dimensions for SH EMATs (two required).
- Item 102 Transmitter power amplifier, back panel.
- Item 102 Transmitter power amplifier, component layout.
- Item 102 Transmitter power amplifier, schematic.
- Item 102 Transmitter power amplifier, transformer details.
- Item 103 SH transmitter impedance matching network, component layout and schematic.
- Item 104 SH transmitter PPM EMAT.
- Item 105 SV transmitter impedance matching network, component layout and schematic.
- Item 106 SV transmitter EMAT
- Items 107, 108, 117 & 118. Combined SR transmitter/receiver impedance matching networks and EMATs.
- Item 117 SR receiver impedance matching network, component layout and schematic.
- Item 109 Peak detector and window, front panel.
- Item 109 Peak detector and window, back panel.
- Item 109 Peak detector and window, component layout.
- Item 109 Peak detector and window, schematic.
- Item 110 Video detectors, front panel.

Item 110 Video detectors, back panel.

Item 110 Video detectors, component layout for 250 kHz unit.

Item 110 Video detectors, component layout for 500 kHz unit.

Item 110 Video detectors, component layout for 2 MHz unit.

Item 110 Video detectors, schematics.

Item 111 Receiver amplifier, front panel.

Item 111 & Receiver amplifier and preamplifier, back panel.  
112

Item 111 Receiver amplifier, component layout.

Item 111 Receiver amplifier, schematic.

Item 112 Low noise preamplifier, component layout.

Item 112 Low noise preamplifier, schematic.

Item 113 SH receiver impedance matching network (schematic) and quadrature detector.

Item 113 SH receiver quadrature detector, schematic.

Item 114 SH receiver EMAT.

Item 114 SH receiver, PC board design.

Item 115 SV receiver impedance matching network, component layout and schematic.

Item 116 SV receiver EMAT.

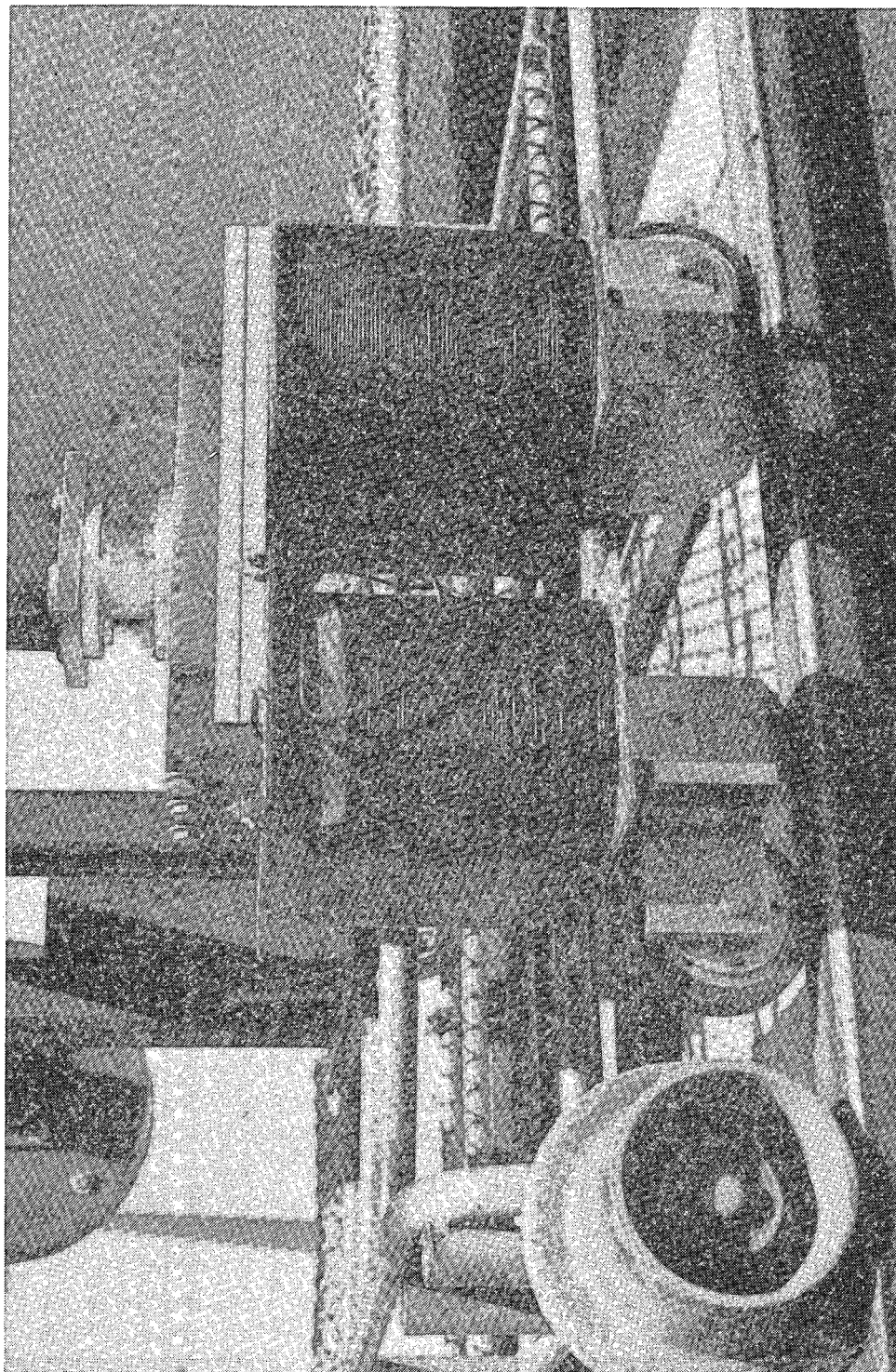
Item 119 Optical shaft encoder I/O, front panel.

Item 119 Optical shaft encoder I/O, back panel.

Item 119 Optical shaft encoder I/O, component layout.

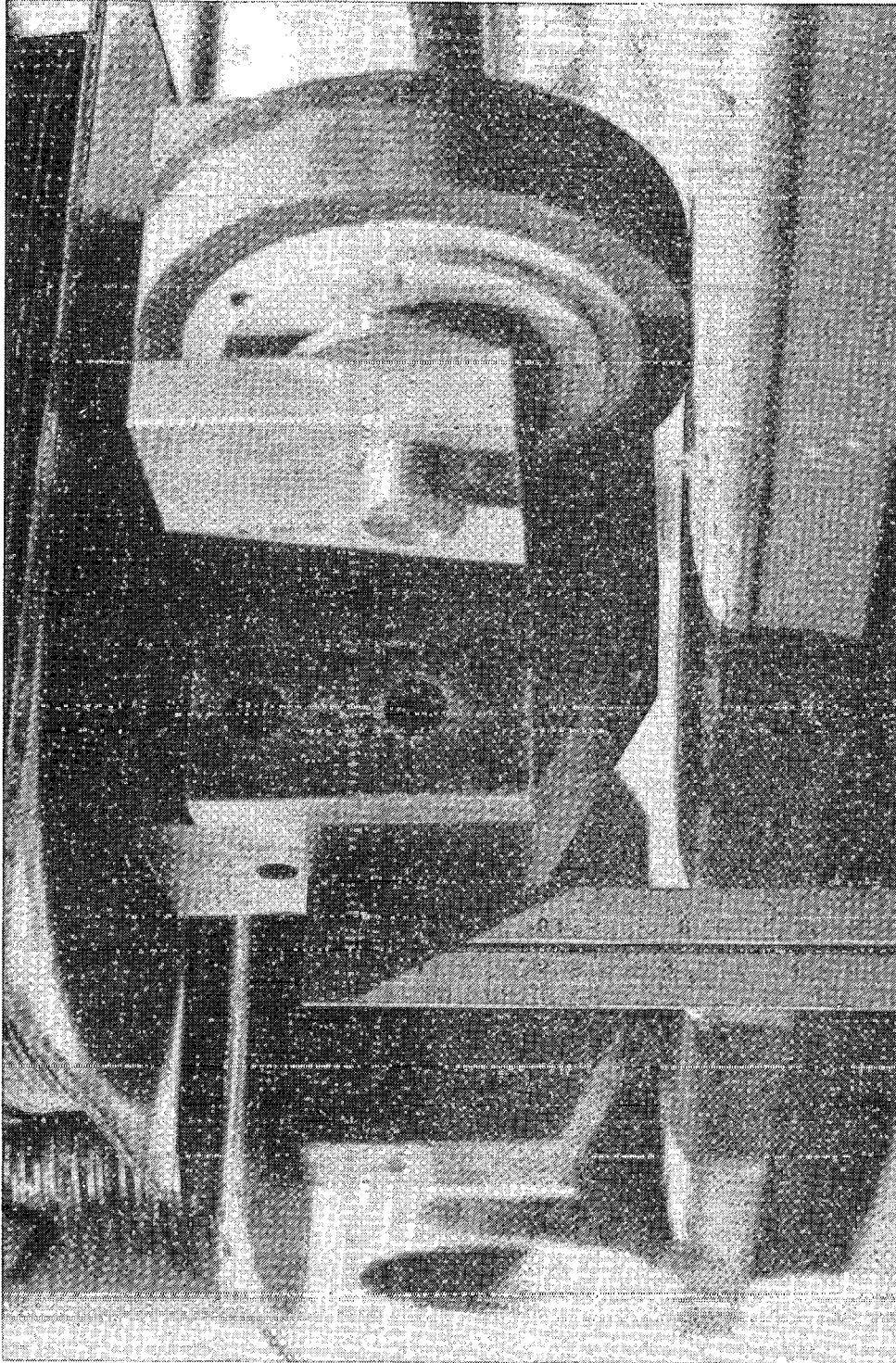
Item 119 Optical shaft encoder I/O, schematic.

SC36645

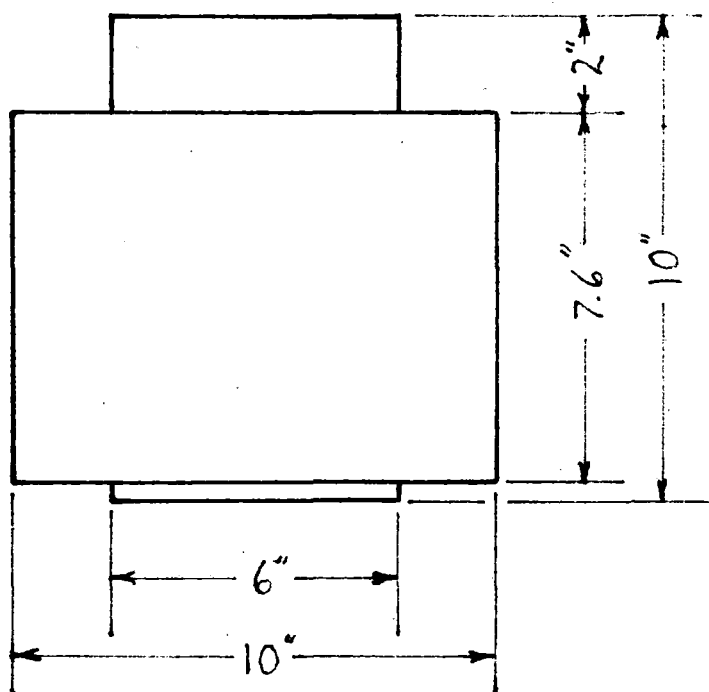
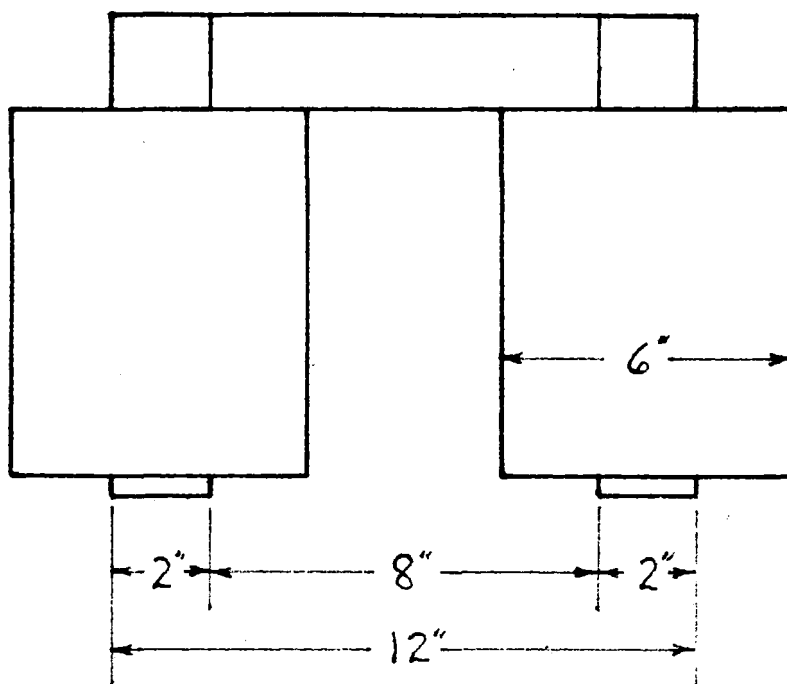


Item 101 Electromagnet photo.

SC36646

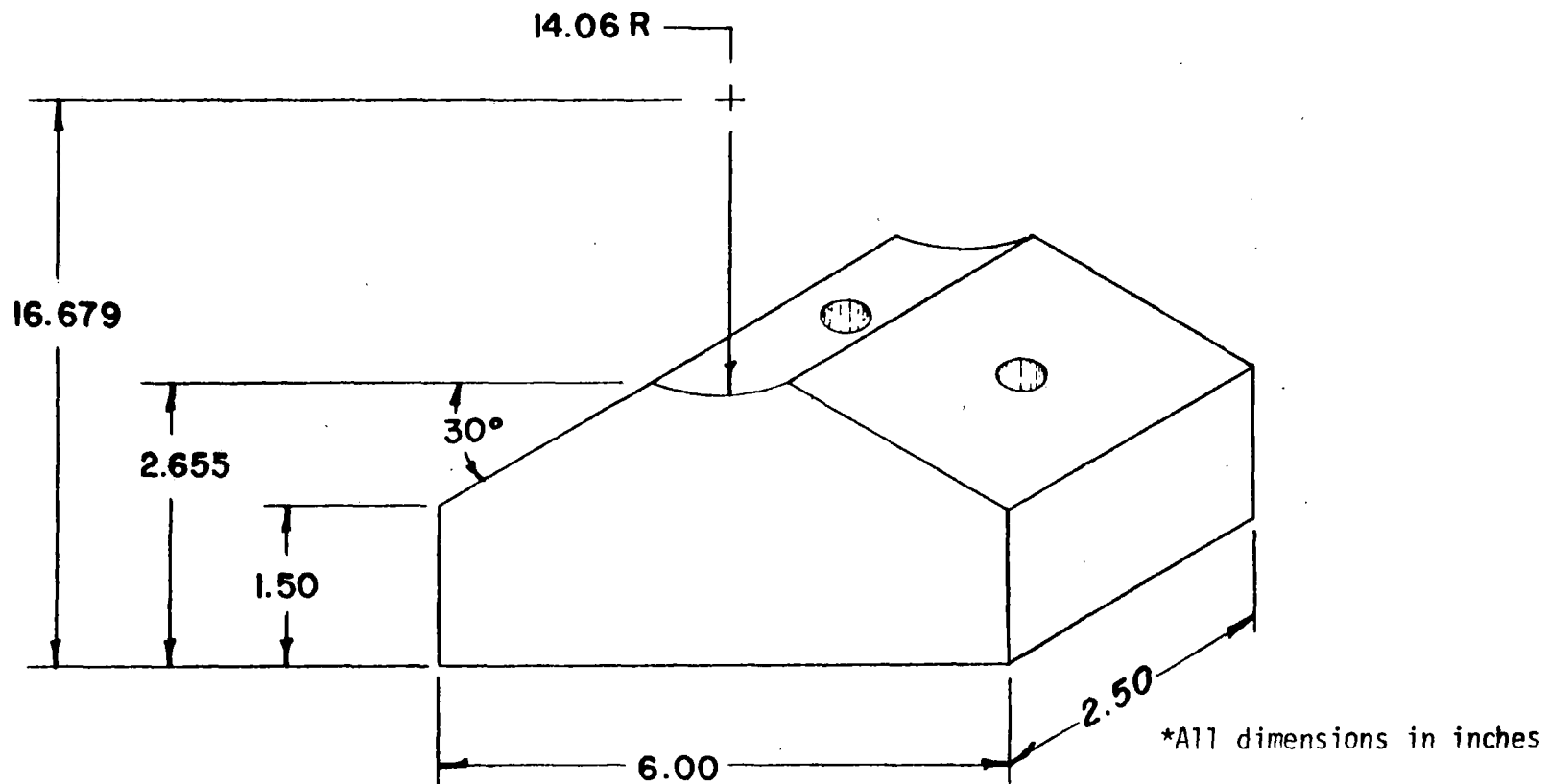


Item 101 Pole pieces for SV and SR EMATs.

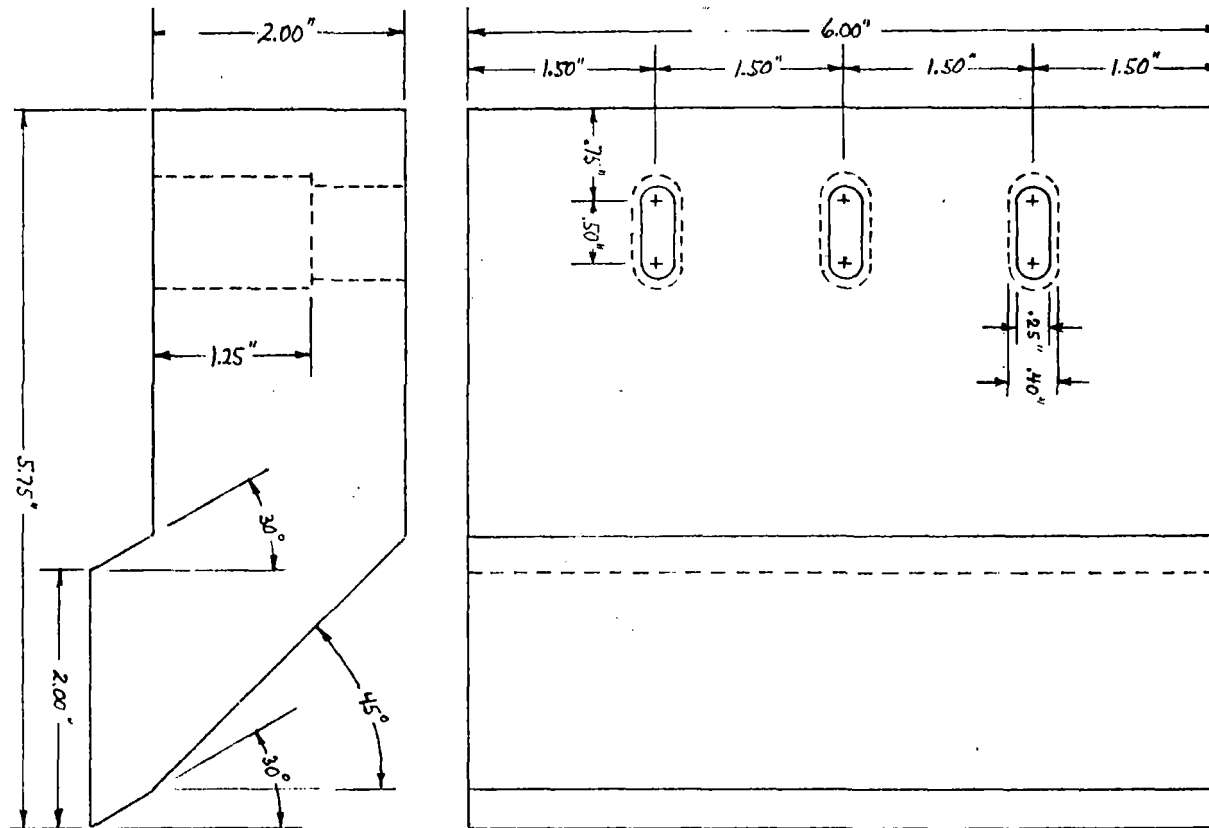


Item 101 Electromagnet dimensions.

A-10



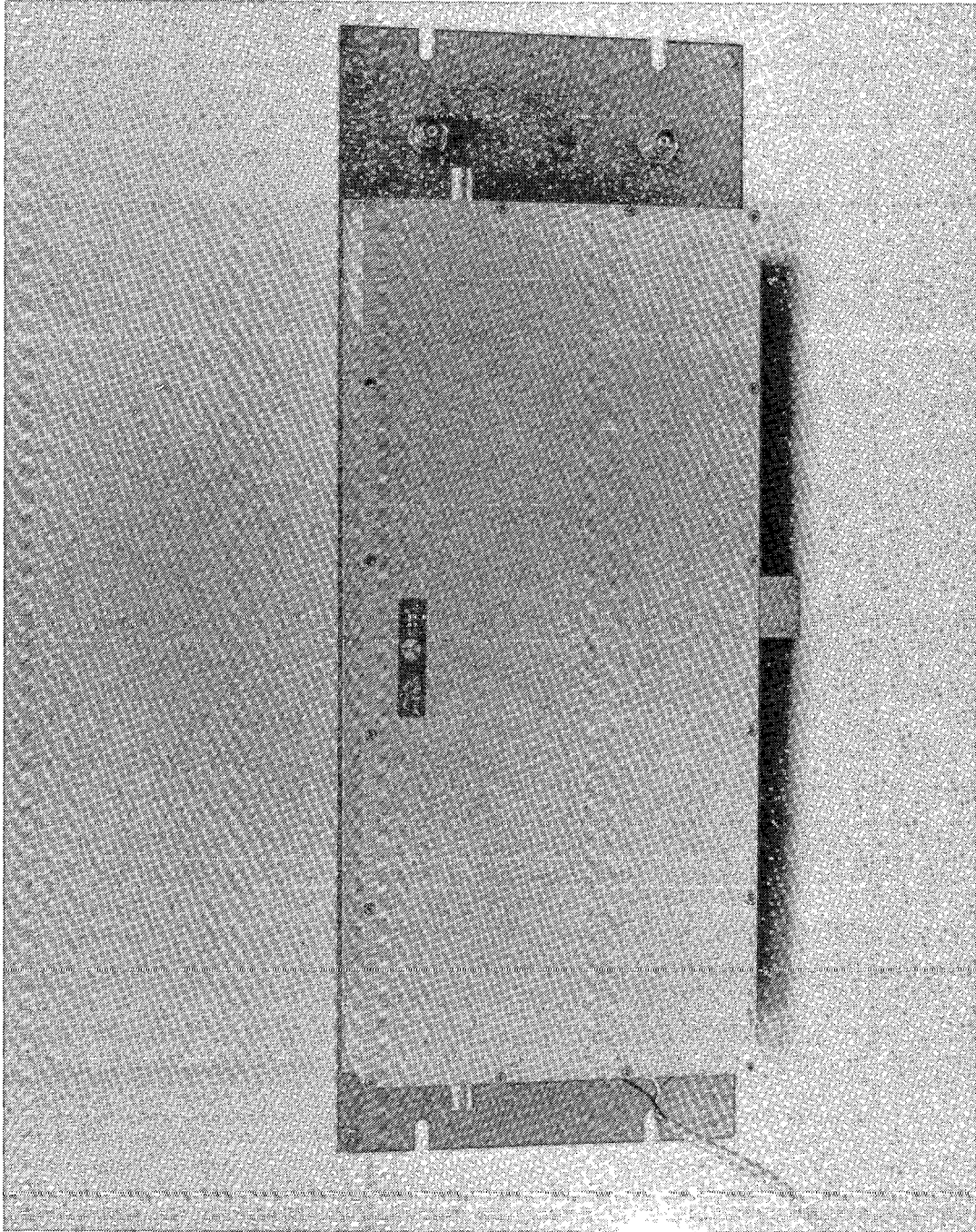
Item 101 Pole piece dimensions for SV and SR EMATs (two required).



Item 101 Pole piece dimensions for SH EMATs (two required).

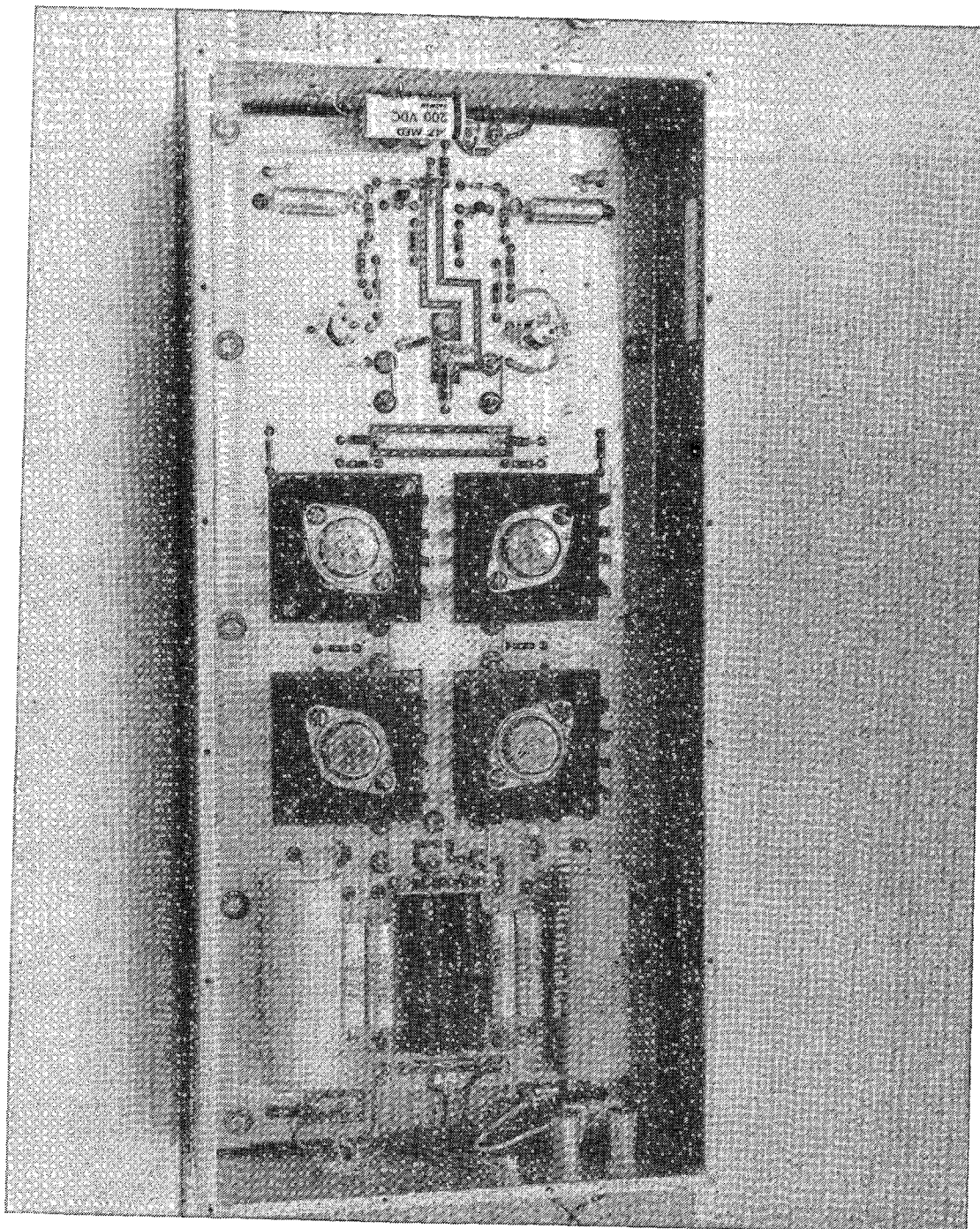


SC36644



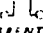
Item 102 Transmitter power amplifier, back panel.

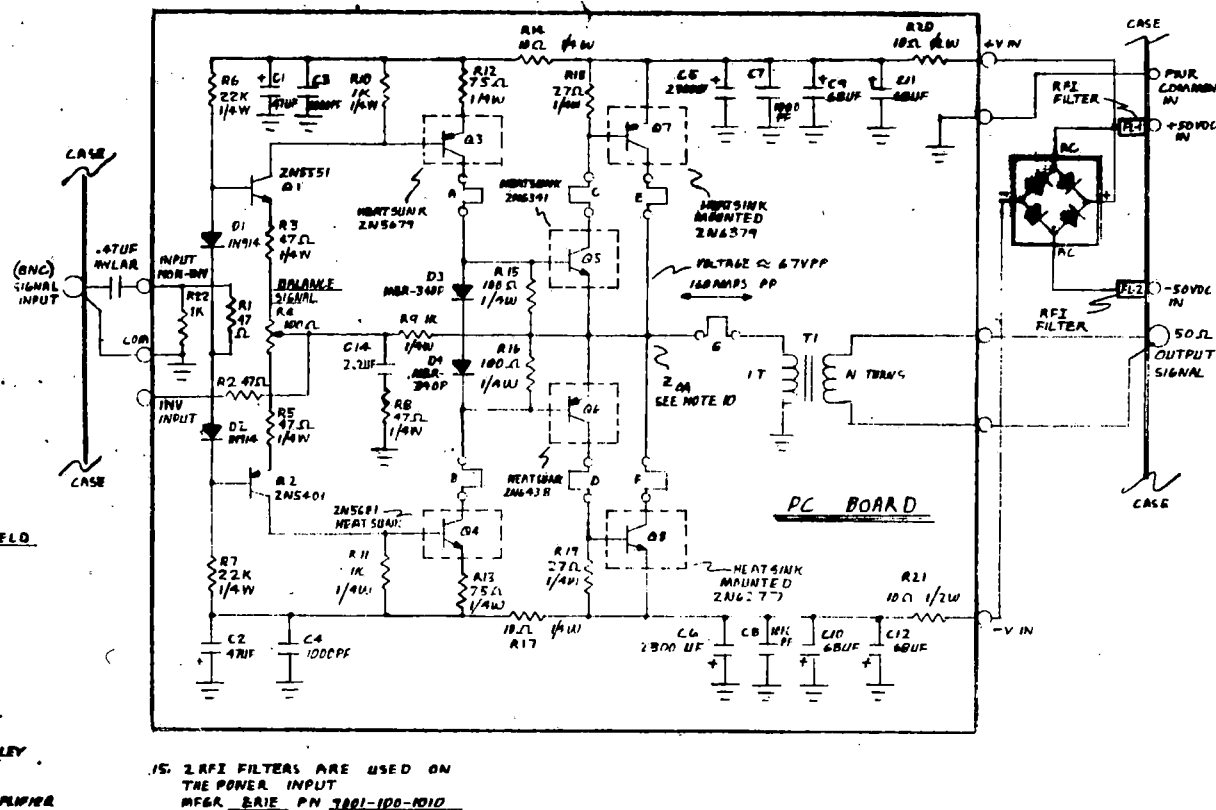
SC36643



Item 102 Transmitter power amplifier, component layout.

NOTES: UNLESS OTHERWISE SPECIFIED

1. ALL RESISTORS ARE CARBON COMP 50% TOLERANCE UNLESS OTHERWISE SPECIFIED
2. C1 & C2 47 UF 75VDC  
MFG: SPARGUE  
PN 4000476F015048
3. C9, C10, C11, C12 ARE 68 UF 75VDC  
MFG: SPARGUE  
PN 400068G F0750074
4. C5, C6 ARE 2200 UF 50VDC  
MFG: MALLORY  
PN 166222UD CON3L
5. D1 & D4 ARE SIGNALING DIODES
6. SYMBOL  DENOTES CURRENT OF CURRENT FLOW  
7. PWD (A, B, C, D, E, F, G)
7. D3 & D4 MOUNTED IN HEATSINK FOR HEATSINK HOLDER IN CASE
8. R5, R6, R7, R8 ARE 10K RESISTORS  
MOUNTED ON HEATSINK MFG: MALLORY  
PN 400010K-A
9. TRANSFORMER T1 CUSTOM WOUND -  
SEE DRAWING: IMPEDANCE XFORMER  
FOR DETAILED CONSTRUCTION
10. CIRCUIT IMPEDANCE OF AMPLIFIER  
(INTO T1) AT 20A IS  $\approx 34 \Omega$
11. PC BOARD REF DRAWING: XMTA BOARD  
FOR DETAILS
12. RA IS 100  $\Omega$  1% MFG: ALLEN BRADLEY  
PN A2A101
13. TO USE CIRCUIT AS A INVERTING AMPLIFIER  
THE SIGNAL IS APPLIED TO THE INVERTING  
INPUT & INPUT COMMON  
THE NON-INVERTING INPUT MUST BE  
GROUNDED TO INPUT COMMON IN THIS  
MODE.
14. TO USE CIRCUIT AS NON-INVERTING AMPLIFIER  
SIGNAL IS APPLIED TO THE NON-INVERTING INPUT  
& INPUT COMMON  
THE INVERTING INPUT IS LEFT OPEN

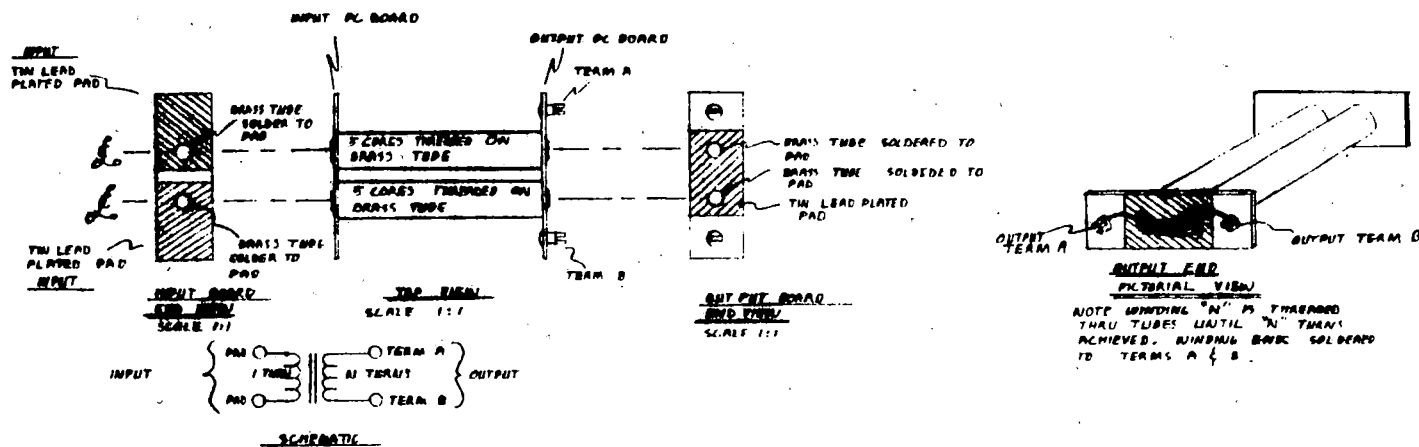


TITLE: SCHEMATIC EMPT XMTA

DEWN WLF 12-14-81

101 101

Item 102 Transmitter power amplifier, schematic.



### NOTES:

1. TRANSFORMER USES 10 LBS TOTAL IN 2 SETS OF 5 LBS. THRU 5 CORES ON EACH OF 2 BRASS TUBES AS SHOWN IN TOP VIEW. (SEE DRAWING)
2. BRASS TUBES & SHRINK TUBE TO BE USED SHALL BE AS SHOWN IN TOP VIEW.
3. CUT TUBES TO LENGTH AS REQ'D
4. CAREFULLY GRAB ON TUBES WITH SHRINK SLEEVE & SOLDER TO END
5. ASSEMBLE TUBING & CORES ON PC BOARD AND PLOTS
6. TIN LEAD SOLDER TUBES TO INPUT AND BOARD, ONLY.
7. INITIAL TEAM A & TEAM B ON OUTPUT SIDE. SOLDER IN PLACE & SOLDER TO TERMINAL BRASS PROVIDED

8. SOLDER BRASS TUBING TO OUTPUT BOARD PAD
9. SCRAPE & REMOVE SOLDER FROM INSIDE OF BRASS TUBING AT ALL 4 EXPOSED ENDS
10. SHARPLY CHAMFER 2 PICES OF CHAMFER SLEEVE UNTIL THEY FIT TIGHT INSIDE BRASS TUBES.
11. SLIP SHRINK SLEEVE ENTIRELY THROUGH BRASS TUBES, LEAVING INSIDE SURFACE
12. CUT SHRINK SLEEVE EXCEEDS OFF 10 IN BEYOND TUBE ENDS. THIS PROTECTS OUTPUT WINDING INSULATION FROM DAMAGE WHEN CROSSLING CHAMFER TUBE END EDGES

13. WIND SECONDARY FOR IMPEDANCE REQ'D THAN TUBES OUTPUT WINDING (N IN SCHEMATIC) TO MATCH
- (A) 34 OHMS TO 100 OHMS USE AWG NO. 24 HEAVY FORMVAR N=17 TURNS
- (B) 34 OHMS TO 50 OHMS USE AWG NO 24 HEAVY FORMVAR N=12 TURNS
14. COMPLETED TRANSFORMER AS SHOWN IN PICTORIAL

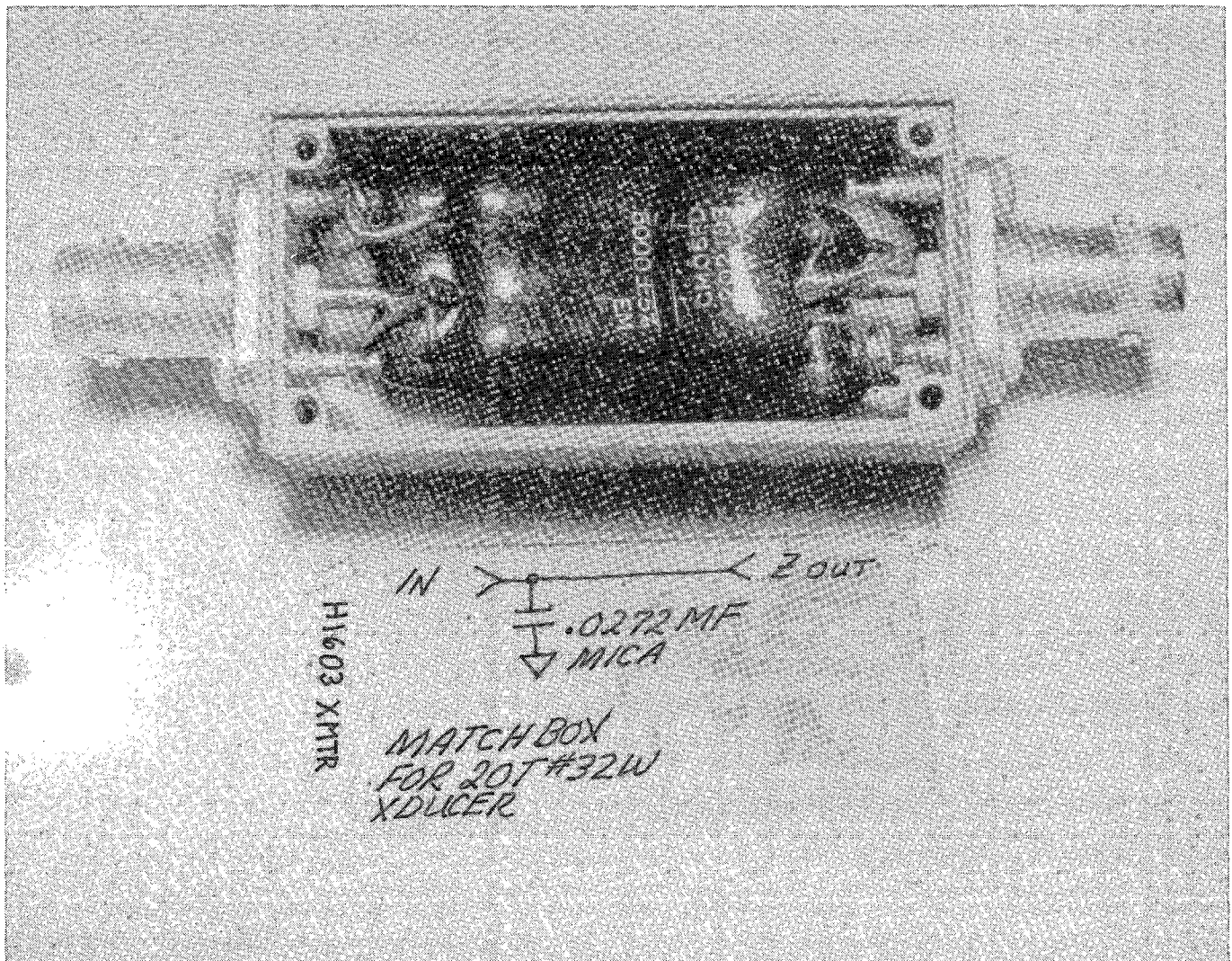
TITLE IMPEDANCE XFR.

DRAWN RFP DATE 2/15/79

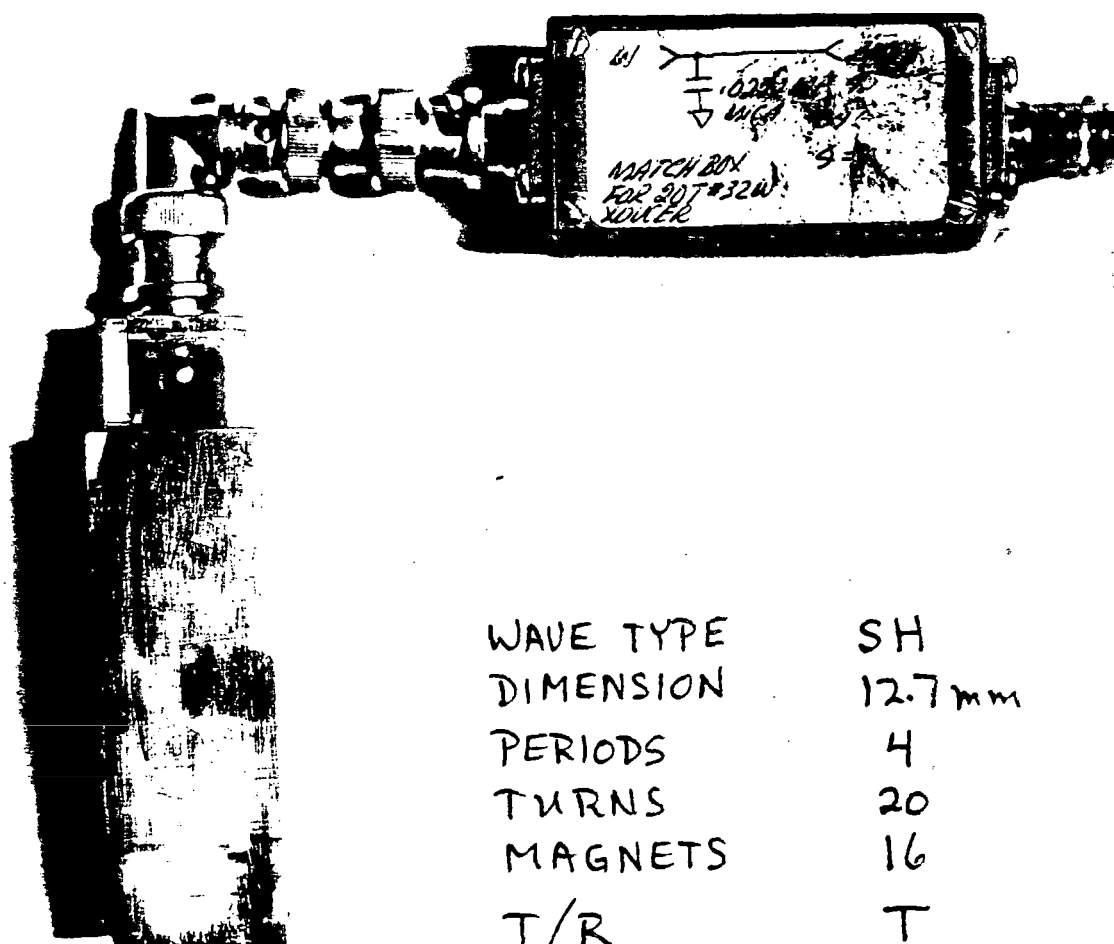
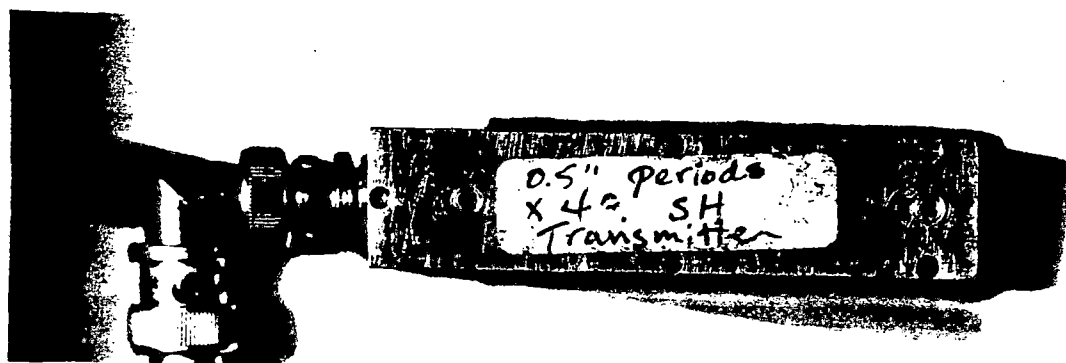
SHT 1 OF 1

Item 102 Transmitter power amplifier, transformer details.



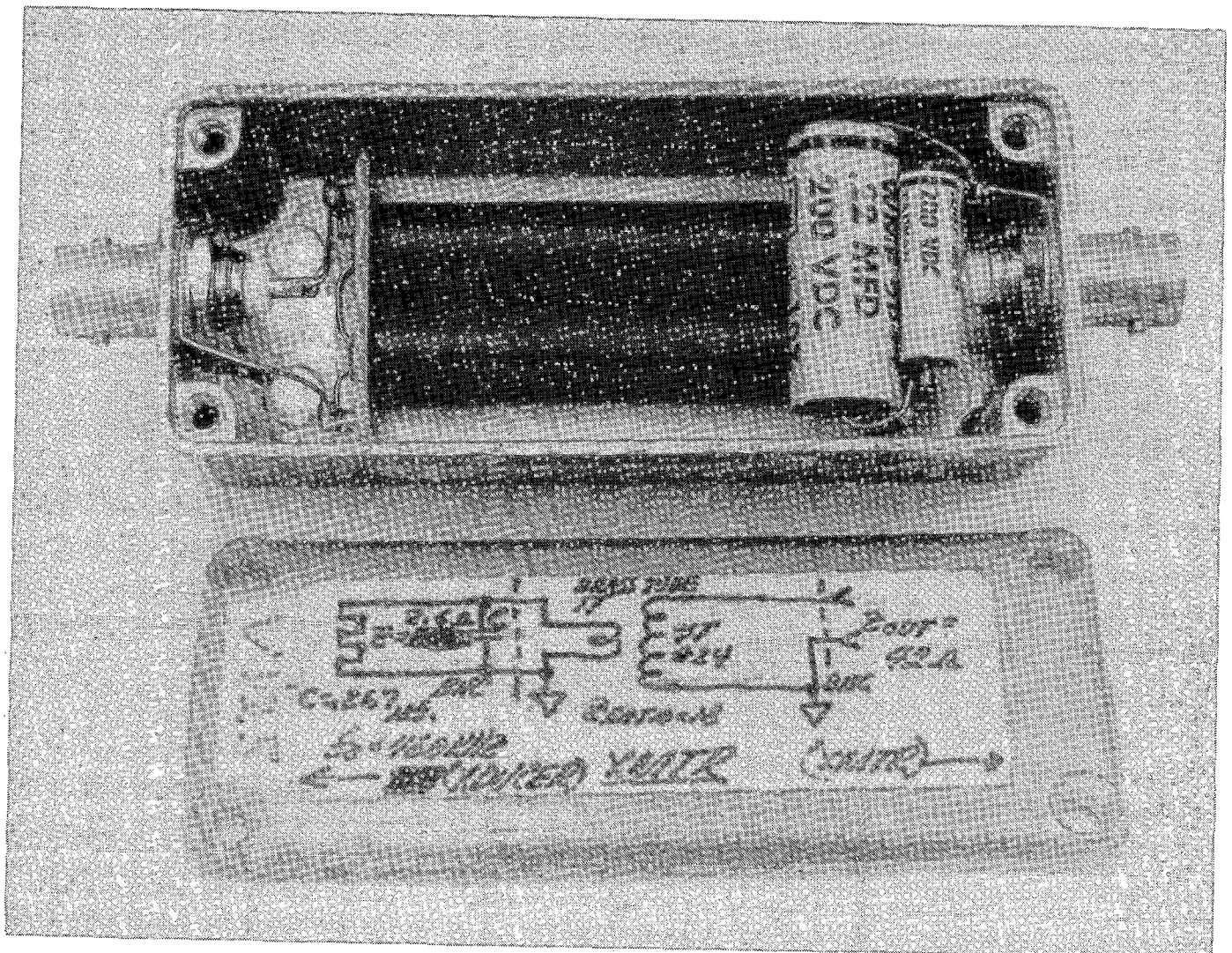


Item 103 SH transmitter impedance matching network,  
component layout and schematic.



WAVE TYPE	SH
DIMENSION	12.7 mm
PERIODS	4
TURNS	20
MAGNETS	16
T/R	T
SN	SH-13-4-20-H16 03

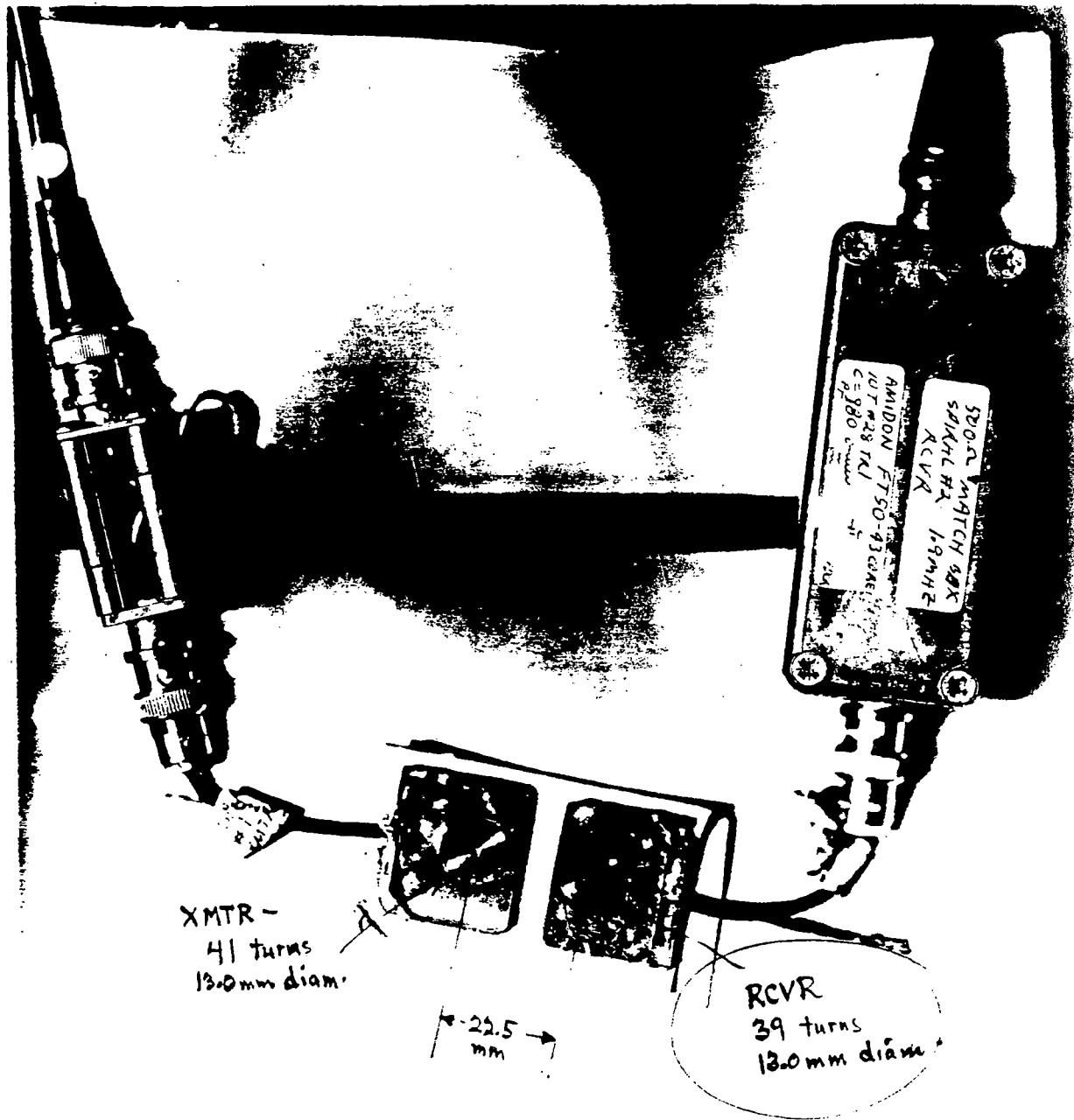
Item 104 SH transmitter PPM EMAT.



Item 105 SV transmitter impedance matching network, component layout and schematic.

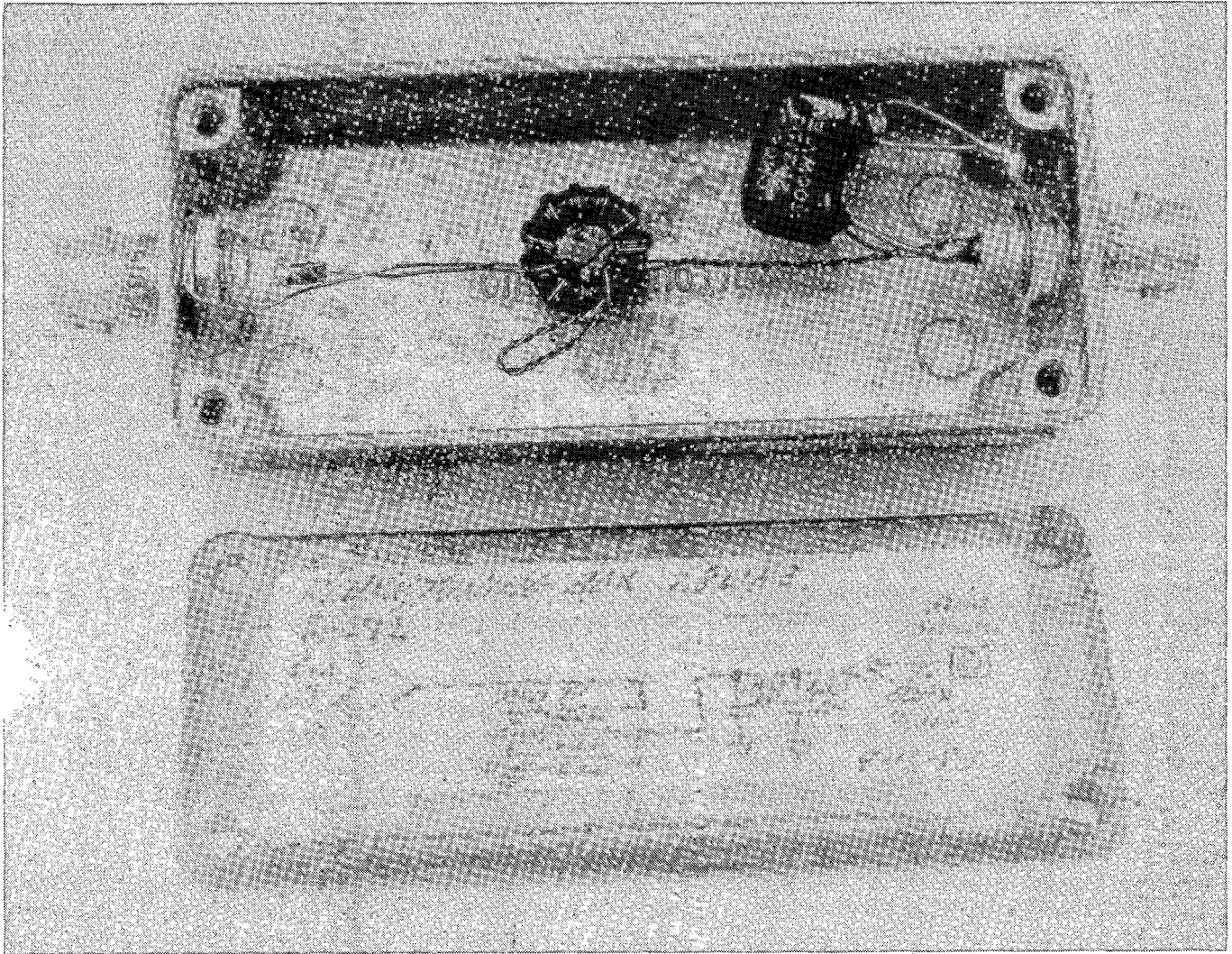






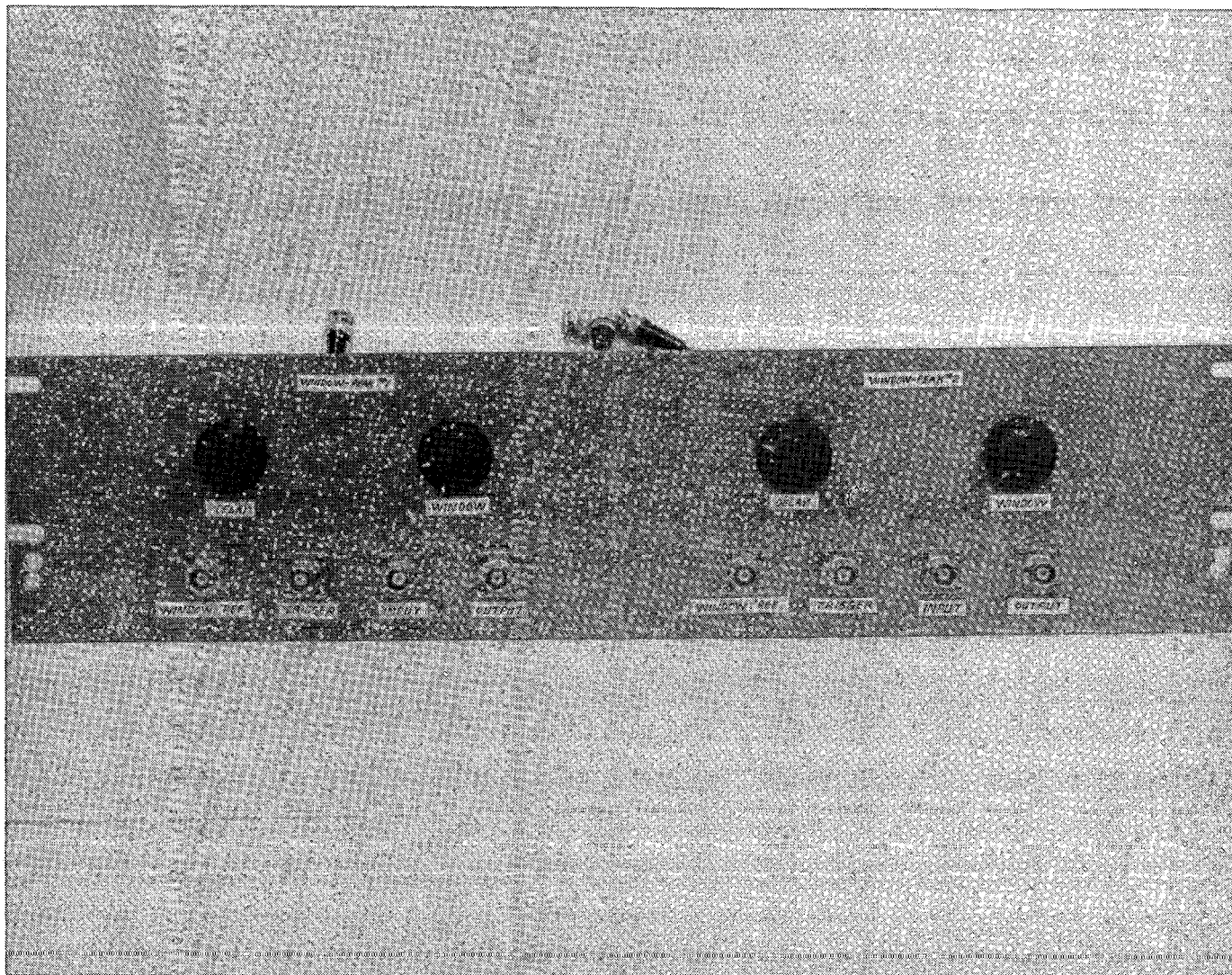
SR-13-1-40-R172

Items 107, Combined SR transmitter/receiver impedance matching networks 108, 117 & 118, and EMATs.



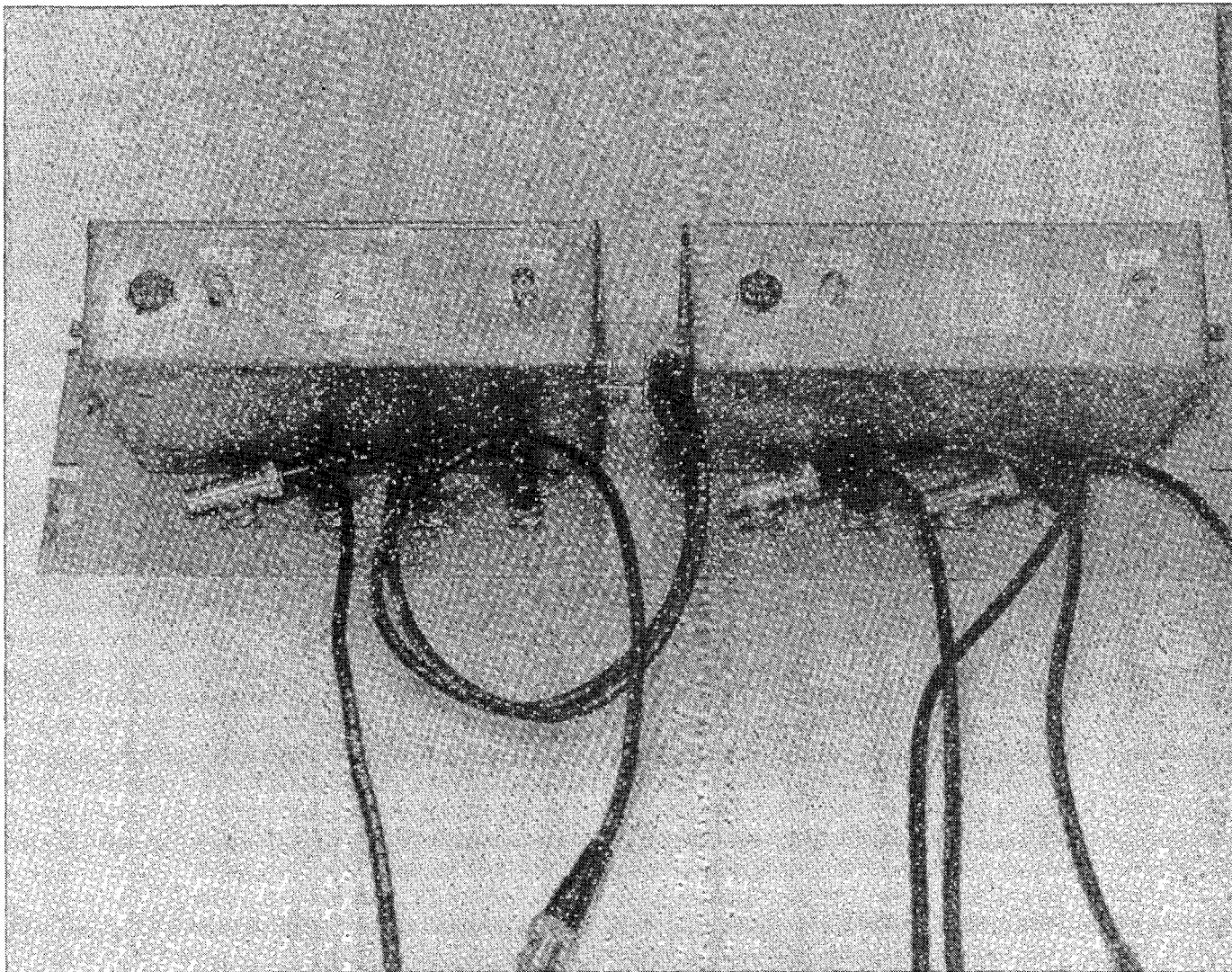
Item 117 SR receiver impedance matching network, component layout and schematic.

SC36639



Item 109 Peak detector and window, front panel.

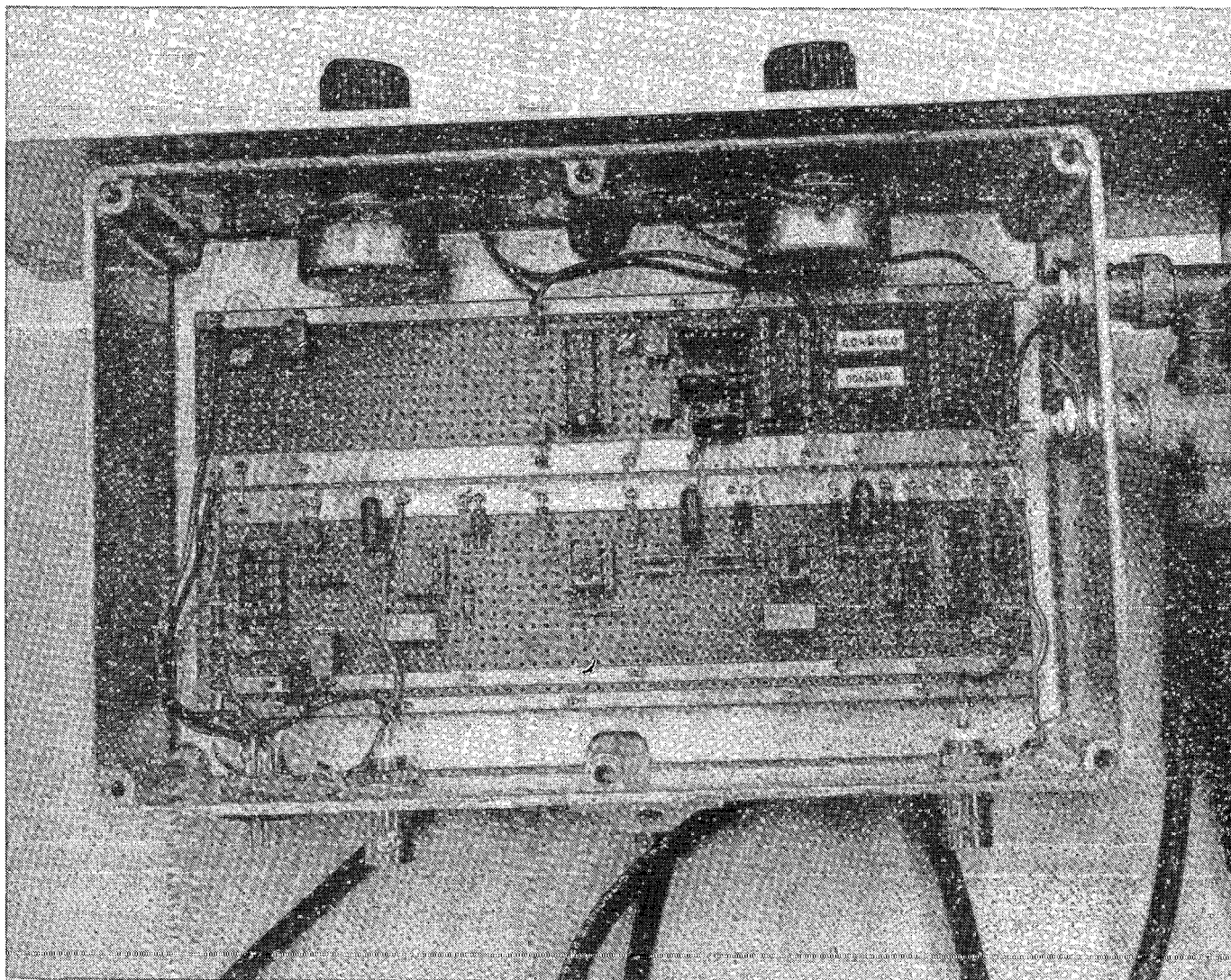
SC36638



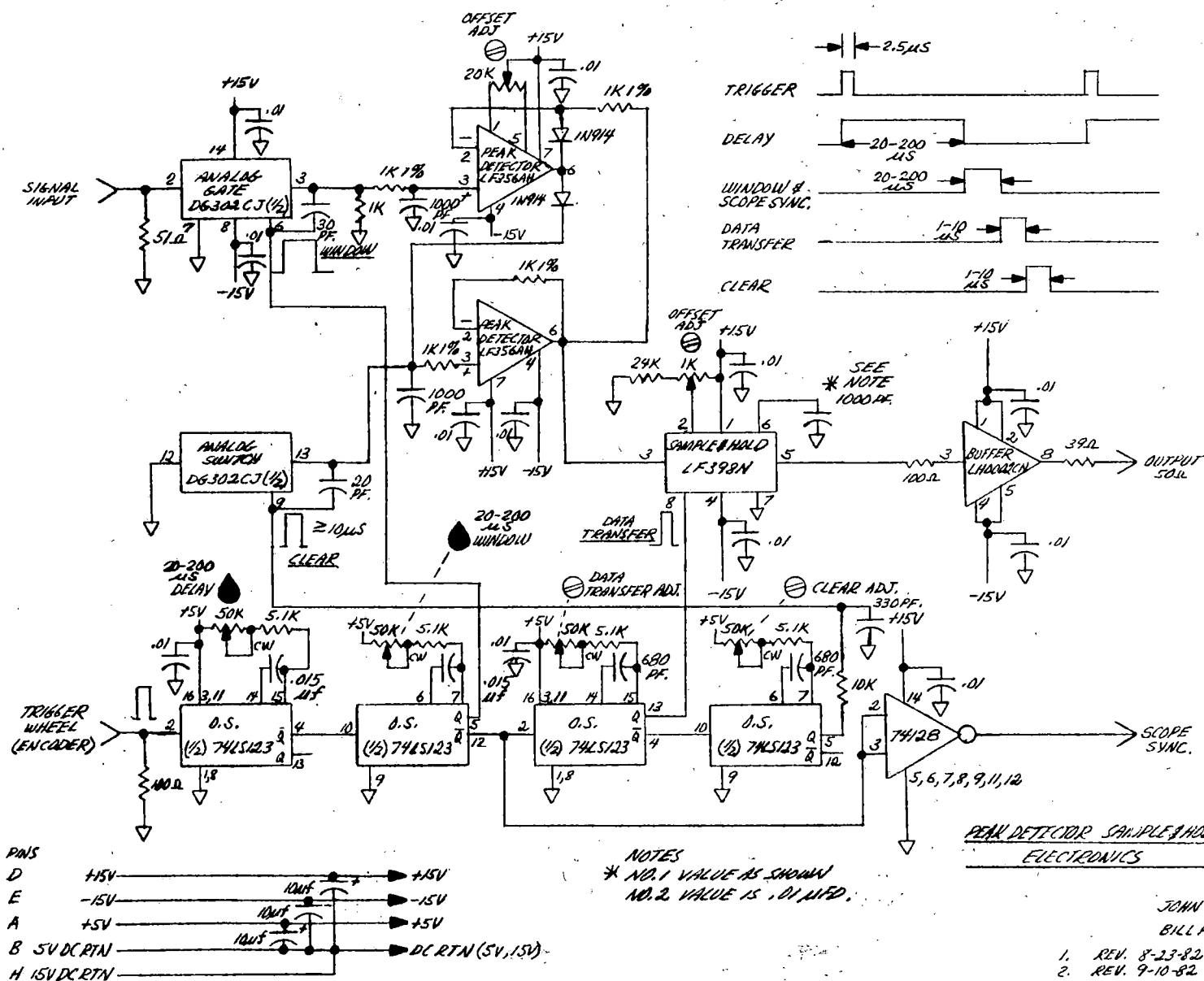
Item 109 Peak detector and window, back panel.



SC36637

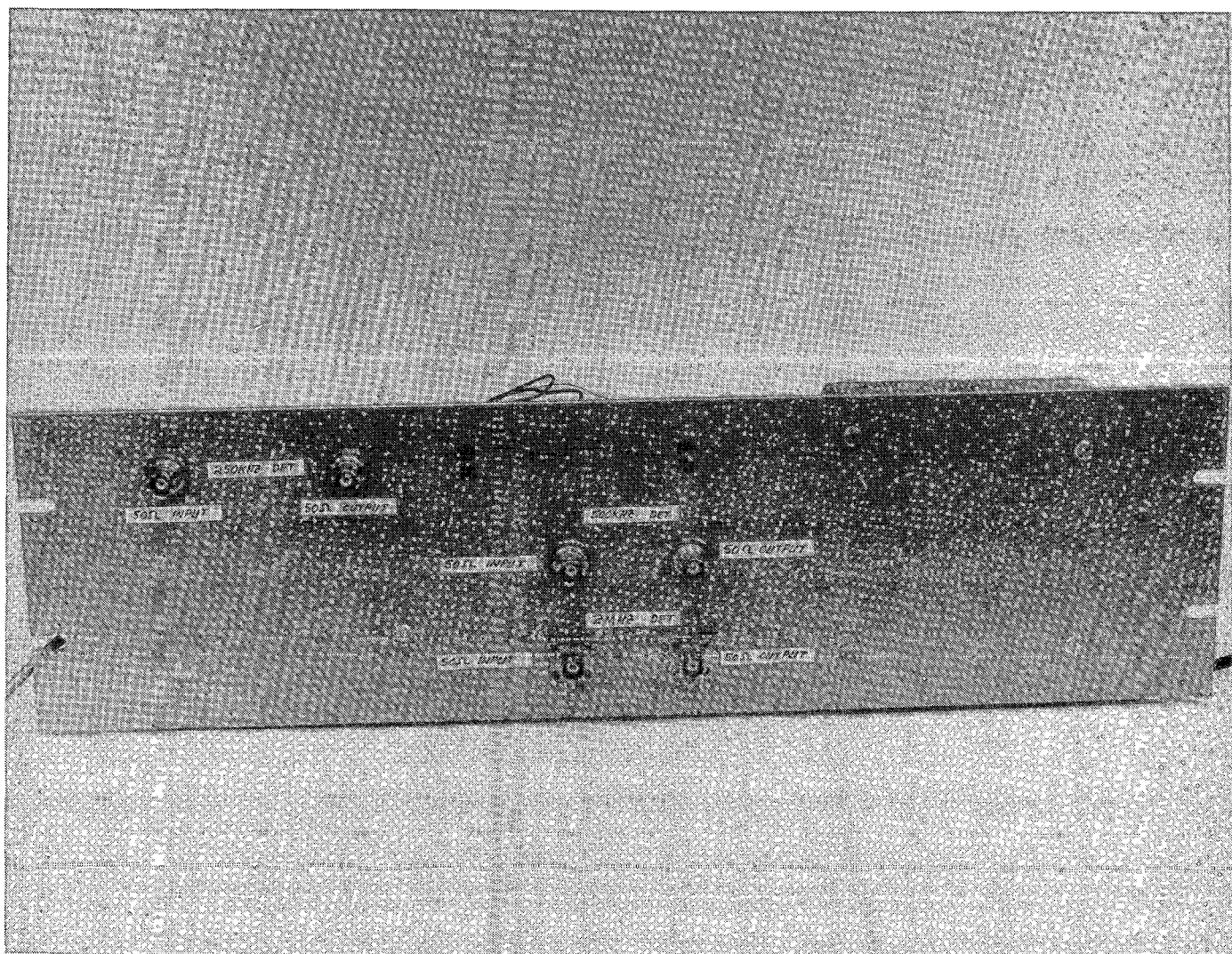


Item 109 Peak detector and window, component layout.



Item 109 Peak detector and window, schematic.

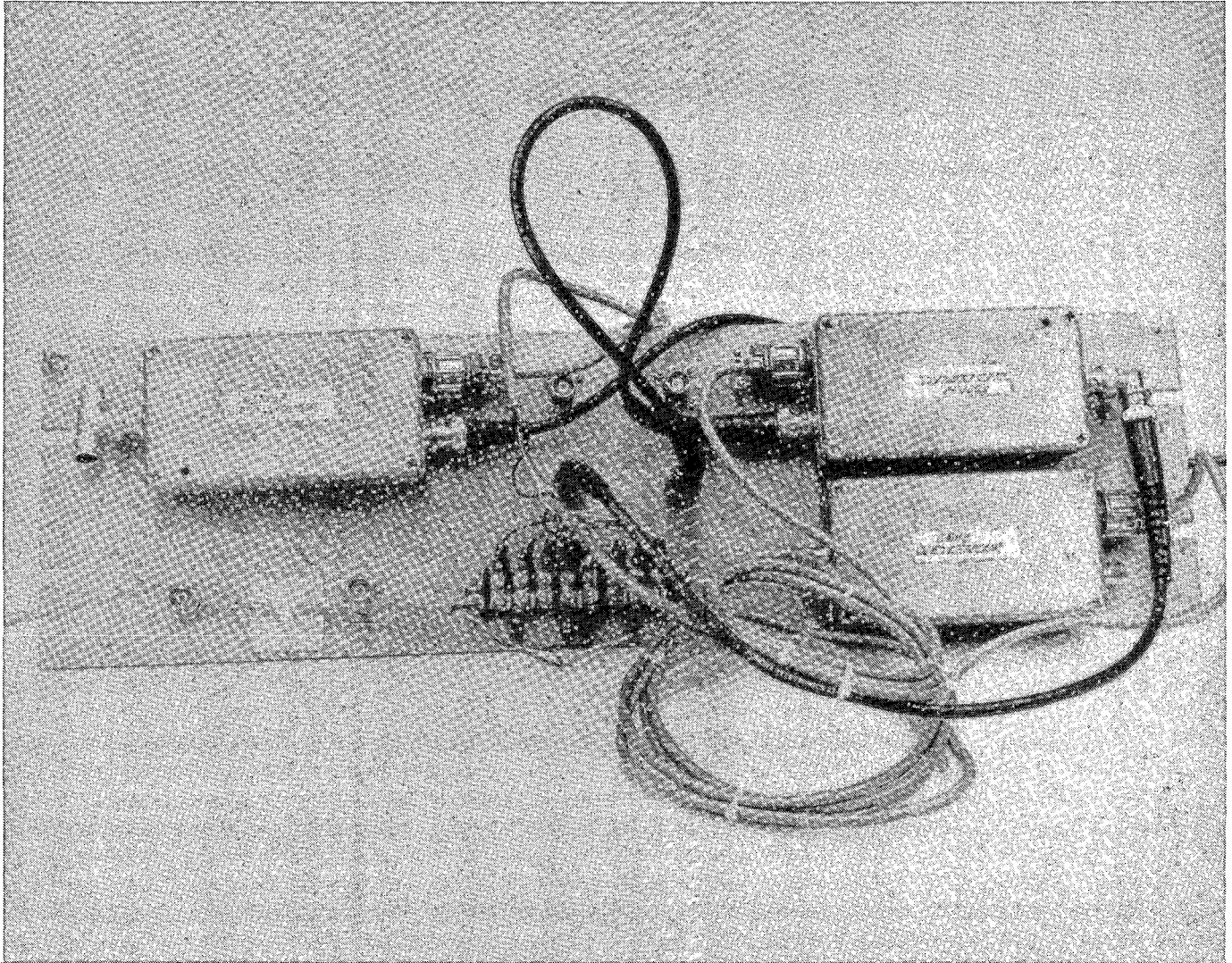
SC36636



Item 110 Video detectors, front panel.

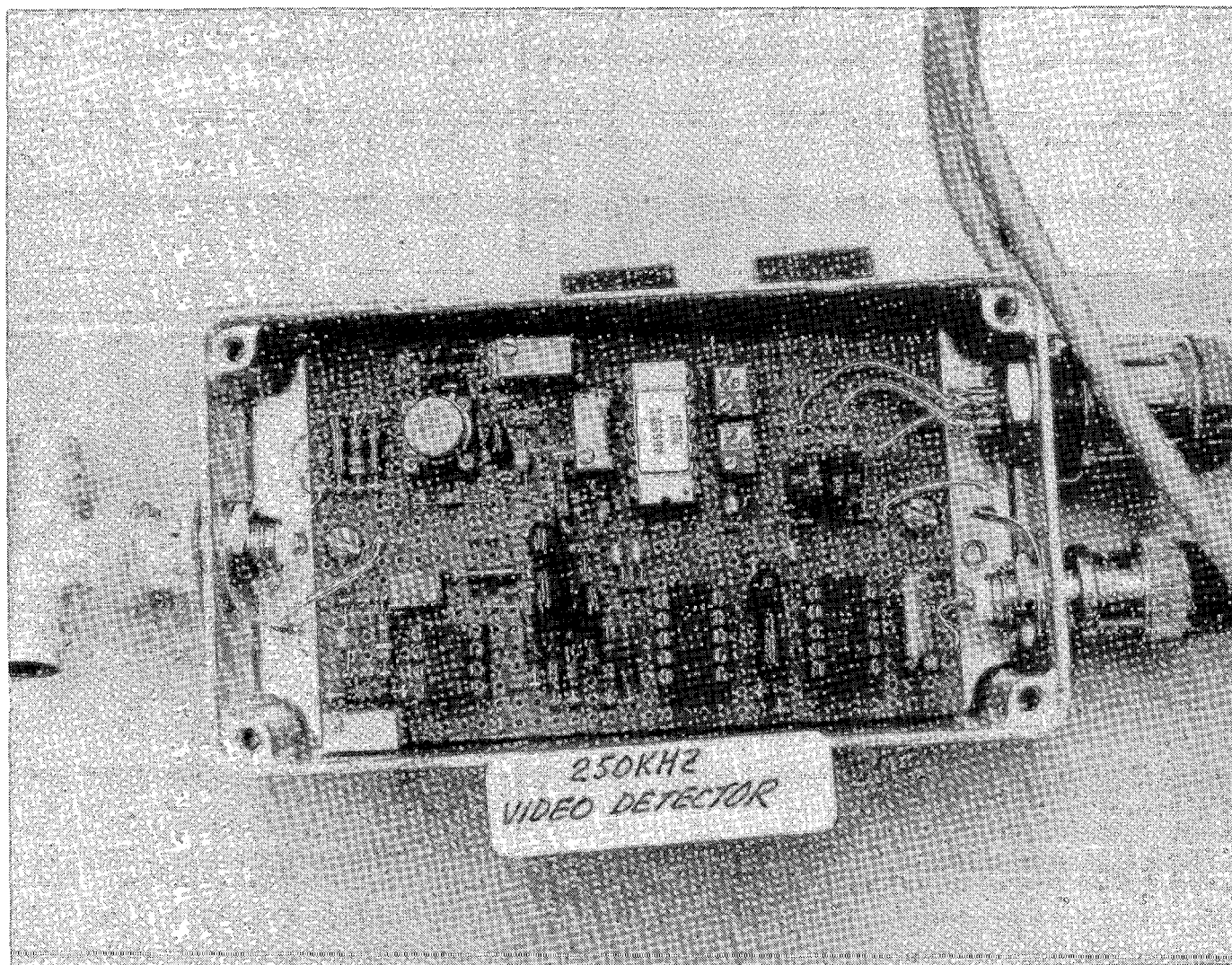


SC36635



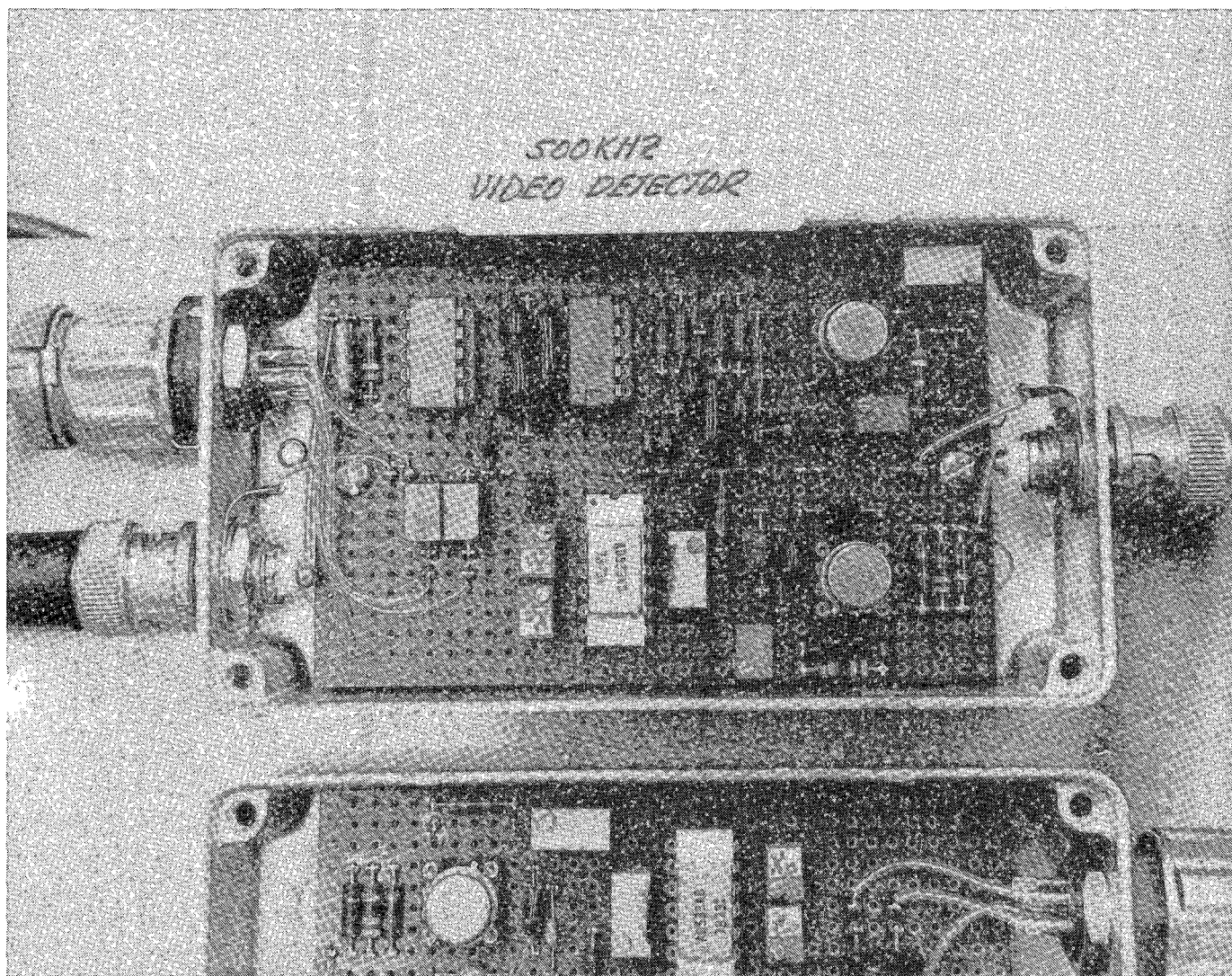
Item 110 Video detectors, back panel.





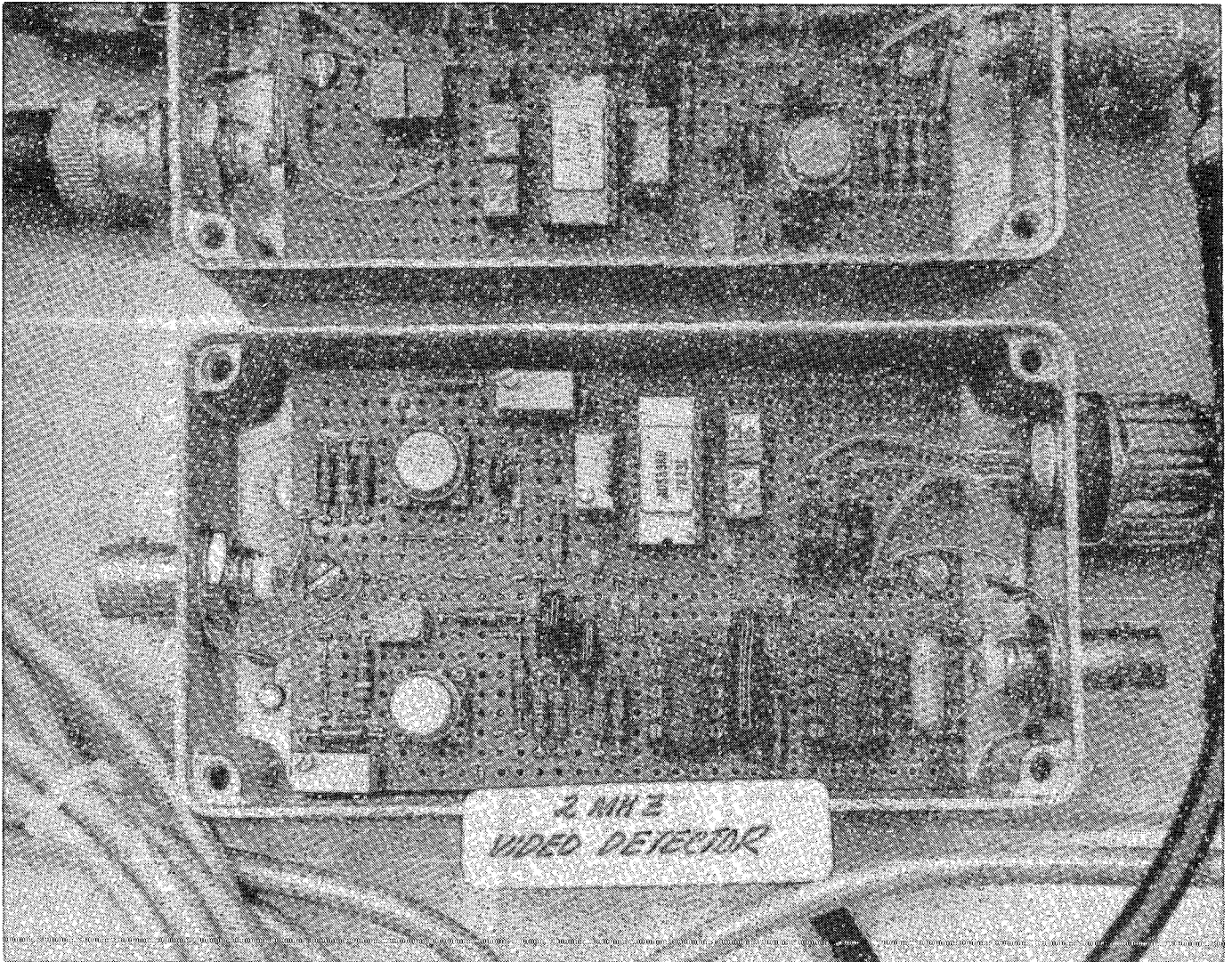
Item 110 Video detectors, component layout for 250 kHz unit.

SC36633



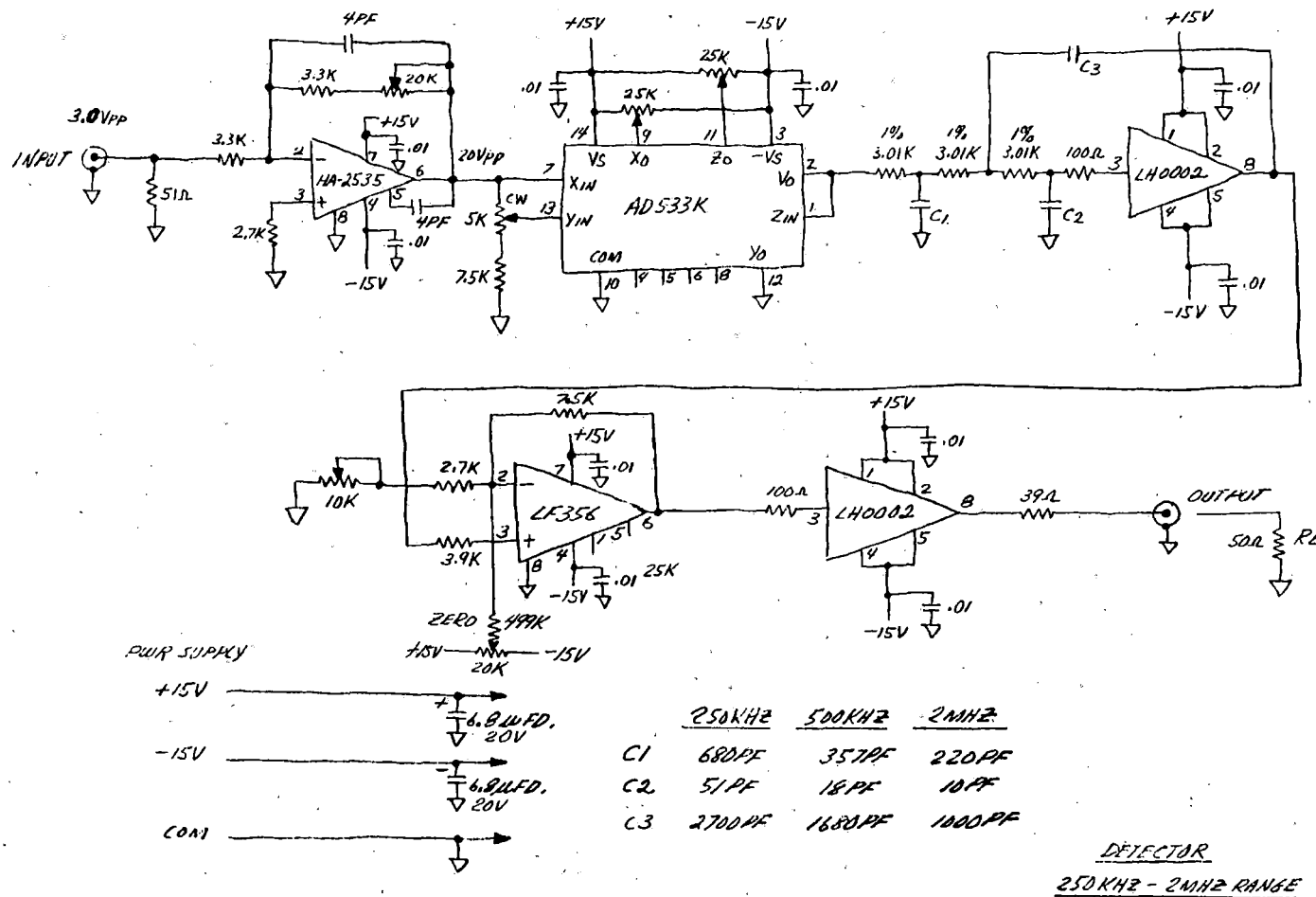
Item 110 Video detectors, component layout for 500 kHz unit.

SC36632



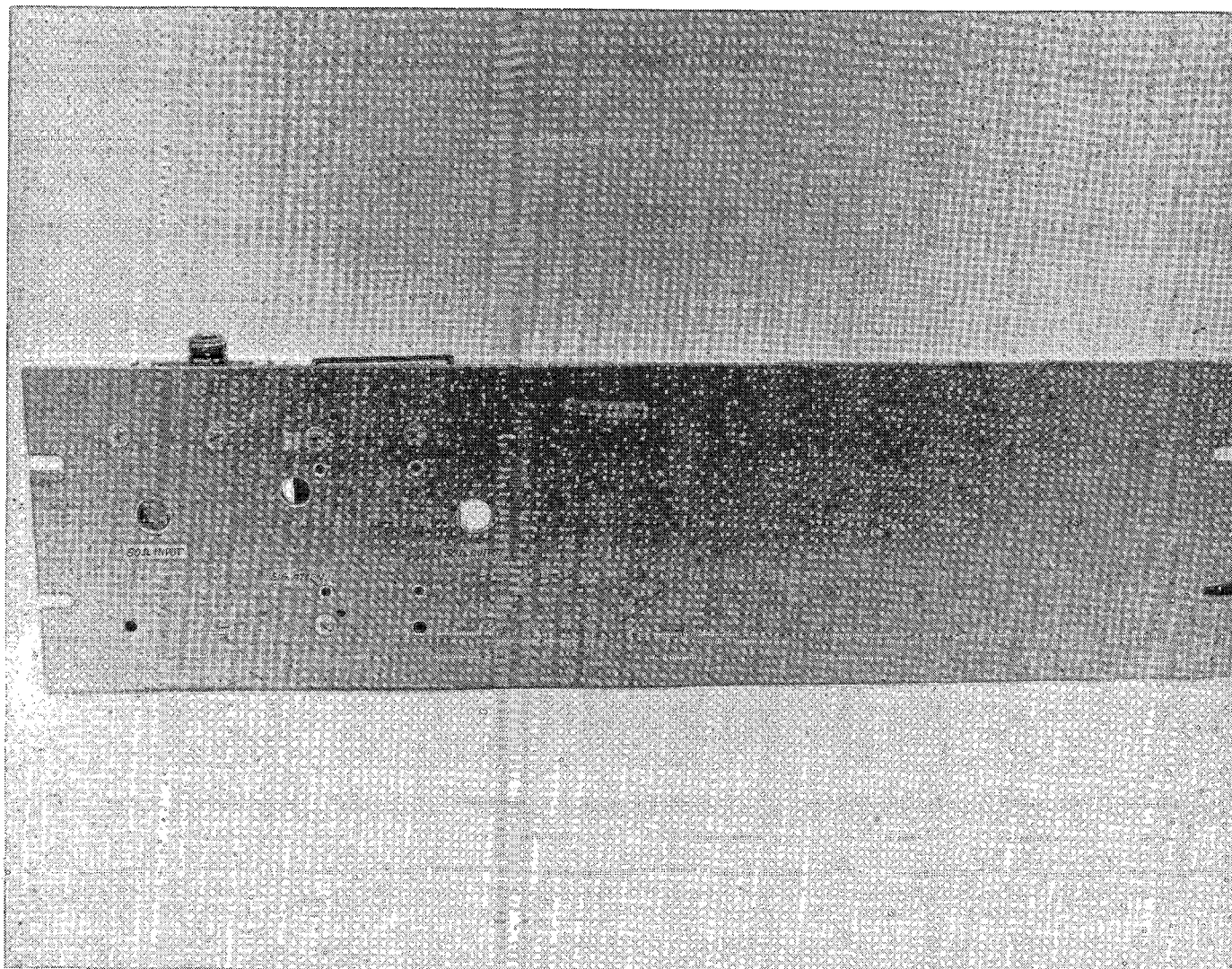
Item 110 Video detectors, component layout for 2 MHz unit.





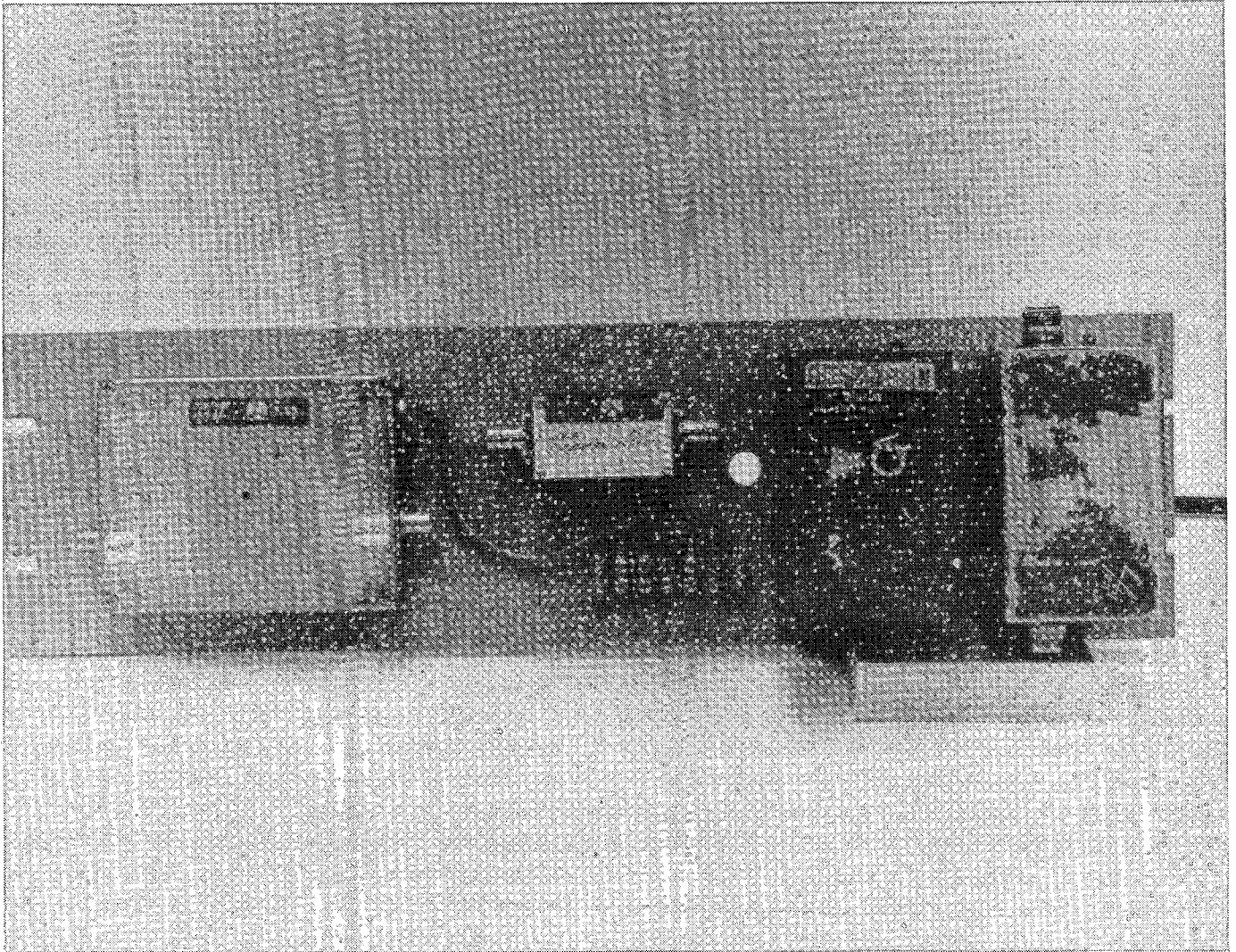
Item 110 Video detectors, schematics.

SC36631



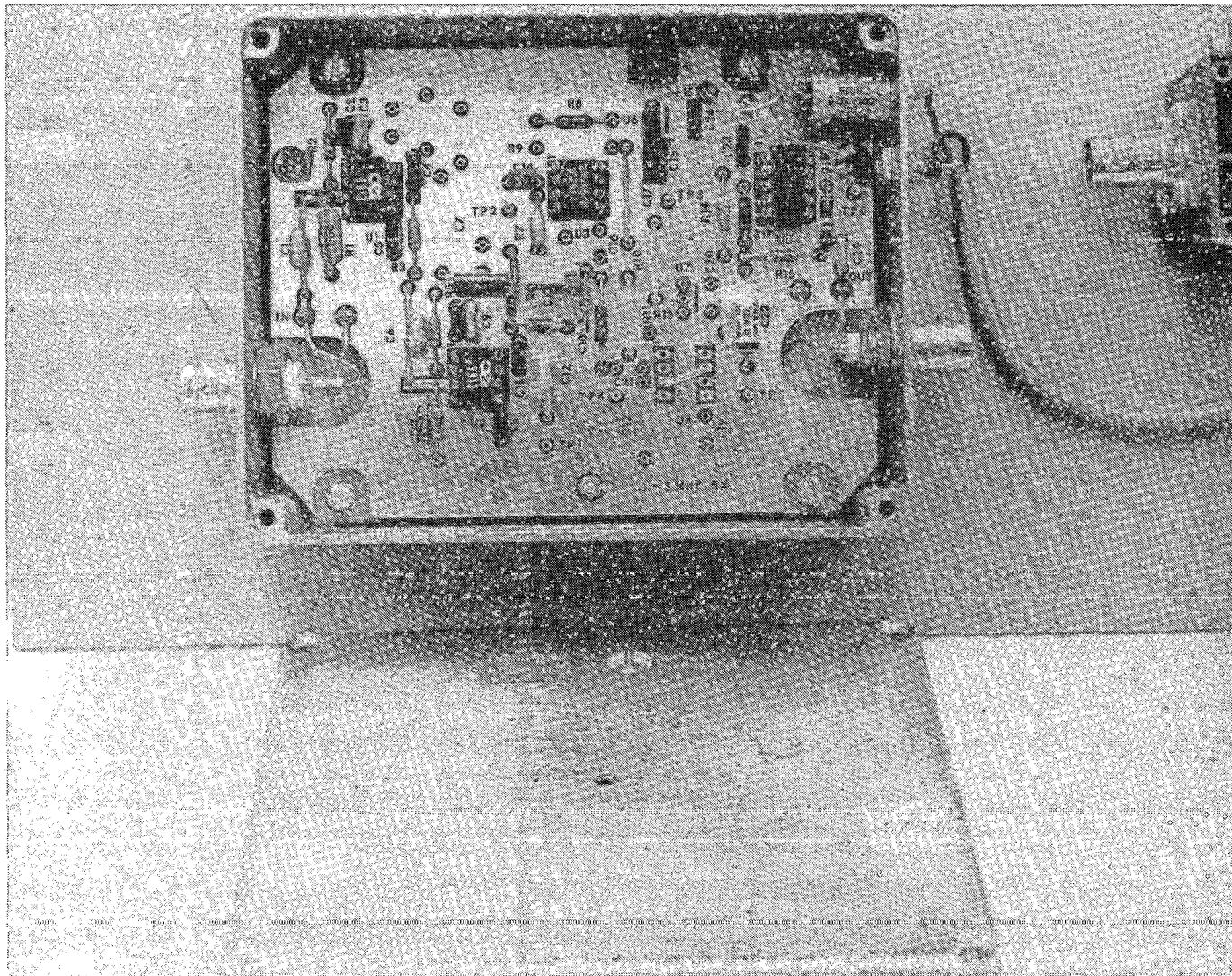
Item 111 Receiver amplifier, front panel.

SC36630



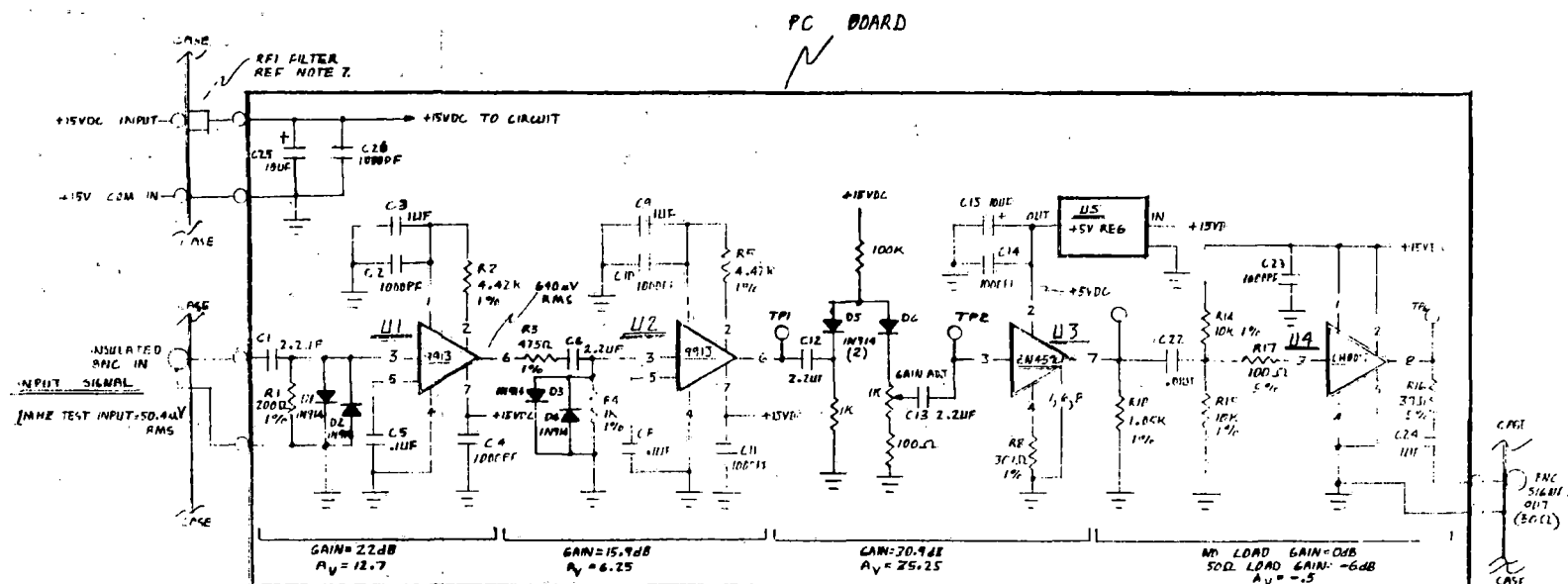
Item 111 & 112 Receiver amplifier and preamplifier, back panel.

SC36629



Item 111 Receiver amplifier, component layout.





## NOTES

1. ALL 1% RESISTORS ARE METAL FILM
2. ALL 5% RESISTORS ARE 1/4W CARBON COMP.
3. U1 & U2 MFGA QEI PN 9913
4. U3 MFGA FERRANTI PN EM549C
5. U4 MFGA NATIONAL SEMI. PN LM8002CN
6. U5 3LEAD +5V REGULATOR PN LM130LA3-5.0

7. RFI FILTER MFGA ERIE PN 9200-300-0013

- TEST NOTES: 1) (NO LOAD) 1 MHZ GAIN=73dB  
GAIN ADJ AT MAX GAIN
- 2) (NO LOAD) MAX INPUT SIG= 100mV RMS AT 1 MHZ
  - 3) 1 MHZ 50Ω LOAD GAIN=67dB
  - 4) 2VPP MAX OUTPUT NO LOAD AT 1 MHZ

TITLE 100' H.F. T. 5A. 1. V1

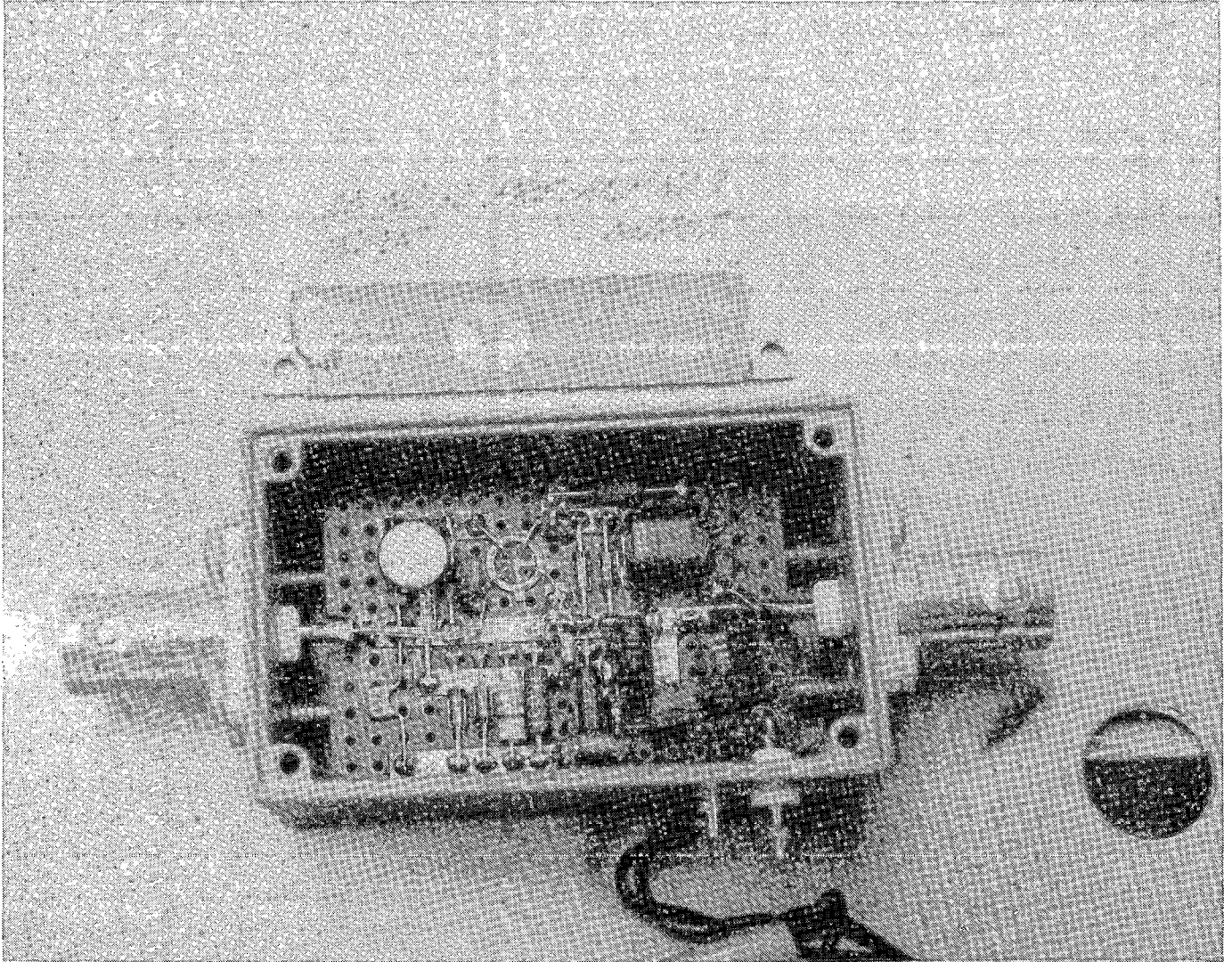
DRAWN WEP 01/1 1-3-82

SHEET 1 OF 1

Item 111 Receiver amplifier, schematic.



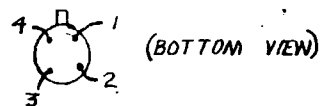
SC36628



Item 112 Low noise preamplifier, component layout.

**DETAIL A**

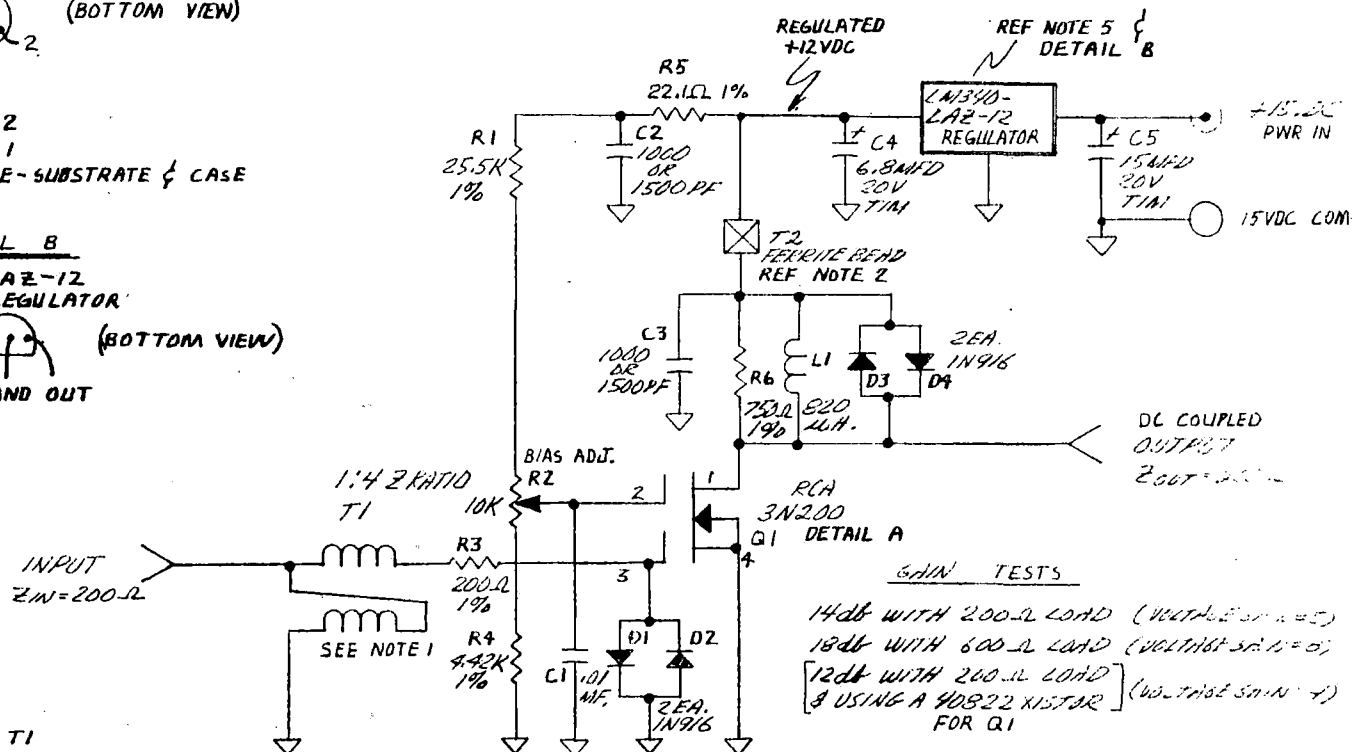
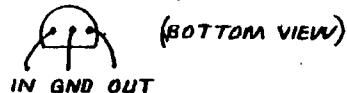
Q1 3N200 LEAD POSITIONS



1. DRAIN
2. GATE 2
3. GATE 1
4. SOURCE-SUBSTRATE & CASE

DETAIL B

LM-340 LAZ-12  
POS 12V REGULATOR



## NOTES

1. TRANSFORMER T1  
MATERIAL #43  
CORE MFGR FERRITE INC  
P/N 2843002902  
16T NO. 36 BIFILAR WIRE
2. FERRITE BEAD-T2  
MFGR- AMIDON  
PN FB-75-B-101  
1T NO.24 WIRE
3. ALL RESISTORS RN55D TYPE

4. C4 & C5 MFGR MALLORY  
C4 = 6.8UF 20V  
PN = \_\_\_\_\_  
C5 = 15UF 20V  
PN = \_\_\_\_\_
5. 3 TERMINAL REGULATOR (+12VDC) .1A  
MFGR NATIONAL SEMICONDUCTOR  
PN LM340-LAZ-12
6. POT R2 MFGR ALLEN BRADLEY  
PN A2A103

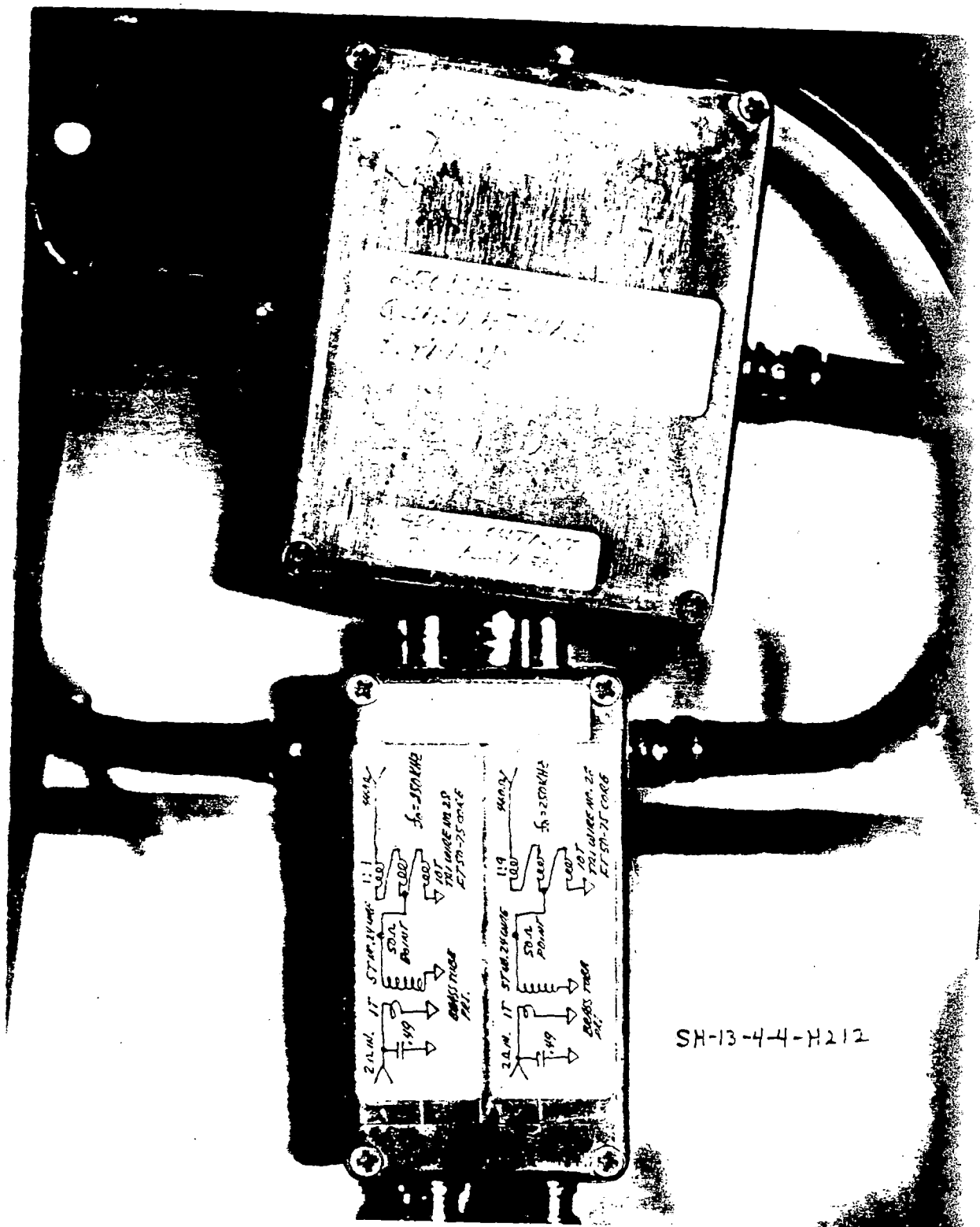
## GNN TESTS

14dB WITH 200- $\Omega$  LOAD (VOLTAGE S/N = 5)  
18dB WITH 600- $\Omega$  LOAD (VOLTAGE S/N = 6)  
[12dB WITH 200- $\Omega$  LOAD] (VOLTAGE S/N = 4)  
& USING A 40822 KISTAR  
FOR Q1

TITLE LOW NOISE PREAMP

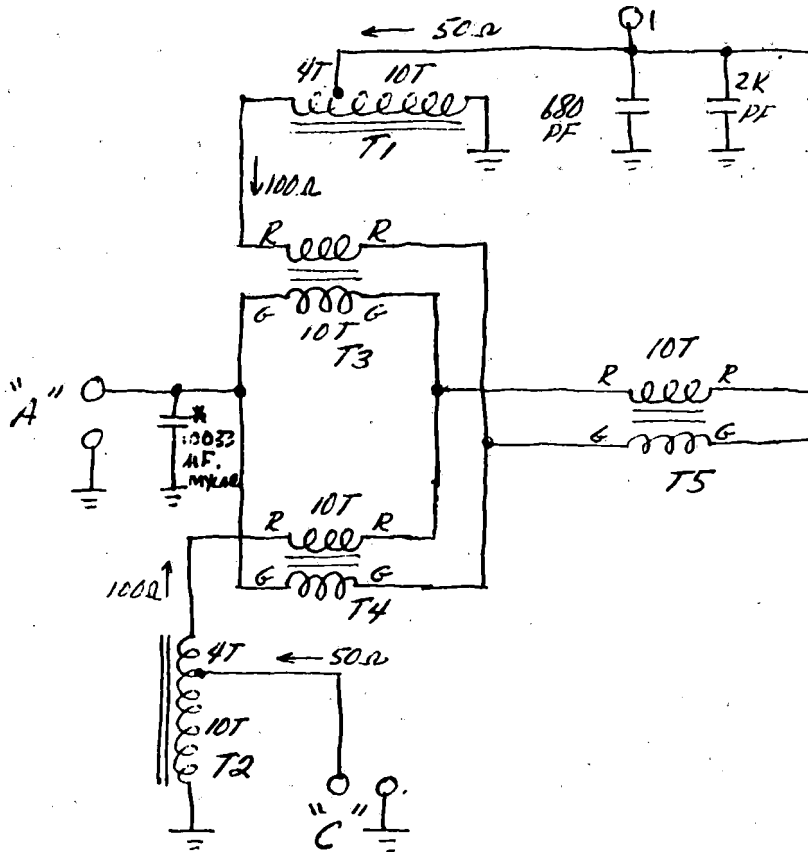
DRAWN W.E. PETERSON

DATE 12-1-81



Item 113 SH receiver impedance matching network (schematic) and quadrature detector.

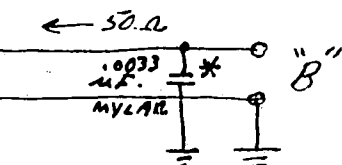
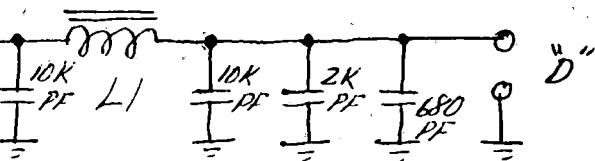
250 KHz 90° HYBRID



**A-39**

Item 113 SH receiver quadrature detector,

22T #34 WIRE FT50-61 CORE  
31.8  $\mu$ H



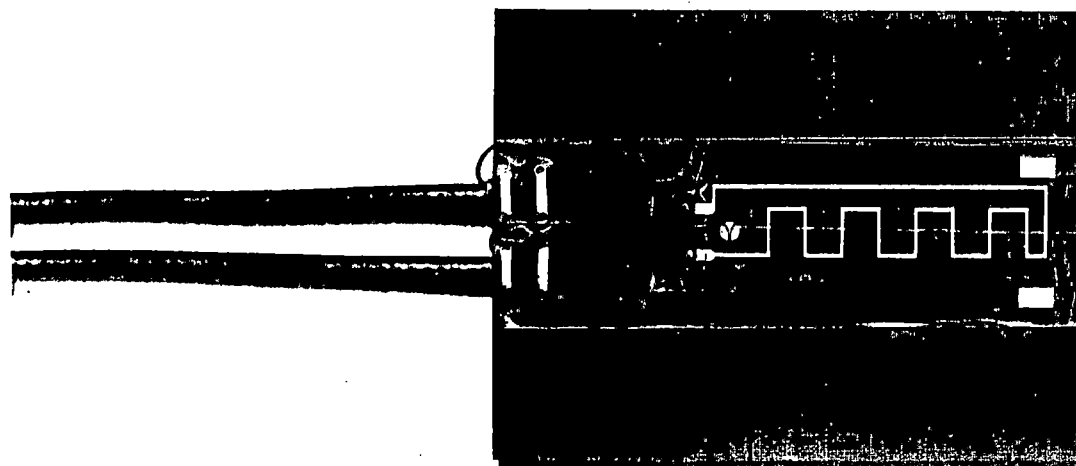
\* NOTE:  
Added compensation  
cap.

T1, T2 = USE FAIRRITE 43  
CORE MATERIAL  
PIN 2843000302  
14 TURNS TAPE @  
10 TURNS #26 WIRE

T3, T4, T5 = USE FAIRRITE 43  
CORE MATERIAL  
PIN 2843000302  
10 TURNS #28 BI  
WIRE.

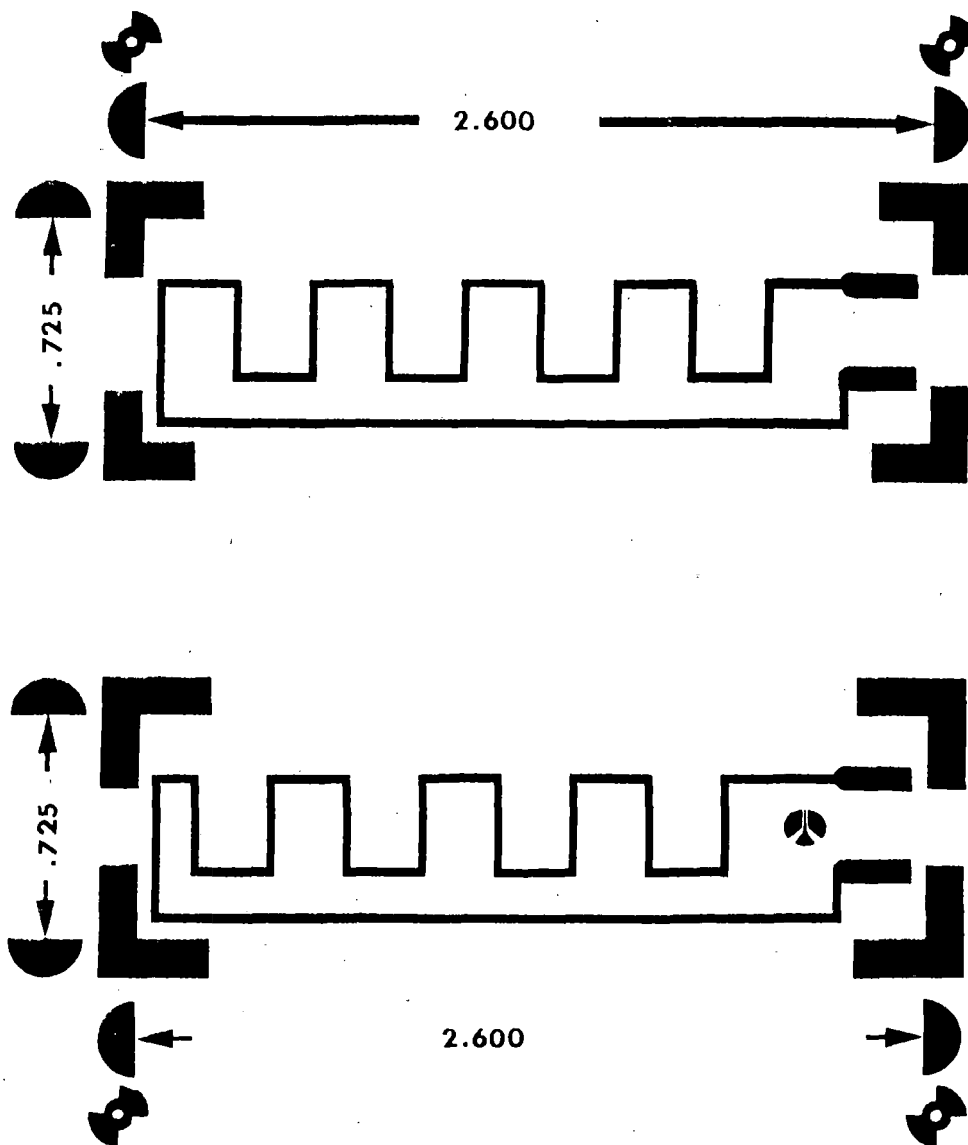
schematic.

A-40

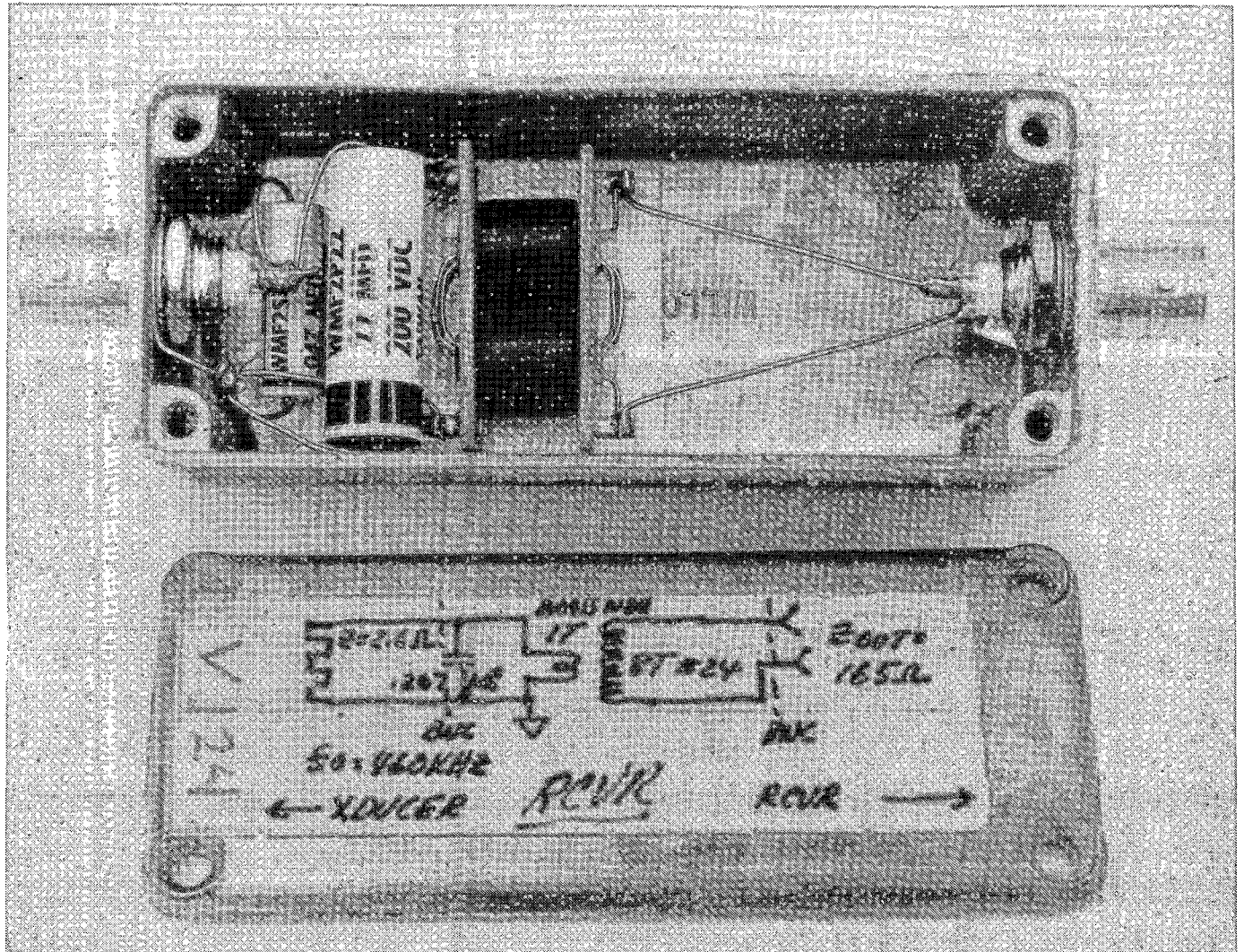


WAVE TYPE	SH
DIMENSION	13.0 mm
PERIODS	4
TURN S	4
MAGNETS	2
T/R	R (460.Ω)
SN	SH-13-4-4-H212

Item 114 SH receiver EMAT.



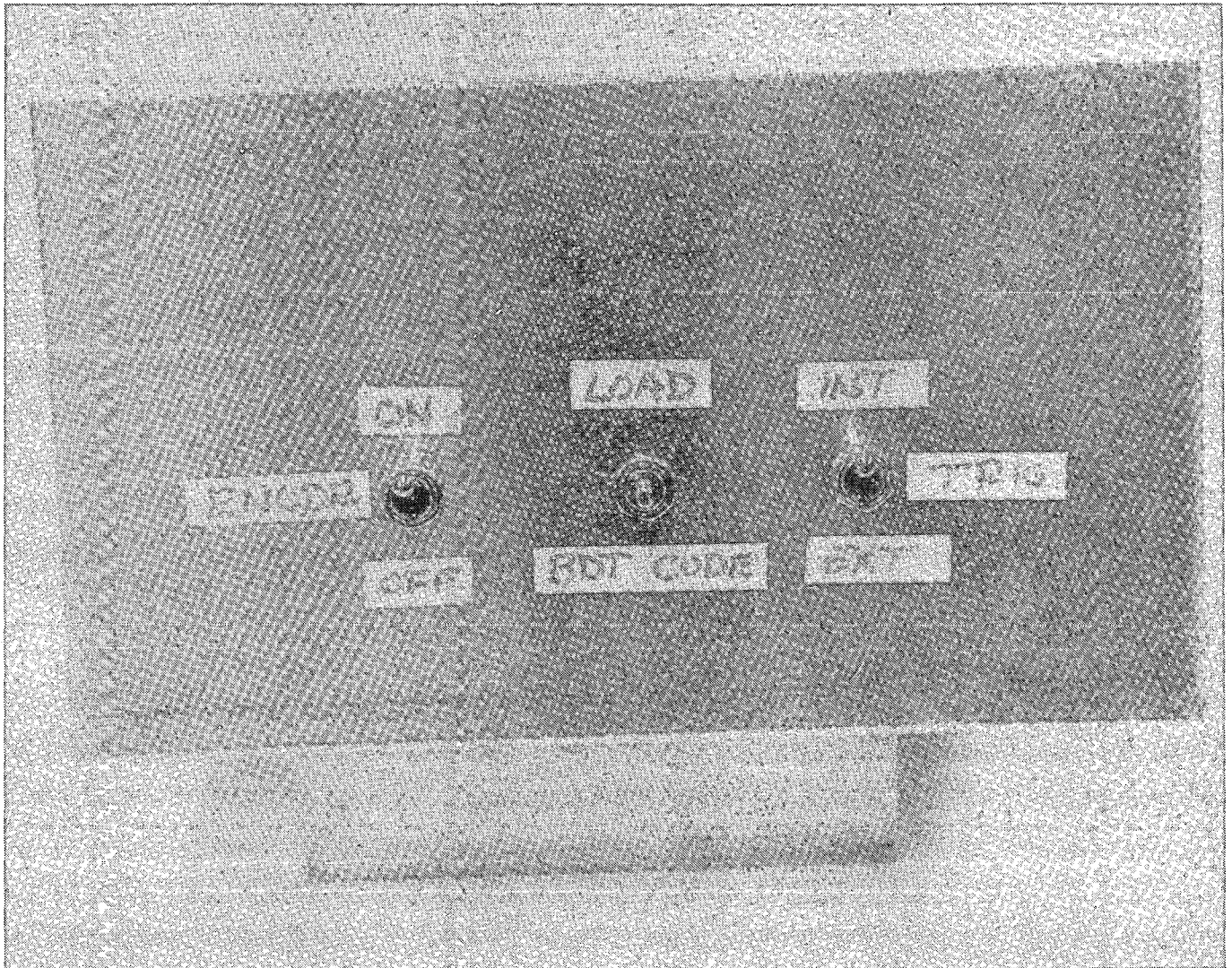
Item 114 SH receiver, PC board design.



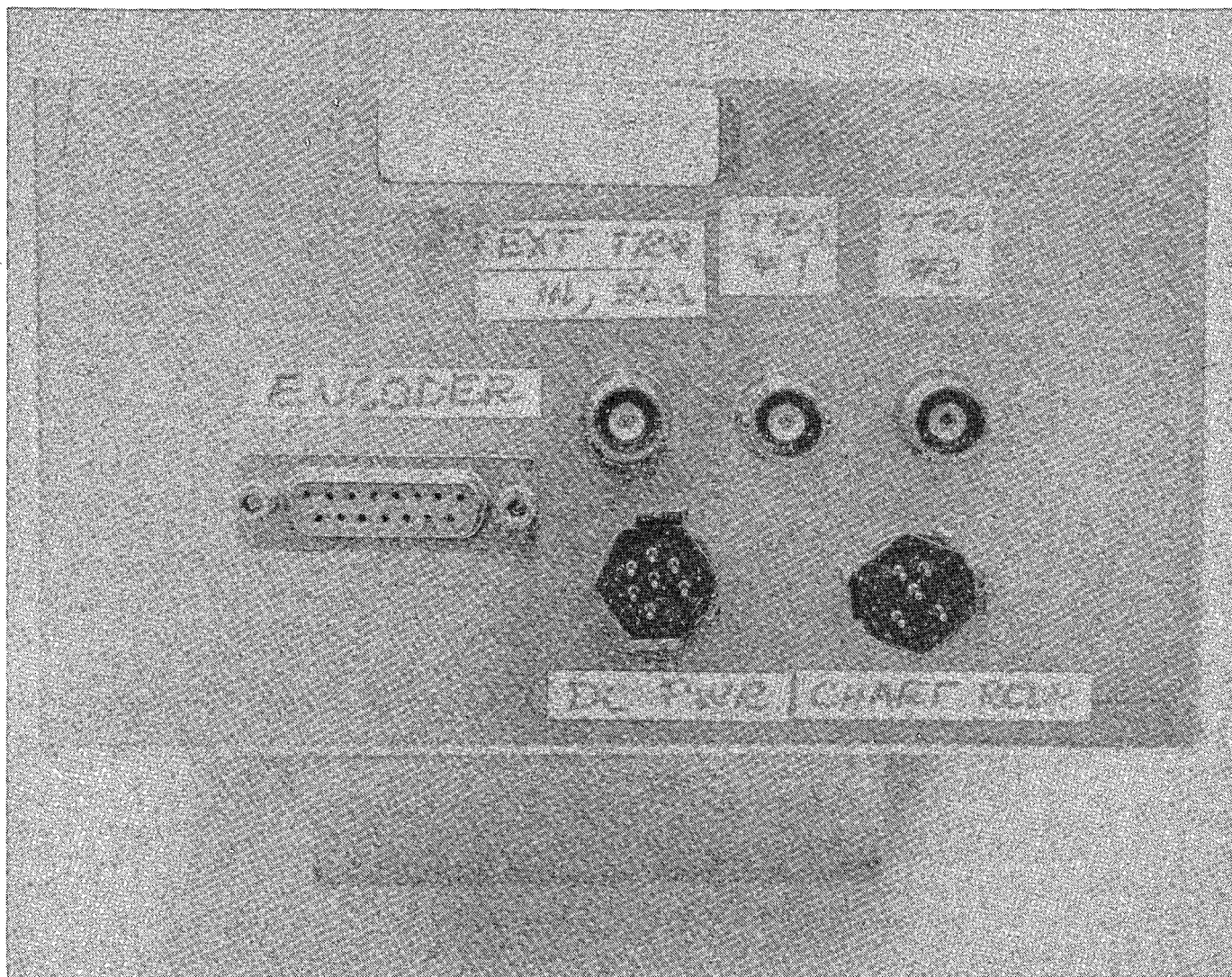
Item 115 SV receiver impedance matching network, component layout and schematic.







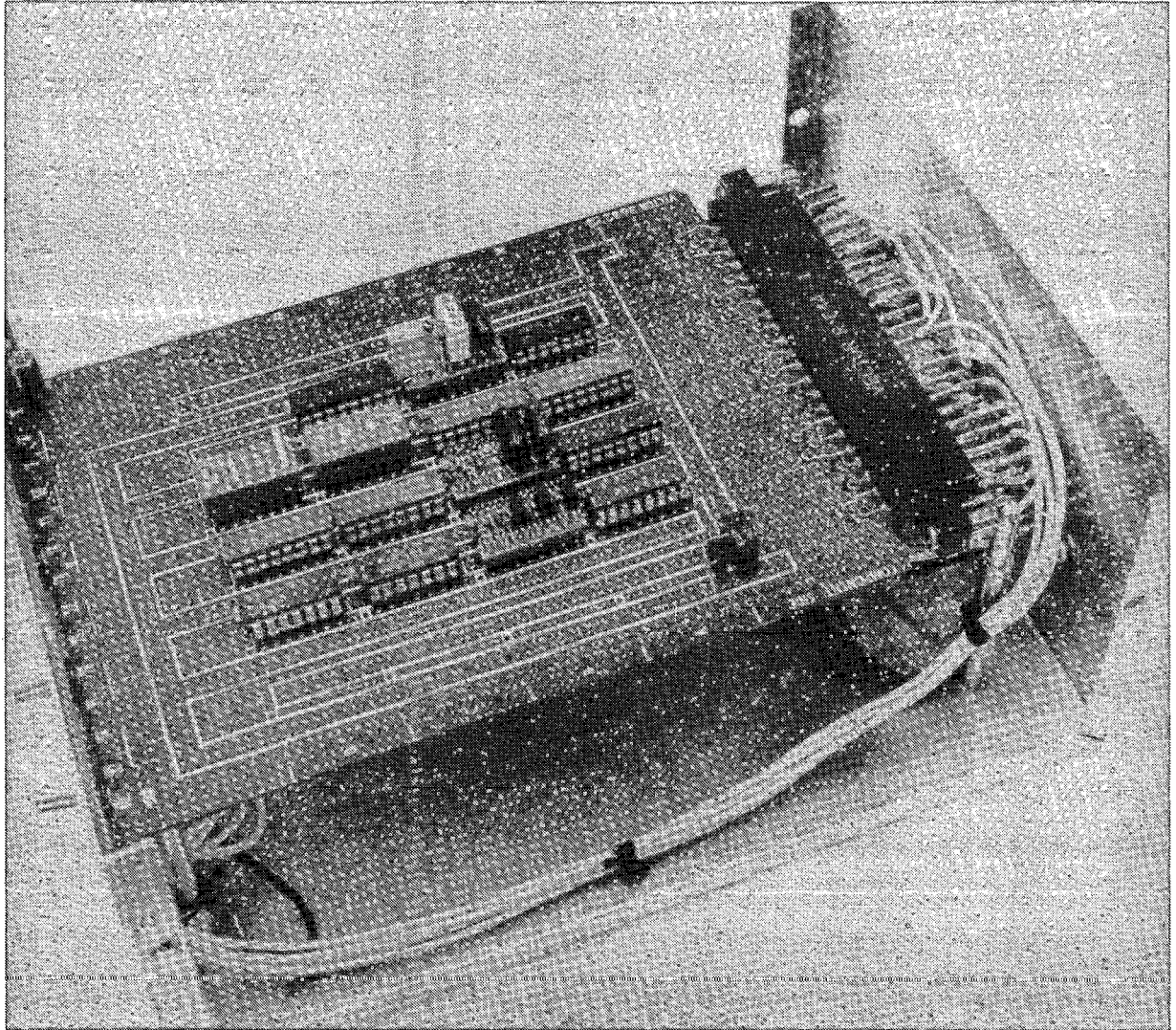
Item 119 Optical shaft encoder I/O, front panel.



Item 119 Optical shaft encoder I/O, back panel.



SC36624



Item 119 Optical shaft encoder I/O, component layout.

174 E

## APPENDIX B - DEFECT DOCUMENTATION

An attempt was made to measure the defect size and orientation as accurately as possible using conventional ultrasonics for each of the 44 laboratory rail specimens listed in Table B-1. For transverse defects, hand scanning was done using a 70° shear wave generated by a wedge transducer. The "6 dB down method" described in the main body of this report was used to determine their sizes and tilt angles. Comparison with the actual sizes of six of the transverse defects which were later exposed by breaking the rails showed that these measured sizes were generally too small. Table B-2 contains descriptions of these six defects from visual observation, and Fig. B-1 shows photographs of the rail ends after being broken open at the defects.

For longitudinal defects, hand scanning was done using a 0° longitudinal transducer. Their positions and extent could be determined very accurately by measuring the time of occurrence of the ultrasonic reflection and the position at which the amplitude of that signal was down by 6 dB. Scanning was along the top surface of the rail for horizontally oriented defects (HSH, HWS, BHC) and along the sides of the head for vertically oriented ones (VSH). These measurements were supplemented by visual observations of surface emergence of the defects where appropriate.

Sketches of each of the defects starred in Table B-1 and notes regarding their size measurements are contained in the remaining figures in this Appendix. Documentation of each of the defects found in the field tests is contained in the main body of the report.

TABLE B-1 RECEIVED RAIL SPECIMENS

SRS No.	Specimen Length, in.	Defect Type	Defect Length, in.	Remarks
6	12	HSR	7	
-	21	Crushed head	7	
32*	24	BHC	2	
219*	24	HWS	5	
-	21	Weld repairs	4	
302*	102	DWP		Curve worn rail
303*	100	TDT		True trans. def./small
304*	103	TDD		High in head
305*	91	TDT		Head-free rail
306*	92	TDD		Deep in head
307	95	-		Moderate shelling (TDD exposed at one end)
308*	110	TDD		Possible compound
309	73	-		Originally EBF, but sample cut at EBF
310*	96	VSH	38	
311*	39	VSH	4	Most of VSH cut off, head-free rail
312	62	-		New, 1% chrome
313	44	-		New, chrome-vanadium

TABLE B-1 RECEIVED RAIL SPECIMENS (Cont'd)

SRS No.	Specimen Length, in.	Defect Type	Defect Length, in.	Remarks
314	72	-		New, standard carbon
315	72	Crushed head		
316*	63	CF		
318	59	-		Engine burn (no defect)
319*	60	EBF		
320*	64	TD		Under Stellite field weld patch
321	61	-		New, full heat treat
322	61	-		New, curve master
323*	55	HSB		
324	12			
325	12			
326	18			
328	73	-		Severe head checking
330*	65	DF (two)		Shelling
331*	77	DWP		Weld defect under shelling
332	85	-		Shelling
333	70	-		Shelling
334*	67	VSH	48	
335*	62	VSH	43	



TABLE B-1 RECEIVED RAIL SPECIMENS (Cont'd)

SRS No.	Specimen Length, in.	Defect Type	Defect Length, in.	Remarks
336*	26	VSH	26	
337*	70	VSH	21	
338*	80	VSH	56	
339*	65	VSH	21	
340*	70	VSH	14	
341*	72	VSH	17	
342*	77	VSH	26	
343*	73	VSH	6	No VSH found under surface depression

TABLE B-2. DESCRIPTION OF DEFECTS EXPOSED BY BREAKING RAIL SPECIMENS

Rail No. 305

Defect: TDT-S (Transverse Fissure)  
 Size: .312 W x .1875 H = 1.4%  
 Head-free rail - air-cooled  
 Excellent reflecting surface  
 N&W Railroad

Rail No. 308

Defect: TDT-S (Transverse Fissure)  
 Size: 1.5 W x 1.25 H = 41%  
 Some minor compounding  
 N&W Railroad

Rail No. 320

Defect: TDC-M (Compound Fissure)  
 Size: 1.5 W x .75 H = 29%  
 Result of surface weld separation  
 B&M Railroad

Rail No. 330<sub>L</sub>

Defect: TDD (Detail Fracture)  
 Size: 1.5 W x 1.25 H = 37%  
 Detailed from surface harden zone  
 AT&SFe Railroad

Rail No. 330<sub>S</sub>

Defect: TDD (Detail Fracture)  
 Size: .875 W x .625 H = 11%  
 Detailed from surface harden zone  
 Ten inches from defect listed above  
 AT&SFe Railroad

Rail No. 331

Defect: DWP (Flash Butt Weld)  
 Size: 2.250 W x 1.875 H = 86%  
 Started from small slag inclusion  
 AT&SFe Railroad

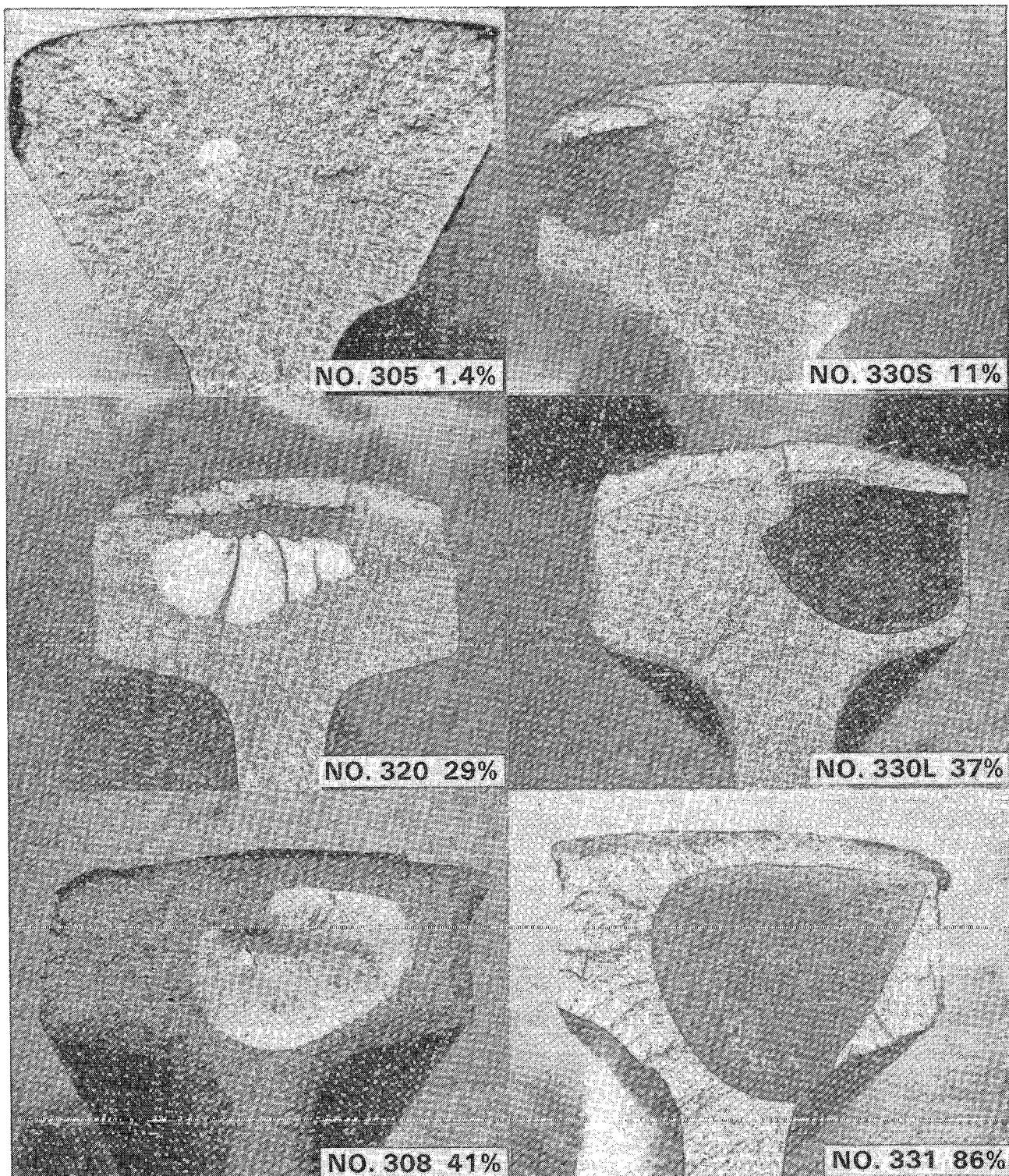
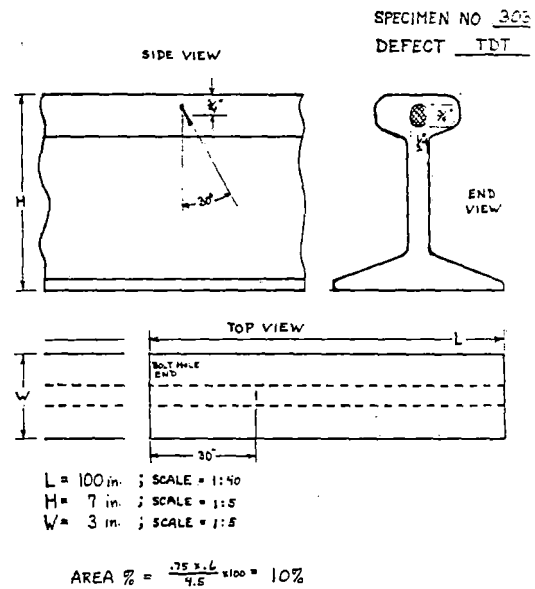
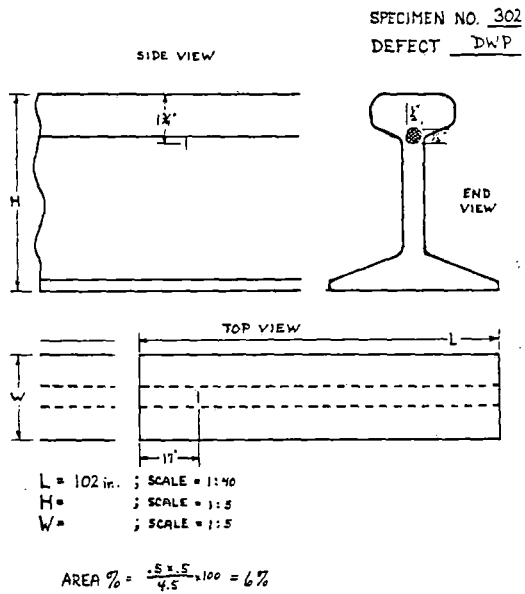
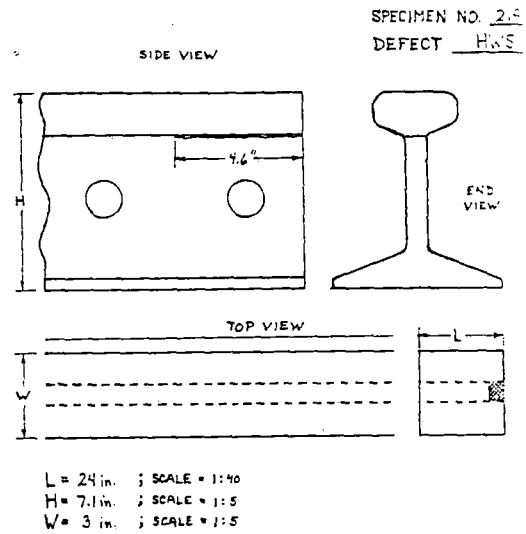
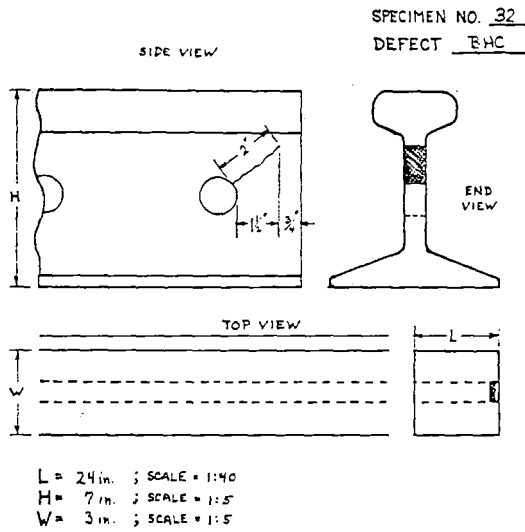
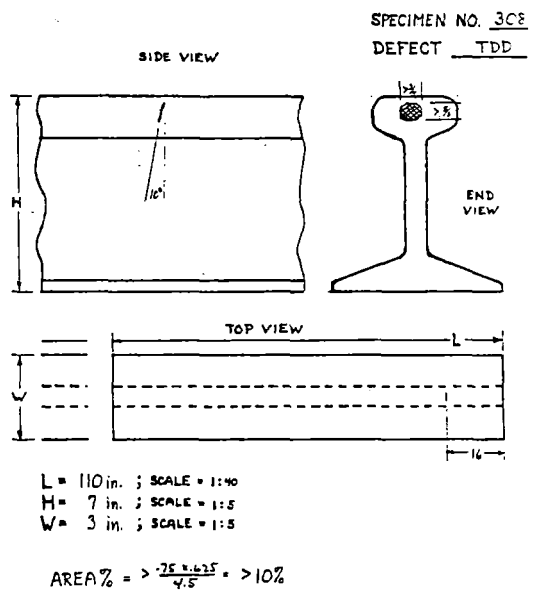
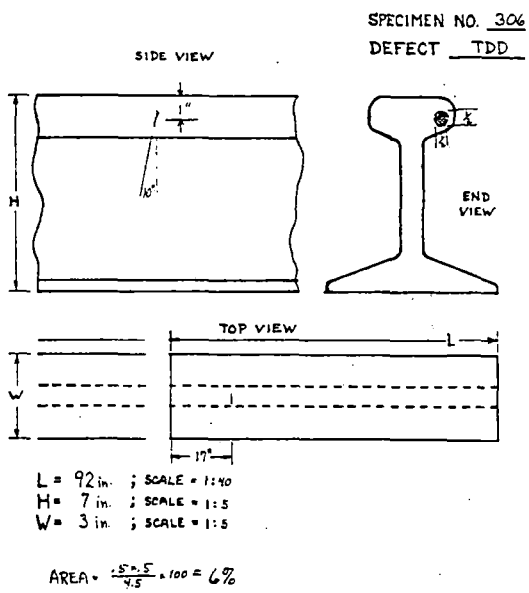
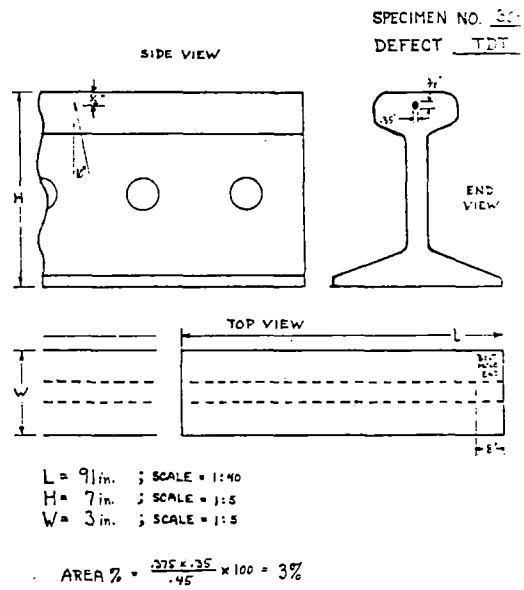
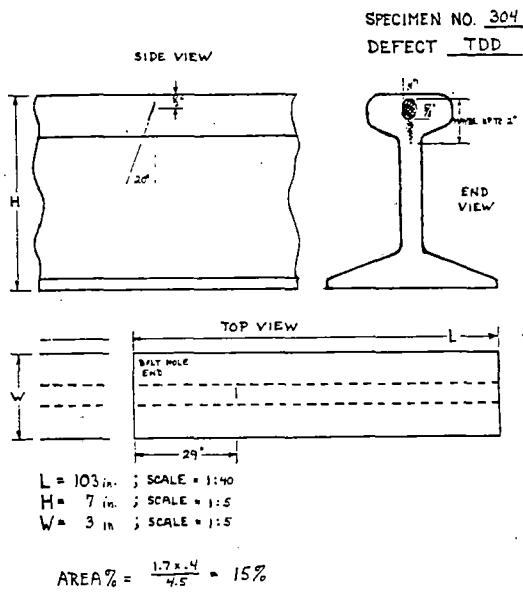
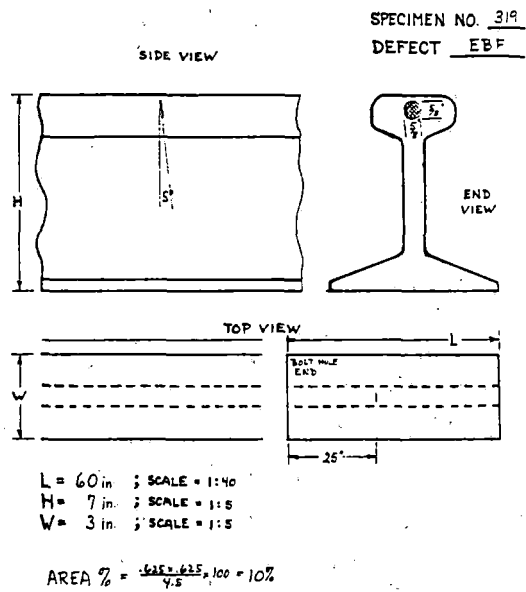
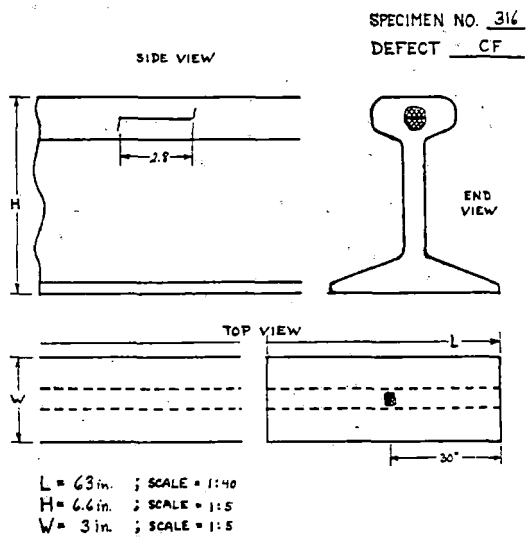
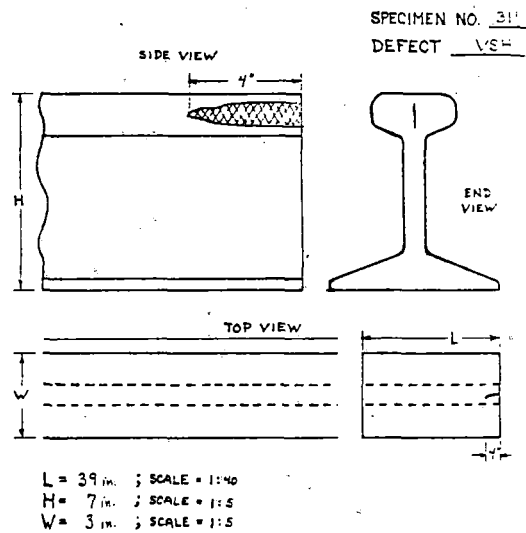
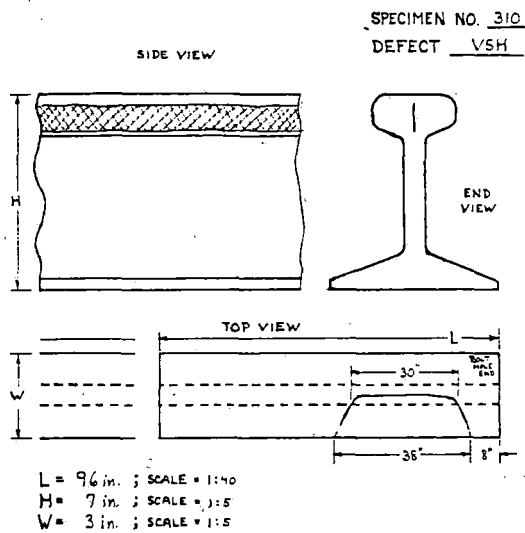
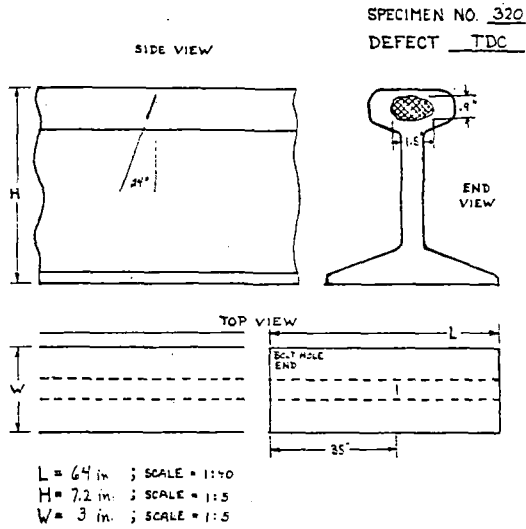


Figure B-1. Photographs of rail ends broken at six of the transverse defects tested.

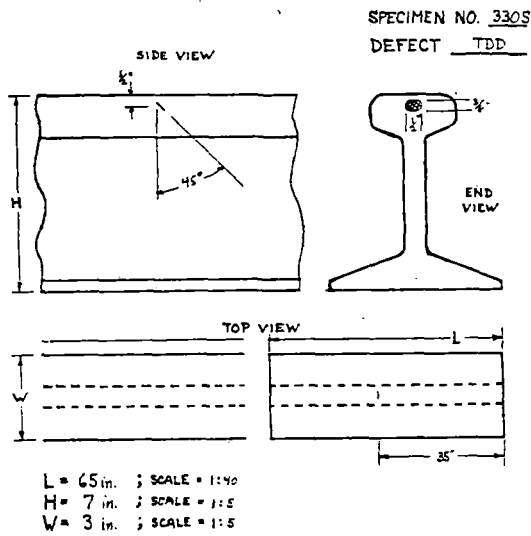
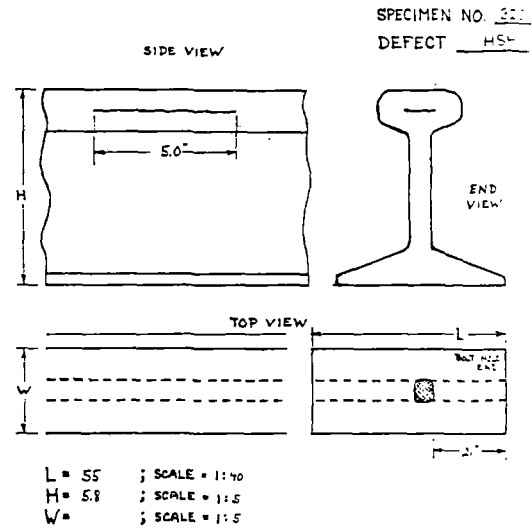




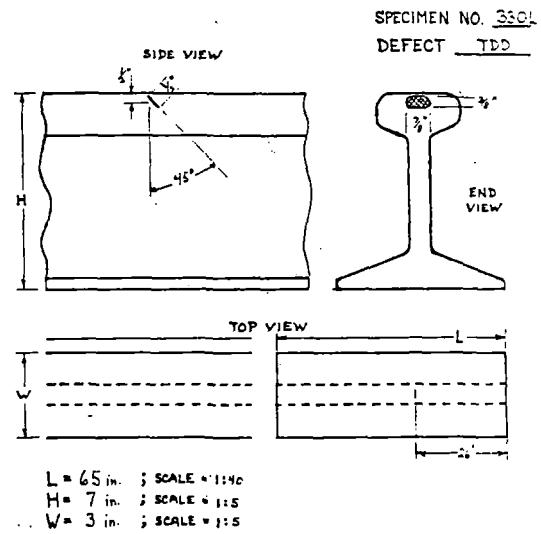




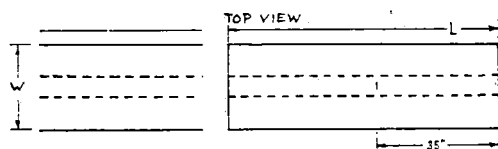
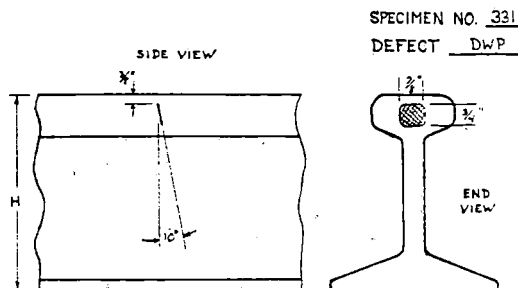
$$\text{AREA \%} = \frac{1.5 \times .9}{4.5} \times 100 = 30\%$$



$$\text{AREA \%} = \frac{.5 \times .375}{7.5} \times 100 = 4\%$$

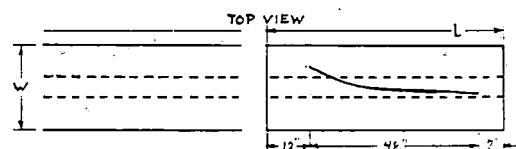
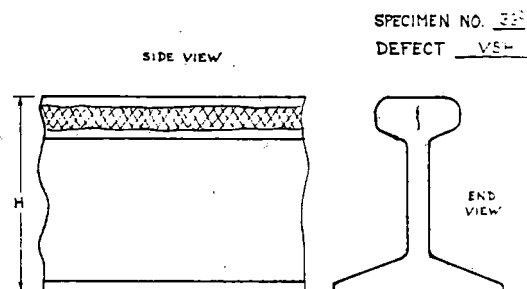


$$\text{AREA \%} = \frac{.975 \times .375}{4.5} \times 100 = 7\%$$

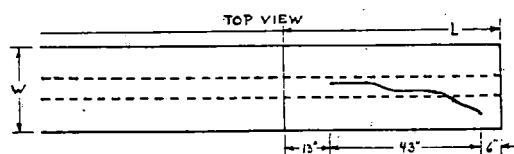
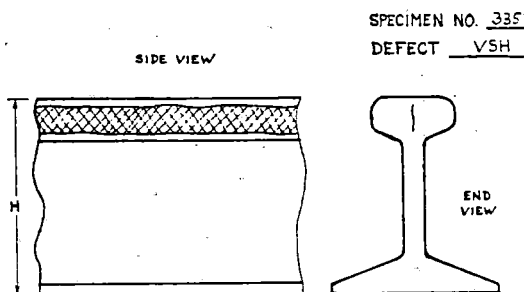


L = 77 in. ; SCALE = 1:40  
H = 7 in. ; SCALE = 1:5  
W = 3 in. ; SCALE = 1:5

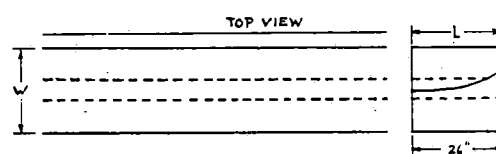
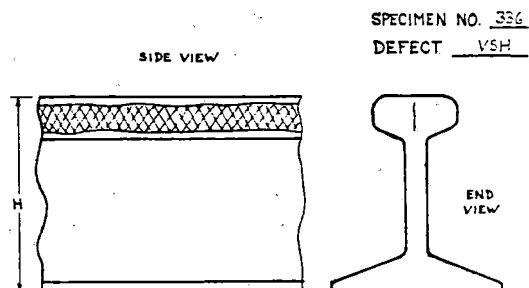
$$\text{AREA} \% = \frac{.875 \times .750}{4.50} \times 100 = 15\%$$



L = 67 in. ; SCALE = 1:40  
H = 5.2 in. ; SCALE = 1:5  
W = 2.5 in. ; SCALE = 1:5

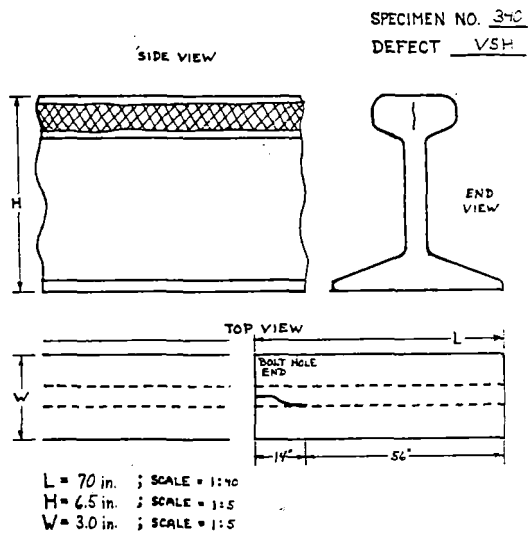
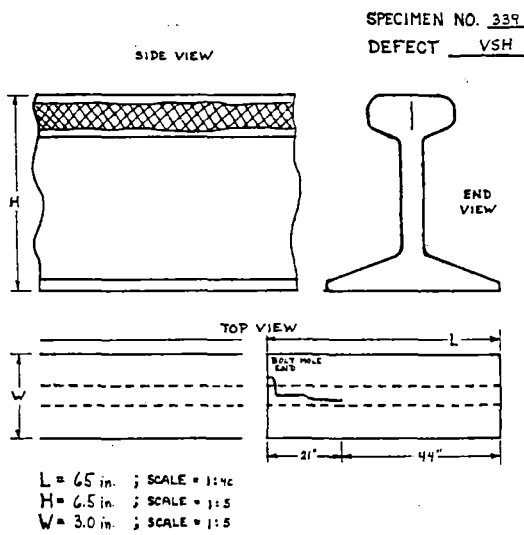
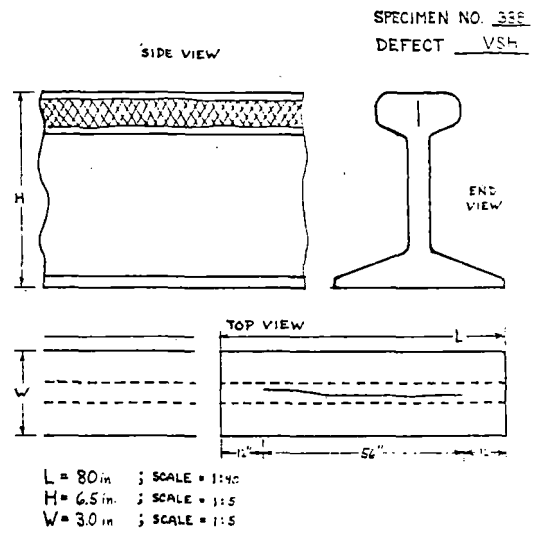
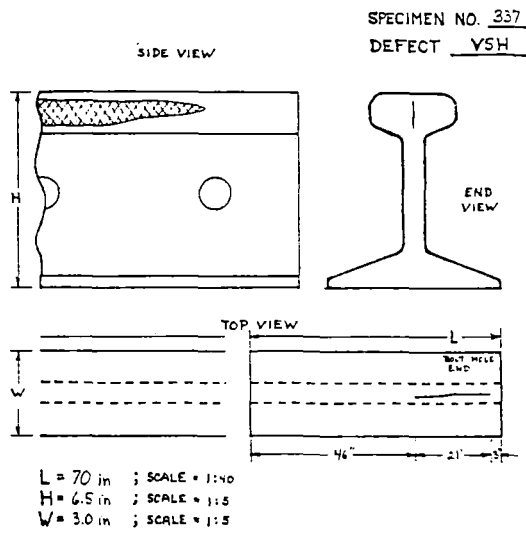


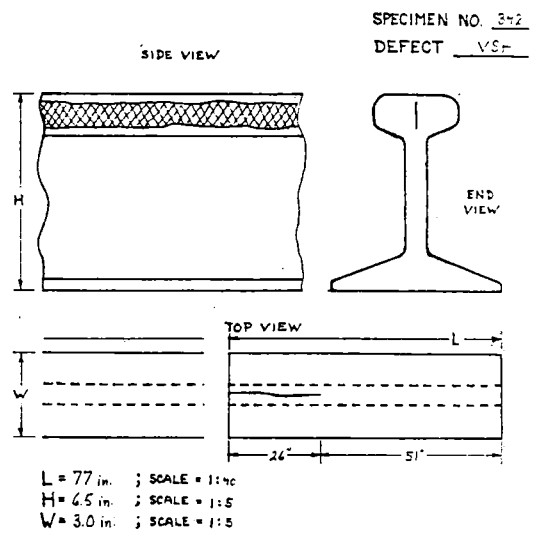
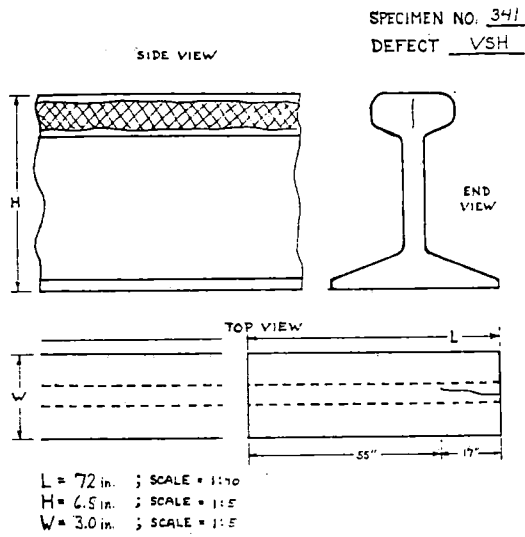
L = 62 in. ; SCALE = 1:40  
H = 5.2 in. ; SCALE = 1:5  
W = 2.5 in. ; SCALE = 1:5



L = 26 in. ; SCALE = 1:40  
H = 6.5 in. ; SCALE = 1:5  
W = 3.0 in. ; SCALE = 1:5







## APPENDIX C - EXPERIMENTAL DATA

Many strip chart recordings were made under various conditions for each of the defects and rail conditions studied. Representative recording for most of these are included here. They are arranged in three groups; laboratory rail specimens, Sante Fe Test Track defects, and FAST Track defects. Tables at the beginning of each group list the defects in the order that the strip charts are presented.

## APPENDIX C - LIST OF TABLES AND FIGURES

### Table C-1. LABORATORY RAIL DEFECT SPECIMENS

Figure C-1. Lab. Spec. #303 - 10% TDT

Figure C-2. Lab. Spec. #305 - 1.4% TDT; a) moving W to E, b) moving E to W.

Figure C-3. Lab. Spec. #308 - 41% TDD.

Figure C-4. Lab. Spec. #304 - 10% TDD.

Figure C-5. Lab. Spec. #306 - 6% TDD.

Figure C-6. Lab. Spec. #330 - 11% and 37% DFs.

Figure C-7. Lab. Spec. #320 - 29% TD under a Stellite field weld patch.

Figure C-8. Lab. Spec. #319 - 10% EBF.

Figure C-9. Lab. Spec. #331 - 86% DWP.

Figure C-10. Lab. Spec. #316 - 2.8 in. CF.

Figure C-11. Lab. Spec. #323 - 5 in. HSH.

Figure C-12. Lab. Spec. #310 - detection of 38 in. VSH with SR, SH and SV EMATs.

Figure C-13. Lab. Specs. #310 and #311 - 38 in. and 4 in. VSHs.

Figure C-14. Lab. Spec. #334 - 48 in. VSH defect (chart recording not available).

Figure C-15. Lab. Spec. #335 - 43 in. VSH defect (chart recording not available).

Figure C-16. Lab. Spec. #336 - 26 in. VSH defect (chart recording not available).

Figure C-17. Lab. Spec. #337 - 21 in. VSH defect.

Figure C-18. Lab. Spec. #338 - 56 in. VSH defect.

Figure C-19. Lab. Spec. #339 - 21 in. VSH defect.

Figure C-20. Lab. Spec. #340 - 14 in. VSH defect.

Figure C-21. Lab. Spec. #341 - 17 in. VSH defect.

- Figure C-22. Lab. Spec. #342 - 26 in. VSH defect.
- Figure C-23. Lab. Spec. #219 - 5 in. HWS defect.
- Figure C-24. Lab. Spec. #32 - 2 in. BHC defect.
- Figure C-25. Lab. Specs. #32 and #310 - SV-EMAT pitch-catch patterns at bolt holes.
- Figure C-26. Lab. Specs. #32 and #310 - SV-EMAT pulse echo patterns at bolt holes.
- Figure C-27. Lab. Spec. #318 - SH, SR and SV EMAT signals at EB.
- Figure C-28. Lab. Spec. #332 - shelly rail.
- Figure C-29. Lab. Spec. #333 - shelly rail.
- Figure C-30. Lab. Spec. #343 - crushed head.

TABLE C-2. DEFECTS IN EAST RAIL OF SANTA FE TEST TRACK

TABLE C-3. DEFECTS IN WEST RAIL OF SANTA FE TEST TRACK

- Figure C-31. Illustrations of anomalous ST-base behavior at tie plates and angle bars and limited resolution of small holes drilled through the rail web.
- Figure C-32. Detection of VSH defect in #3E with ST- and SH-EMATs compared to hand-mapping result. Evidence of two small TDs in SH-trace confirmed by hand-scanning.
- Figure C-33. Three modes of detection of large TDs with SH-EMAT in #9E.
- Figure C-34. Detection of small TD in #10E with SH-EMAT.
- Figure C-35. Detection of VSH defect in #10E with ST- and SH-EMATs compared to hand-mapping results. Scattering of SH-wave from defect also seen in reflection modes at the top of the figure.
- Figure C-36. Detection of 2-TDs in #11E with SH-EMAT. Also illustrates the electronic noise problem that occurred at times.
- Figure C-37. Detection of 3-TDs in #3W with SH- and ST-EMATs.

- Figure C-38. Detection of 2-TDs in #4W with SH- and ST-EMATs. Also illustrates local variability in SH-direct transmission signal amplitude and ST-base echo loss at some tie plates.
- Figure C-39. Continuation of charts from Fig. C-38 showing detection of another large TD in #4W.
- Figure C-40. Illustrating the poor detectability of the large TD in #5W, possibly due to an electromagnetic coupling anomaly.
- Figure C-41. Detection of 1/4 in. deep saw cut in the side of the rail head in #7W.
- Figure C-42. Detection of small VSH with SH-EMAT in #11W. The ST-EMAT did not detect this defect.

#### TABLE C-4. DEFECTS AT FAST TRACK

- Figure C-43. FAST Sec. #10, TD-472-0, 0.5 MPH; a) ST, 17 dB; b) SHT, 60 dB; c) SHR, 64 dB; d) SHF, 64 dB.
- Figure C-44. FAST Sec. #10, TD-513-0, 0.5 MPH; a) ST, 17 dB; b) SHT, 60 dB; c) SHR, 64 dB; d) SHF, 64 dB.
- Figure C-45. FAST Sec. #10, TD-560-0, 0.5 MPH; a) ST, 17 dB; b) SHT, 60 dB; c) SHR, 64 dB; d) SHF, 64 dB.
- Figure C-46. FAST Sec. #10, TD-611-0, 0.5 MPH; a) ST, 17 dB; b) SHT, 60 dB; c) SHR, 64 dB; d) SHF, 64 dB.
- Figure C-47. FAST Sec. #10, TD-659-0, 0.5 MPH; a) ST, 17 dB; b) SHT, 60 dB; c) SHR, 64 dB; d) SHF, 64 dB.
- Figure C-48. FAST Sec. #10, TD-611-0, SHF; a) 0.2 MPH, 62 dB; b) 0.5 MPH, 62 dB; c) 1.0 MPH, 62 dB; d) 1.5 MPH, 62 dB; e) 2.0 MPH, 62 db: showing increase in background noise with increasing speed.
- Figure C-49. FAST Sec. #10, ST-background noise; a) 0.5 MPH, 17 dB; b) 2.0 MPH, 16 dB; c) 4.0 MPH, 16 dB; d) 6.0 MPH, 16 dB; e) 8.0 MPH, 16 db: showing small increase in background noise with increasing speed.
- Figure C-50. FAST Sec. #10, ST, TD-659-0, a) 0.5 MPH, 17 dB; b) 2.0 MPH, 16 dB; c) 4.0 MPH, 16 dB; d) 6.0 MPH, 16 dB; e) 8.0 MPH, 16 db: showing decreased spatial resolution with increasing speed due to limited pulse repetition rate.
- Figure C-51. FAST Sec. #10, SH-detection of four TDs in inner rail.

- Figure C-52. FAST Sec. #10, SH-detection of large unmarked TD in inner rail near Tie #650.
- Figure C-53. FAST Sec. #7, marginal SH-detection of 3% TD near Tie #007.
- Figure C-54. FAST Sec. #7, marginal SH-detection of 7% TD near Tie #149 with weld joint and SHELL nearby.
- Figure C-55. FAST Sec. #10, ST-base echo, 16 dB, 1.5 MPS; examples of HSH.
- Figure C-56. FAST Sec. #10, ST-base echo, 16 dB, 1.5 MPH; examples of SHELL and the appearance of an enlarged bolt hole (or BHC) at Tie #513.
- Figure C-57. FAST Sec. #7; 2" SHELL at Tie #073. Rare example of a SHELL being nearly detected as a defect by SH-EMAT.
- Figure C-58. FAST Sec. #7; 1" SHELL at Tie #345. SHELL is not detectable as a defect; motor/generator electrical noise spikes are apparent.

Table C-1. LABORATORY RAIL DEFECT SPECIMENS

SRS No.	Specimen Length (in.)	Rail Height (in.)	Defect Type	Defect Size	Remarks
303†	100	7.0	TDT	(10%)*	True trans. def./small
305†	91	7.0	TDT	1.4%	Head-free rail
308†	110	7.0	TDD	41%	Possible compound
304†	103	7.0	TDD	(15%)	High in head
306†	92	7.0	TDD	(6%)	Deep in head
330†	65	7.0	DF (two)	11%, 37%	Under shelling
320†	64	7.2	TD	29%	Under Stellite field
319†	60	7.0	EBF	(10%)	weld patch
302	102	7.0	DWP	(6%)	Curve worn rail
331†	77	7.0	DWP	86%	Under shelling
316†	63	6.6	CF	(> 10%)	HSH component of 2.8 in.
6	12	7.0	HSH	7 in.	
323†	55	5.8	HSH	5 in.	
310†	96	7.0	VSH	38 in.	
311†	39	7.0	VSH	4 in.	Head-free rail; most
334†	67	5.2	VSH	48 in.	of VSH cut off
335†	62	5.2	VSH	43 in.	
336†	26	6.5	VSH	26 in.	
337†	70	6.5	VSH	21 in.	
338†	80	6.5	VSH	56 in.	
339†	65	6.5	VSH	21 in.	
340†	70	6.5	VSH	14 in.	
341†	72	6.5	VSH	17 in.	
342†	77	6.5	VSH	26 in.	
219†	24	7.1	HWS	5 in.	
32†	24	7.0	BHC	2 in.	
318†	59	7.0	---		Engine burn, no defect
328	73	7.0	---		Severe head checking
307	95	7.0	---		Moderate shelling
332†	85	7.0	---		Shelling
333†	70	7.0	---		Shelling
315	72	7.0	---		Crushed head
343†	73	6.5	---		Crushed head

\* The transverse defect sizes in parentheses are estimates from conventional ultrasonic measurements. The others were measured after breaking the rails at the defects.

† Indicates that strip chart recordings are included in this Appendix.



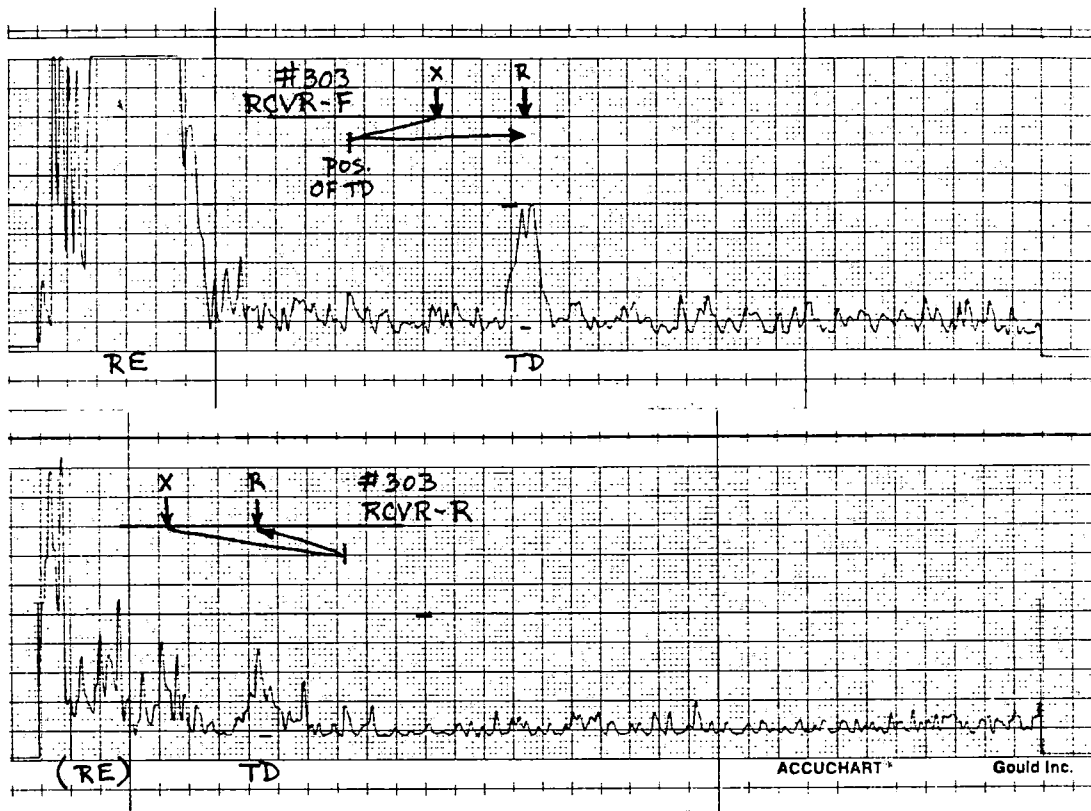
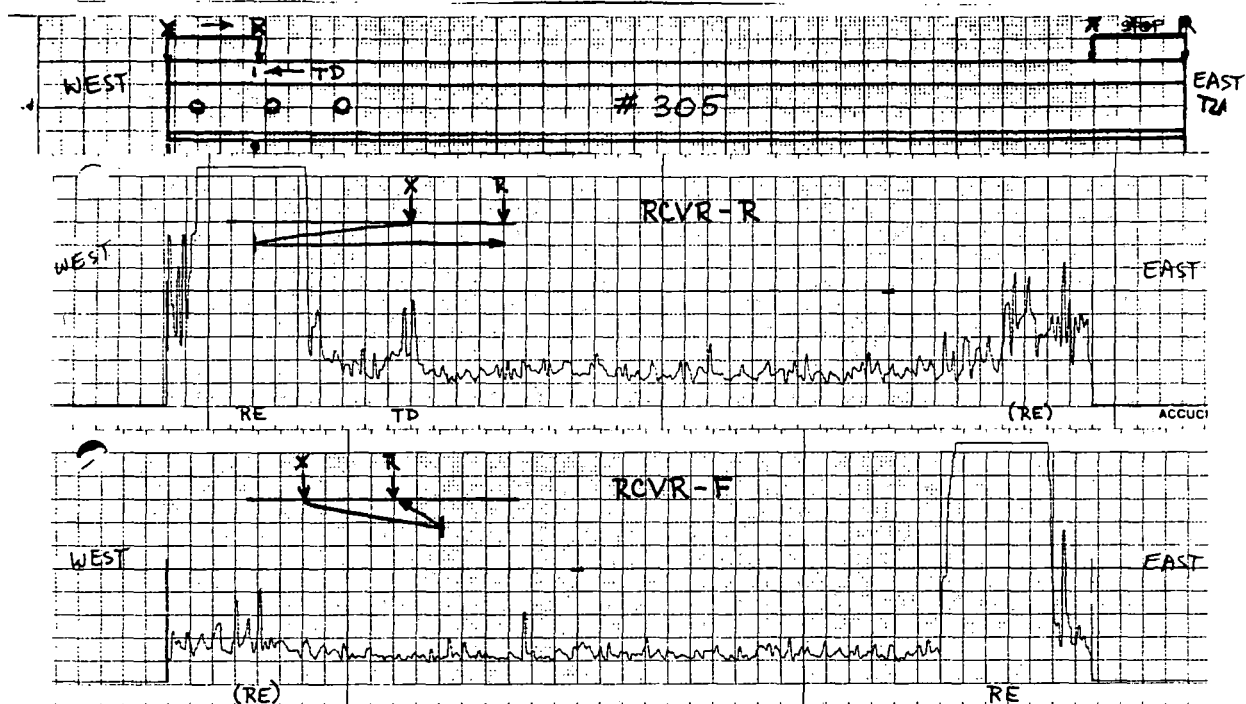
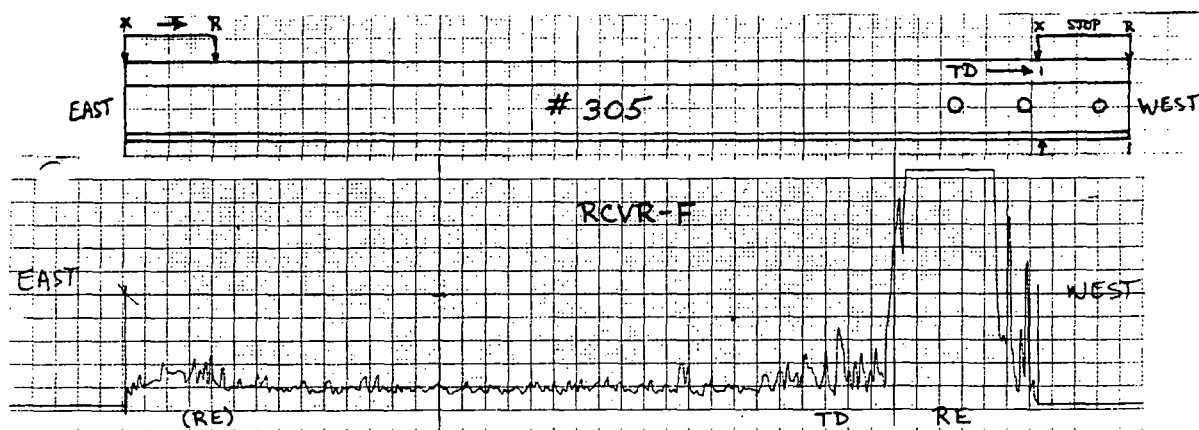


Figure C-1. Lab. Spec. #303 - 10% TDT



(a)



(b)

Figure C-2. Lab. Spec. #305 - 1.4% TDT; a) moving W to E, b) moving E to W.

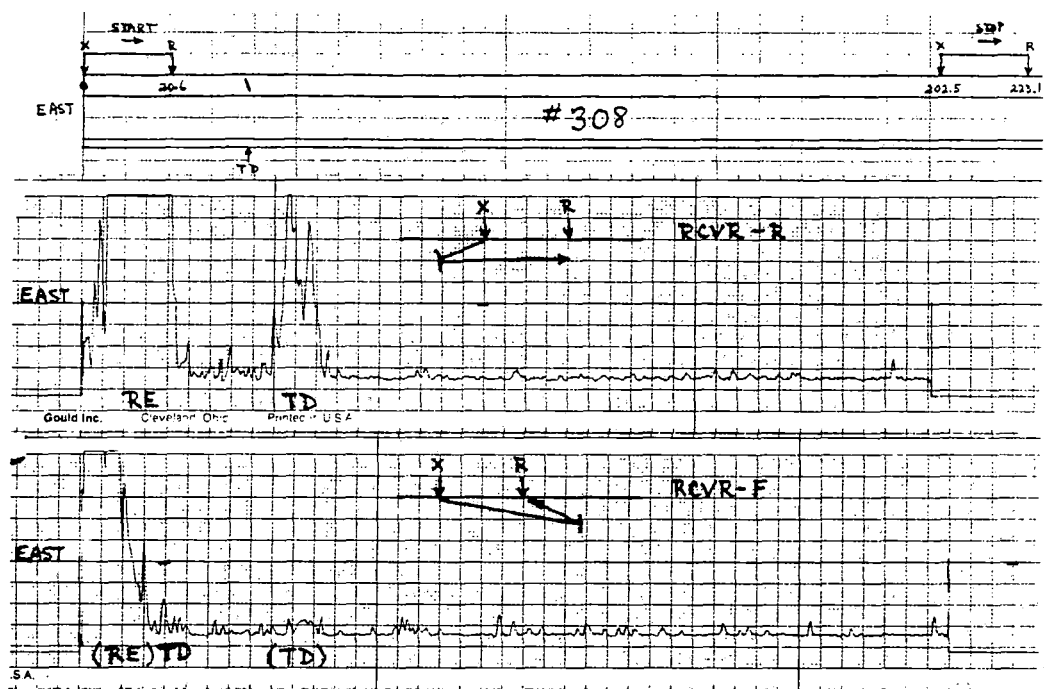


Figure C-3. Lab. Spec. #308 - 41% TDD.

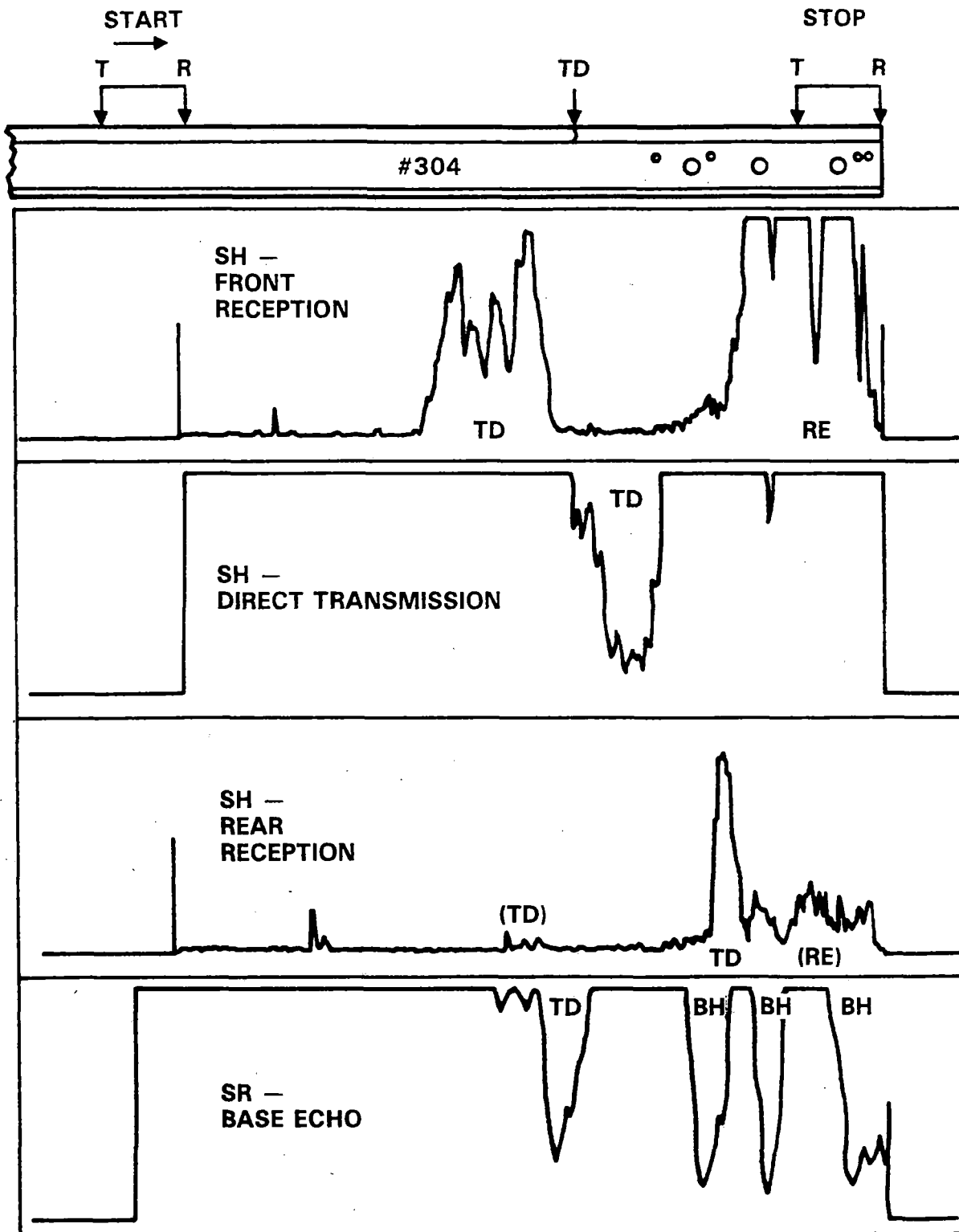


Figure C-4. Lab. Spec. #304 - 10% TDD.

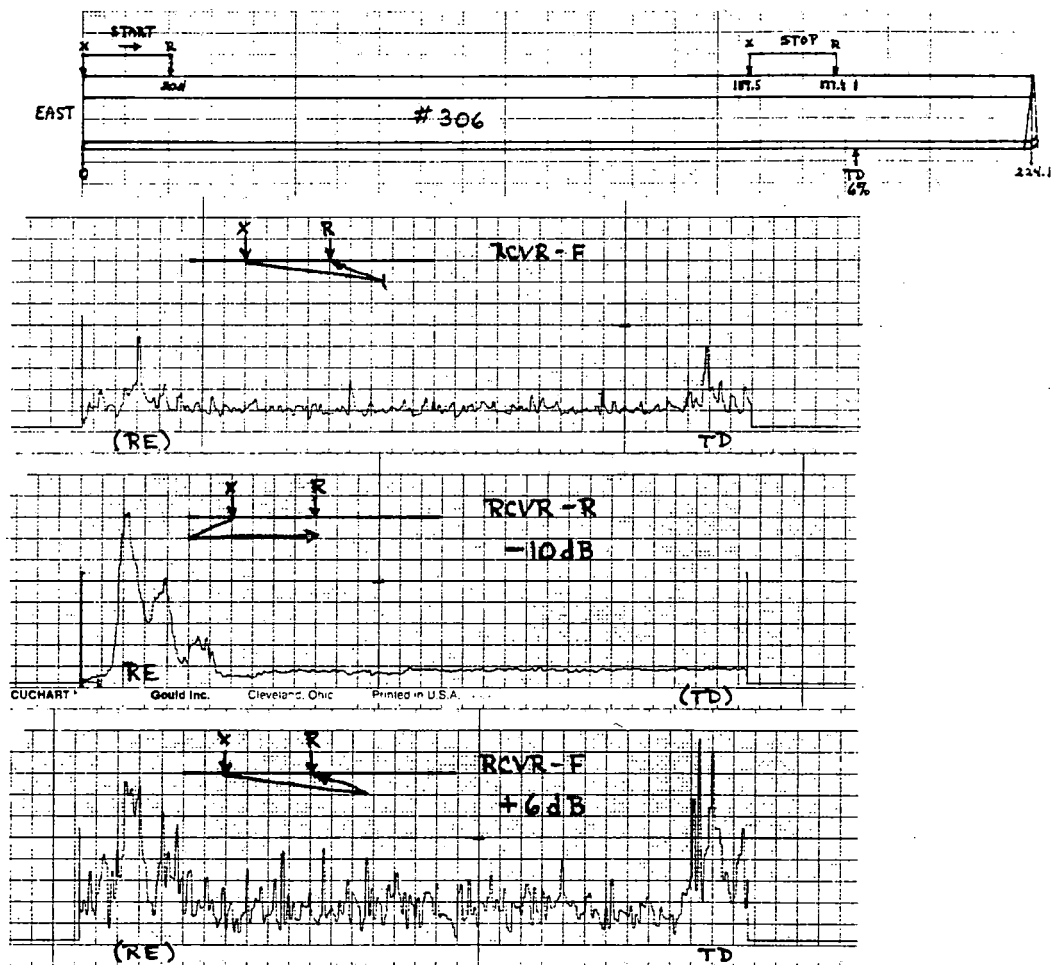
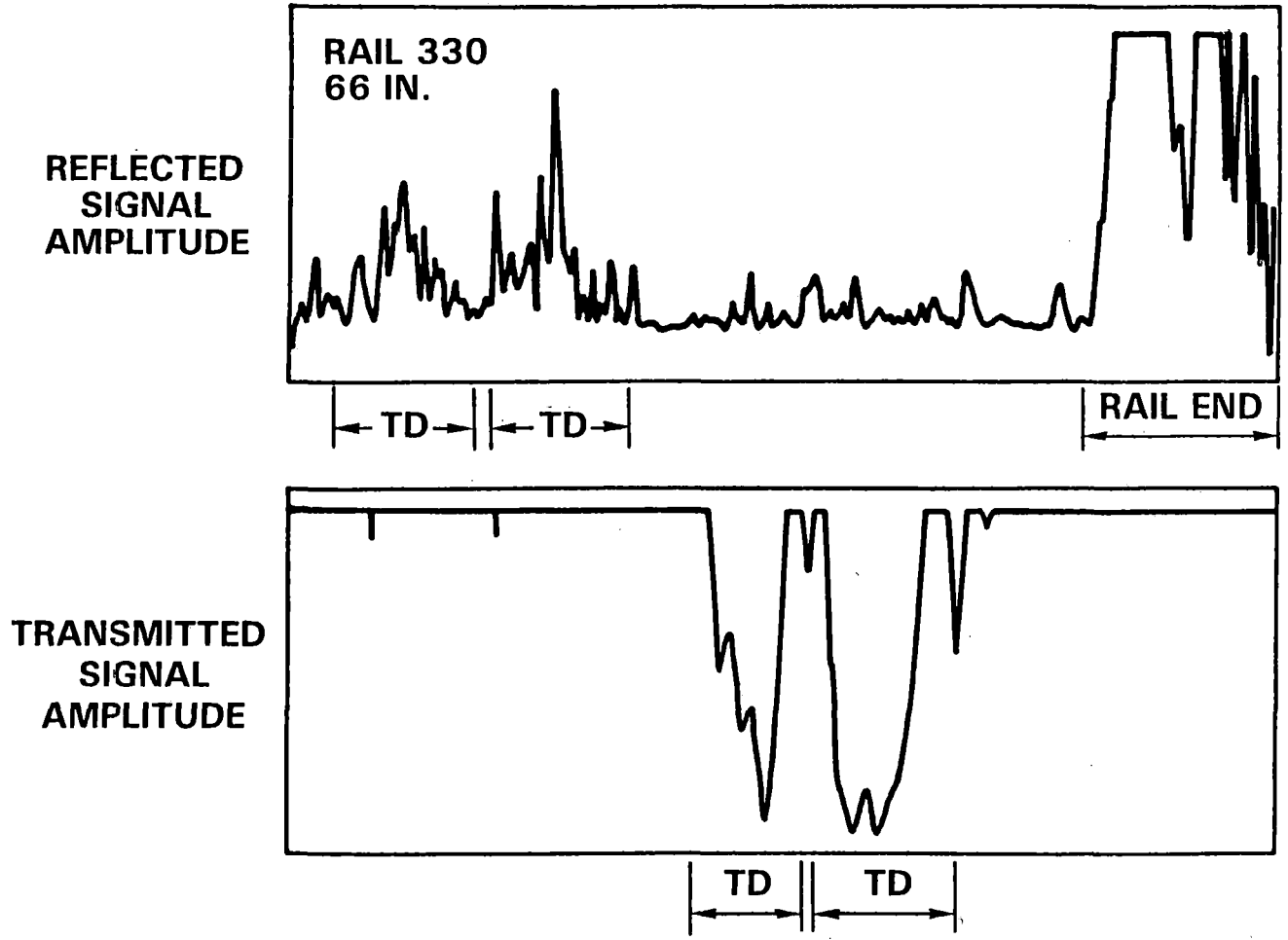


Figure C-5. Lab. Spec. #306 - 6% TDD.



C-12

Figure C-6. Lab. Spec. #330 - 11% and 37% DFs.

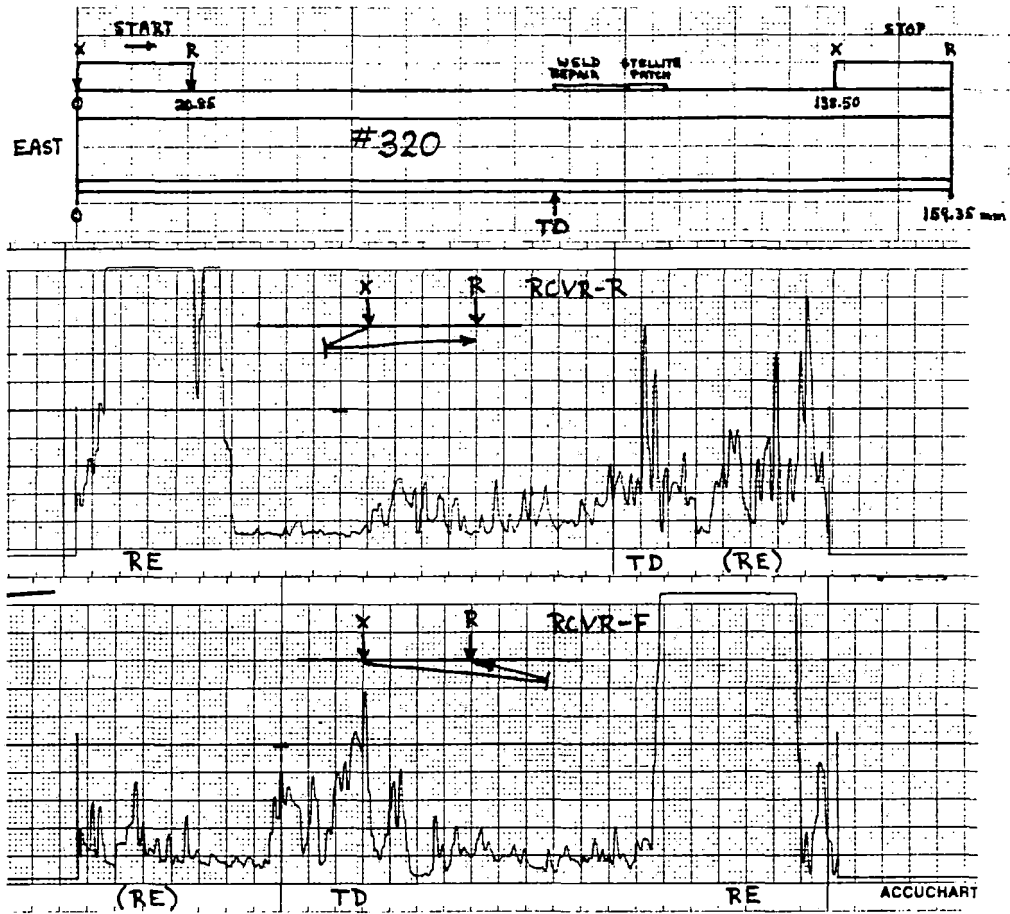


Figure C-7. Lab. Spec. #320 - 29% TD under a Stellite field weld patch.

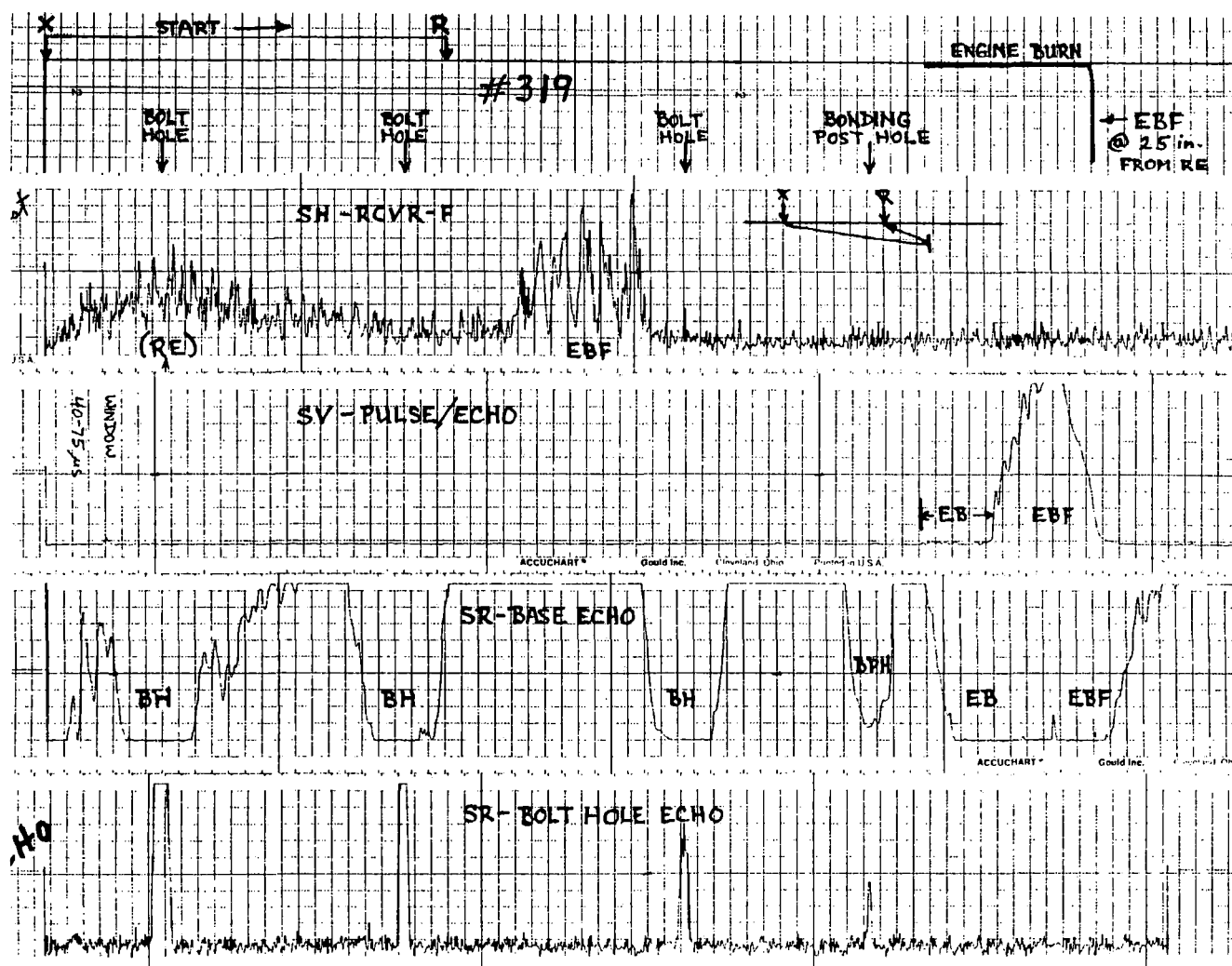


Figure C-8. Lab. Spec. #319 - 10% EBF.



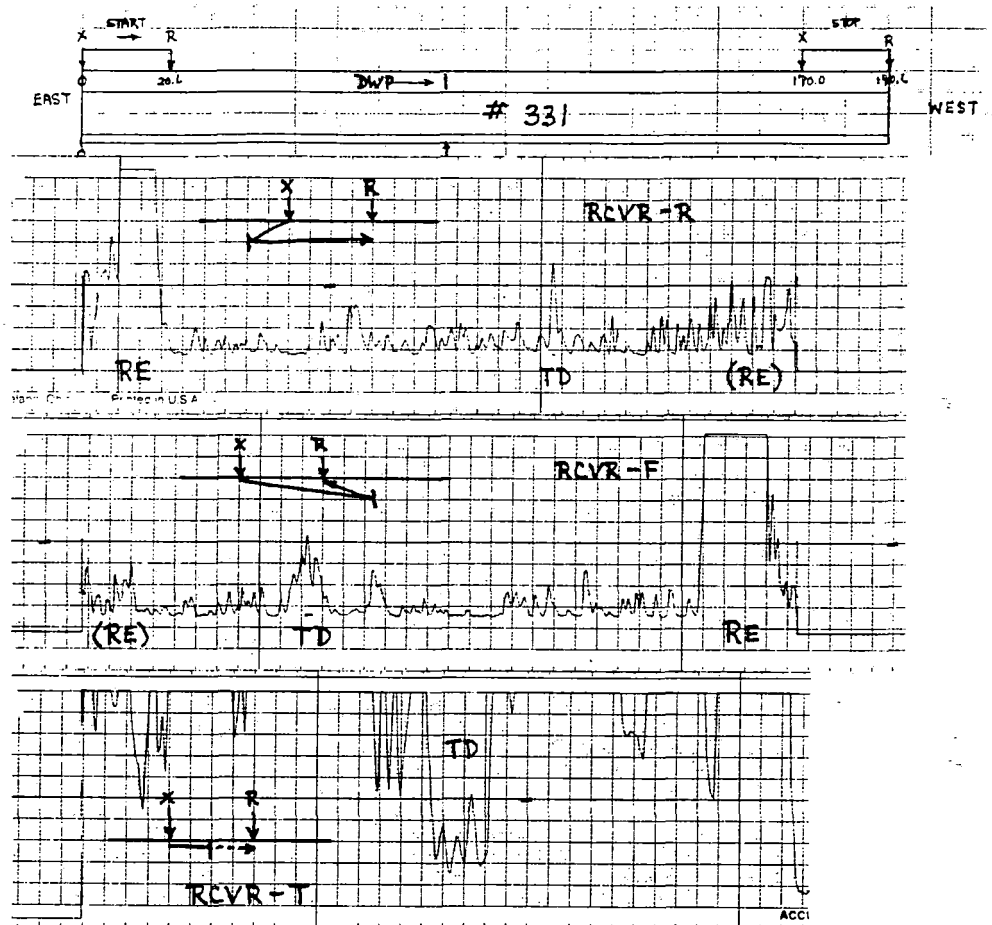


Figure C-9. Lab. Spec. #331 - 86% DWP.

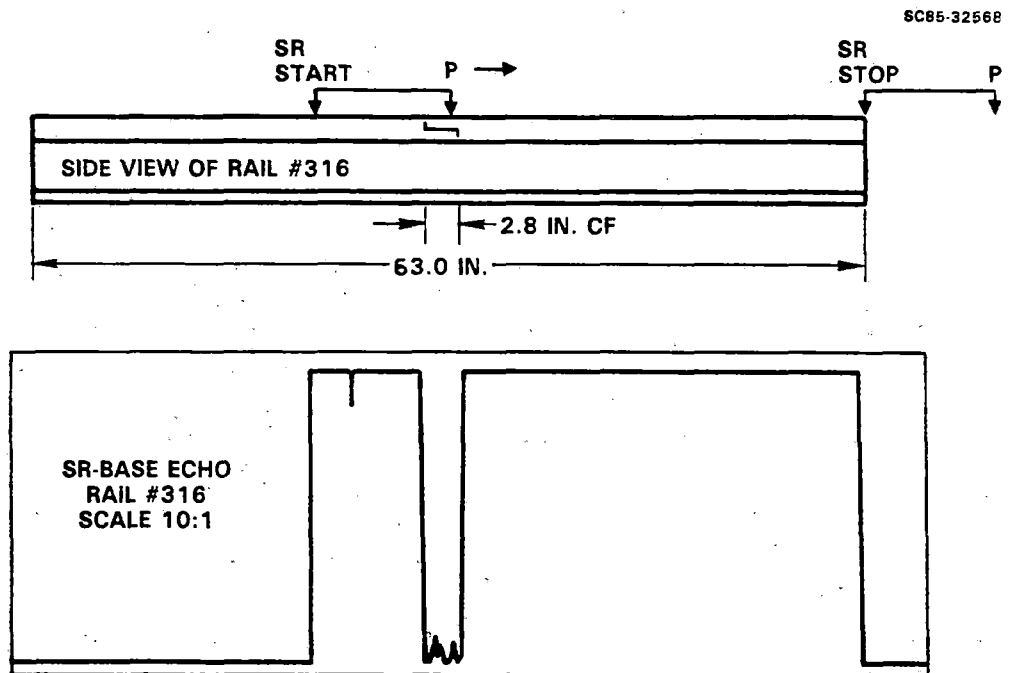


Figure C-10. Lab. Spec. #316 - 2.8 in. CF.

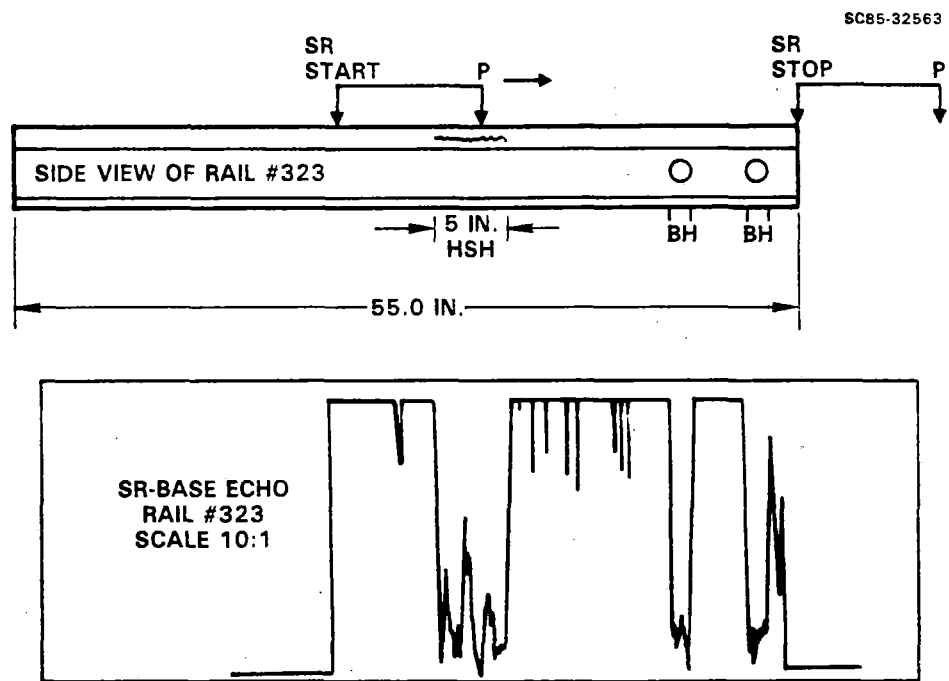


Figure C-11. Lab. Spec. #323 - 5 in. HSH.

TOP VIEW OF RAIL HEAD  
SHOWING POSITION OF VSH DEFECT  
IN RAIL #310

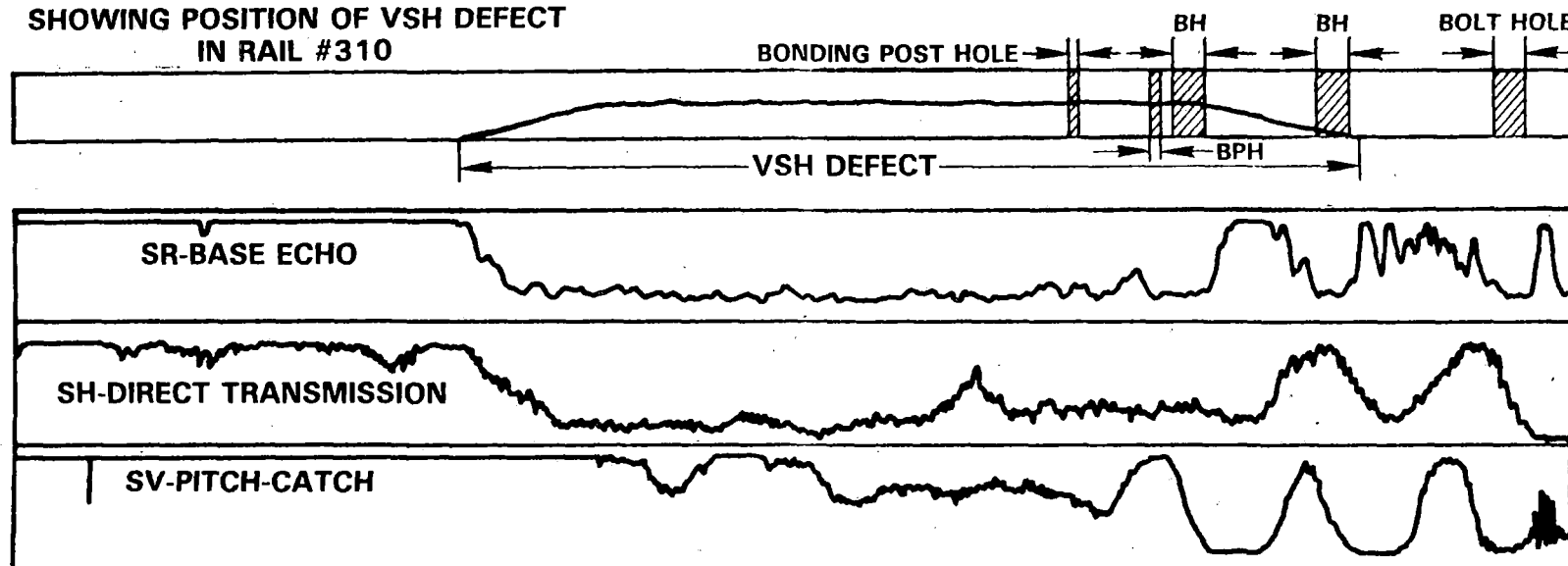


Figure C-12. Lab. Spec. #310 - detection of 38 in. VSH with SR, SH and SV EMATs.

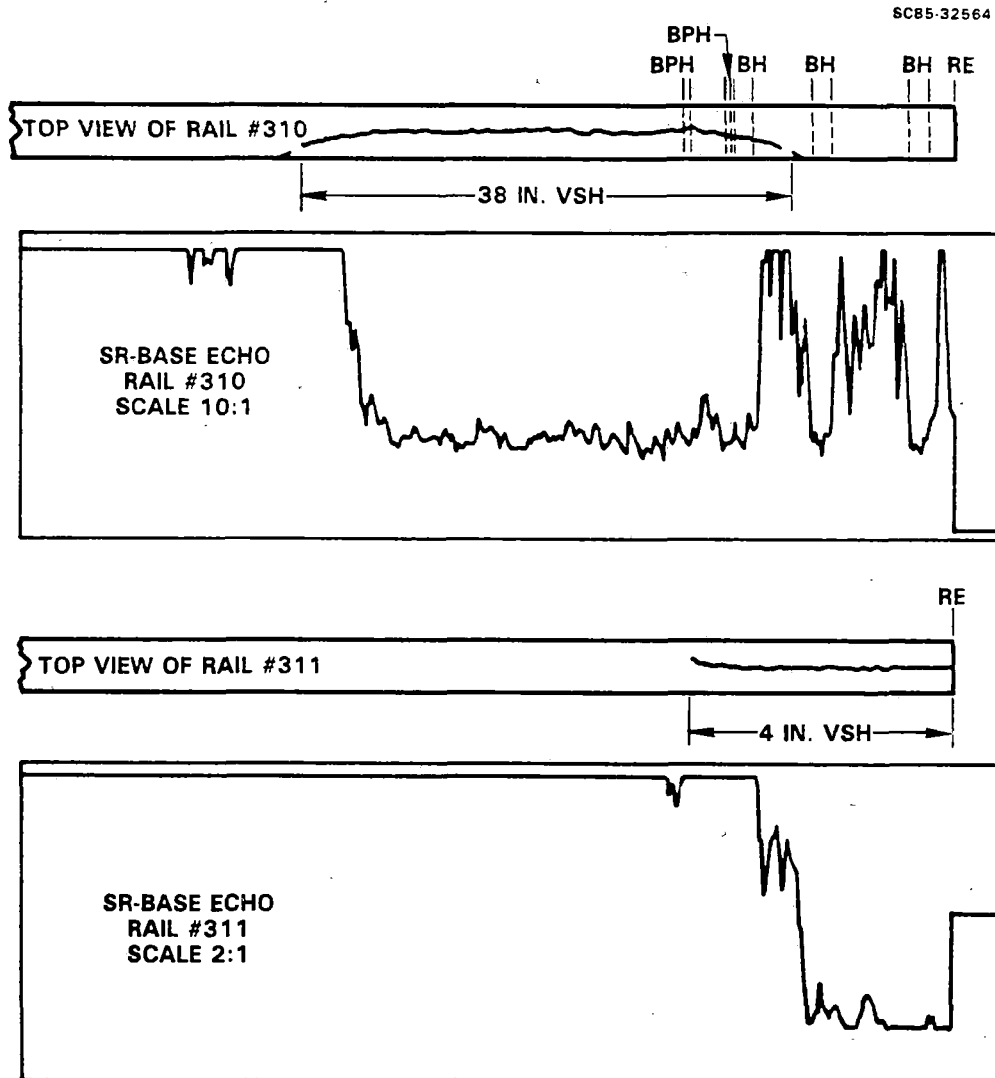


Figure C-13. Lab. Specs. #310 and #311 - 38 in. and 4 in. VSHs.

SCALE : 1 in. RAIL = 2.45 mm CHART RAIL # 334 66.8" LONG - 5.2" HIGH 8-26-83

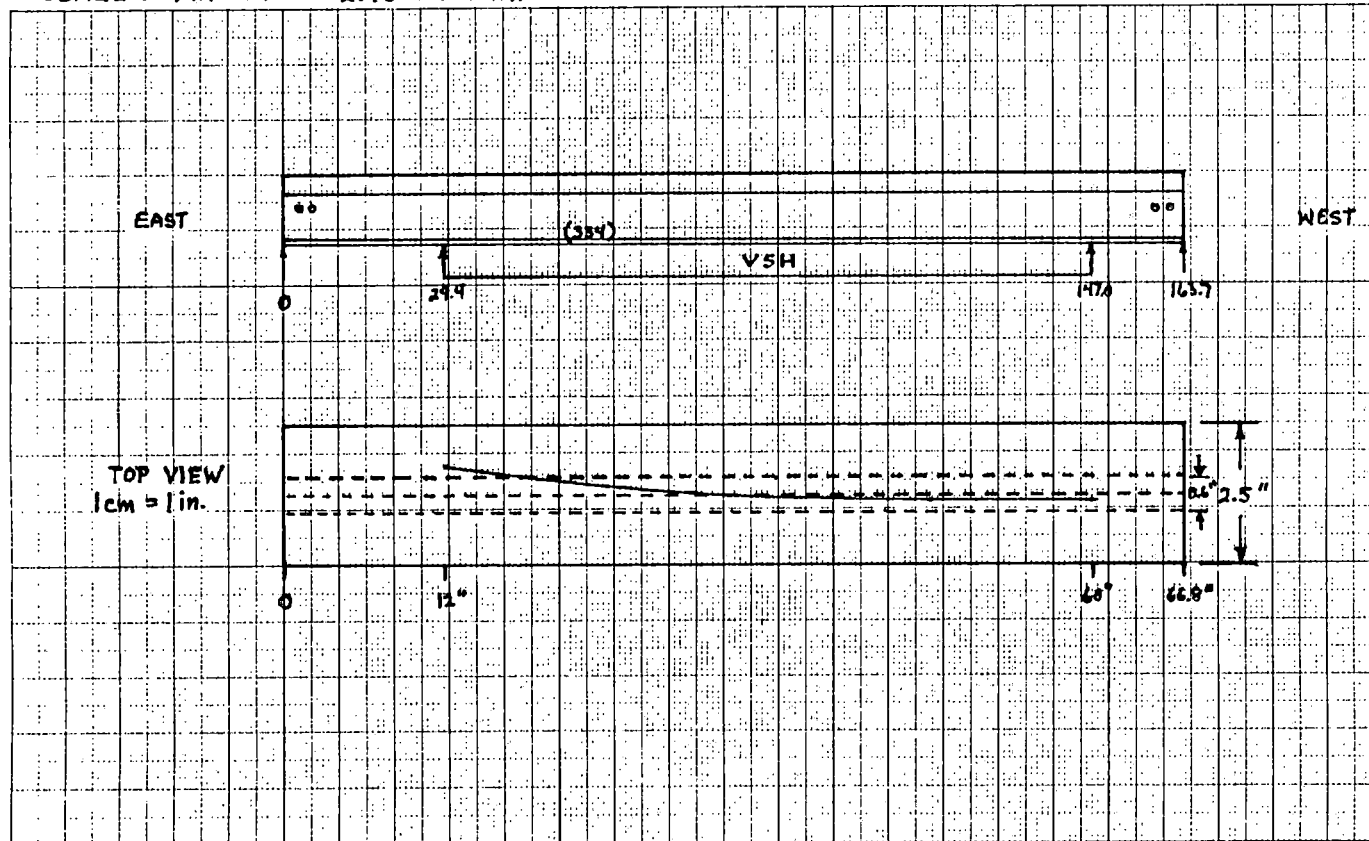


Figure C-14. Lab. Spec. #334 - 48 in. VSH defect (chart recording not available).

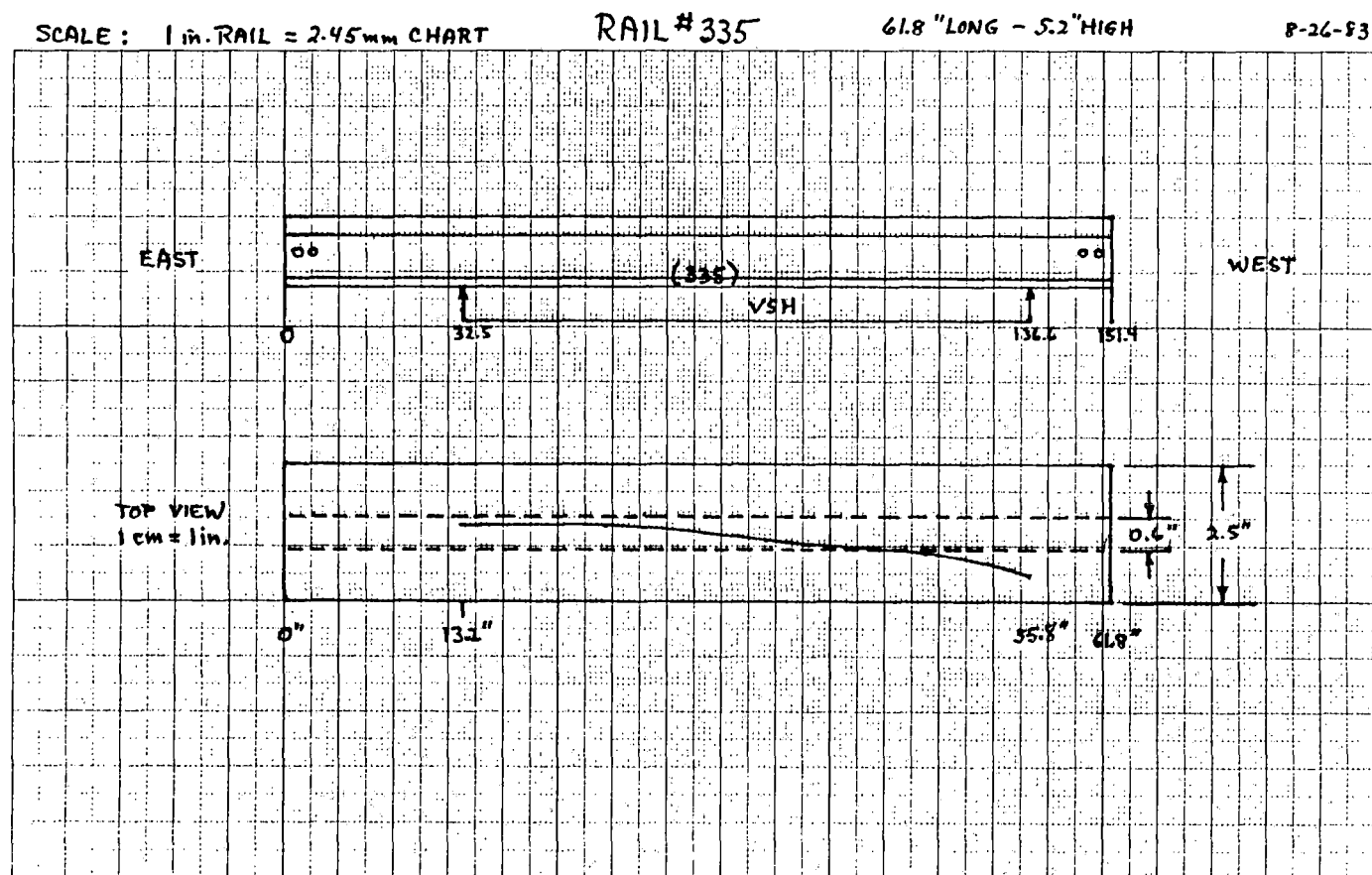


Figure C-15. Lab. Spec. #335 - 43 in. VSH defect (chart recording not available).

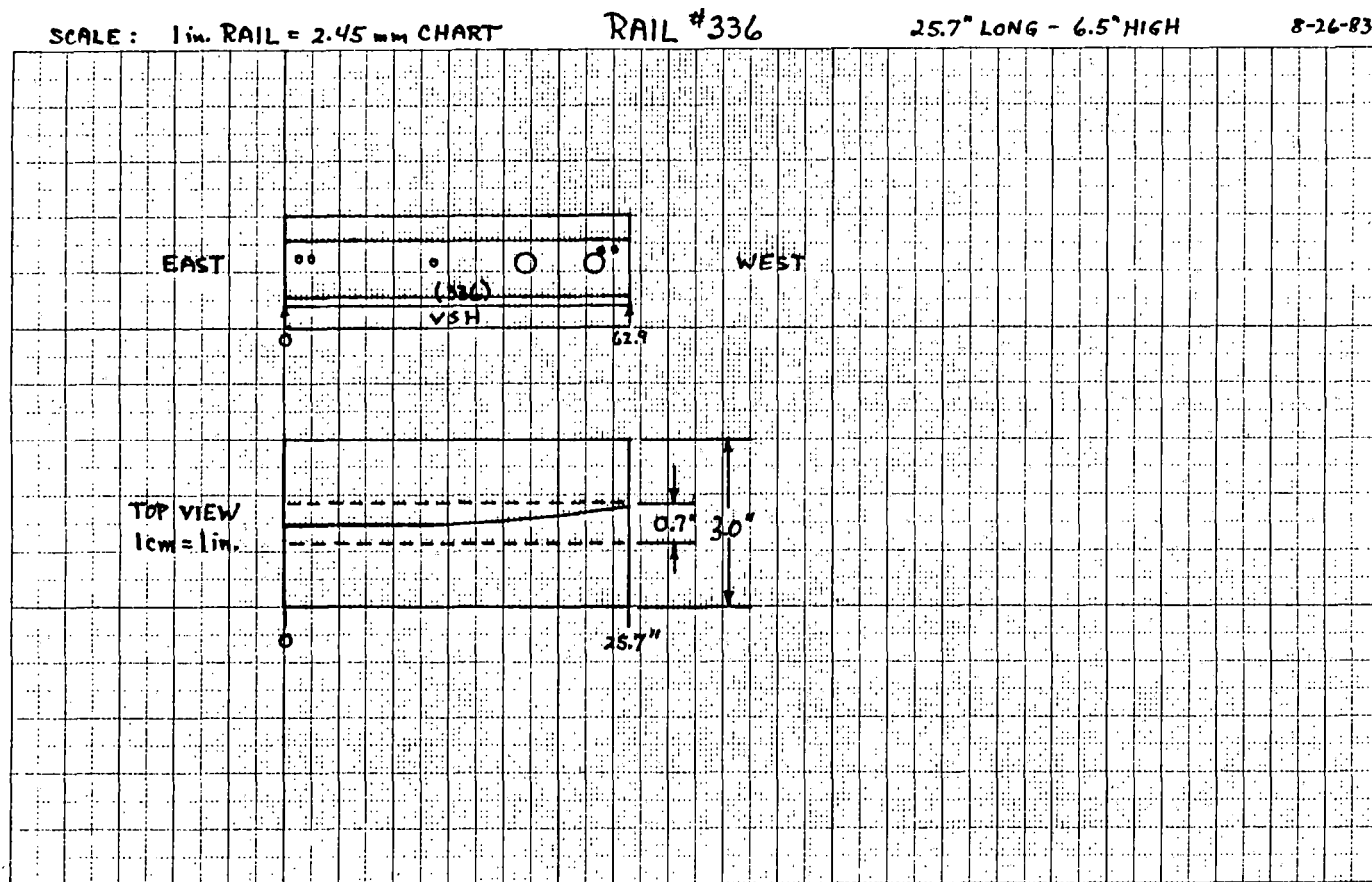


Figure C-16. Lab. Spec. #336 - 26 in. VSH defect (chart recording not available).



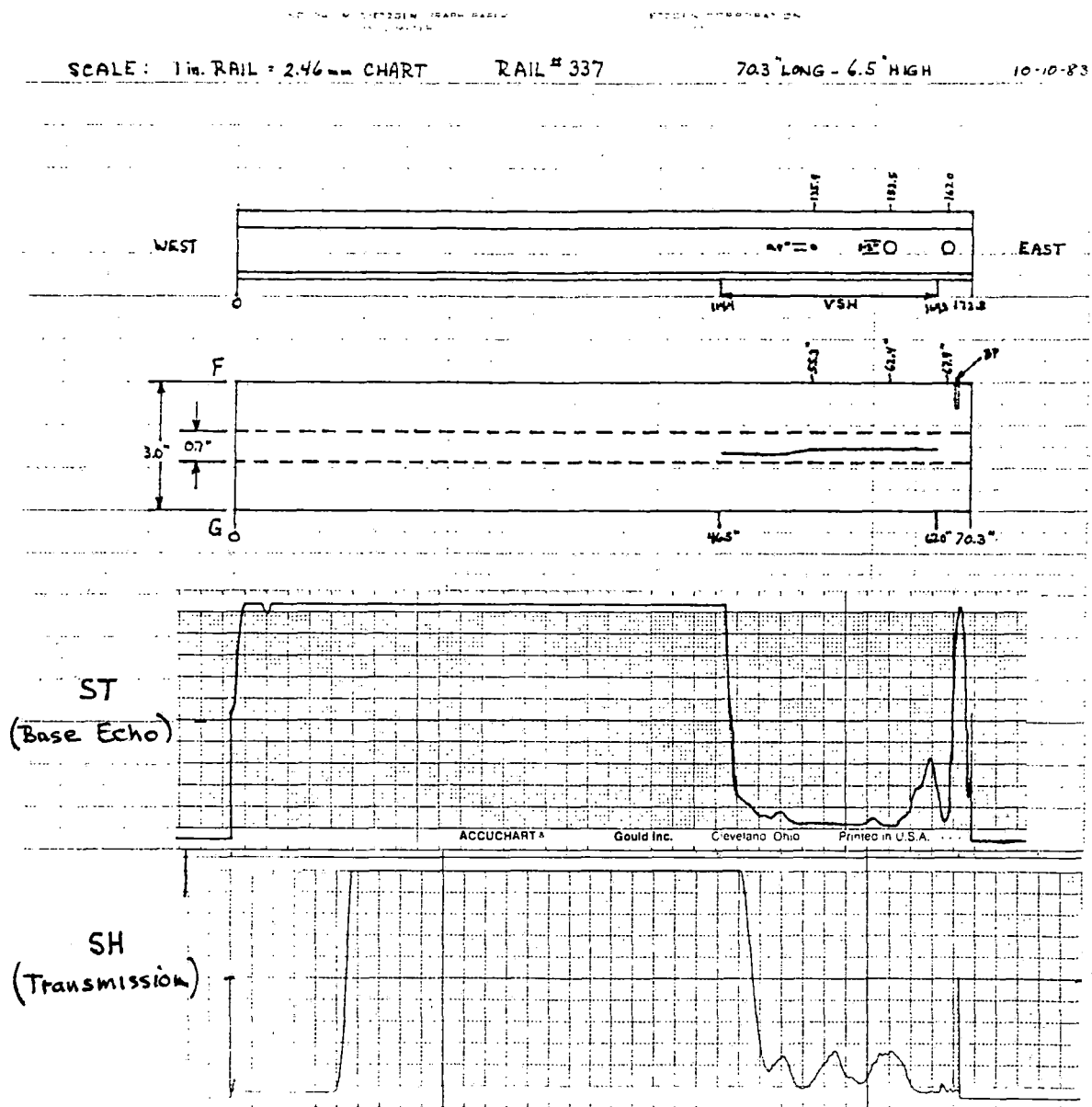


Figure C-17. Lab. Spec. #337 - 21 in. VSH defect.

SCALE: 1 in. RAIL = 2.46 in. CHART

RAIL #338

80.1" LONG - 6.5" HIGH

10-10-83

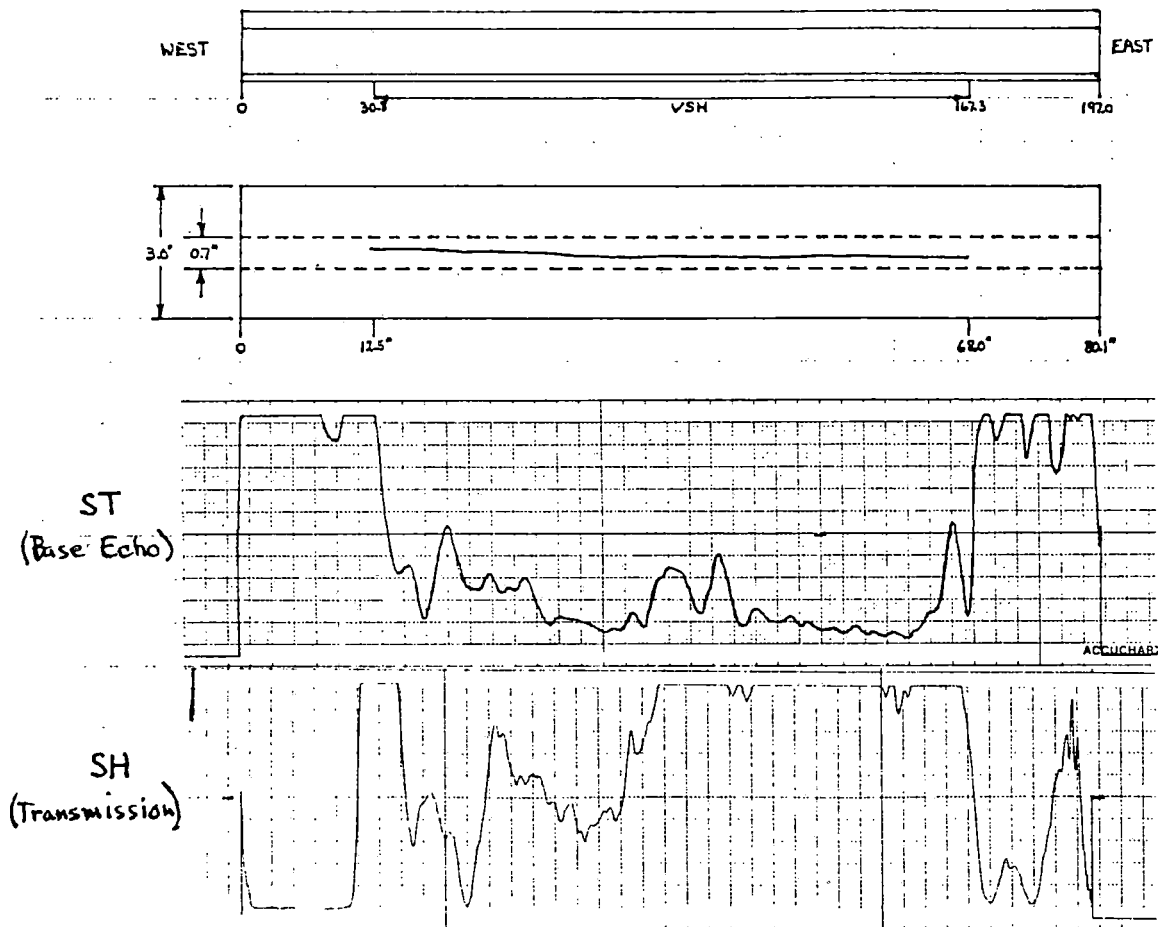


Figure C-18. Lab. Spec. #338 - 56 in. VSH defect.

NO. 34 M. C. DETZEN RAIL FILER DETZEN CORPORATION  
 SCALE: 1 in. RAIL = 2.46 in. CHART RAIL #339 65.3" LONG - 6.5" HIGH 10-10-83

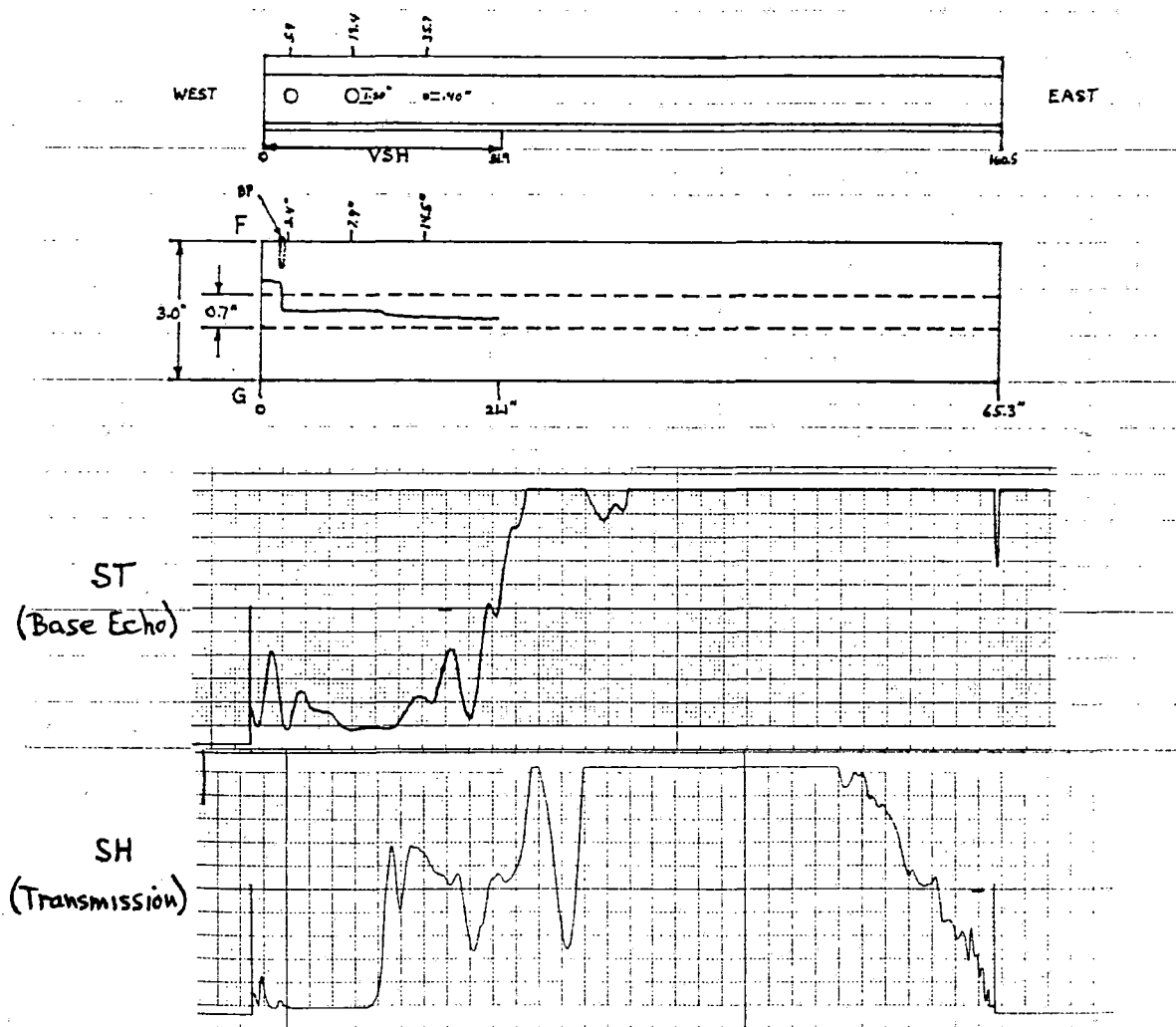


Figure C-19. Lab. Spec. #339 - 21 in. VSH defect.

SCALE: 1 in. RAIL = 2.46 in. CHART

RAIL #340

69.9" LONG - 6.5" HIGH

10-10-83

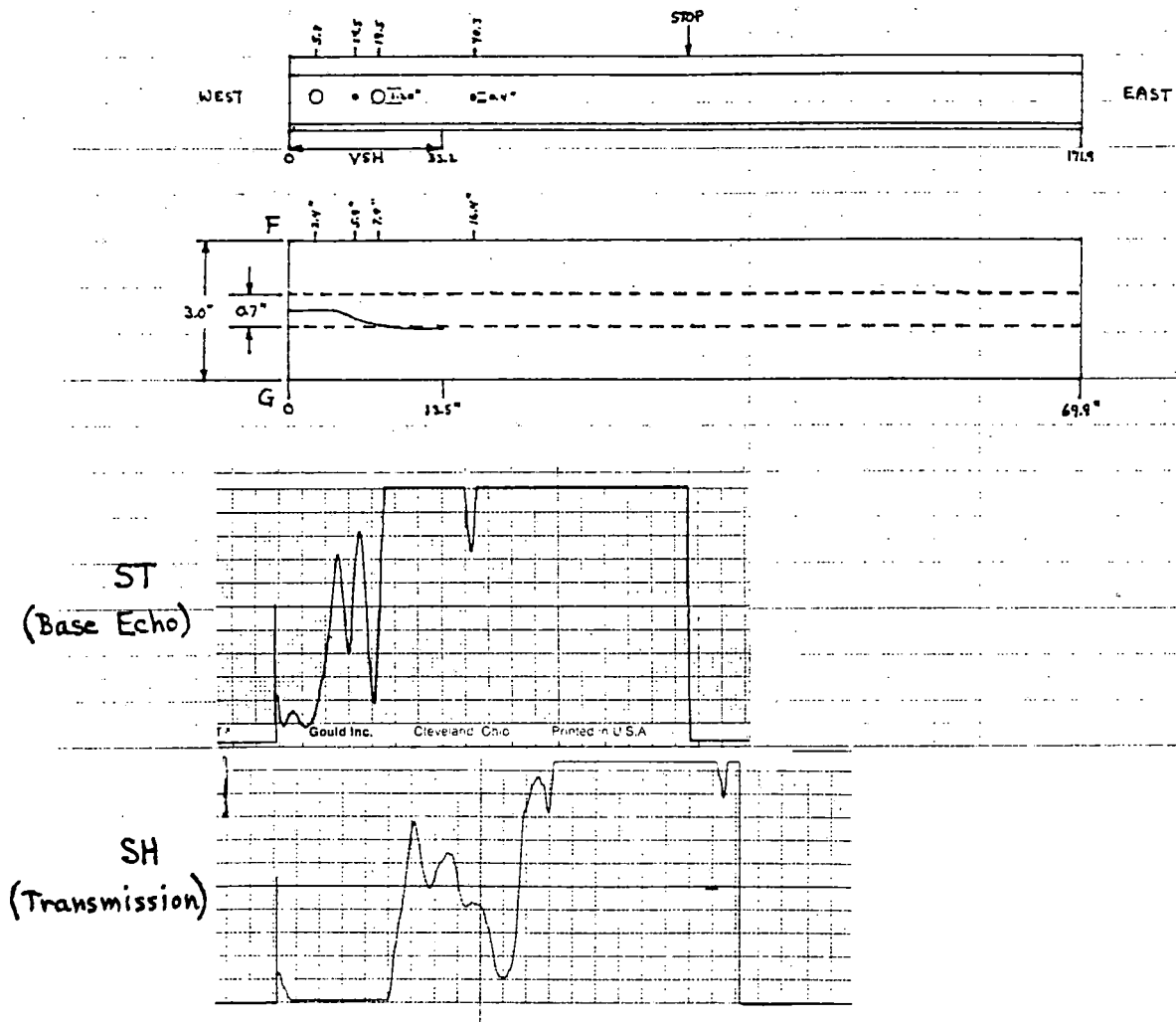


Figure C-20. Lab. Spec. #340 - 14 in. VSH defect.

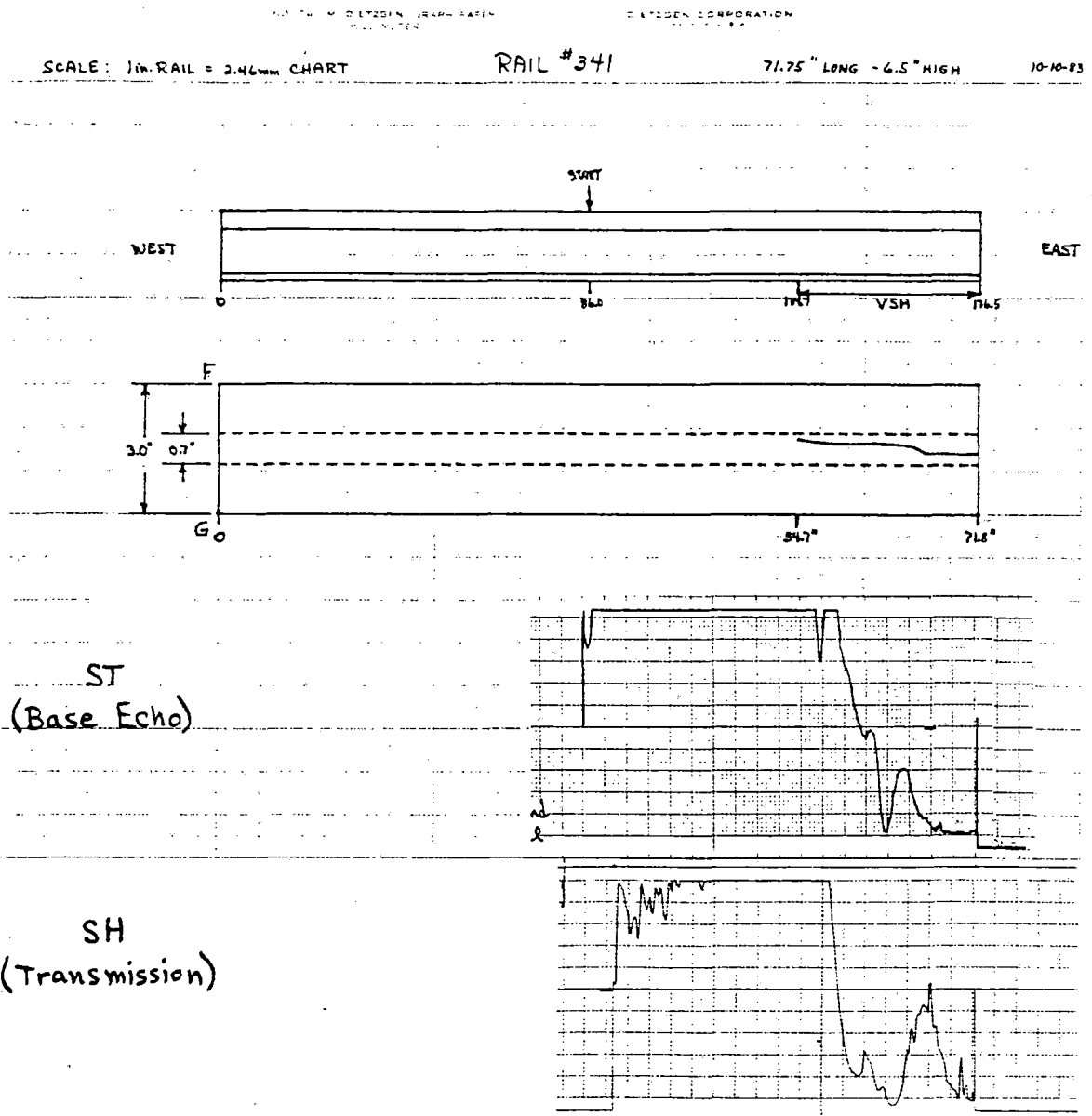


Figure C-21. Lab. Spec. #341 - 17 in. VSH defect.

SCALE: 1 in. RAIL = 2.46 in. CHART

RAIL # 342

76.6" LONG - 6.5" HIGH

10-10-73

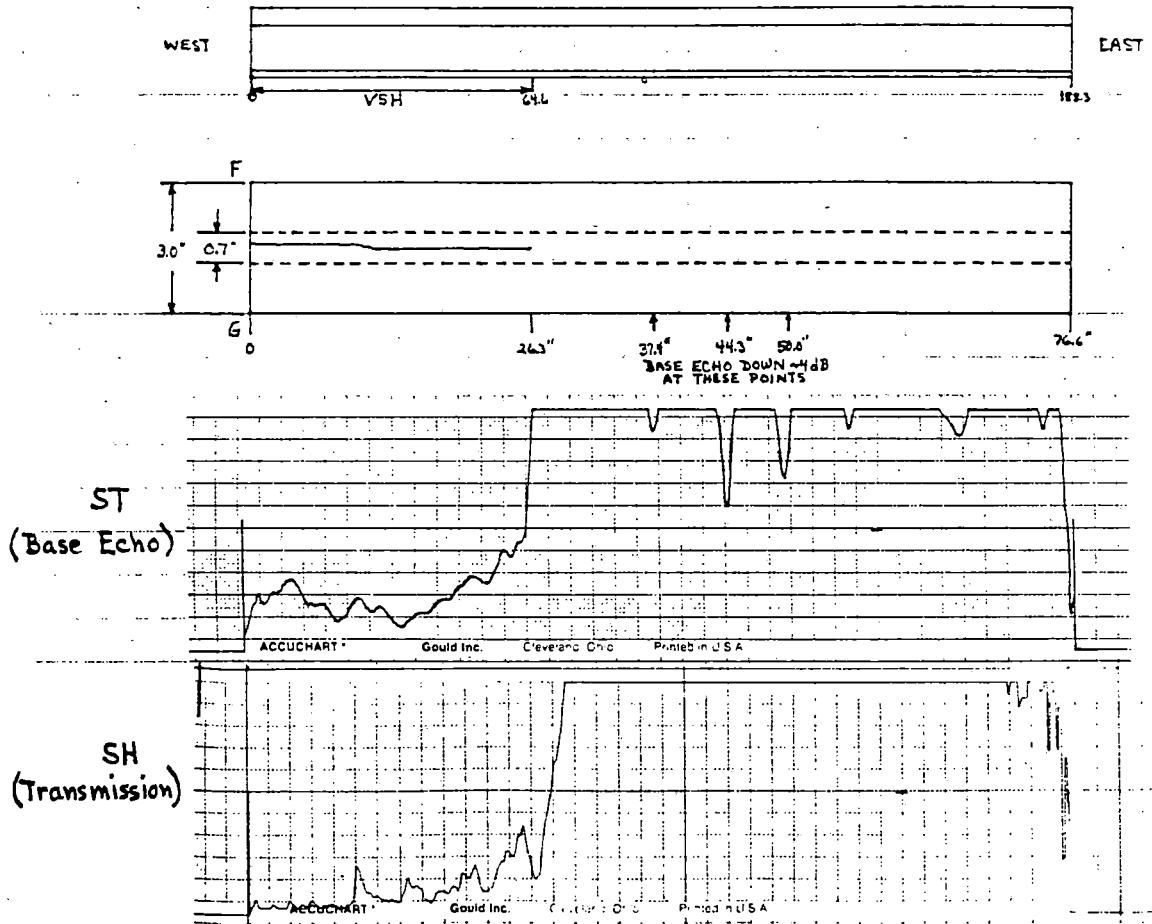


Figure C-22. Lab. Spec. #342 - 26 in. VSH defect.

SC85-32570

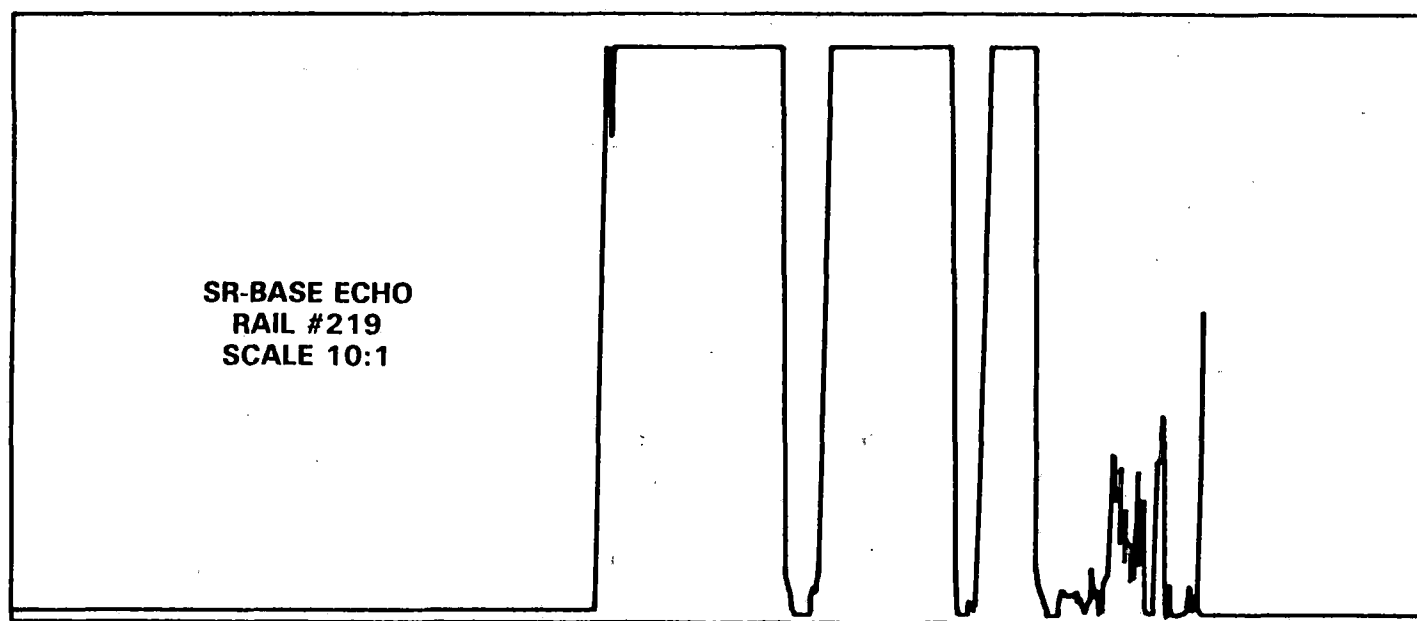
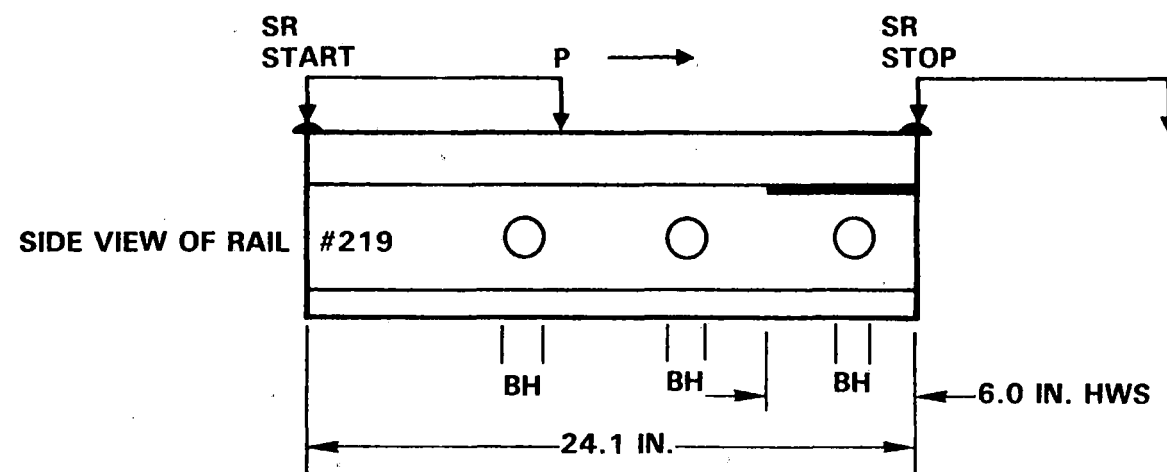


Figure C-23. Lab. Spec. #219 - 5 in. HWS defect.

SC83-21058

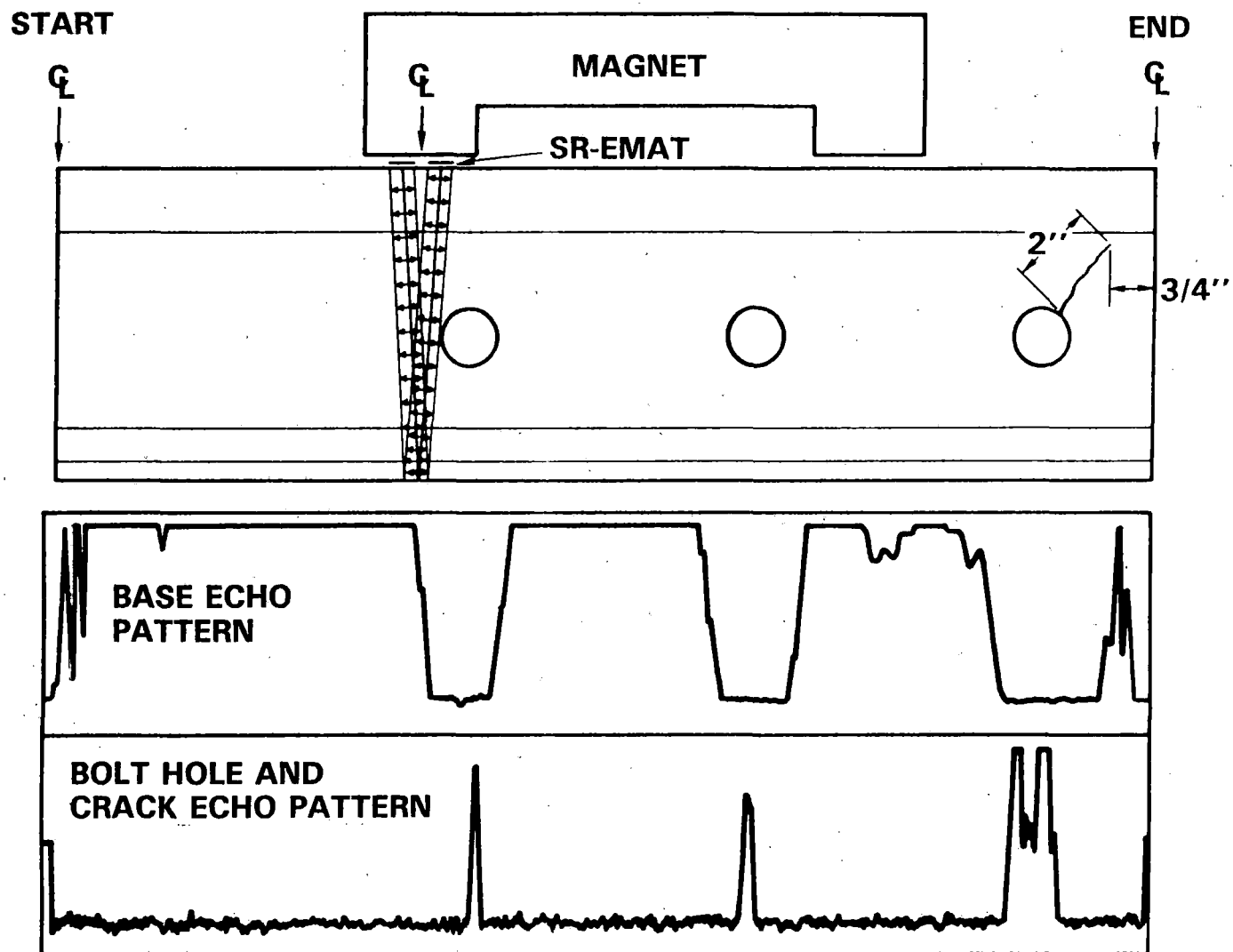


Figure C-24. Lab. Spec. #32 - 2 in. BHC defect.



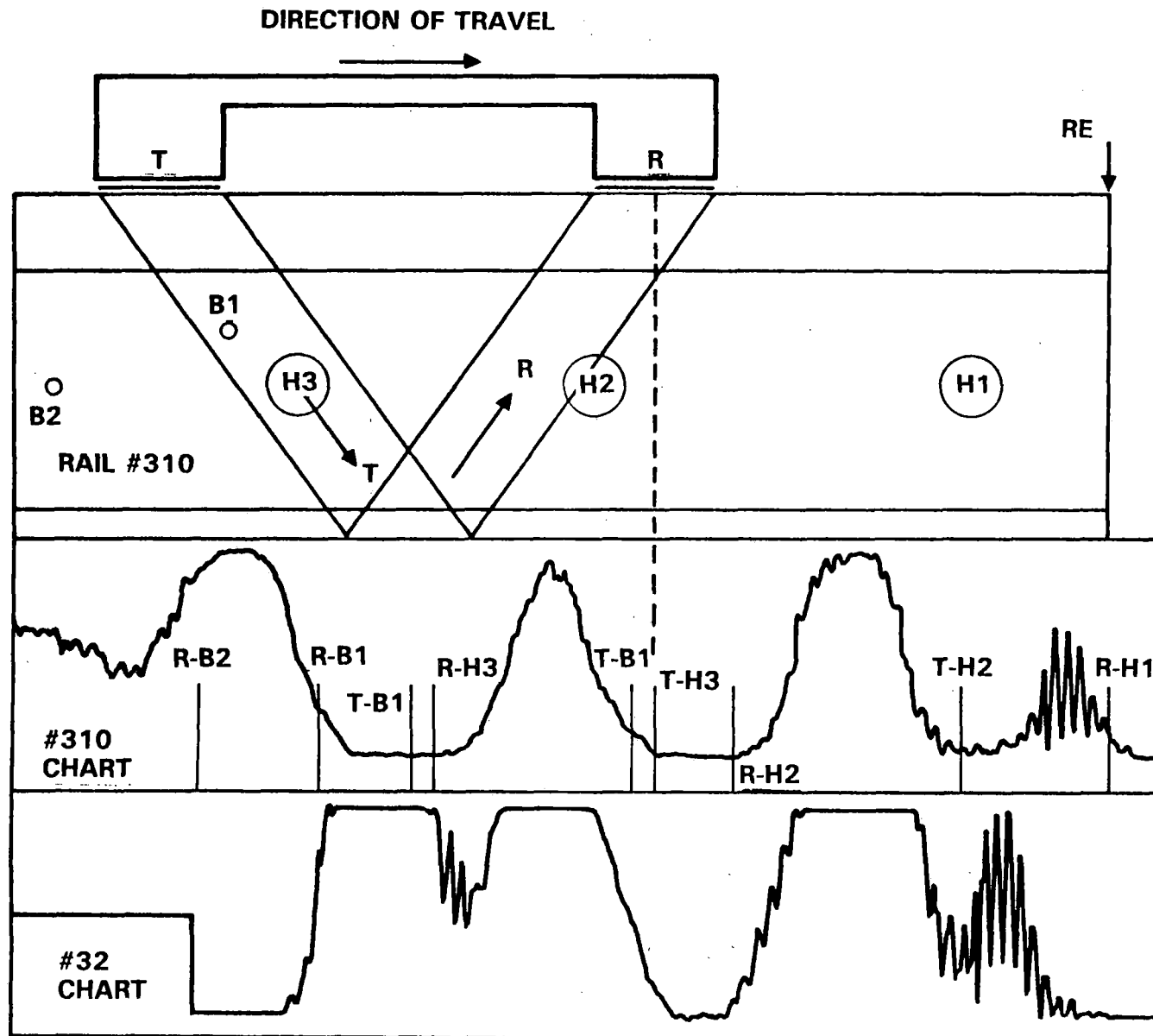


Figure C-25. Lab. Specs. #32 and #310 - SV-EMAT pitch-catch patterns at bolt holes.

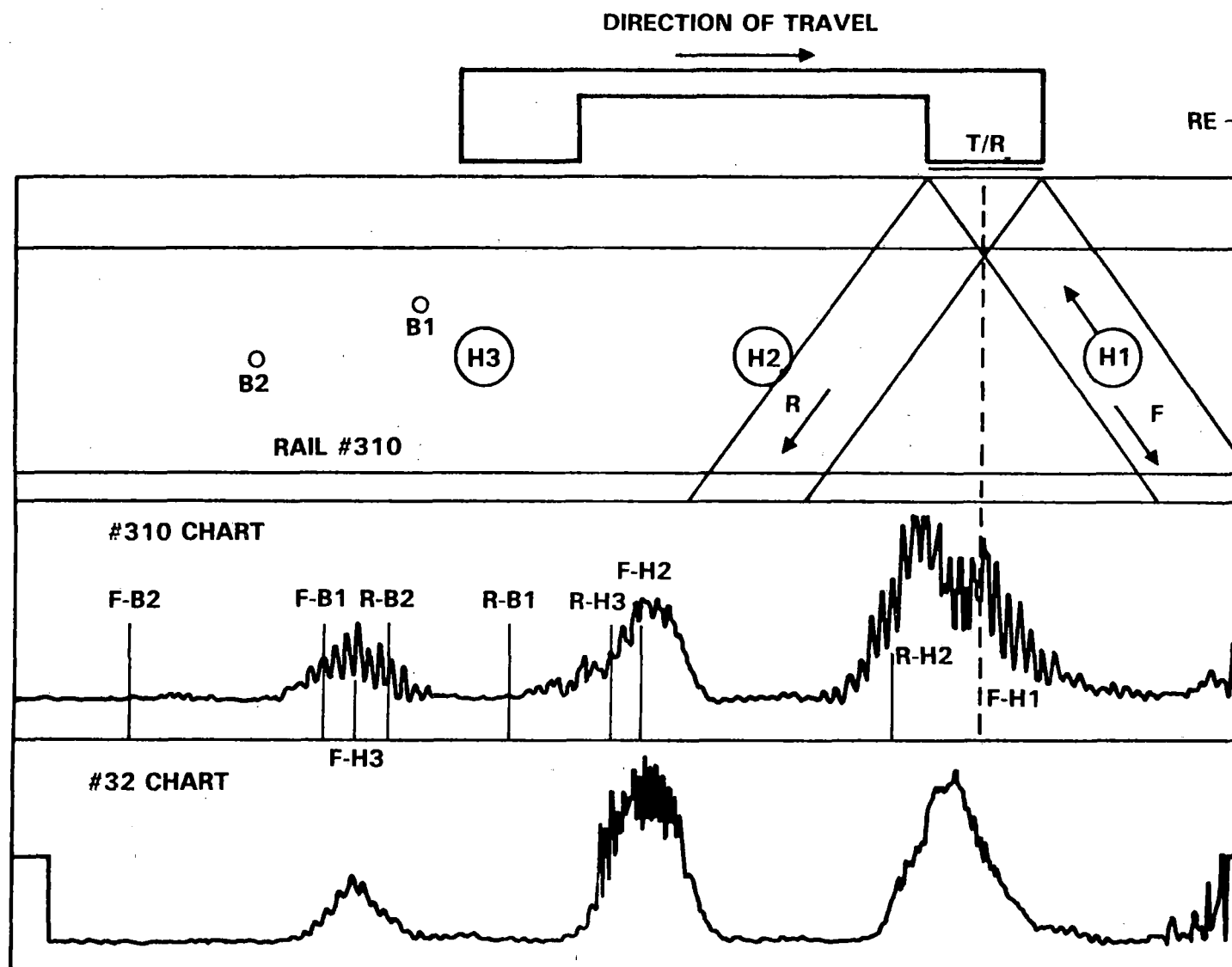


Figure C-26. Lab. Specs. #32 and #310 - SV-EMAT pulse echo patterns at bolt holes.

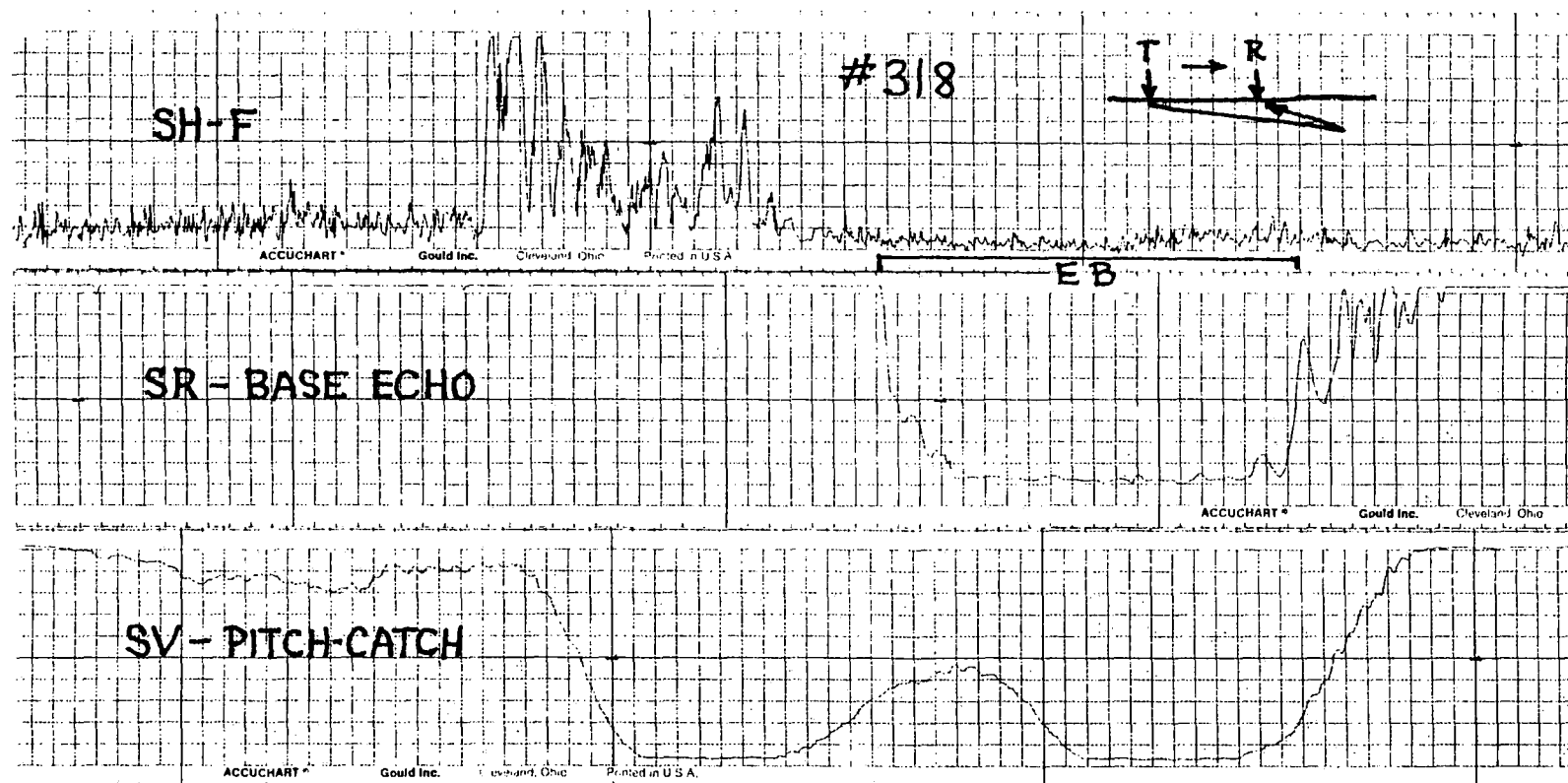


Figure C-27. Lab. Spec. #318 - SH, SR and SV EMAT signals at EB.

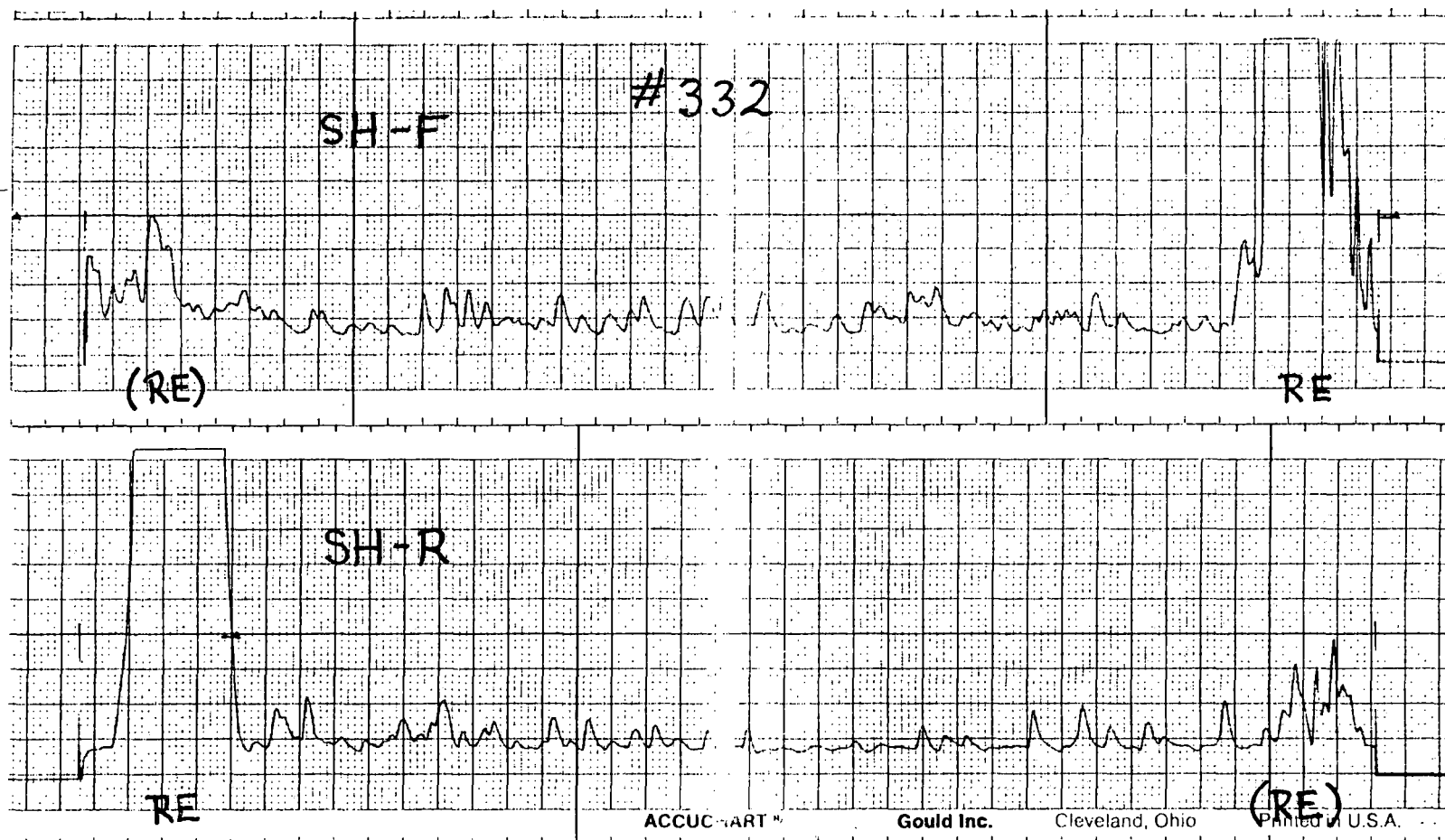


Figure C-28. Lab. Spec. #332 - shelly rail.

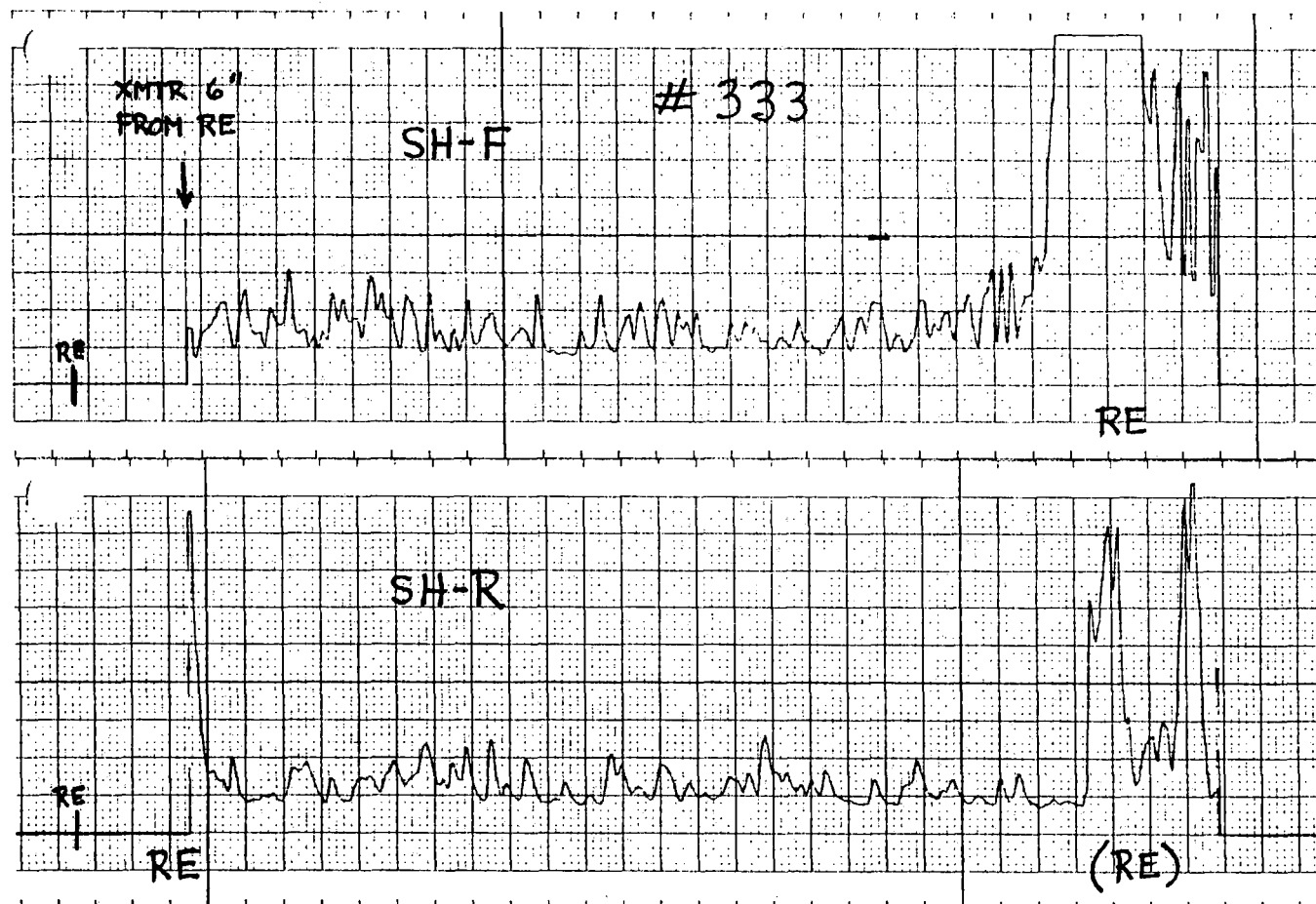


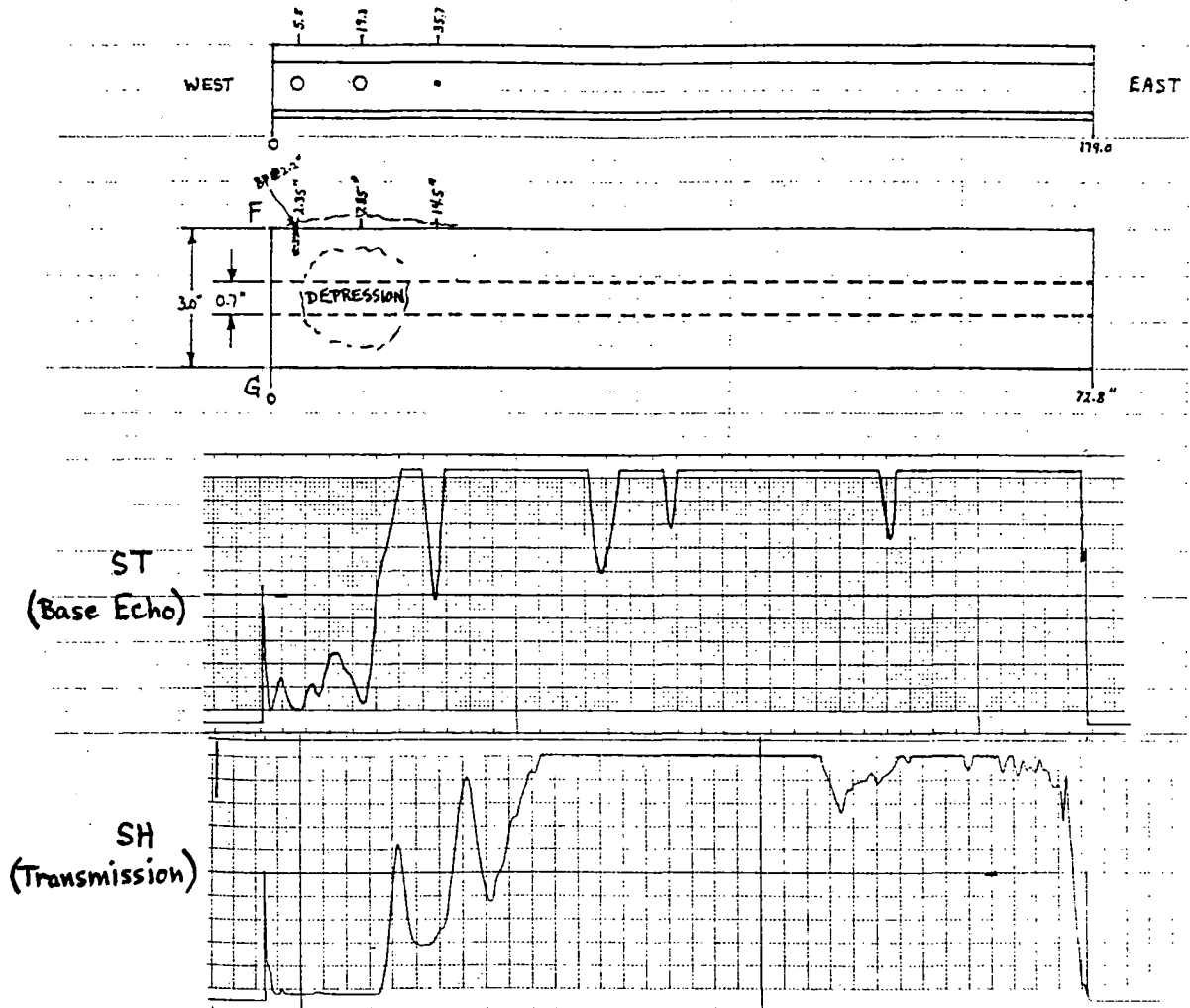
Figure C-29. Lab. Spec. #333 - shelly rail.

SCALE: 1 in. RAIL = 2.46 mm CHART

RAIL # 343

72.8" LONG - 6.5" HIGH

10-10-83



Note: This was labelled as a VSH but was not - instead it had an ~ 8 in. long region on top of the head that was depressed and rough (weld repair? , EB?).

Figure C-30. Lab. Spec. #343 - crushed head.

TABLE C-2. DEFECTS IN EAST RAIL OF SANTA FE TEST TRACK

Rail No.	Position (in. from North end)	Description
1E†	242.5 244.3	* 3/8 in. hole drilled thru web at ~ 1/2 height * 3/8 in. hole drilled thru web at ~ 1/2 height
2E	211.0 213.0	* 3/8 in. hole drilled thru web at ~ 1/2 height * 3/8 in. hole drilled thru web at ~ 1/2 height
3E†	317.3 362.6 405.0-458.4	TD, small TD, small? * VSH, 53 in. long
4E	211.4 212.8	* 3/8 in. hole drilled thru web at ~ 1/2 height * 3/8 in. hole drilled thru web at ~ 1/2 height
5E	260.8	* Corner saw cut ~ 1/4 in. deep, bottom corner, G
6E	42.5	* Corner saw cut ~ 1/4 in. deep, bottom corner, G
7E	196.8 199.5	* Bonding post hole * Bonding post hole
8E	11.5 13.2	TD, small TD, small
9E†	14.4 22.0 23.3 51.0 55.0	TD, large TD, small TD, small TD, large TD, medium
10E†	127.0 191.9-234.4	TD, small? * VSH, 42 in. long
11E†	24.0 207.5	TD, large TD, small
12E	301.6	TD, small?

\* Marked by Santa Fe or artificial flaw

† Indicates that strip chart recordings are included in this Appendix.

NOTE: G designates the gauge side of the railhead and F the field side

TABLE C-3. DEFECTS IN WEST RAIL OF SANTA FE TEST TRACK

Rail No.	Position (in. from South end)	Description
1W	---	-----
2W	61.0 333.0	TD, small TD, medium (possibly EBF)
3W†	161.6 199.8 218.1	TD, small TD, small * TD, large
4W†	85.7 156.4 265.4	* TD, large, surface emerging on F * TD, small * TD, large, surface emerging on F
5W†	202.3 349.5	TD, large * TD, large, surface emerging on G
6W	41.8	* Corner saw cut 1/4 in. deep, bottom corner G
7W†	267.5	* Side saw cut 1/4 in. deep, vertical on F
8W	---	---
9W	126.0 188.5 198.0 241.1	TD, small TD, small, deep in head Shell? 1/2 in. longitudinal crack 0.6 in. from G TD, medium
10W	235.0 243.0 331.5 329.0	* 1 in. bolt hole through web * 1 in. bolt hole through web * 1 in. bolt hole through web * 1 in. bolt hole through web
11W†	316.3 329.4-334.0	TD, medium VSH, 5 in. long

\* Marked by Santa Fe or artificial flaw

† Indicates that strip chart recordings are included in this Appendix.

NOTE: G designates the gauge side of the railhead and F the field side



Figure C-31. Illustrations of anomalous ST-base echo behavior at tie plates and angle bars and limited resolution of small holes drilled through the rail web.

Figure C-32. Detection of VSH defect in #3E with ST- and SH-EMATs compared to hand-mapping result. Evidence of two small TDs in SH-trace confirmed by hand-scanning.

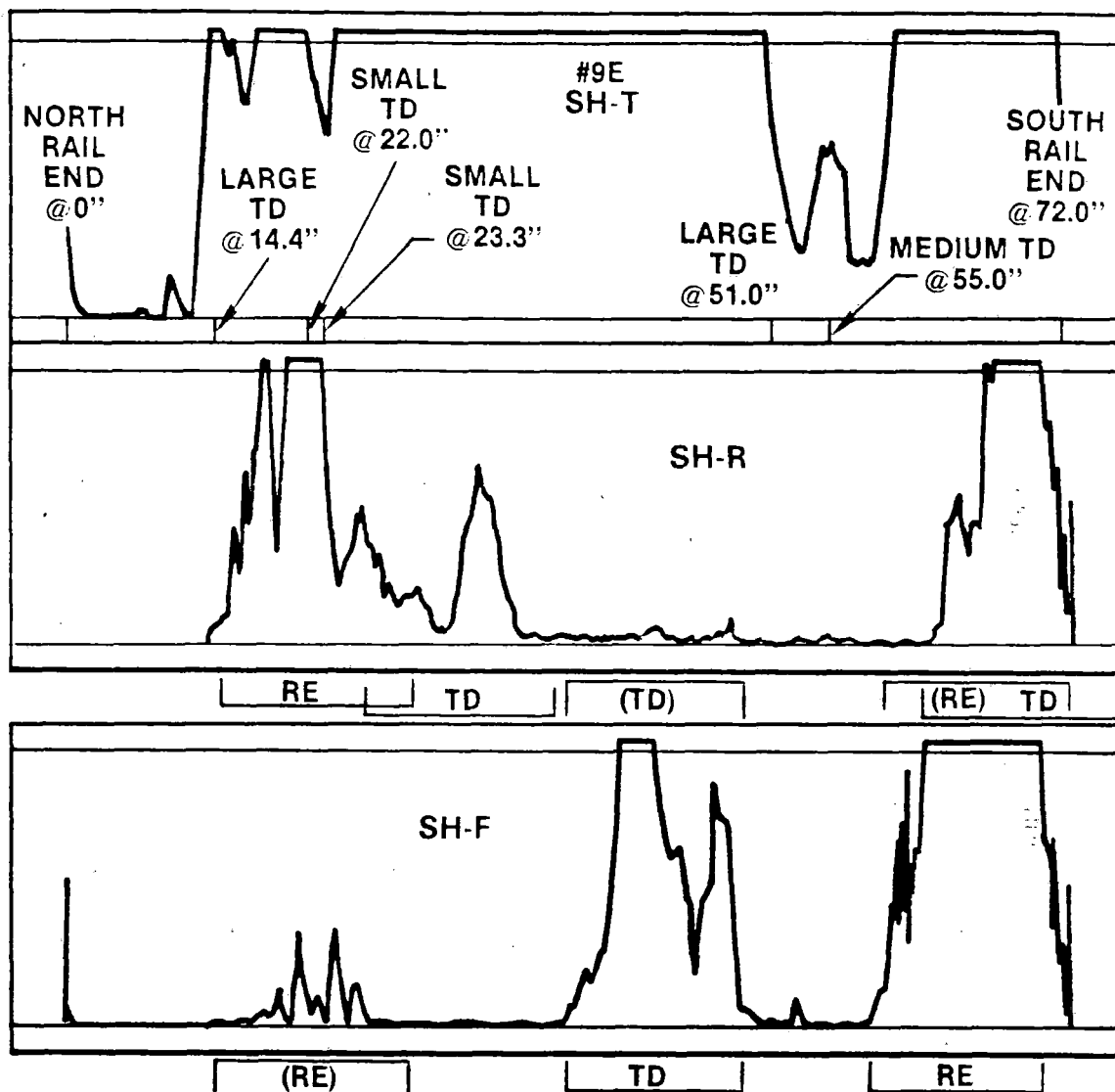


Figure C-33. Three modes of detection of large TDs with SH-EMAT in #9E.

Figure C-34. Detection of small TD in #10E with SH-EMAT.

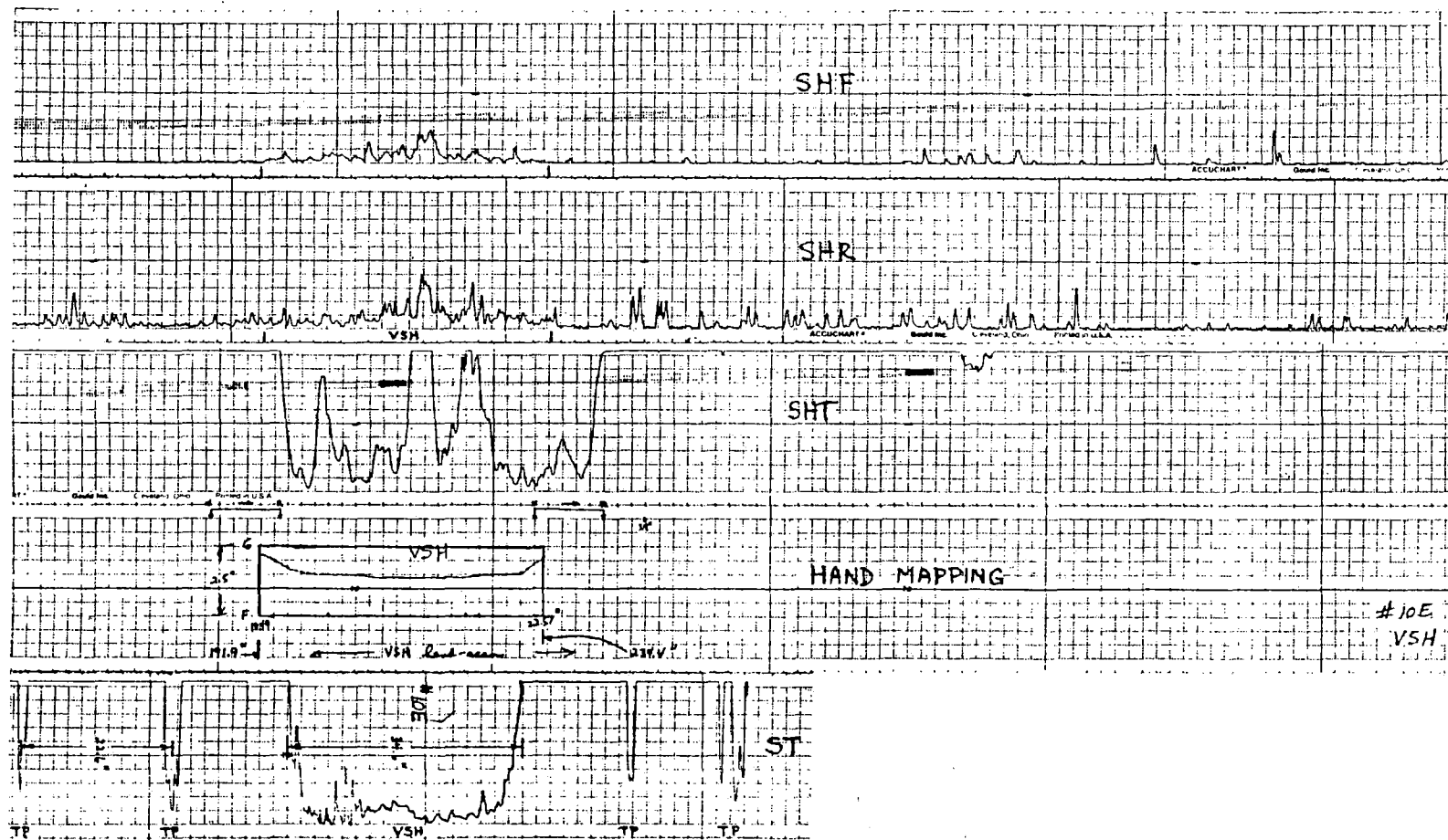


Figure C-35. Detection of VSH defect in #10E with ST- and SH-EMATs compared to hand-mapping results. Scattering of SH-wave from defect also seen in reflection modes at the top of the figure.

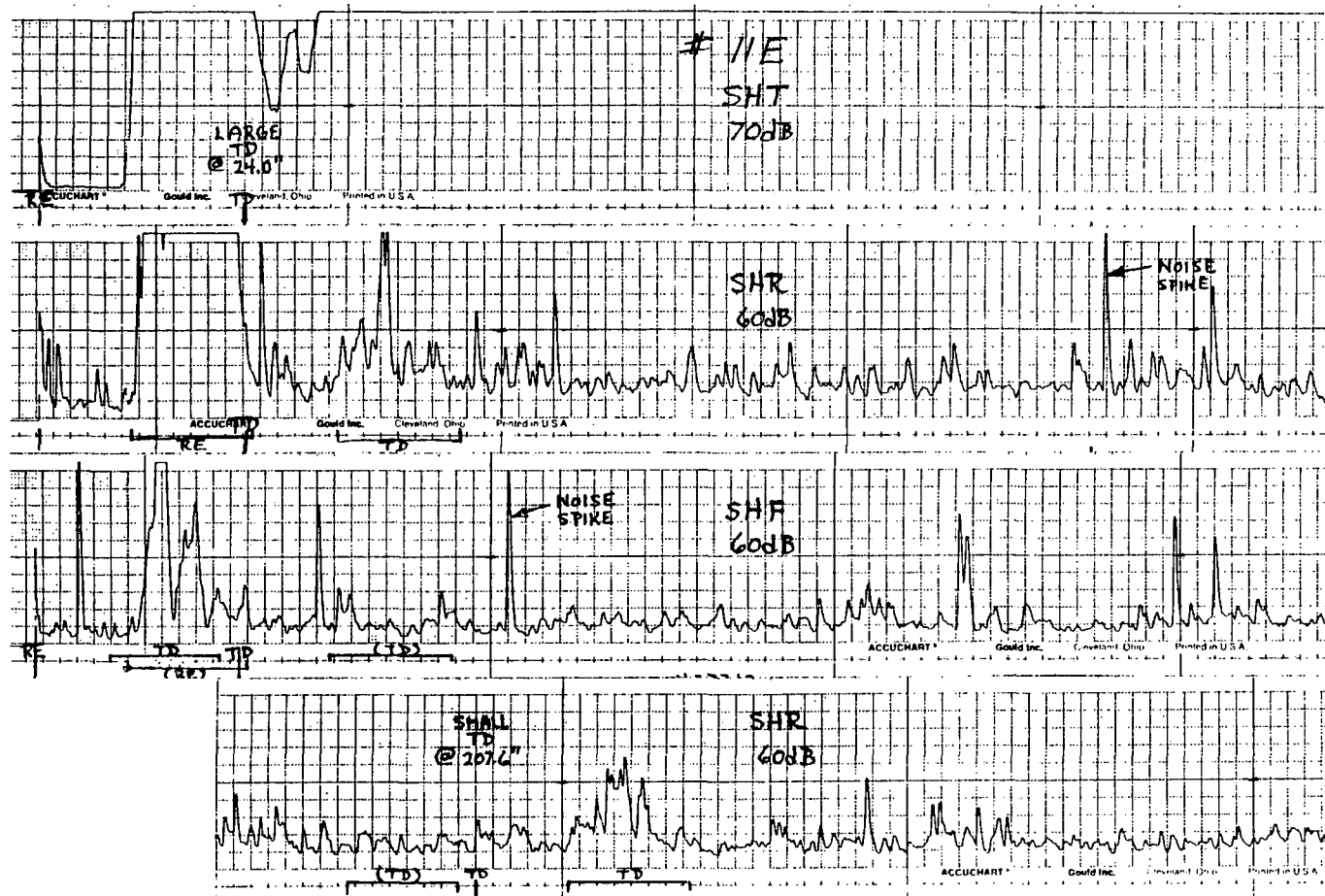


Figure C-36. Detection of 2-TDs in #11E with SH-EMAT. Also illustrates the electronic noise problem that occurred at times.

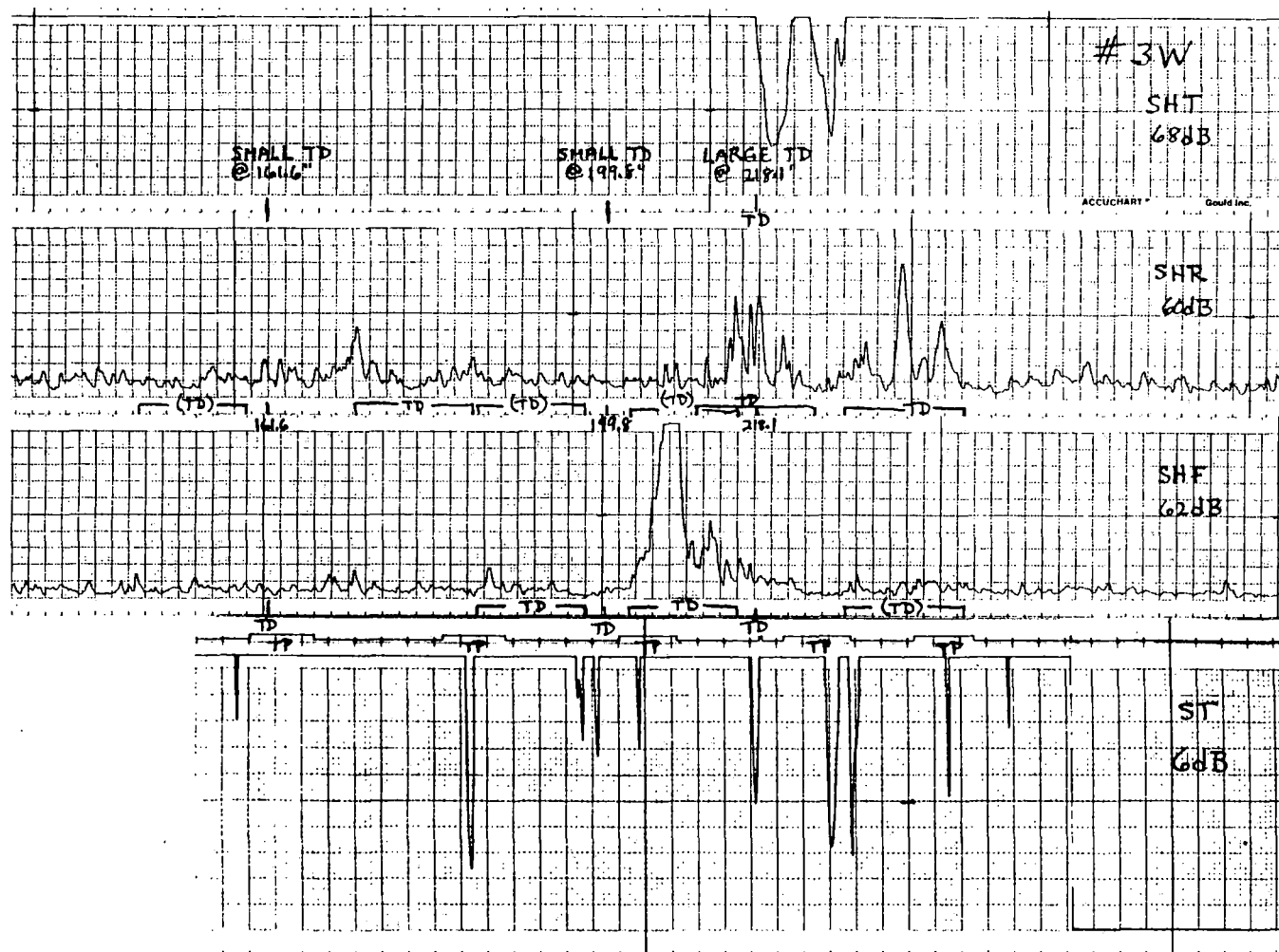


Figure C-37. Detection of 3-TDs in #3W with SH- and ST- EMATs.

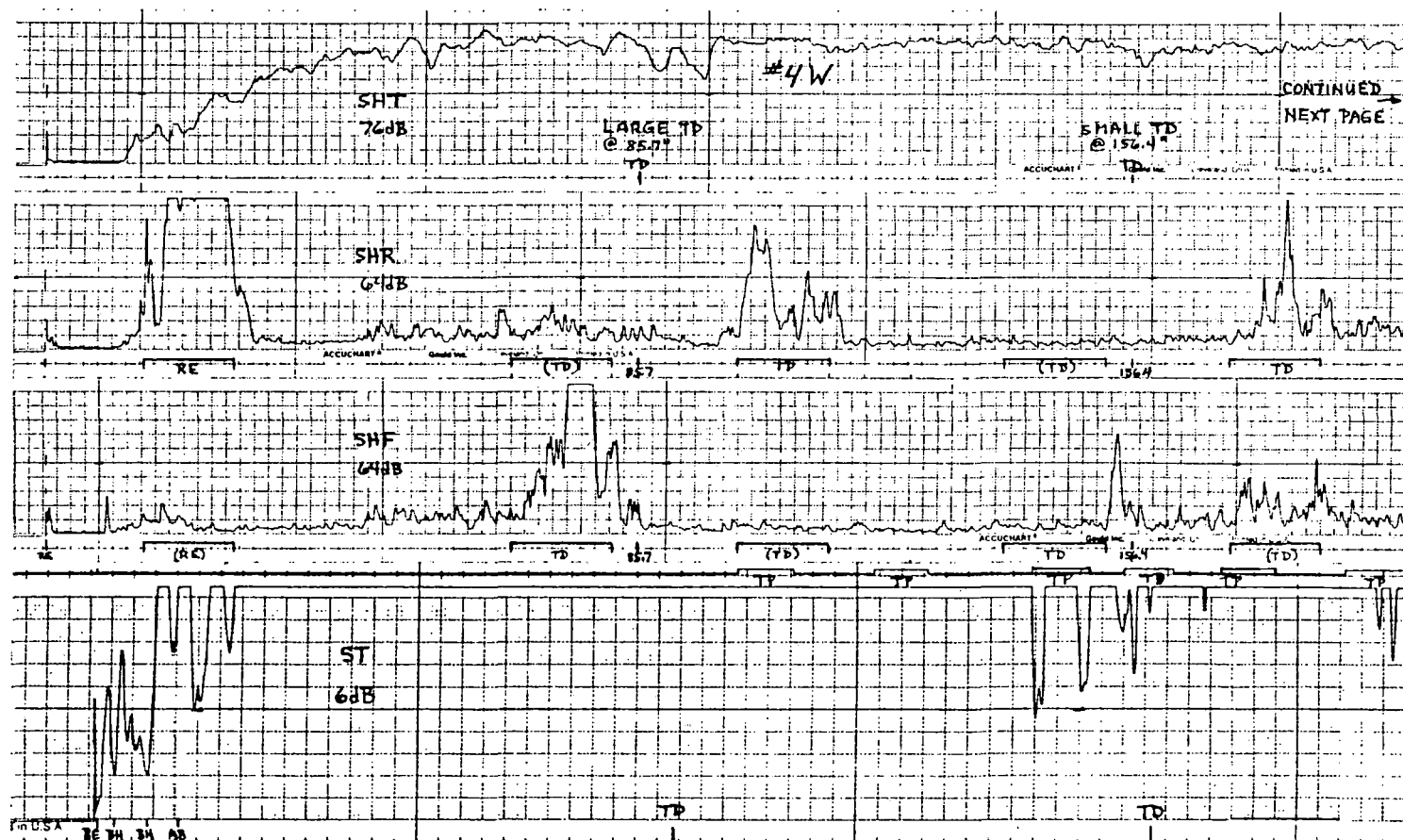


Figure C-38. Detection of 2-TDs in #4W with SH- and ST-EMATs. Also illustrates local variability in SH- direct transmission signal amplitude and ST- base echo loss at some tie plates.



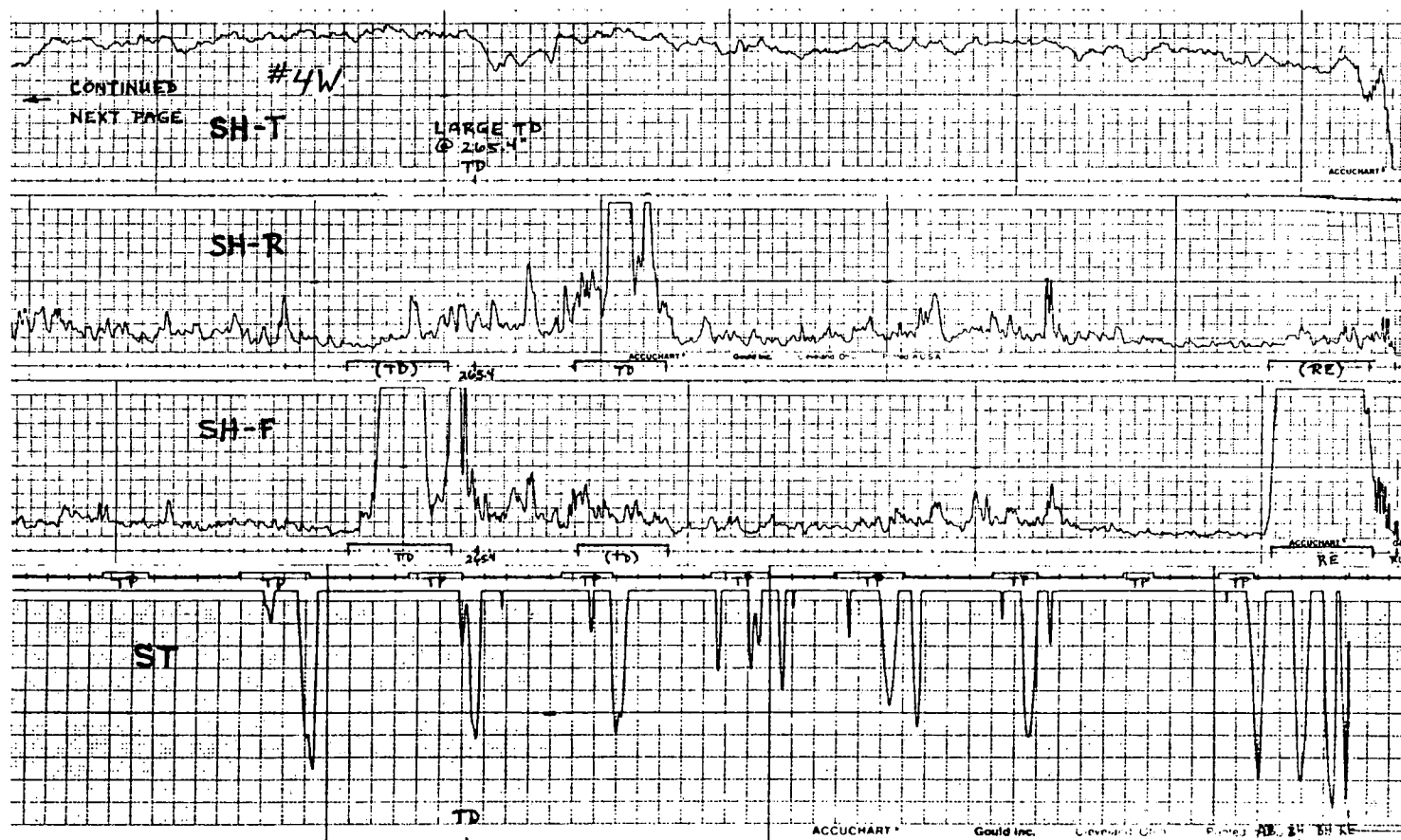
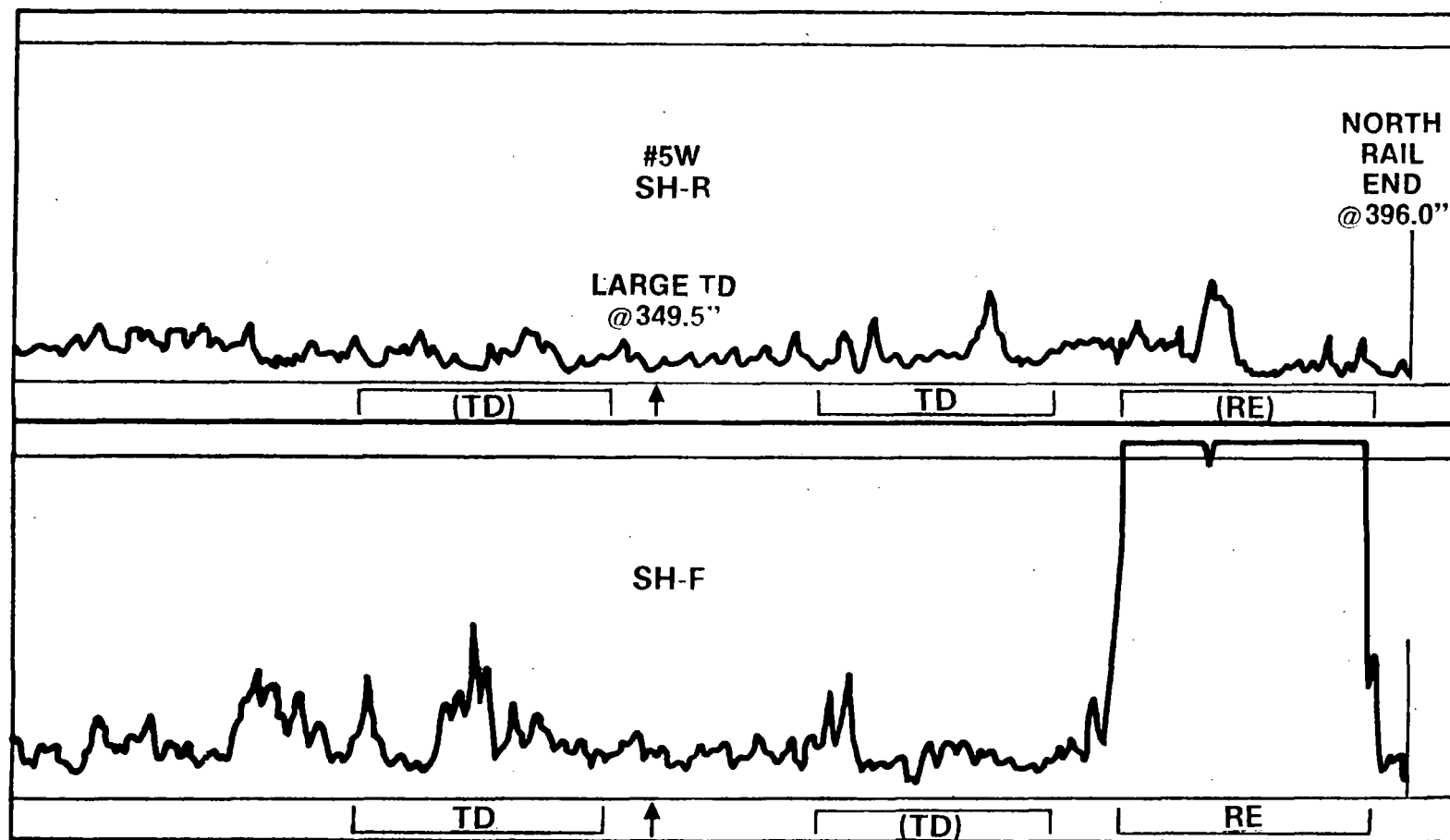


Figure C-39. Continuation of charts from Fig. II-11 showing detection of another large TD in #4W.



C-48

Figure C-40. Illustrating the poor detectability of the large TD in #5W, possibly due to an electromagnetic coupling anomaly.

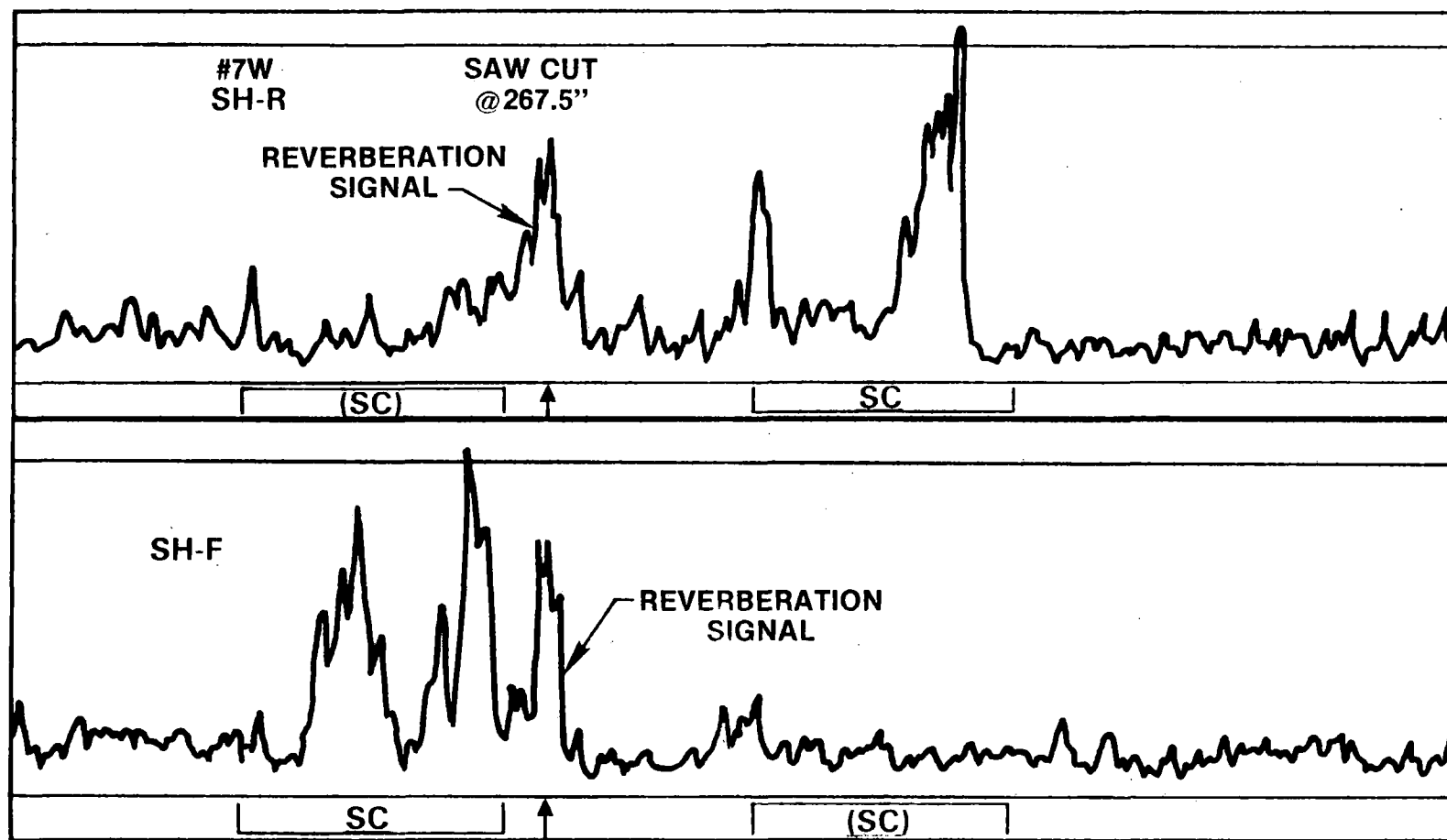


Figure C-41. Detection of 1/4 in. deep saw cut in the side of the rail head in #7W.

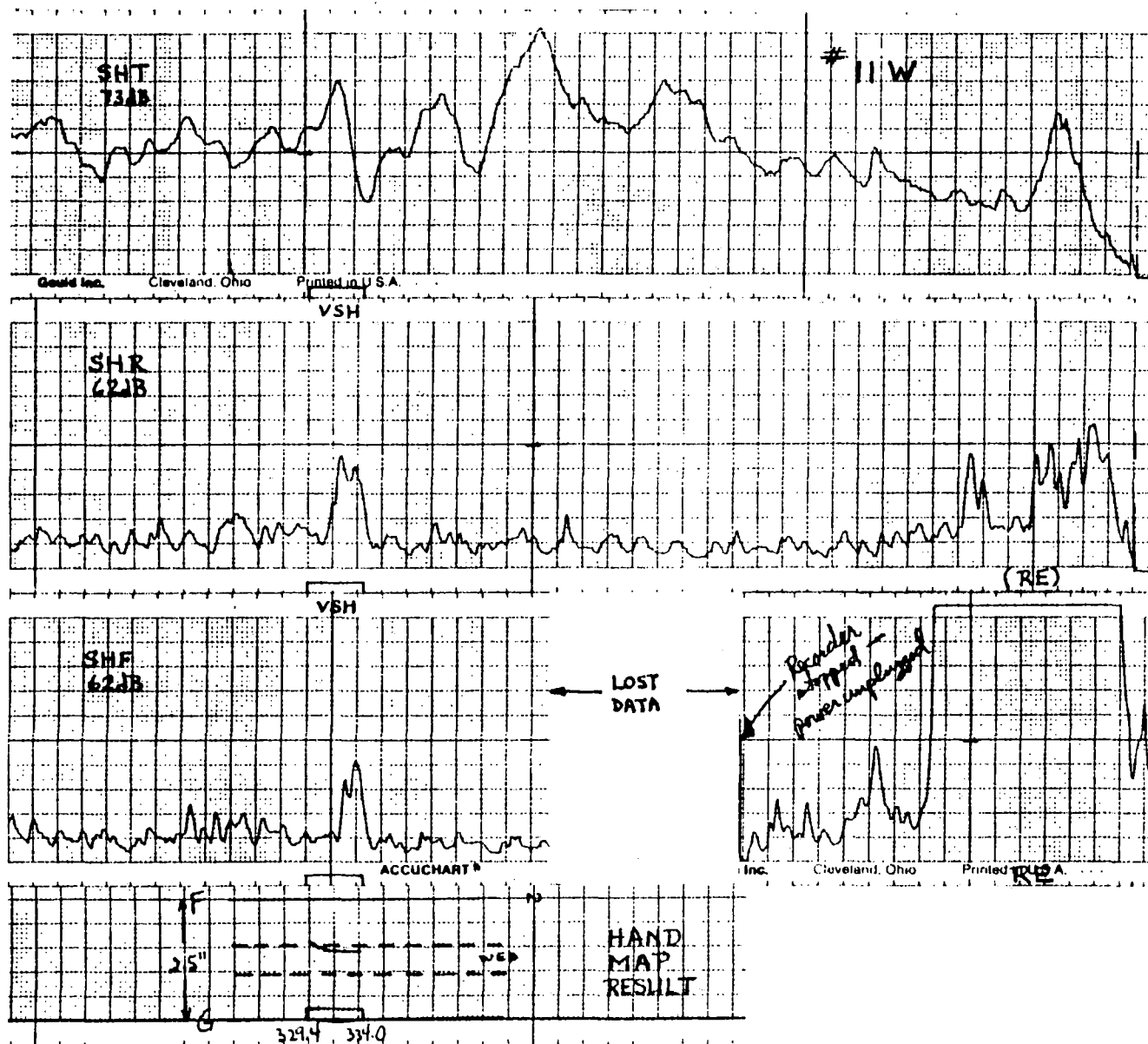


Figure C-42. Detection of small VSH with SH-EMAT in #11W. The ST-EMAT did not detect this defect.

TABLE C-4. DEFECTS AT FAST TRACK

Sec. No.	Tie No.	Rail	Defect Type	Known Size
10	472	0	TD	39%
10	513	0	TD	25%
10	560	0	TD	27%
10	611	0	TD	24%
10	659	0	TD	32%
10	466	I	TD	17%
10	592	I	TD	17%
10	629	I	TD	22%
10	~650	I	TD	Large
7	7	I	TD	3%
10	149	I	TD	7%
10	149R	0	HSH	1 in.
10	222R	0	HSH	4 in.
10	222L	0	HSH	2 in.
10	366R	0	HSH	1 in.
10	343	0	Shell	1 in.
10	445	0	Shell	4 in.
7	73	I	Shell	2 in.
7	149	I	Shell	3 in.
7	345	I	Shell	1 in.

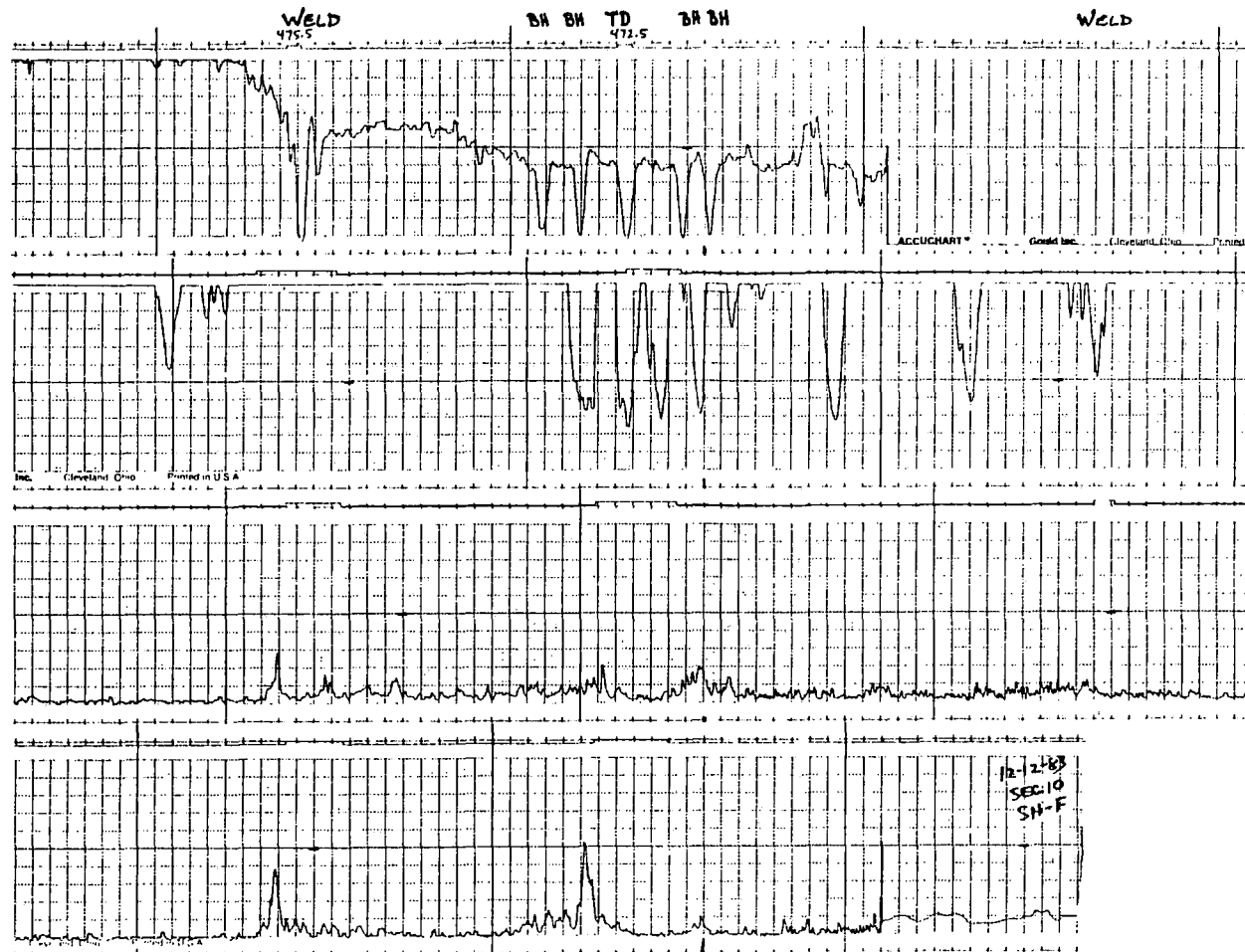


Figure C-43. FAST Sec. #10, TD-472-0, 0.5 MPH; a) ST, 17 dB; b) SHT, 60 dB; c) SHR, 64 dB; d) SHF, 64 dB.

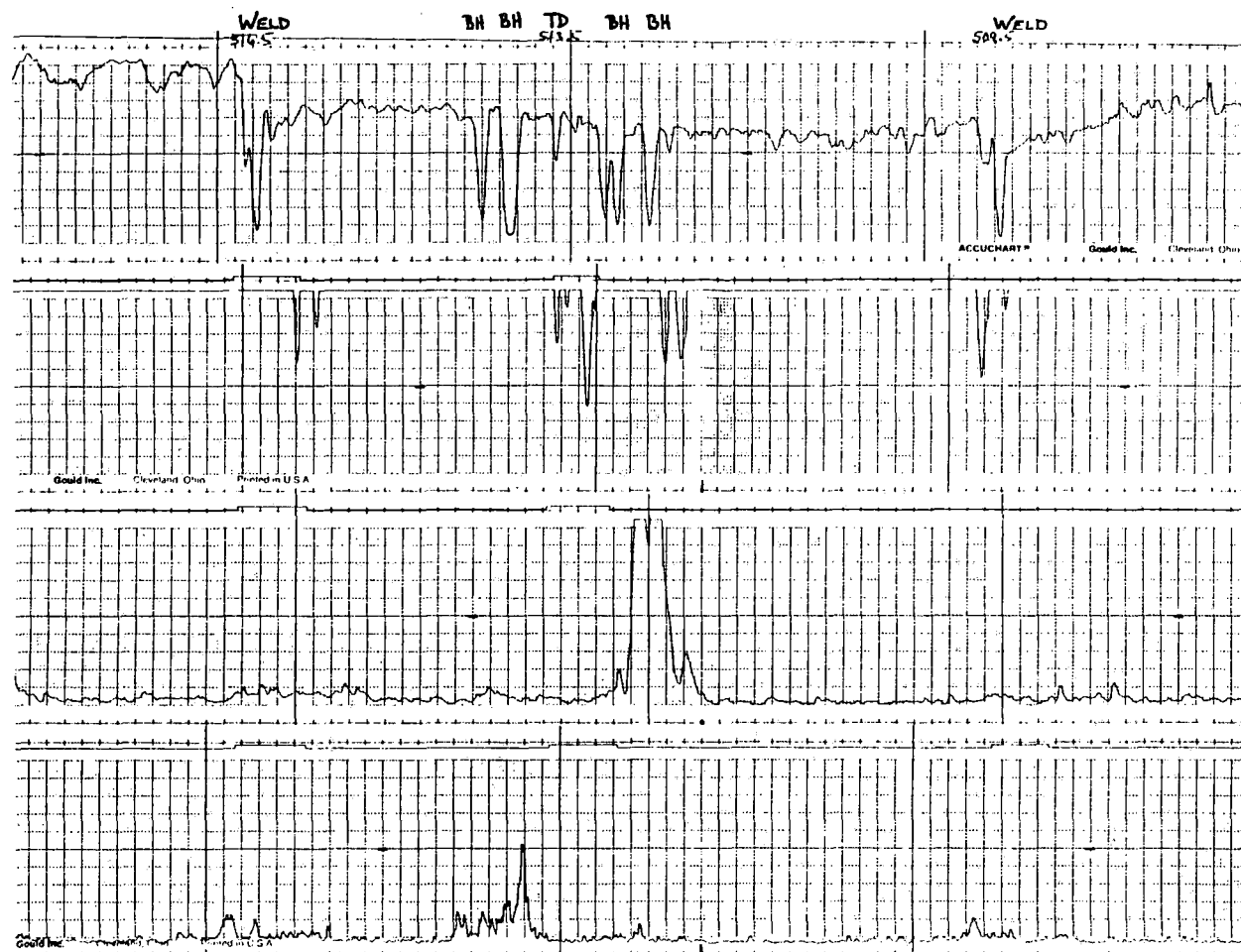


Figure C-44. FAST Sec. #10, TD-513-0, 0.5 MPH; a) ST, 17 dB; b) SHT, 60 dB; c) SHR, 64 dB; d) SHF, 64 dB.



Figure C-45. FAST Sec. #10, TD-560-0, 0.5 MPH; a) ST, 17 dB; b) SHT, 60 dB; c) SHR, 64 dB; d) SHF, 64 dB.



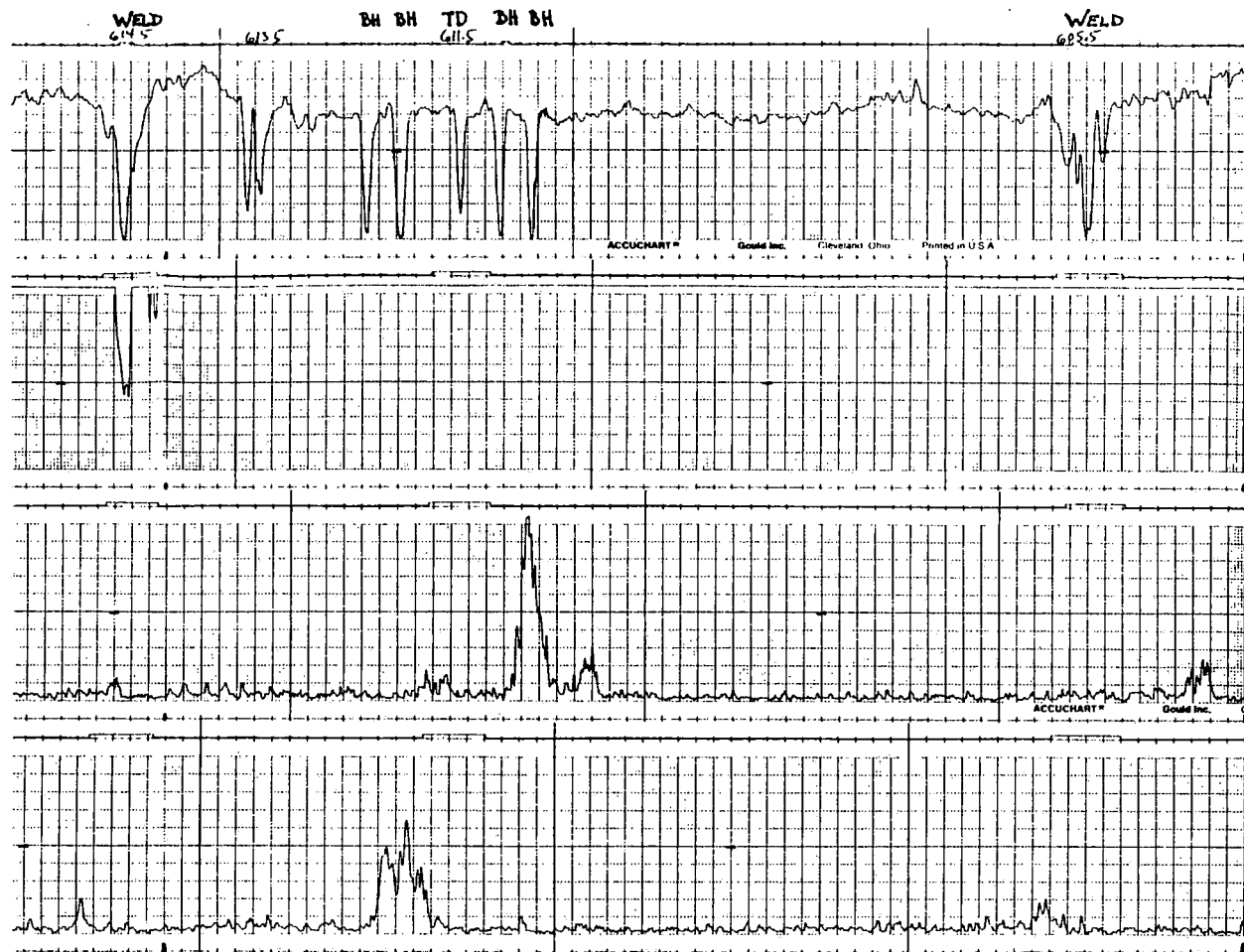


Figure C-46. FAST Sec. #10, TD-611-0, 0.5 MPH; a) ST, 17 dB; b) SHT, 60 dB; c) SHR, 64 dB; d) SHF, 64 dB.

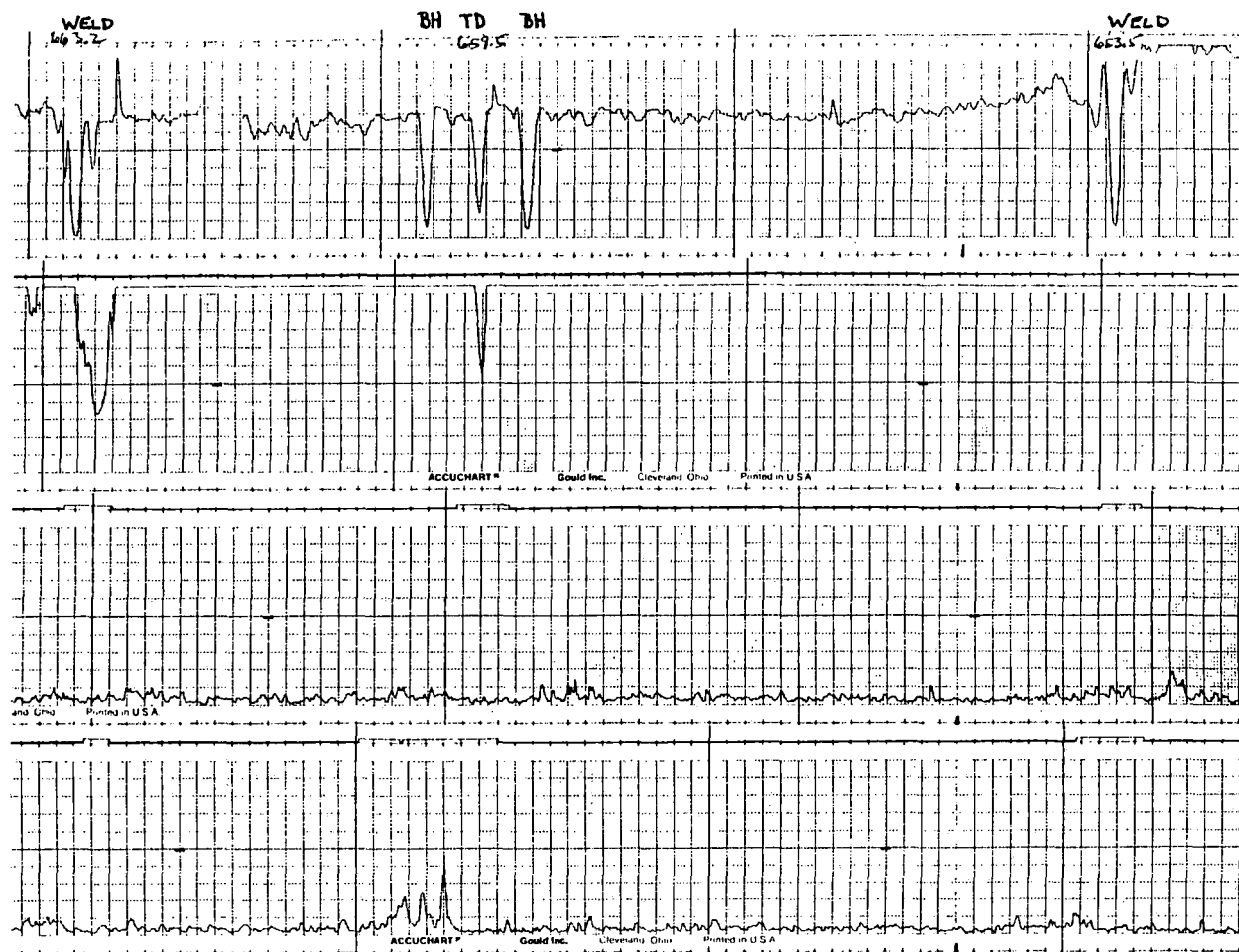


Figure C-47. FAST Sec. #10, TD-659-0, 0.5 MPH; a) ST, 17 dB; b) SHT, 60 dB; c) SHR, 64 dB; d) SHF, 64 dB.

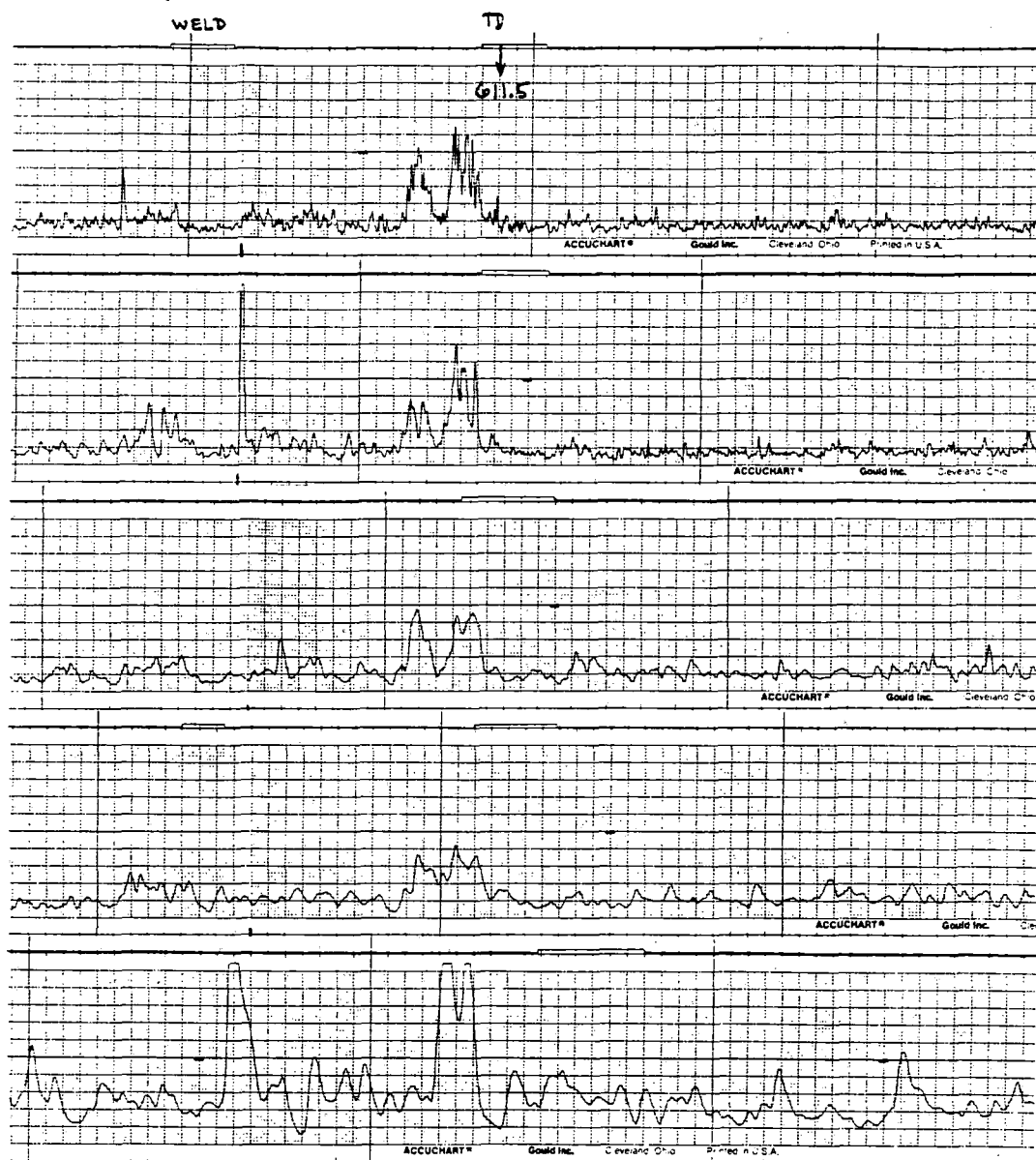


Figure C-48. FAST Sec. #10, TD-611-0, SHF; a) 0.2 MPH, 62 dB; b) 0.5 MPH, 62 dB; c) 1.0 MPH, 62 dB; d) 1.5 MPH, 62 dB; e) 2.0 MPH, 62 dB: showing increase in background noise with increasing speed.

# ST- SPEED TEST - NOISE BACKGROUND

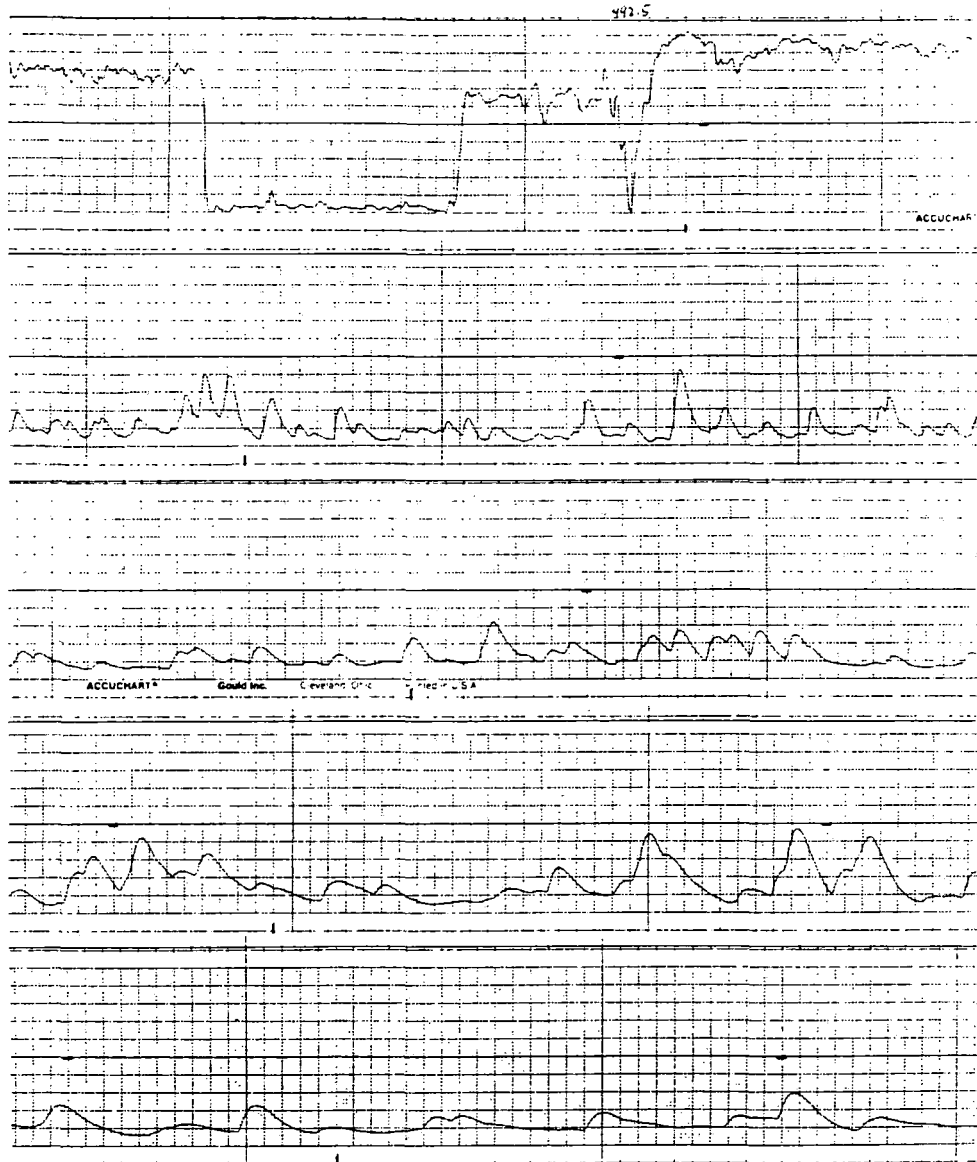


Figure C-49. FAST Sec. #10, ST-background noise; a) 0.5 MPH, 17 dB; b) 2.0 MPH, 16 dB; c) 4.0 MPH, 16 dB; d) 6.0 MPH, 16 dB; e) 8.0 MPH, 16 dB: showing small increase in background noise with increasing speed.

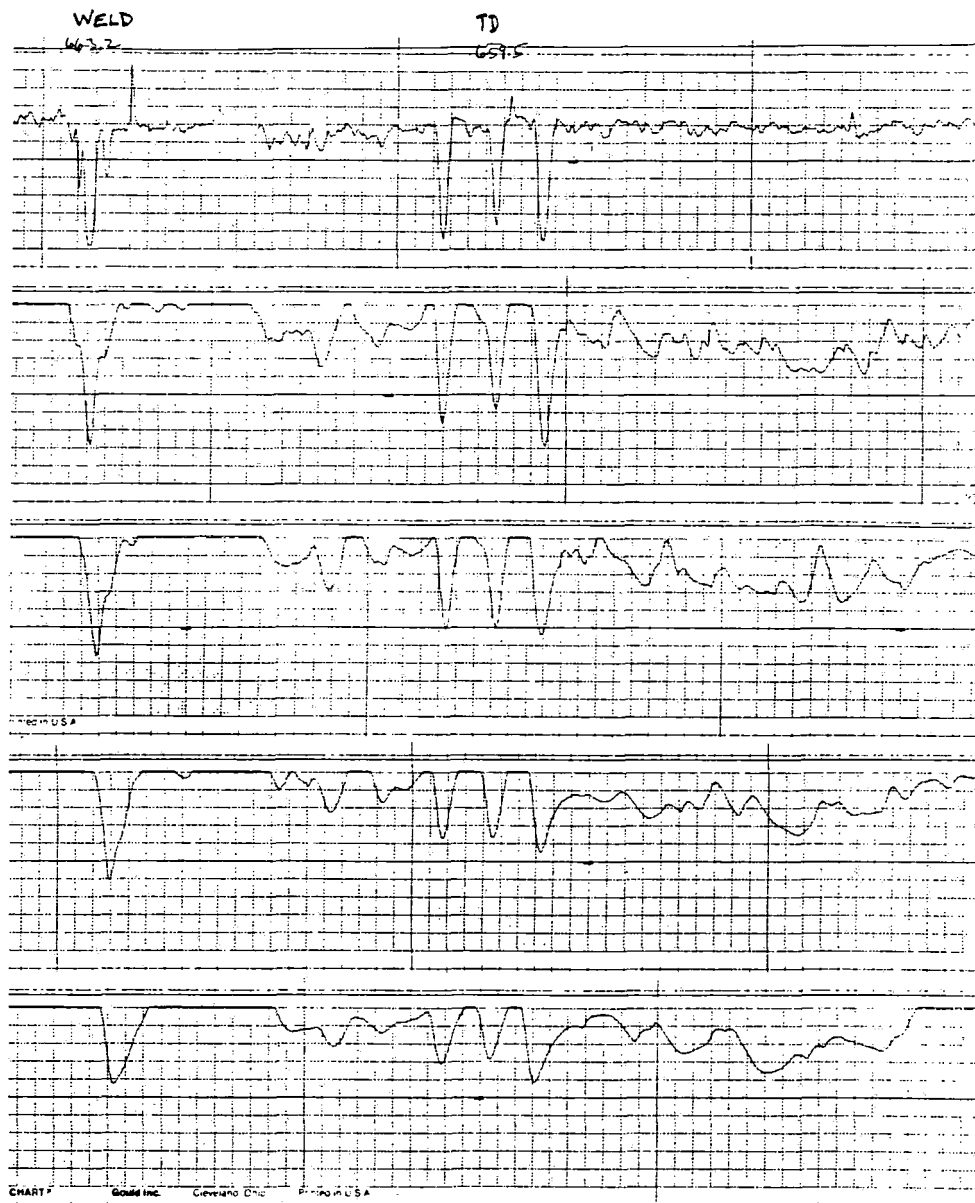


Figure C-50. FAST Sec. #10, ST, TD-659-0, a) 0.5 MPH, 17 dB; b) 2.0 MPH, 16 dB; c) 4.0 MPH, 16 dB; d) 6.0 MPH, 16 dB; e) 8.0 MPH, 16 dB: showing decreased spatial resolution with increasing speed due to limited pulse repetition rate.

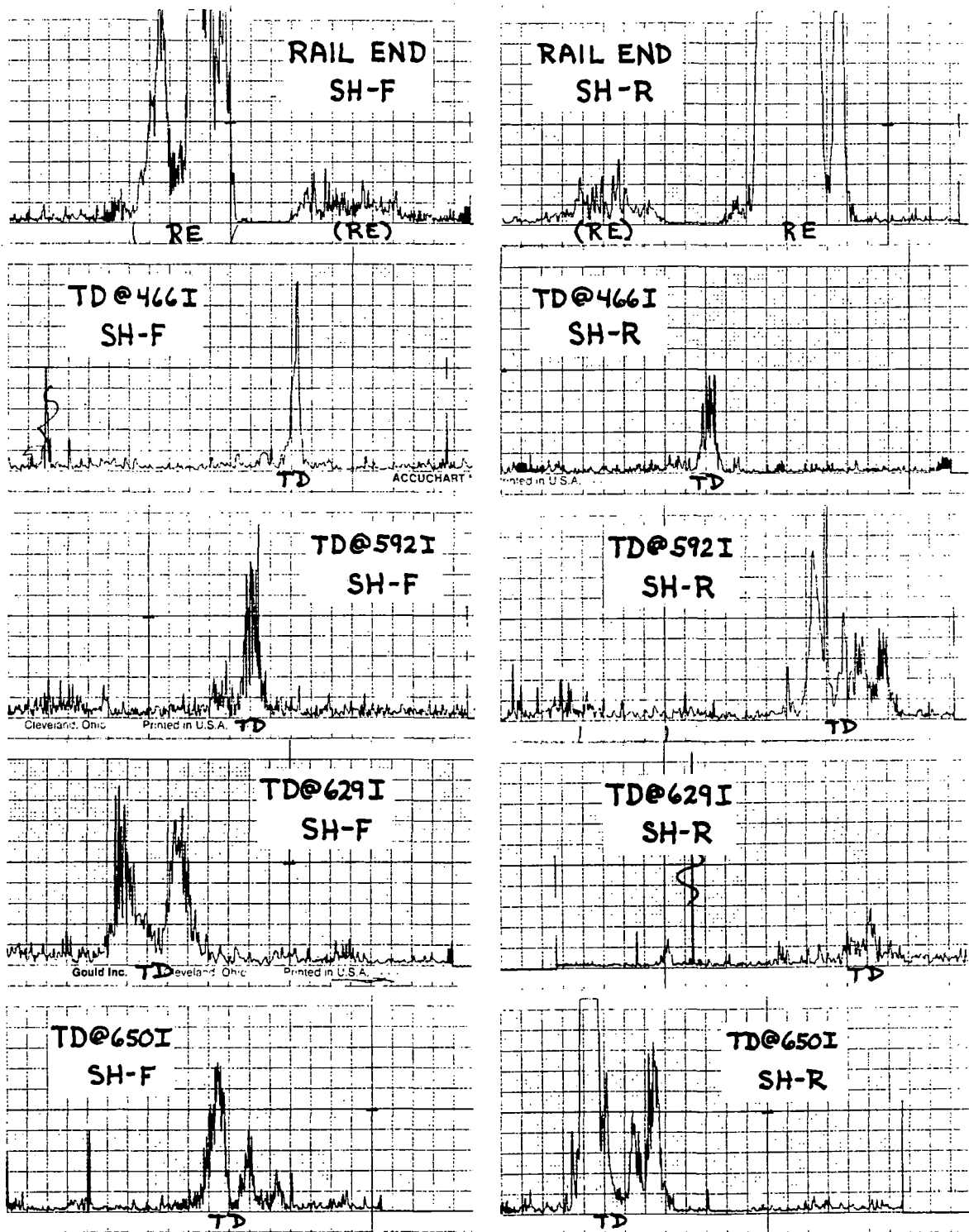


Figure C-51. FAST Sec. #10, SH-detection of four TDs in inner rail.

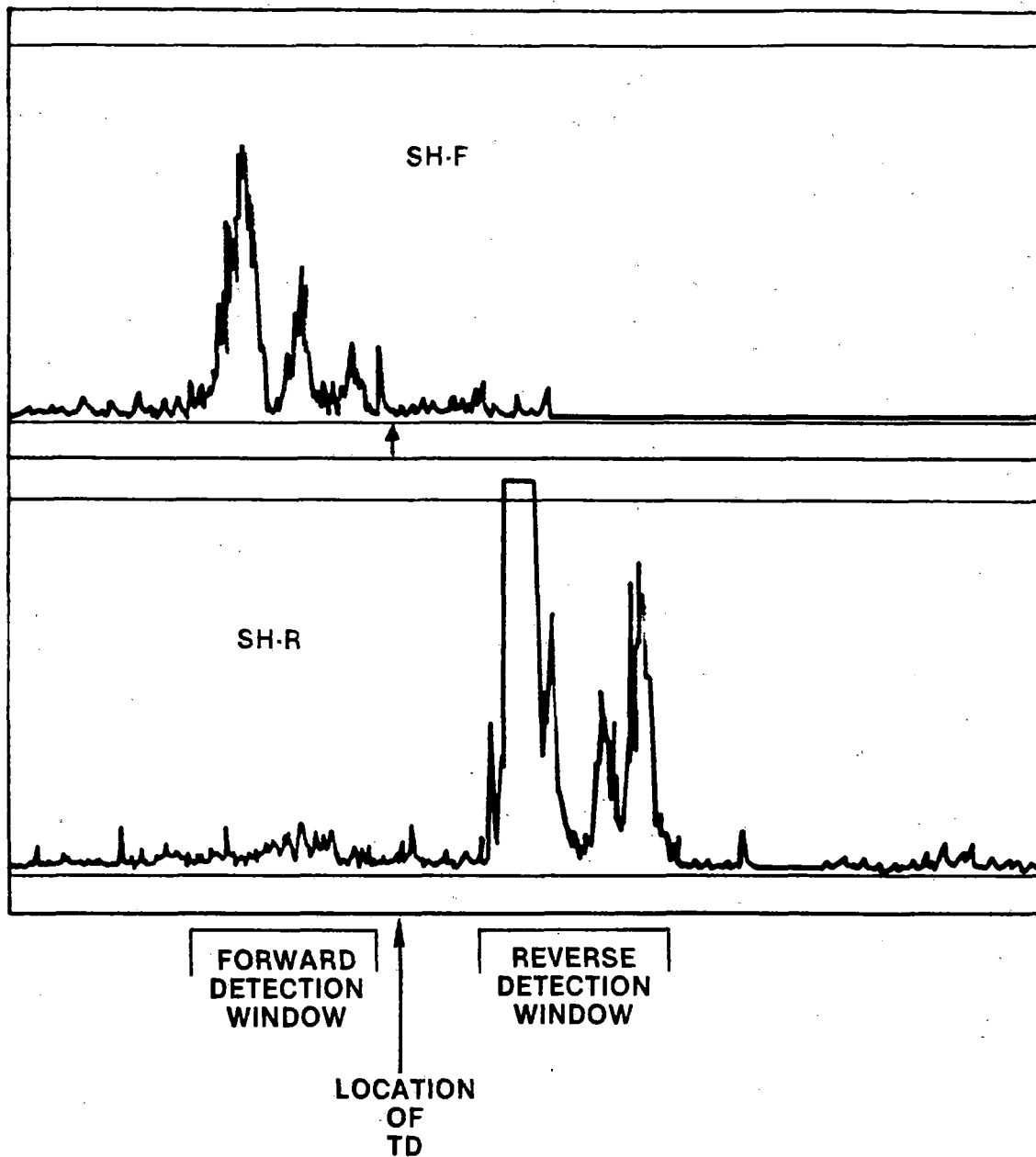


Figure C-52. FAST Sec. #10, SH-detection of large unmarked TD in inner rail near Tie #650.

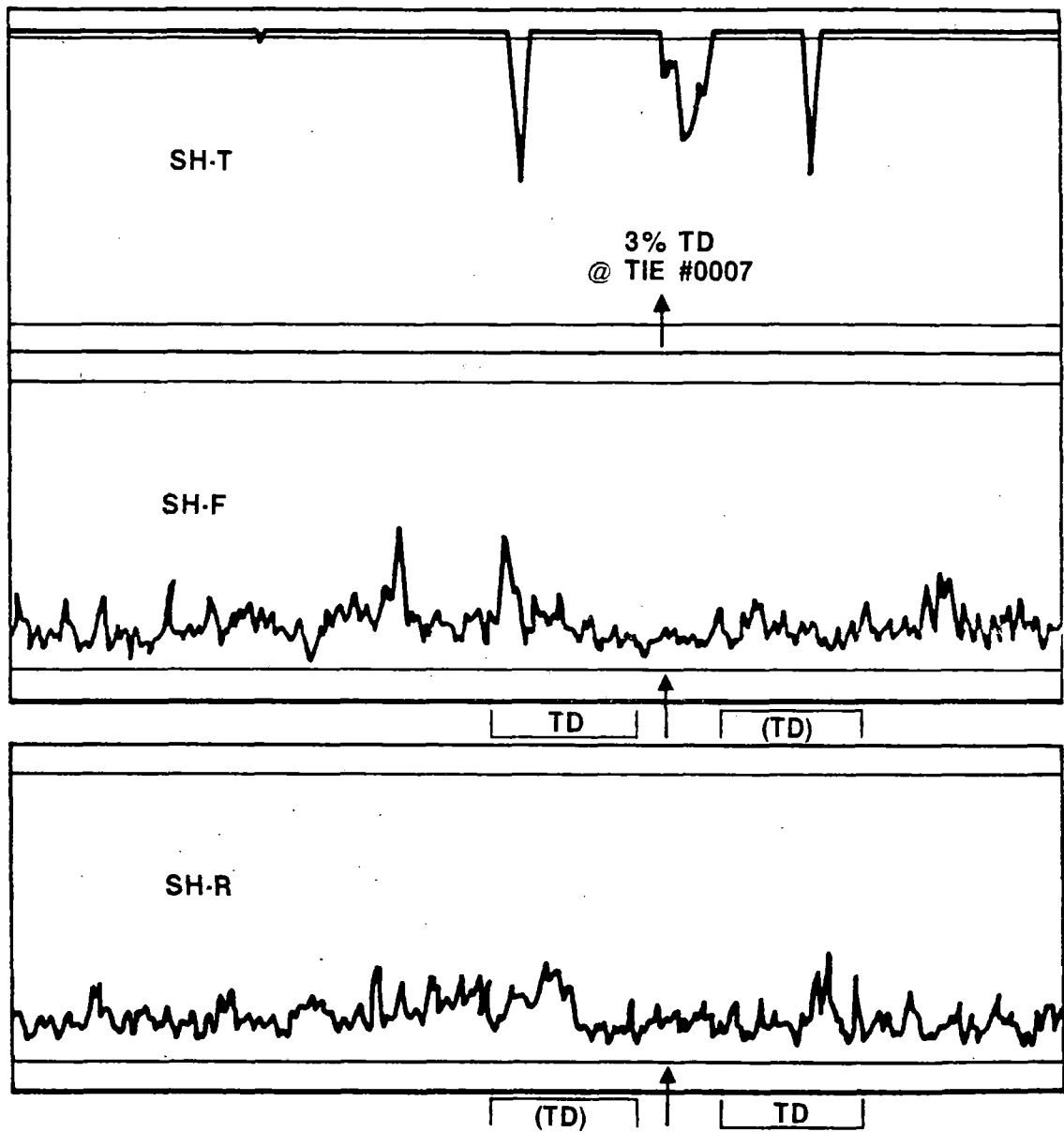


Figure C-53. FAST Sec. #7, marginal SH-detection of 3% TD near Tie #007.



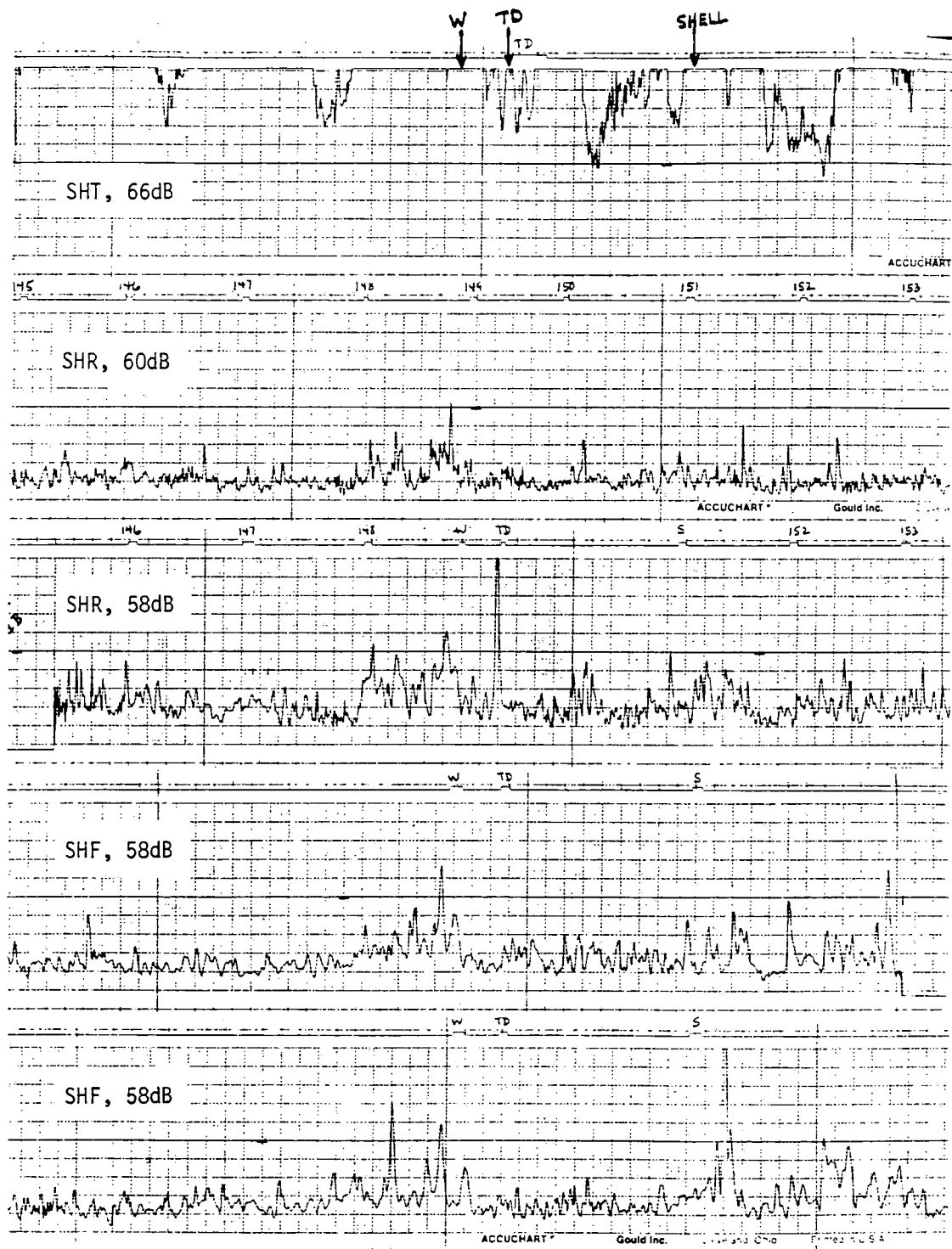


Figure C-54. FAST Sec. #7, marginal SH-detection of 7% TD near Tie #149 with weld joint and SHELL nearby.

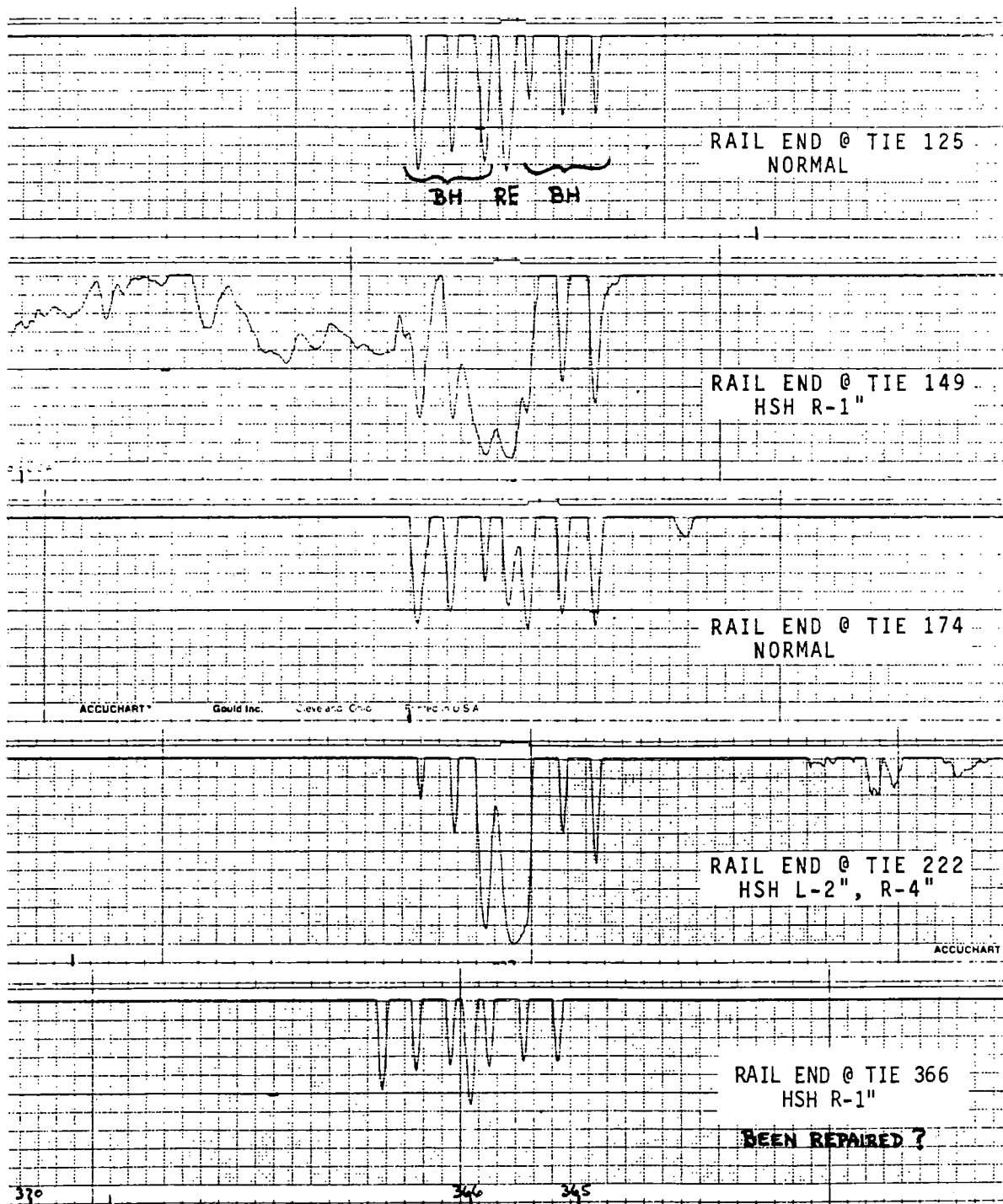


Figure C-55. FAST Sec. #10, ST-base echo, 16 dB, 1.5 MPS; examples of HSH.

C-65

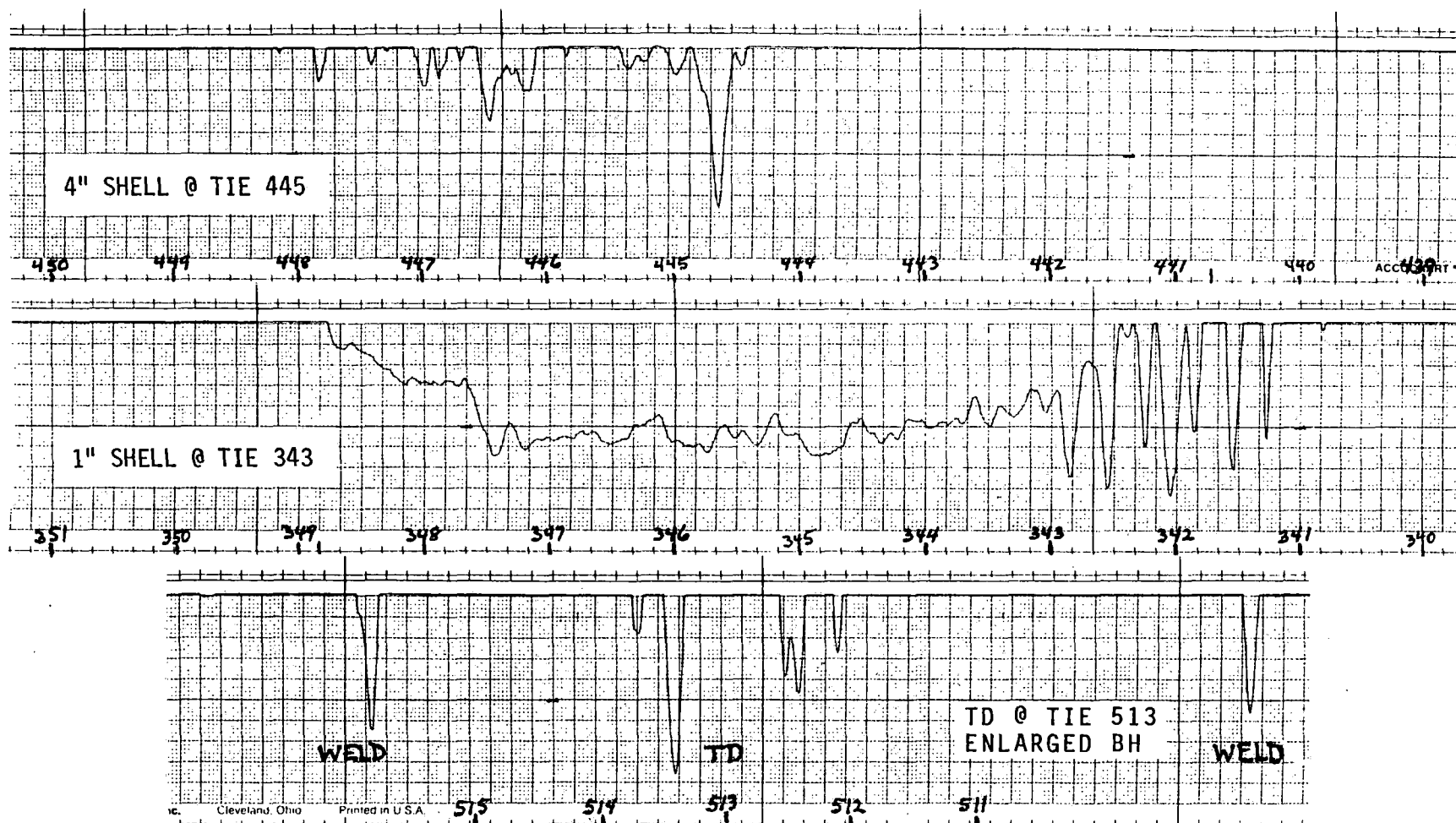


Figure C-56. FAST Sec. #10, ST-base echo, 16 dB, 1.5 MPH; examples of SHELL and the appearance of an enlarged bolt hole (or BHC) at Tie #513.

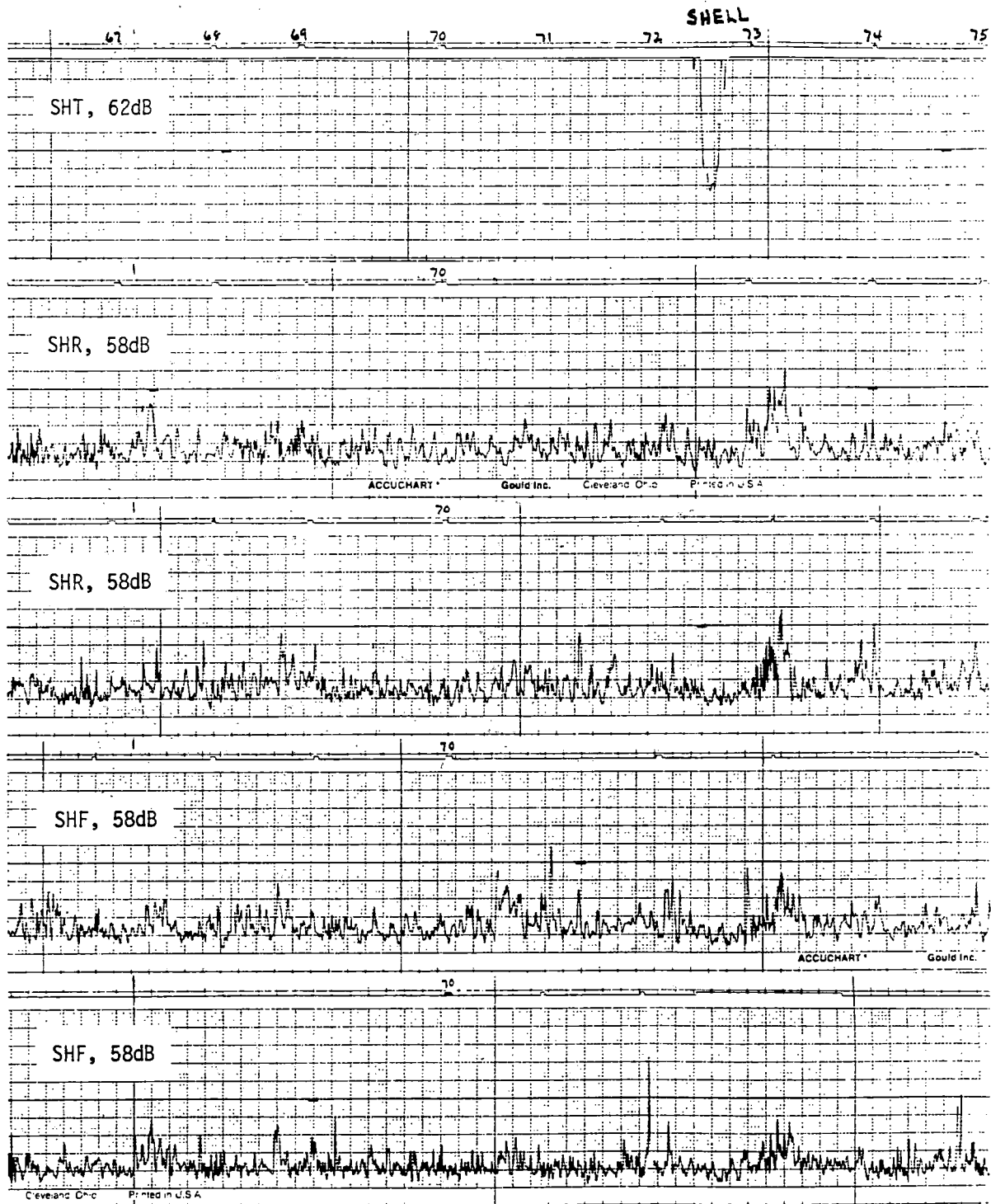


Figure C-57. FAST Sec. #7; 2" SHELL at Tie #073. Rare example of a SHELL being nearly detected as a defect by SH-EMAT.

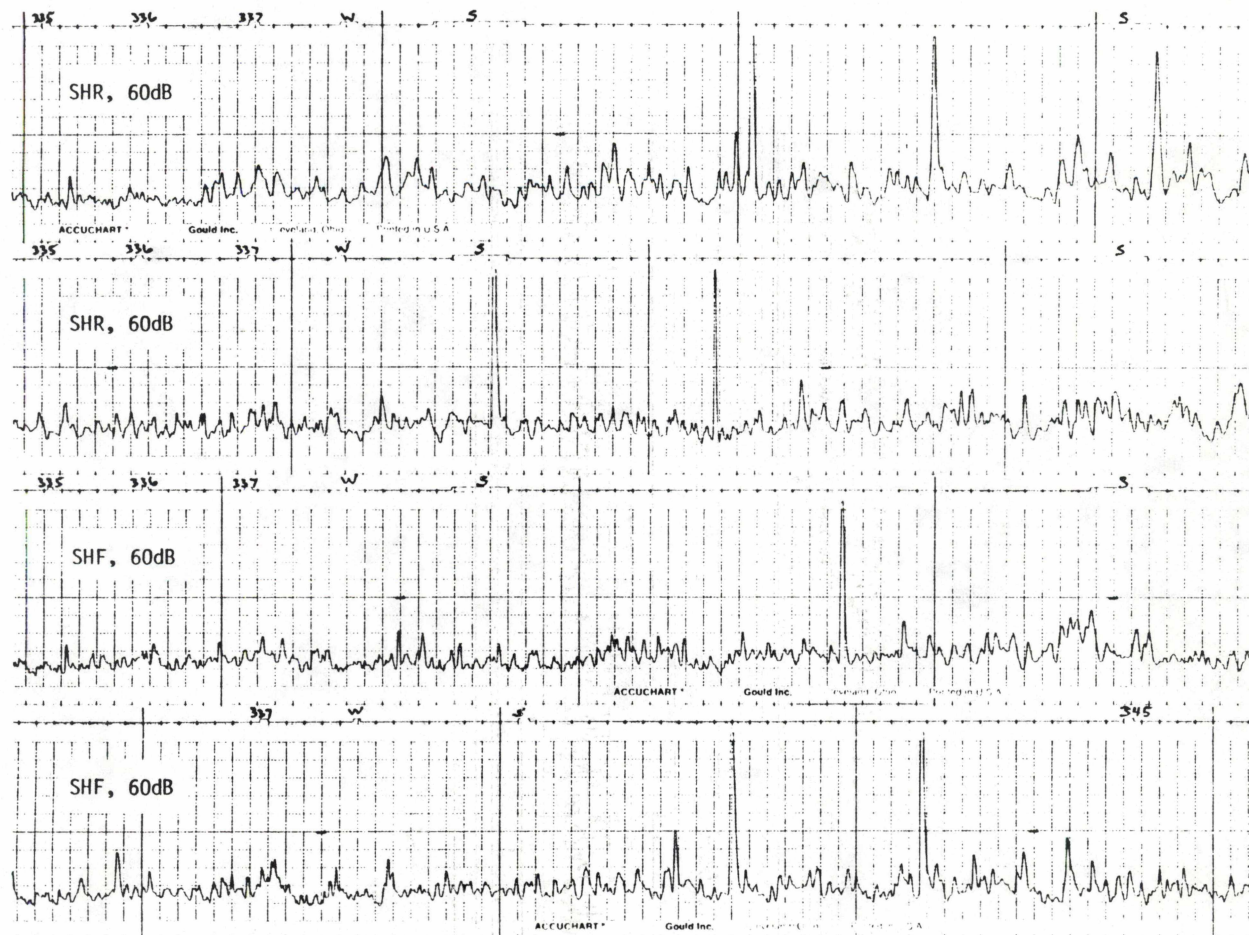


Figure C-58. FAST Sec. #7; 1" SHELL at Tie #345. SHELL is not detectable as a defect; motor/generator electrical noise spikes are apparent.

Ultrasonic Inspection of Railroad Rails by  
Electromagnetic Acoustic Transducers  
(EMATS), 1986

**Ultrasonic Inspection of Railroad Rails by  
Electromagnetic Acoustic Transducers  
(EMATS), 1986**  
US DOT, FRA, Lloyd J Graham, Jim F Martin  
(Rockwell International Science

PROPERTY OF FRA  
RESEARCH & DEVELOPMENT  
LIBRARY